# USING RAMAN SPECTROSCOPY TO STUDY FOULING MECHANISMS IN REVERSE OSMOSIS DESALINATION

By

DANIELLE J. PARK

M.S. University of Colorado Boulder, 2021
B.S. University of Michigan Ann Arbor, 2018

A thesis submitted to the

Faculty of the Graduate School of the

University of Colorado in partial fulfillment

of the requirement for the degree of

Doctor of Philosophy

Department of Mechanical Engineering

2022

Committee Members:

Victor Bright

Yifu Ding

Juliet Gopinath

Alan Greenberg

Richard Noble

Anthony Straub

Abstract

Despite an increased focus on alternative approaches, the dominant technology for desalination remains reverse osmosis (RO). However, like all membrane-based separation processes, RO suffers from membrane fouling, resulting in higher operating costs and energy consumption. Inorganic fouling, usually known as scaling, is a common form of fouling observed in RO-based membrane desalination of high-salinity seawaters and brackish waters. The presence of a variety of inorganics in brackish and seawater feeds, along with high spatial dependence of the concentration polarization-driven scale-formation process, necessitates a high spatial resolution, sensitive, and real-time fouling detection scheme with chemical identification of the foulants. This is crucial for devising an efficient scale removal and prevention strategy. Without real-time local scaling and chemical metrics, scale-control processes can rely on trial-and-error iterations, which can waste valuable resources in the form of energy and capital.

Raman spectroscopy is a nondestructive, in situ (local), real-time methodology based on inelastic light-matter interactions. Raman spectra can provide the chemical fingerprint of the fouling species with spatial resolution (on order of microns) and a rapid temporal response (on the order of seconds). To demonstrate the capability of this technique, I designed and built a bench-scale flat sheet RO system capable of performing multi-day crossflow experiments. The custom flow cell of the RO system featured optical access to the membrane, interfacing with a Raman microscope.

Chapters 1 defines the scope of the work and describes the organization of the dissertation. Chapters 2 and 3 present important technical background on reverse osmosis desalination and Raman spectroscopy. In Chapter 4, real-time Raman detection and monitoring was applied to the deposition and removal of gypsum scale. This study showed that Raman spectroscopy could provide crucial real-time chemical composition and spatial distribution information during membrane cleaning, which can inform more effective antiscaling and cleaning strategies. In Chapter 5, a new RO system and in-house Raman system were designed and assembled to enable the study of lateral scaling progression of calcium carbonate (i.e., scaling as a function of axial position) during longer scaling experiments. The limitations of the prior RO

flow cell, namely nonuniform channel height and small, fixed optical window were resolved. The time evolution of the downstream and upstream calcium carbonate Raman signal was evaluated with respect to computed values of local concentration at the membrane surface, revealing a statistically significant dependence ($p<0.001$). The real-time Raman data were bolstered by results of post-mortem analysis (scanning electron microscopy, gravimetric measurements, laser interferometry), which additionally revealed that the employed technique was capable of detecting crystals with characteristic lengths <50 μm. Chapter 6 addressed real-time Raman detection of two-component scaling using calcium sulfate and calcium carbonate as model scalants (components). First, the limitations of a single-point sampling strategy were demonstrated using the RO flow cell and system presented in Chapter 4. The average dimensions of the two scaling components and the Raman laser beam spot size were identified as important Raman sampling parameters. Flux decline as low as 0.4% and 0.5% was observed at the time of gypsum and calcium carbonate Raman detection, respectively. This supported the Raman sensor's early detection capability and utility as a real-time decision-making tool during plant operation. Additionally, the spatial distribution of the crystals was quantified using a normalized formulation of Ripley's *K* function. Results indicated that crystal distribution pattern was a critical design driver in the optimization of Raman sampling strategy. Chapter 7 summarizes the conclusions of the dissertation work and with recommendations for future work.

DEDICATION

To Umma and Appa, for their endless love and support.

ACKNOWLEDGEMENTS

This work has been primarily funded by the Membrane Science, Engineering and Technology Center (NSF IUCRC Award IIP 1624602) at the University of Colorado Boulder; the National Science Foundation (Award No. CBET 1826542); and the Paul M. Rady Department of Mechanical Engineering for funding support over the past 2 semesters. This work would not have been possible without the guidance and help of many people. In particular, thank you to Dr. Omkar Supekar and my advisors, Dr. Victor Bright, Dr. Juliet Gopinath, and Dr. Alan Greenberg.

Thank you also to the following people who played crucial roles in this thesis work: Dragan Mejic (CU Boulder): fabrication of the crossflow cell; Craig Joy (CU Boulder): fabrication guidance in the machine shop; Dr. Joseph Swisher (EPRI) for helpful technical discussions; Dr. Emily Gibson (CU Anschutz) for lending us their spectrometer, detector, and laser system; Dr. Colin Ingram (Princeton Instruments) for providing demo instruments/software and helpful technical discussions; Colorado Shared Instrumentation in Nanofabrication and Characterization (COSINC, CU Boulder) for SEM/EDS instrumentation; Materials Instrumentation and Multimodal Imaging Core Facility (MIMIC, CU Boulder) for Raman instrumentation; Chris Buelke, Dr. Emanuele Sortino, Sydney Sykes, and Dr. Masoud Aghajani, Lange Simmons, Dr. Jonas Gertsch, Dr. Wei Lim, Dr. Mo Zohrabi for helpful discussions in various aspects of the work.

Thank you to current MEMS research group members: Olivia McIntee, Eddie Miscles, Diane Jung, and Sam Gilinsky.

## Table of Contents

## List of Tables

## List of Figures

# Chapter 1 Introduction

## 1.1 Motivation

Exactly one month before my defense, there was a hearing before the Senate Committee on Energy and Natural Resources, where the Bureau of Reclamation's Commissioner, Camille Calimlin Touton, emphasized that an additional 2 to 4 million acre-feet of *additional* conservation was necessary to simply protect critical water levels in Lake Powell and Lake Mead (Figure 1-1).

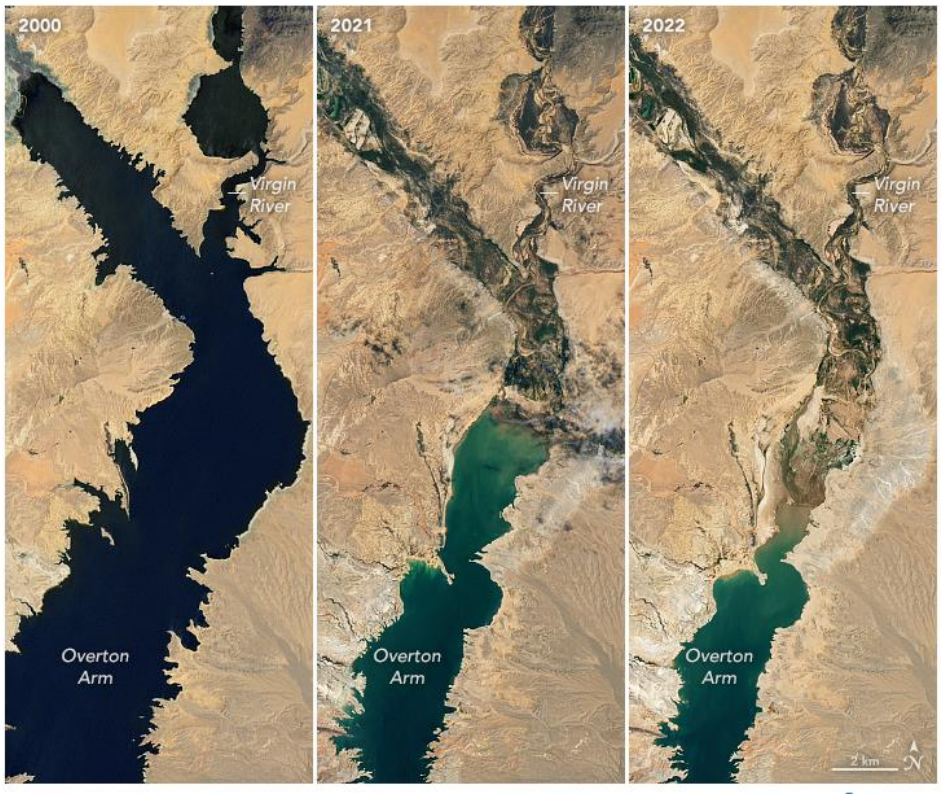


Figure 1-1. As the Colorado River Basin enters its 23rd year of a historic drought, Lake Mead, one of the largest reservoirs in the United States, has reached critical levels and is expected to drop to 27% capacity by the end of the year. The lake water elevation in 2000, shown left, was more than 150 ft higher than the present water elevation, shown right (NASA).

In the past four years as a graduate student at the University of Colorado Boulder, I have read countless journal articles about water scarcity and desalination (the removal of salt from water), and I have

also witnessed some of the serious consequences of the Colorado River Basin's ongoing historic drought. Even so, I regularly fail to grasp the urgency and enormity of the water-related challenges at hand, thanks to a combination of privilege and The Science of What Makes People Care [1]. As a remedy attempt, I often catch myself conjuring up memories of backpacking/camping trips in an effort to reactivate a mindset of water conservation: the difficulty of washing dishes or brushing my teeth with only half a bottle of water seems to serve as an effective brain hack.

As for the relevance of this monologue, I have found that a water conservation mindset, and in turn, a more personal connection to the present water crisis, was absolutely necessary for the greater appreciation of underlying motivation for my research—the optimization of desalination technologies and relief for water-stressed communities (locally and globally). This is not to say that desalination is a perfect solution. More often than not, it is a fairly divisive topic due to issues such as high energy consumption and resulting cost, which could disproportionately affect low-income families. Still, desalination is a proven and reliable technology that can be incorporated in a holistic solution towards water *security*. In fact, during the Senate hearing noted earlier, the Bureau of Reclamation Commissioner mentioned desalination as one of the agency's freshly funded Bureau of Reclamation infrastructure projects, which also included water storage projects, water recycling projects, and drought contingency plans. Therefore, a more consistent practice of personally connecting with water issues, can allow us to keep an open mind about desalination and see that any improvements in the desalination efficiency, large or small, have the potential for positive ripple effects.

In membrane-based desalination, reverse osmosis (RO) desalination (Figure 1-2) has emerged as the leading technology for its combination of reliable water quality, ability to process high-salinity feed waters, and low energy consumption compared to thermal desalination technologies [2–4].

Figure 1-2. A full-scale desalination plant, featuring spiral wound membranes connected in series to form larger units called membrane trains. Fortunately, membrane trains are designed to be modular, so a single train can come offline for cleaning while the rest of the plant continues to operate (Dr. Sergio Salinas).

Despite the widespread implementation of the technology, RO suffers from the negative effects of membrane fouling, which causes decreases in permeate flux and permeate quality, increased plant downtime associated with membrane cleaning, and shortened membrane lifespan. All of these effects give rise to greater energy consumption and higher operating costs [5]. Membrane fouling is a broad term for the accumulation of undesired deposits on or within the membrane, causing increased energy consumption and operating costs, lower membrane performance and shorter membrane lifespans [5–7]. In particular, inorganic fouling (Figure 1-3) poses a particular obstacle for RO desalination of high salinity seawater and brackish water, due to the high concentrations of mineral salts in the feed water. When supersaturated concentrations of dissolved mineral ions are present, solid salts can precipitate out of solution and subsequently deposit onto the membrane surface. The deposited crystals, known as scale, can form a tenacious layer that can be difficult to remove. If detected too late, the scaling layer can become irreversible, requiring costly and time-consuming membrane replacement.

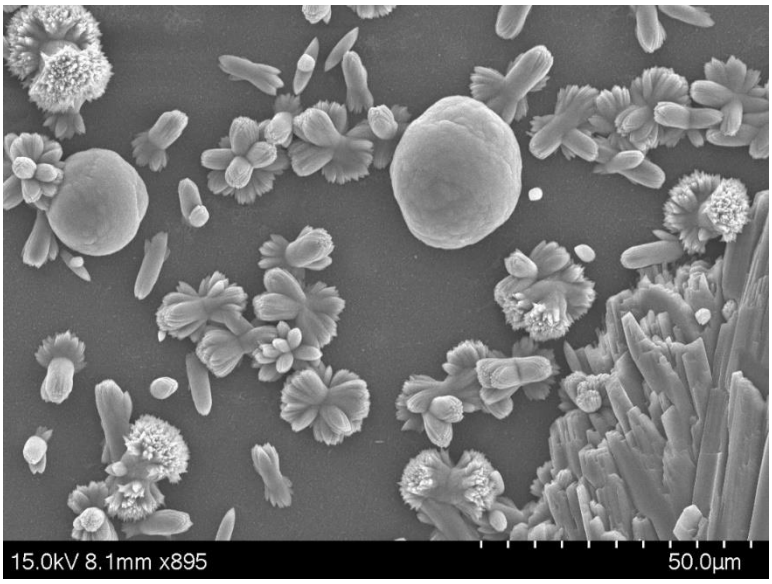


Figure 1-3. Scanning electron microscope (SEM) image of calcium sulfate and calcium carbonate scaling on a reverse osmosis membrane (author's own image).

Figure 1-4. Scanning electron microscope (SEM) image of calcium sulfate and calcium carbonate scaling on a reverse osmosis membrane (author's own image).

In order to mitigate the negative effects of scaling, the performance of the membrane modules should be monitored closely. This typically involves the measurement of global metrics such as permeate flux decline, increases in transmembrane pressure, or increases in salt rejection. However, due to a spatial dependence of the onset of membrane scaling, global metrics can lack the spatial resolution necessary for the detection of membrane scaling, since they are averaged over a large area. Alternatively, more local measurements placed in strategic locations can lead to improved spatial resolution necessary for detection of early onset scaling, and therefore, greater chances of successful scale control. In addition to local early detection, effective scale treatment is highly specific to the scalant chemistry. Thus, knowledge of the location and timing of early scale formation is necessary but insufficient for optimum mangement. One example of scale control is the usage of pretreatment steps, such as feedwater acidification, before passing on the feed to the RO stage. Acidification works by increasing the solubility of calcium carbonate crystals, effectively lowering the chances of precipitation. However, it is important to note that natural feed waters can contain many different scaling and fouling species, such that scale-control techniques may not always

result in a desired effect. Therefore, real-time chemical sensing is necessary not only for early detection of membrane scaling, but also for the development of strategies for optimized scaling prevention, cleaning, and control, which can ultimately lead to valuable increases in RO efficiency.

Thus, the unique capabilities of Raman spectroscopy are utilized in this work to obtain the chemical fingerprints of the problematic scaling crystals. Raman spectroscopy is an optical technique favored for its ability to noninvasively and nondestructively identify the chemical composition of materials with Raman active cross sections. Moreover, scaling necessarily occurs in a water environment. For an optical technique such as infrared (IR) spectroscopy, a water environment would result in IR spectra dominated by intense absorption bands arising from water's O-H stretching vibrations. On the other hand, water is a weak Raman scatterer, such that Raman spectroscopy is particularly well suited for the present application of studying scaling on reverse osmosis membranes in real-time.

## 1.2 Scope of the Work

### 1.2.1 *Research aim*

This dissertation work aims to implement Raman spectroscopy as a real-time sensor for membrane scaling detection in reverse osmosis desalination, and belongs to a broader group of techniques known as in-situ monitoring [8] (also known as on-line [9], direct [10], or real-time monitoring [11]). Since the performance of the Raman sensor is evaluated using existing knowledge of membrane scaling, the presented work is largely solution-driven and thus appropriately characterized as applied research. However, the work also incorporates elements of basic research that seeks to expand the present understanding of membrane scaling phenomena, and in particular, multi-component scaling.

### 1.2.2 *Problem statement*

A literature review of in-situ monitoring techniques (Chapter 2.4) reveals a lack of real-time chemical identification capability, resulting in a significant number of laboratory fouling studies that only focus on single-salt (also termed single-species or -component) scaling detection. Even when complex feed

compositions are utilized (e.g., ultrafiltration of paper mill effluent [10]), discussion is generally limited to morphological descriptions of the fouling layer. Thus, a more in-depth understanding of scaling mechanisms involving multiple species/components is largely unavailable. However, this is crucial missing information since the feed waters used in field settings contain multiple scaling species [12], and the success of scale-control techniques relies on the chemistry of the deposited scales. Hence, a Raman-based methodology was developed to detect and monitor scaling of reverse osmosis membranes with real-time chemical sensing of both single-component and multi-component membrane scaling.

### 1.2.3 *Research questions*

The following research questions (RQ) guide this work.

**RQ 1:** How does the Raman sensor respond to **single-component** scaling compared to standard reverse osmosis (RO) performance metrics such as flux decline?

**RQ 2:** How does the Raman sensor respond to **multi-component** scaling compared to standard RO performance metrics such as flux decline?

For each of the aforementioned research questions, four additional sub-questions are identified. RQ 3–5 raise issues related to assessing the performance of the Raman sensor, and based on the performance assessment, RQ 6 asks how the developed technique can be improved.

**RQ 3:** What is the extent and composition of membrane scaling at the time of Raman detection?

**RQ 4:** Can the systematic increase/decrease in Raman signals be related to the local progression of membrane scaling?

**RQ 5:** What is the Raman signal response to membrane scaling as a function of membrane axial position?

**RQ 6:** What are the most important factors to consider in an optimized Raman sampling strategy, and how do they influence the performance of the Raman sensor?

### 1.2.4 *Research objectives*

The following research objectives have enabled the investigation of the proposed research questions:

1. Design, build, and test a bench-scale crossflow reverse osmosis (RO) module. The module requires an optical window that has dimensions suitable for Raman data collection at multiple axial locations and should withstand operating pressures of up to 1.35 MPa. The distance between the Raman microscope objective and the membrane surface should not exceed the working distance of the microscope objective.
2. Design, build, and test a bench-scale RO system capable of multi-day operation. This enables implementation of a wider range of RO operating conditions and scaling experiment durations.
3. Design, build, and characterize performance of an in-house Raman microscope. The Raman microscope should provide sufficient signal-to-noise ratios and spectral resolution to distinguish relevant Raman bands of interest.
4. Develop a standard experimental procedure for scaling tests (e.g., membrane pretreatment/compaction, membrane scaling, RO system cleaning and shutdown).
5. Develop a Raman signal processing procedure which will be consistently applied to all Raman datasets to minimize the introduction of artifacts in the spectral data.
6. Acquire Raman data at different axial positions on the membrane during RO desalination of single-component and two-component salt feed solutions.
7. Modify the Raman microscope to enable more sophisticated Raman sampling strategies for more accurate and representative membrane scaling detection.

## 1.3 Summary and Organization of the Dissertation

**Chapter 1** serves to motivate and define the scope of the completed work.

**Chapter 2** provides an overview of reverse osmosis desalination and identifies membrane fouling as the technology's main limiting factor. It explains why the development of in-situ monitoring techniques

can play a key role in membrane scaling and fouling mitigation by delving into a literature review of the currently available in-situ monitoring techniques. A critique of the existing techniques serves as a rationale for Raman spectroscopy as a viable in-situ monitoring technique, and the feasibility of the Raman sensor's bench-scale and commercial-scale implementation is briefly discussed. Finally, important design drivers for the reverse osmosis system are outlined.

**Chapter 3** presents the main principles of Raman spectroscopy, beginning with an explanation of Raman scattering in free molecules. Once the theory is laid out for a single molecule, we introduce scattering by solids. The selection rules for Raman activity and the dependencies of the Raman intensity are laid out. Finally, a comprehensive overview of the Raman instrumentation used in this dissertation work is also provided.

**In Chapter 4,** real-time Raman data and permeate flux were recorded during a series of membrane scaling and cleaning experiments. A single-component $CaSO_4$ solution was used as the model feed solution (**RQ 1**), and deionized water was the representative cleaning agent. A fixed, single-point laser beam was positioned at the center of the membrane for real-time Raman data collection during the scaling/cleaning experiments. Any systematic increases/decreases in the Raman data (**RQ 4**) were compared to permeate flux decline to assess the performance of the Raman sensor during in-situ monitoring of membrane scaling/cleaning. The extent and composition of membrane scaling/scaling removal (**RQ 3**) were investigated via post-mortem imaging of the cleaned membrane surfaces and compared to the real-time Raman data. Additionally, a larger-area Raman scan (**RQ 6**) of the post-mortem scaled/cleaned membrane samples elucidated the relationship between sampling area and Raman detection representativeness. Finally, the nonuniform feed channel height at the Raman sensing location and the small circular optical window which prevented Raman detection at other membrane locations are identified as limitations of the work.

**In Chapter 5,** a single-salt solution containing precursors for $CaCO_3$ scaling was used as a model feed (**RQ 1**) in a series of membrane scaling experiments. A new, custom RO system and Raman system

were designed and assembled to resolve the prior system limitations, namely the nonuniform channel height and fixed optical window. The new RO flow cell featured a rectangular optical window with a length sufficient for Raman detection at different downstream and upstream locations on the membrane, enabling the study of lateral scaling progression (**RQ 5**) of calcium carbonate (i.e., scaling as a function of axial position). The time-evolution (systematic increases or decreases) of the calcium carbonate Raman band intensities and permeate flux decline were recorded for downstream and upstream membrane detection (**RQ 4, 5)**. The membrane samples underwent post-mortem characterization including gravimetric analysis and SEM imaging to confirm the extent and composition of the membrane scale (**RQ 3**). The Raman laser beam spot size and the average sizes of the scaling crystals were identified as critical length-scales (dimensions) of representative Raman sampling (**RQ 6**).

**Chapter 6** addressed real-time Raman detection of two-component scaling (**RQ 2**) using calcium sulfate and calcium carbonate as model scalants (components). First, the limitations of a single-point sampling strategy were demonstrated using the RO flow cell and system presented in Chapter 2. The mean sizes of the two scaling components, the Raman laser beam spot size, as well as the length of the crystal voids were identified as important factors in the optimization of Raman sampling parameters (**RQ 6**). A modified Raman sampling strategy implemented sequential sampling of multiple points, resulting in successful real-time detection of both components. Raman detection times were compared between downstream and upstream locations (**RQ 5**), and to concurrent values of flux decline, suggesting early detection capability (**RQ 3**). The uncertainty in the repeatability of sampling point positioning somewhat limited the interpretation of any systematic increases/decreases in the scalant Raman signals.

**Chapter 7** summarizes the conclusions of the dissertation and provides recommendations for future directions of the work.

# Chapter 2 Reverse Osmosis: Background, Literature Review, and Design Considerations

In reverse osmosis (RO), a semipermeable membrane is placed between a salt solution (feed) and product water (permeate), as shown in Figure 2-1. A hydrostatic pressure that is greater than the osmotic pressure of the salt concentration in the feed is applied. The resulting pressure gradient drives water molecules from the salt solution to the permeate side of the membrane [13].

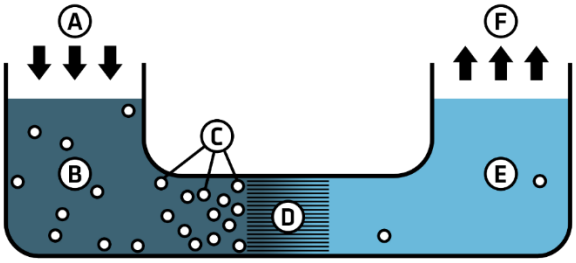


Figure 2-1. A simplified schematic of reverse osmosis. Key: A – Applied hydrostatic pressure; B – Feed water with osmotic pressure related to its salt concentration; C – Contaminants; D – Semipermeable membrane; E – Product water (permeate); F – Distribution of product water. © Colby Fisher, CC BY-SA 3.0

Reverse osmosis is the most widely implemented membrane-based desalination technology [3]. Other membranes used in filtration, such as microfiltration (MF), ultrafiltration (UF), and nanofiltration (NF) membranes feature pores that allow passage of water molecules and reject contaminants larger than the pore size. RO membranes lack distinct pores. Consequently, water molecules must follow a tortuous path through the dense polymer matrix. Here, the benefit is that RO membranes are particularly suited for the rejection of monovalent ions, resulting in product water that meets stringent water quality standards.

Despite its advantages, RO desalination can be a costly means of producing freshwater. Required operating pressures increase with increasing feed water salinity, which is why seawater RO (SWRO) desalination tends to be more expensive than brackish water RO (BWRO) desalination. Still, since the advent of RO membranes in the 1960's, the cost of operating desalination facilities has significantly decreased, as state-of-the-art SWRO plants now require only ~3–5 kWh/m$^3$ compared to the ~10+ kWh/m$^3$

that was required about two or three decades ago [14]. As the demand for freshwater will only increase over time, further technological advances in the optimization of RO desalination, including the development of in-situ monitoring techniques, are necessary to meet the growing need.

## 2.1 Feed Waters

Seawater feeds are sourced from beach wells or seawater intake systems while brackish water sources can be naturally saline aquifers or groundwater that has become saline by either natural or anthropogenic forces [3]. In general, both feed waters share many constituents in common, such as major mineral cations and anions (sodium, magnesium, calcium, chloride, sulfate, and bicarbonate [15,16]), in addition to some organic matter and biomaterials [2]. Despite a good understanding of standard seawater and brackish water composition, it is still necessary to conduct a comprehensive analysis of a source water's exact composition as it can vary due to influences from the local climate, geographic location, and anthropogenic activities.

Consequently, feed water composition is a fundamental design parameter for RO desalination plants [15]. The salinity of the feed water is particularly noteworthy because it drives the selection of system operating pressures (related to energy consumption) and RO recovery (related to product output) [17]. More saline waters require a greater operating pressure to counteract the high osmotic pressure of the feed. Since seawater has higher salt concentrations than brackish water, seawater reverse osmosis (SWRO) tends to be more energy intensive than brackish water reverse osmosis (BWRO), with a total energy of 3─4 and 0.5─2.5 kWh/$m^3$ for SWRO and BWRO, respectively.

## 2.2 Membrane Scaling

Membrane fouling is the deposition of undesirable contaminants on the membrane surface during filtration. The composition of the deposited foulant is determined by factors such as the membrane properties, filtration system operating conditions, and feed water composition [18], and can be classified as inorganic, organic, microbial (biofouling), or colloidal [19]. Inorganic fouling (scaling) is the deposition of

sparingly soluble salts on the membrane when the solubility limit of the scaling species is exceeded. Organic fouling can include humic substances, polysaccharides, proteins, and cell components, among many others, broadly categorized as natural organic matter (NOM) in seawater and brackish water desalination. Microbial or biofouling is the adhesion and subsequent proliferation of microorganisms on the membrane surface. In colloidal fouling, the inorganic (aluminum silicate minerals, silica, iron oxides) or organic materials exist as fine suspended particles ranging from the nanometer to micrometer length-scale [19]. In this dissertation work, inorganic fouling, or scaling, will be the main focus. This is due to the high salinity content of seawater and brackish waters which makes scaling a common occurrence in RO desalination and exerts severe limitations on wider adoption of the technology. Moreover, common scales encountered in RO desalination, such as calcium sulfate and calcium carbonate, have well-characterized, Raman-active cross sections [20–22].

Negative consequences of scaling include increased energy consumption and operating costs, lower membrane performance and shorter membrane lifespans [5–7]. In a worst-case scenario, membrane failure can occur if the deposited scales are not detected early enough in the deposition process when the crystalline scalants are still treatable (reversible). Undetected, the scaling layer can grow and harden over time, rendering the deposited scale irreversible.

Scaling mechanisms include two general pathways for crystallization, known as surface crystallization and bulk crystallization [5,23], both of which are capable of causing flux decline. In surface crystallization, scaling crystals nucleate and grow directly on the surface of the membrane. Subsequent lateral growth of these surface crystals results in a gradual reduction of the active membrane area, resulting in permeate flux decline and a potential increase in salt passage [24]. The other mechanism is known as bulk crystallization, which describes the deposition of crystals originally formed in the bulk feed solution on the membrane surface, as a porous cake layer [24]. This deposited cake layer can then continue to grow, adding to the resistance of the membrane. For each crystallization mechanism, maintaining a constant

applied pressure will result in flux decline or increasing applied pressure (i.e., energy consumption) is required to maintain a constant flux.

A prerequisite for crystallization (also known as precipitation or scale formation) is the existence of a supersaturated concentration of scaling ions. Supersaturation occurs when the concentration of a solute exceeds its equilibrium concentration. According to classical nucleation theory, scale formation is a dynamic process that is generally comprised of simultaneous crystal nucleation and growth of nucleated crystals [25]. Within the concentration polarization boundary layer (analogous to the boundary layer described in fluid mechanics), there are higher concentrations at the downstream membrane surface that can provide the necessary supersaturation levels for salt precipitation. Since higher supersaturation ratios promote faster precipitation of salts, crystals tend to nucleate in the downstream regions first [22]. Once a crystal nucleation site is established on the membrane surface, its growth rate is proportional to the concentration of available scale forming ions. The higher the concentration, the faster the crystals will grow, and they can continue to grow if there is a sufficient supply of scale-forming ions at the crystal-solution interfaces [26].

In surface crystallization, the required supersaturated concentrations of scaling ions are provided by a well-documented phenomenon known as concentration polarization (CP) [8,27–29]. In the CP boundary layer (Figure 2-2), there is a higher concentration at the membrane surface compared to that of the bulk feed. To understand why this occurs, consider a feed-side control volume located near the surface of the membrane during RO operation. As a pressurized feed stream flows tangentially along the membrane, water molecules exit the control volume and permeate through the membrane, while scaling ions remain feed-side, rejected by the membrane. The CP effect increases with increasing axial position which is why the greatest membrane-surface concentrations tend to occur downstream. Consequently, early onset scaling tends to begin downstream [30,31].

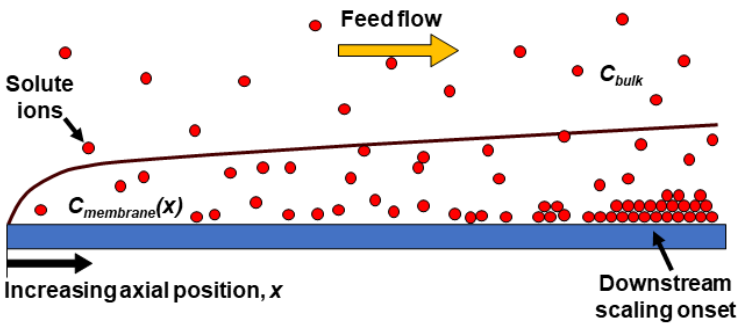


Figure 2-2. Schematic of concentration polarization boundary layer. $C_{bulk}$ is the concentration of solute ions in the bulk feed solution. $C_{membrane}(x)$ is the concentration of solute ions at the membrane surface, which increases as a function of axial position, x. Thus, scaling onset tends to occur downstream.

Higher recovery rates (i.e., permeate flux) and slower feed crossflow velocities (i.e., the velocity of the feed water flowing over the membrane surface) will increase the CP effect, increasing the likelihood of membrane scaling. Therefore, lower recovery rates can aid in decreasing concentration polarization. In fact, recovery rates for seawater RO have been documented to be as low as 30% while recovery rates for lower-salinity brackish water RO can be greater, ranging from 60–95% [3,24].

## 2.3 Scale-control Strategies

Over the years, significant advances have been made in the improvement of membrane permeability and selectivity, as well as scaling and fouling mitigation [7]. Scaling control includes methods such as feed pretreatment [5,6,24], membrane cleaning [3,7], and the use of fouling prediction indices for proactive measures [3,4,7]. Many of these scale-control techniques are derived from the fundamental principles of scaling such as concentration polarization (CP) and crystal nucleation and growth.

For instance, product water recovery levels have successfully been increased by introducing processes such as feed flow reversal. This particular technique capitalizes on the CP effect described in Section 2.2, which provides increasing membrane surface supersaturation levels with increasing axial position [32–35]. This greater downstream scaling propensity is disrupted upon flow reversal. The most concentrated section of the membrane is replaced with undersaturated solution, thereby dissolving early scaling crystals, and deterring the formation of further scale.

Another example of scale-control is the use of chemical additives known as antiscalants, which can delay the onset of scale formation [36] by disrupting at least one aspect of crystallization such as delaying the nucleation phase or retarding crystal growth [24]. It is common to utilize a combination of antiscalants to target multiple scales, however it is critical to identify an accurate dosing and timing plan, as increased dosages do not necessarily increase the efficacy of the treatment. Furthermore, some antiscalants have been known to promote biofouling [37]. Clearly, optimization of scale-control strategies such as antiscalant treatment could benefit from real-time information on scale deposition, enabling timely interventions if improper dosing occurs.

## 2.4 Literature Review of In-situ Monitoring Techniques

Early detection and understanding of scaling fundamentals can lead to innovation in membrane scaling prevention and control, thereby necessitating a suite of in-situ monitoring techniques. In this dissertation work, the development of a Raman-based, in-situ monitoring technique is motivated by overarching goals of early scaling detection and increased understanding of scaling mechanisms. Consequently, this section contains a literature review of in-situ monitoring techniques with emphasis on membrane scaling detection, followed by a critique of the literature. The critique provides balanced perspectives and background information necessary to understand the strengths and limitations of this work.

### 2.4.1 *Conventional indicators of membrane scaling*

Permeate flux and salt rejection [38] are common performance metrics of RO desalination systems. Membrane cleaning regimens are initiated when permeate flux and permeate salinity over time indicate evidence of membrane degradation [39]. Evidence of membrane degradation is typically based on a combination of the following metrics:

- 10–15% decrease in permeate flux
- 10–15% increase in salt passage
- 10–15% increase in pressure drop across an RO module

- >15% increase in applied pressure

The general consensus is that performance metrics such as permeate flux and salt rejection do not provide sufficient information about the temporal and spatial onset, chemical composition, and interaction of the foulants, leading to suboptimal RO operation and cleaning [24,33,34,39].

### 2.4.2 *Visual detection techniques*

Table 2-1. Summary of monitoring techniques that used membrane surface imaging.

| Study | Year | Camera | Lighting | Post-processing | Minimum detectable crystal size (μm) |
|---|---|---|---|---|---|
| [39] | 2007 | Digital camera and wide field optical microscopes | Ultra-bright LEDs | Yes | ~100 |
| [40] | 2018 | Digital microscope camera & stereomicroscope | Ultra-bright LEDs | Yes | 60 |
| [41] | 2021 | DLSR camera (EOS 700D, Canon) | Macro ring flash | Yes | 50 |

Table 2-2 summarizes the findings of visualization monitoring techniques. To understand the spatial progression of membrane scaling during RO operation, visual observation techniques have been implemented in a variety of membrane scaling studies in laboratory-scale plate-and-frame RO modules. Real-time image capture of the membrane surface is aided by special lighting and post-processing techniques to extract useful information about membrane scaling progression, which could be beneficial for developing realistic scale formation models [15].

Uchymiak et al. [15] presented the first demonstration of direct visual monitoring of mineral scale development on RO membranes at realistic plant operating conditions. They developed an ex-situ scale observation detector (EXSOD) to study the (a) onset of surface crystallization (which is more sensitive than permeate flux decline), (b) quantify the crystal population growth, using surface number density (#/cm$^2$), and (c) study fundamental growth kinetics, and single surface crystal growth and dissolution. About 10 h into a scaling test, 20 surface crystals were detected accompanied by a ~5% permeate flux decline, with the first surface crystal appearing only 30 min into the scaling test. Since permeate flux is an area-averaged

indicator of membrane performance, real-time imaging can serve as a relatively more localized metric enabling early detection of scale formation. By measuring the evolution of single-surface crystal size and the number of single surface crystals in the viewable area, they were able to study fundamental nucleation and growth kinetics of gypsum scale.

Similar to the EXSOD, Benecke et al. [40,48] used a digital microscope camera and stereomicroscope to take high resolution images of a 17.2 mm × 12.9 mm section of an RO membrane during gypsum scaling. Sarker et al. [39] used a DSLR camera with a macro ring flash to study gypsum scale growth in a plate-and-frame RO module. These real-time visualization techniques can monitor evolution and dissolution of crystal growth, providing a means of evaluating the efficacy of cleaning strategies.

### 2.4.3 *Ultrasonic Time-Domain Reflectometry (UTDR)*

Table 2-2. Summary of monitoring techniques that used ultrasonic time-domain reflectometry.

| Study | Year | Feed Composition | Notable Contribution | Shortcomings |
|---|---|---|---|---|
| [42] | 1999 | 1.5 g/L $CaSO_4$ | First systemic study: noninvasive ultrasonic measurements were (1) insensitive to membrane compaction and (2) sensitive to subtle changes in fouling layer, unlike flux-decline measurements. | Single-component feed solution |
| [43] | 2000 | 0.5 g/L $CaSO_4$ | Successful monitoring of fouling growth and cleaning: two-mode $CaSO_4$ fouling layer growth observed | Single-component feed solution |
| [44] | 2002 | 0.5 to 2 g/L $CaCO_3$ solution | Successful detection of fouling initiation and monitoring of growth/cleaning of RO membranes demonstrated | Single-component feed solution |
| [10] | 2003 | Paper mill effluent (inorganic and organic components) | Successful detection of deposition and growth of organic fouling layer and monitoring of cleaning progress of UF membranes demonstrated | SEM images showed particles that were unidentified |
| [45] | 2011 | 0.47 and 1.19 g/L $CaSO_4$ | Miniature-scale ultrasonic transducers were integrated into a flat-sheet cross-flow filtration module. A comparison of internally-mounted and externally-mounted UTDR transducers is presented. | Single-component feed solution |

Table 2-2 summarizes the findings of ultrasonic time-domain reflectometry (UTDR) techniques. UTDR has been demonstrated as a nondestructive monitoring technique of membrane fouling during filtration experiments. This technique utilizes ultrasonic transducers which are made of a piezoelectric material that is excited by a voltage source, causing the material to expand and contract. This material movement produces an acoustic wave which can be applied to the membrane system. The shift in the arrival time and amplitude of the acoustic echoes can be related to the evolution of the scaling layer. Mairal et al. [27,28] showed that these time-domain changes of the acoustic echoes agreed with changes in the permeate flux recorded at the same locations of the acoustic transducers. Cobry et al. [29] developed miniature UTDR sensors that could provide a more localized, point measurement of the fouling layer.

### 2.4.4 *Electrical Impedance Spectroscopy*

Table 2-3. Summary of monitoring techniques that used electrical impedance spectroscopy.

| Study | Year | Feed Composition | Notable Contribution | Shortcomings |
|---|---|---|---|---|
| [46] | 2009 | N/A | Static, osmotic, pressure-driven system ($CaCO_3$/sucrose separated by RO membrane): Reported a measurable difference in electrical properties of different "layers" of the system. | Static experiments (no crossflow) |
| [47] | 2013 | 300 mg/L $Ca^{2+}$ and 330 mg $HCO_3^-$ ($CaCO_3$ scaling) | $CaCO_3$ scaling was monitored in situ, and in real-time. The electrically distinct layers in their membrane system were modeled. Measured thicknesses of the layers were validated with the known thicknesses. | Single-component feed solution<br>Electrically distinct layers may not be able to distinguish different scale compositions |
| [48] | 2015 | Feed 1: Molasses wastewater (organic)<br>Feed 2: colloidal silica (model inorganic)<br>Feed 3: BSA (model protein) | Confirmed in-situ monitoring of membrane fouling. EIS elucidated different fouling mechanisms between organic and inorganic foulants (i.e., gel-layer formation vs loose-cake formation) | Electrically distinct layers may not be able to distinguish different scale compositions |

Table 2-3 summarizes the findings of electrical impedance spectroscopy (EIS) techniques. In EIS, membrane systems can be modeled as an electrical circuit. By studying the phase difference between the

applied alternating currents and measured voltages, the calculated impedance magnitude and phase angle can be related to electrical properties (such as conductance and capacitance) of the various layers of the membrane system. EIS has been applied as a nondestructive method of characterizing membranes [49] and studying membrane-based separation processes such as RO [46,47], MF/UF [49], and ion-exchange [50] membranes to characterize the various layers of the membrane.

Kavanagh et al. [46] defined a four-element electrical circuit model in their static, osmotic pressure-driven membrane system. This membrane system, modeled as an electrical circuit, comprised of a bulk solution element, membrane skin layer element, membrane subsurface layer element, and an element for mass transfer of ions in solution. They reported a measurable difference in electrical properties between these different layers, providing a rationale for using EIS as a diagnostic tool for studying membrane fouling of RO membranes. Later, Antony et al. [47] applied EIS in filtration experiments that used an RO crossflow cell which was operated during more realistic RO flow and pressure conditions. $CaCO_3$ scaling was monitored in situ, and in real-time using EIS and they were able to successfully model the electrically distinct layers in their membrane system, even validating the thicknesses of the layers with the known thickness of the layers in the membrane system. Notably, one of the electrically distinct layers included a nanometer-thick molecular polyamide coating.

### 2.4.5 *Raman spectroscopy*

Table 2-4. Summary of monitoring techniques that used Raman spectroscopy.

| Study | Year | Feed Composition | Notable Contribution |
|---|---|---|---|
| [51] | 2016 | Feed 1: bacteria<br>Feed 2: adenine | Au-NP (gold nanoparticle) surface-enhanced Raman spectroscopy (SERS) sensing area prepared on microfiltration membranes: real-time detection of organic fouling |
| [52] | 2017 | Vanillin | First use of spontaneous Raman as a novel tool for monitoring membrane fouling. Vanillin adsorption improved permeability of membranes. Time-variant Raman signals were related bulk feed concentration. |
| [53] | 2018 | $CaSO_4$ | First demonstration of real-time, in situ inorganic fouling detection of reverse osmosis membranes, using spontaneous Raman |

The use of Raman spectroscopy to characterize filtration membrane fouling is a fairly novel application. Raman spectroscopy has been used to study fouling of a variety of membranes and foulants, including biofoulants [51], organic fouling [52,54], and inorganic fouling [53,55,56]. The chemical identification capability of Raman spectroscopy is very attractive because it provides the opportunity to study foulant-foulant [55] and foulant-membrane [54] interactions of feed solutions with multiple fouling components.

### 2.4.6 *Shortcomings of in-situ monitoring techniques*

The application of UTDR for membrane fouling detection has been applied to module configurations outside of the typical bench-scale, plate-and-frame modules [57,58]. This technique can demonstrate high sensitivity to changes in the fouling layer (nanometer length-scale). While UTDR is capable of providing more localized information about the fouling layer compared to permeate flux, it is still challenging to relate the sensor signals to specific contributions of distinct components in the fouling layer. Similarly, although EIS is useful as an early-warning tool that can distinguish the onset and

development of both organic and inorganic fouling, it is still a global measurement whereby EIS measurements account for fouling-component contributions of the entire membrane. Once again, when there are multiple fouling components in the feed, it is challenging to determine which specific foulants are included in the EIS signal and to what extent they are contributing to the signal.

Visual detection techniques utilize images of the membrane surface to provide information regarding localized scaling crystal growth kinetics and macroscopic development of crystal coverage on membranes over time. However, a drawback of real-time visualization techniques is that successful scale detection requires that the crystal grows to a certain size or groups of crystals need to accumulate into a detectable presence (Table 2-1). This leads to assumptions regarding the growth kinetics of crystals below the detectable size limit that are difficult to confirm.

Overall, the most significant shortcoming arises from the fact that many of the aforementioned techniques lack the capability of specific chemical identification, aside from Raman spectroscopy. Chemical identification of scalants/scalants is vital when studying complex feeds with many different fouling components. For example, real-time knowledge of the chemical composition of the detected foulants could inform the selection of the best cleaning strategy including the choice of cleaning chemicals, dosage, and timing. Without knowledge of the chemical composition, the detection result would simply alert the plant operator that a foulant has deposited. The plant operator could then attempt to identify the composition of the deposited foulant, but with considerable uncertainty, since there are many fouling components in the feed water.

For example, Li et al. [10] presented an excellent case for UTDR sensing of organic fouling layers caused by filtration of paper mill effluent, but when they discovered additional particles on the fouled membrane in post-mortem SEM imaging, they did not comment on the composition of the particles. Because of the lack of chemical identification, many of the bench-scale, fouling studies utilize idealized feeds that are comprised of known fouling species. Except for a handful of studies that use real water samples/feeds with more than one fouling species, this is clearly observed in the tables summarizing the

model feed solutions used in each study (Table 2-2 and Table 2-3). This presents a significant gap in the wider applicability of the reviewed in-situ monitoring techniques because it is unlikely that the feedwaters processed by the pilot or full-scale plant will containing a single known foulant.

Lastly, it is important to note that the implementation of Raman spectroscopy in scaling and fouling detection is not necessarily the panacea for in-situ monitoring. Optical techniques such as Raman spectroscopy and visual imaging rely on optical access to the membrane. This is difficult to achieve in spiral wound membrane modules, the preferred configuration in commercial RO desalination. So, although the proposed Raman sensor can be implemented on a lab-scale flat sheet (plate-and-frame) flow cell with relative ease, applying the methodology to pilot-scale or full-scale RO desalination requires either the use of a bypass line in conjunction with a flat sheet RO flow cell, or a clever means of obtaining optical access to the tightly packed, spiral-wound membranes. Still, given the critical need for real-time chemical identification, development of the Raman sensor is a part of the necessary work in the optimization of RO desalination and overall efforts to mitigate global freshwater scarcity.

## 2.5 Design Considerations

This work utilized two separate reverse osmosis flow cells and systems. My colleague, Omkar Supekar spearheaded the design and fabrication of the first system, which was used in conjunction with a commercial Raman microscope to provide proof-of-concept demonstrations of real-time detection of membrane scaling. I also used this system to demonstrate early detection of $CaSO_4 \cdot 2H_2O$ scaling and scale removal (Chapter 4). More details regarding the flow cell and system can be found in Chapter 4 and previous works [53,55]. After identifying the strengths and limitations of the first system, I designed and fabricated the second system according to the research objectives summarized in Section 1.2.4. Table 2-5 provides an overview of the most important design drivers of the second RO flow cell and RO system. Here, the design considerations describe the necessary qualities of the reverse osmosis flow cell, and the corresponding engineering requirements and target values translate the design considerations into actionable engineering problems.

Table 2-5 An overview of Design Considerations, Engineering Requirements and corresponding Target Values for the design and fabrication of the reverse osmosis flow cell and reverse osmosis system.

| Design Considerations | Engineering Requirements | Targets Values/ Criteria |
|---|---|---|
| Flow cell must withstand applied pressures. | The applied pressure must not exceed flow cell material strength (tensile/compressive/shear). | Safety factor >3 |
| The flow cell must provide relevant hydrodynamic conditions in Raman-sampled regions. | Feed flow should remain in the laminar regime. | Reynolds number <100 |
| | Feed flow direction should be tangential to the membrane. | Multi-jet design for feed and retentate ports |
| | The feed channel height must be uniform in this region. | ~2 mm channel height |
| | The velocity profile of the feed flow must be fully developed in the optical window. | Entrance length does not overlap with optical window |
| | The optical window must be positioned away from dead zones in the flow. | >2 cm distance between the optical sensing region and any irregular flow patterns |
| The dimensions of the optical window must be suitable for Raman data collection at different axial positions. | The feed concentration as a function of axial position should vary enough to give rise to a downstream onset of scaling. | Downstream concentrations should be about double that of upstream concentrations |
| The RO flow cell and system must withstand multi-day exposure to high-concentration salt solutions and potentially relevant cleaning solutions | Compatibility of wetted materials with salt solutions over extended periods of time. | An 'Excellent – No effect' rating for chemical resistance to common ions in seawater and brackish water: $Na^+$, $Ca^{2+}$, $SO_4^{2-}$, $CO_3^-$, $Cl^-$ |
| Flow cell must operate under reasonable temperatures | Flow cell material does not change characteristics for specified temperature range. | 20-28°C |
| The flow cell must provide optical access to the membrane for the Raman microscope. | The optical window must be constructed of a material that introduces the least amount of interference with the Raman laser. | Properties of the optically transparent material:<br>- Surface roughness of N/4–N/6<br>- Scratch/dig 60–40 |
| | The applied pressure must not exceed the optically transparent material strength (tensile/compressive/shear). | Safety factor >3 |
| Real-time Raman data collection | The Raman microscope should be able to focus on the membrane without making contact with the optical window. | The total thickness of the channel height and optical window thickness > 9 mm*<br>*working distance of the microscope objective is 11 mm |
| | Vibrations/disturbances of the flow cell must be minimized during real-time Raman data collection. | Laser focus should be consistent throughout the entire duration of experiments |

### 2.5.1 *Engineering requirements*

The flow cell design required a custom glass window that allowed for a uniform channel height throughout the entire flow cell. This was especially important for scaling detection experiments because nonuniformity in the channel height can either accelerate or decelerate scale progression compared to other regions on the membrane. For example, the RO flow cell used in Chapter 4 featured a channel height of 2-

mm everywhere except in the region of the circular viewing window, where the height was 4 mm. This was suitable for early-detection scaling experiments because the greater channel height reduced the local velocities momentarily, inducing quicker scale deposition.

The initial flow cell design featured a rectangular optical window with an area of 3.80 x 1.27 $in^2$ (length × width) that would interface with the Raman microscope for scaling detection. The length was slightly increased to 3.9 in during fabrication. The longer length of the optical window allowed for a range of Raman sensing locations along the axial length of the membrane. The top component has an inlet feed port and outlet retentate port. The bottom component has a permeate port where the permeate flux exits the flow cell and is collected for permeate mass-flux measurements. Both top and bottom components were machined from stainless steel to avoid corrosion. A steel mesh plate provides support for the membrane which will be subject to a pressure of 1.2 MPa (175 psi). A double O-ring arrangement provides a proper seal between the top and bottom components. As noted, the flow cell design features a custom glass window that allows for a uniform channel height throughout the entire flow cell. Two additional replicate custom glass windows were ordered as backup parts. The glass window was sealed against the top component using an aluminum optical window clamp and an O-ring. Pressure simulations were conducted for the stepped glass window to ensure that it could withstand the operating pressures (Figure 2-3).

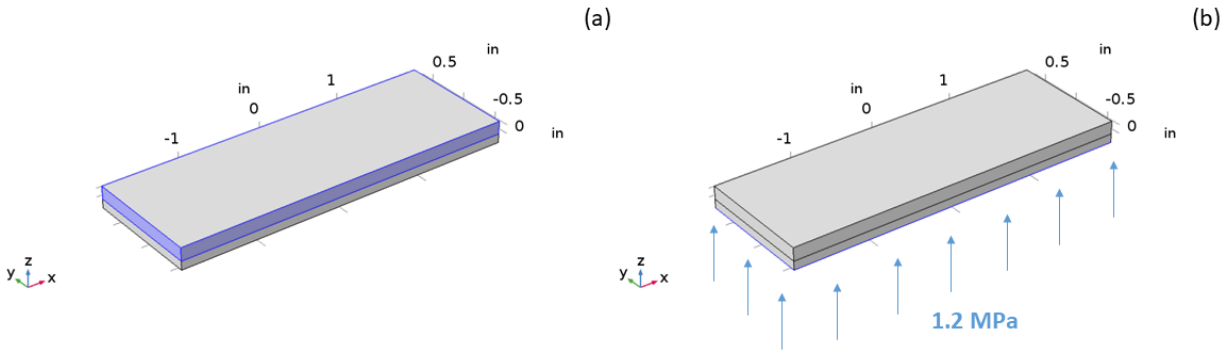


Figure 2-3. Boundary conditions for the optical window stress simulation. (a) Fixed constraint. (b) Boundary pressure load of 1.2 MPa (175 psi).

To model the stresses in the glass plate exerted by the pressure, the glass plate was represented as a simple rectangular prism. Figure 2-3 shows two different loading scenarios. In the first scenario (Figure 2-3a), a fixed constraint was applied on the faces that will be clamped. In the second scenario, a boundary pressure load of 1.2 MPa was applied in the upward direction on the bottom of the window (Figure 2-3b). It was determined that the window could experience a maximum von Mises stress of 37 MPa along the long edges of the optical window (Figure 2-4).

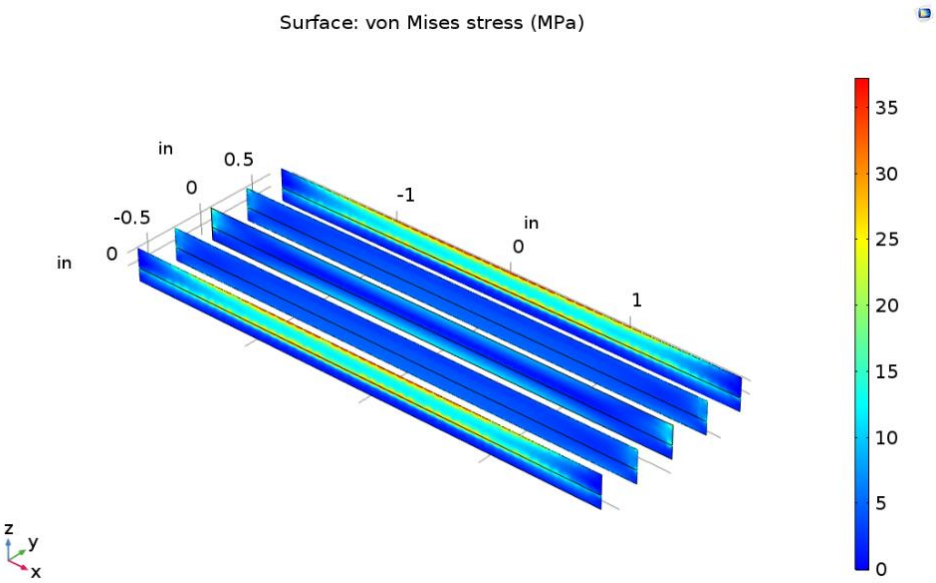


Figure 2-4. Pressure simulations were conducted on the stepped glass window to ensure that it is thick enough to withstand high operating pressure of the flow cell. It was confirmed by COMSOL simulations and hand calculations that the glass plate could withstand 175 psi with a safety factor of ~2.9.

Along the center of the optical window, the von Mises stress was found to be 20 MPa using COMSOL simulations, supported a value of 18 MPa attained from hand calculations (bending plate equations). An applied pressure of 1.2 MPa was selected based on the two main criteria for the selection of the RO membrane. The first criterion involved relevant feed compositions for the scaling experiments. The goal was to start simple; begin with synthetic, single-component solutions of common scalants encountered in desalination ($CaSO_4$ and $CaCO_3$) and eventually expand to multiple-component solutions and even artificial or natural feedwaters. Accordingly, there were three main types of RO membranes available, optimized for three different feed types:  industrial/wastewater, brackish water, and seawater. A brackish

water membrane was selected to best suit our initial use of simplified, single-component salt solutions. The second criterion was the specialization of the membrane, i.e., low energy, high rejection, and chlorine resistant. We focused on low energy membranes, in part, due to the safety aspect of working with extreme pressures. Therefore, the Toray™ 73HA membrane was selected (23.3/73 gfd/psi; 99.0% rejection; polyamide-thin film composite).

Sufficient concentration polarization along the axial direction of the flow was necessary as an engineering requirement for an observable difference between the induction periods of scaling in downstream and upstream locations. The bulk feed concentration as a function of axial position was estimated using simple conservation of mass equations (Figure 2-5).

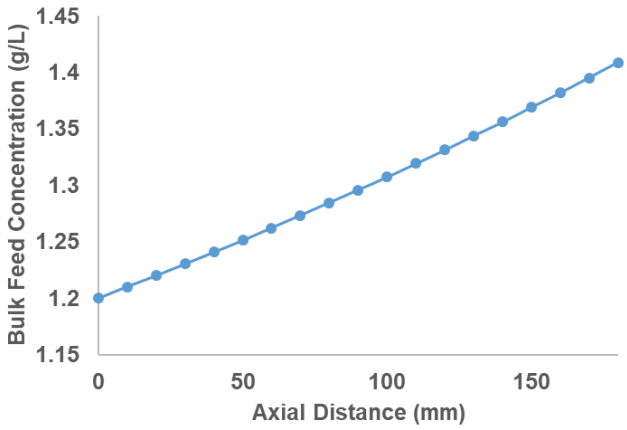


Figure 2-5. Sufficient concentration polarization along the axial direction of the flow is necessary for an observable difference between the induction periods of scaling in downstream and upstream locations. A calculation was performed relating bulk feed concentration with axial position. This calculation was used to inform the cross-flow cell dimensions as well as estimate the induction period of scaling.

This calculation was used to determine the cross-flow cell dimensions as well as estimate the induction period of scaling. With the chosen active membrane area of 125 x 175 $cm^2$ and a feed concentration of 1.2 g/L $CaSO_4$, the bulk concentration downstream (>150 mm) would be ~1.4 g/L. According to previous reference experiments conducted for varying feed concentrations, the scaling

induction time downstream of the membrane was estimated to take about 12 h. For lower feed concentrations, scaling experiments would run longer and require automation.

The flow through the flow channel was also simulated in COMSOL to ensure that the axial flow velocity (x-direction) in the optical window regions (-50 mm < x < 50 mm) remained uniform and laminar (Re < 100). An inlet boundary condition was defined at x = -80 mm for the 10 feed inlet jets with a volume flow rate of 4.17 $cm^3/s$. An exit pressure was defined at x = 80 mm for the 10 retentate outlet jets with an exit pressure of 175 psi. For all other boundaries, a no-slip wall condition was specified.

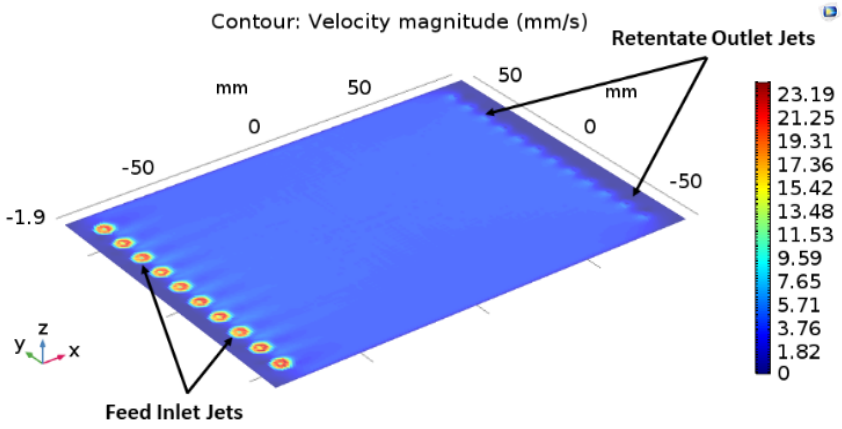


Figure 2-6. An inlet boundary condition was defined at x = -80 mm for the 10 inlet jets with a volume flow rate of 4.167 $cm^3/s$. An exit pressure was defined at x = 80 mm for the 10 outlet jets with an exit pressure of 175 psi. For all other boundaries, a no-slip wall condition was defined. This cross-section was taken 0.1 mm above the bottom wall of the flow channel and shows that the streaks in the velocity profile smooth out at around x = -60 mm, ensuring uniform velocity occurs once the flow reaches the Raman sensor location (x = ~50 mm).

Figure 2-7 shows that there was minimal velocity in the y- and z-directions under the sensing regions, fulfilling the engineering requirement that there should be >2 cm distance between the optical sensing region and any irregular flow patterns.

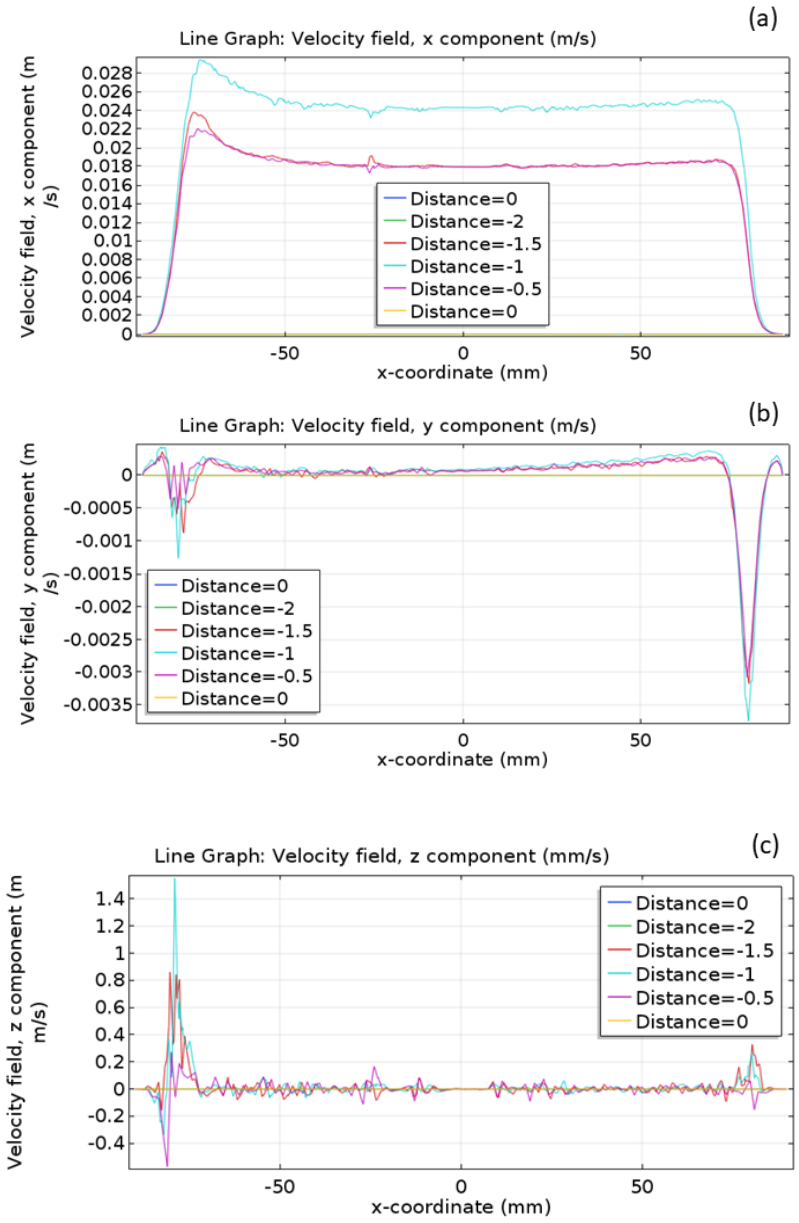


Figure 2-7. Laminar flow COMSOL simulations showing the (a) x-component velocities, (b) y-velocities, and (c) z-velocities along the axial direction in the optical window region. In (a), due to the no-slip boundary condition imposed on the walls of the channel, the x-component velocity is zero. The maximum x-component velocity occurs in the middle of the channel, at x=-1mm. In (b), the negative y-velocities at x=-80mm are due to the jets of water entering the inlet. Likewise, in the outlet, as jets of water exit the channel, y-component velocities are created. Likewise, in (c), z-component velocities are formed around x=-80mm because of the inlet jets and at x=80mm due to the exiting jets of water. However, the most important region is the Raman microscope sensing region from about x=-50mm to x=50mm. Simulations show that there will be minimal y- and z-component velocities that could introduce additional variability in the scaling experiments.

### 2.5.2 *Reverse osmosis flow cell*

In the fabrication of the new RO flow cell, the glass optical window was sealed against the top component using an aluminum optical window clamp and an O-ring. A challenging design consideration was designing and assembling the inset glass window in such a way that the glass did not fracture. The load distribution starting with the load from the tightened bolts created a point load on the glass inset. This point load was successfully removed by reducing the machine tolerance for the aluminum window clamp. The reverse osmosis flow cell (Figure 2-8) used in the work described in Chapters 5 and 6 featured a rectangular optical window with an area of 9.98 cm × 3.23 cm (length × width) that interfaced with the custom Raman microscope for scaling detection. The top component had an inlet feed port and outlet retentate port. The bottom component has a permeate port where the permeate flux exited the flow cell and was measured by a low-flow sensor. The top plate housed the inlet feed and outlet retentate ports, and the bottom plate contained the permeate exit port, from which the permeate flux was measured using an in-line MEMS low-liquid flow sensor (SLF3S-1300, Sensirion); The membrane active area was 125 mm × 175 mm. Both top and bottom components were machined from stainless steel. A steel mesh plate provides support for the membrane which will be subject to a maximum pressure of 1.2 MPa (175 psi). A double O-ring arrangement provided a secure seal between the top and bottom components during the pressurized filtration experiments.

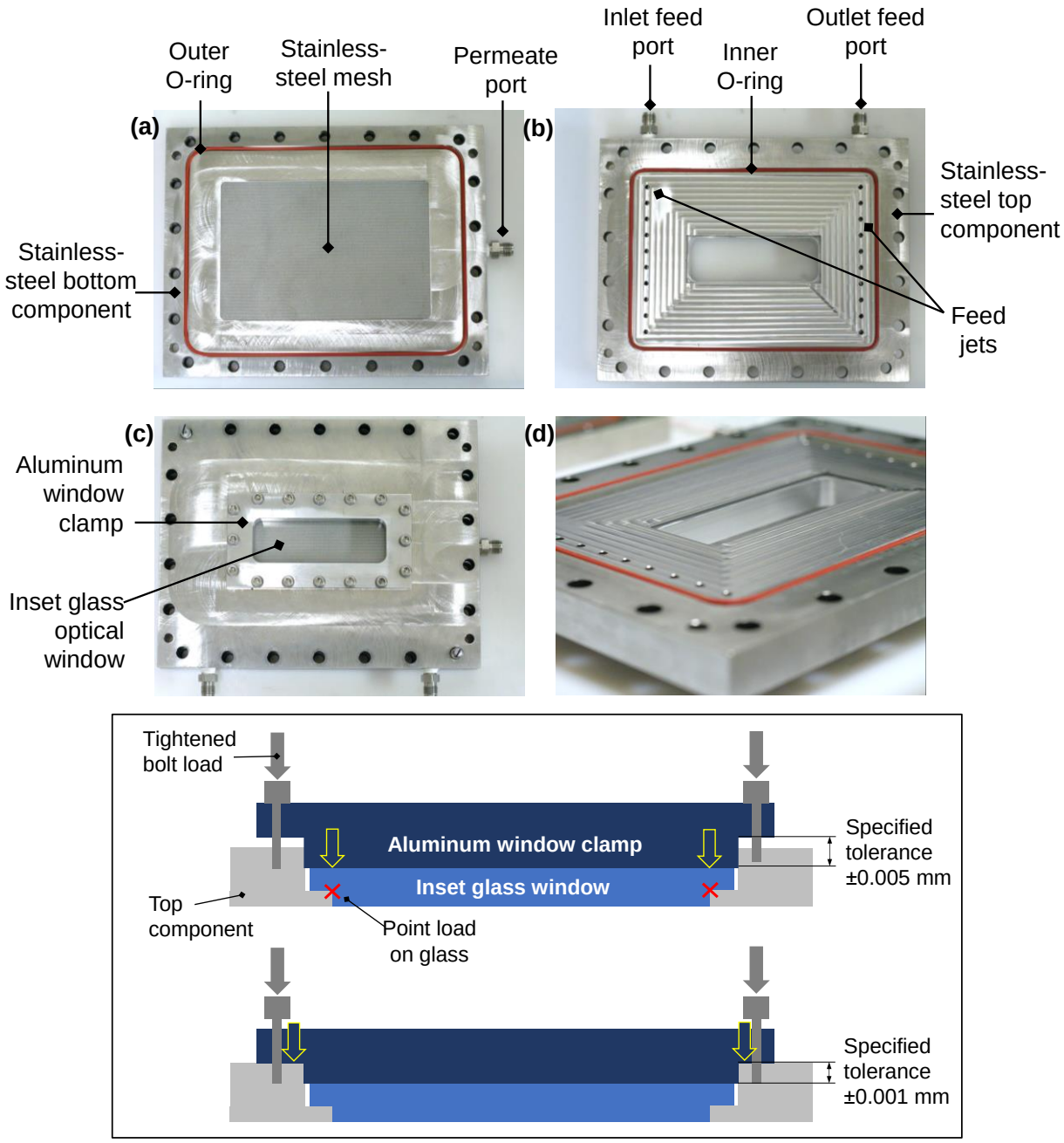


Figure 2-8. (a) Bottom component of the flow cell with a stainless-steel mesh support and outer O-ring. (b) Top component of the flow cell with inlet and outlet ports as well as the inner O-ring. (c) Top view of the flow cell, showing the optical window clamp and guide pins. (d) A more detailed view of the inset glass window that allows for a uniform height (2 mm) everywhere in the feed channel. (bottom) A challenging design consideration was designing and assembling the inset glass window in such a way that the glass remained intact. The load distribution starting with the load from the tightened bolts created a point load on the glass inset. This point load was successfully removed by reducing the machine tolerance for the aluminum window clamp.

### 2.5.3 *Reverse osmosis system*

A bench-scale RO system was built with data acquisition capability to accommodate multi-day filtration tests (Figure 2-9).

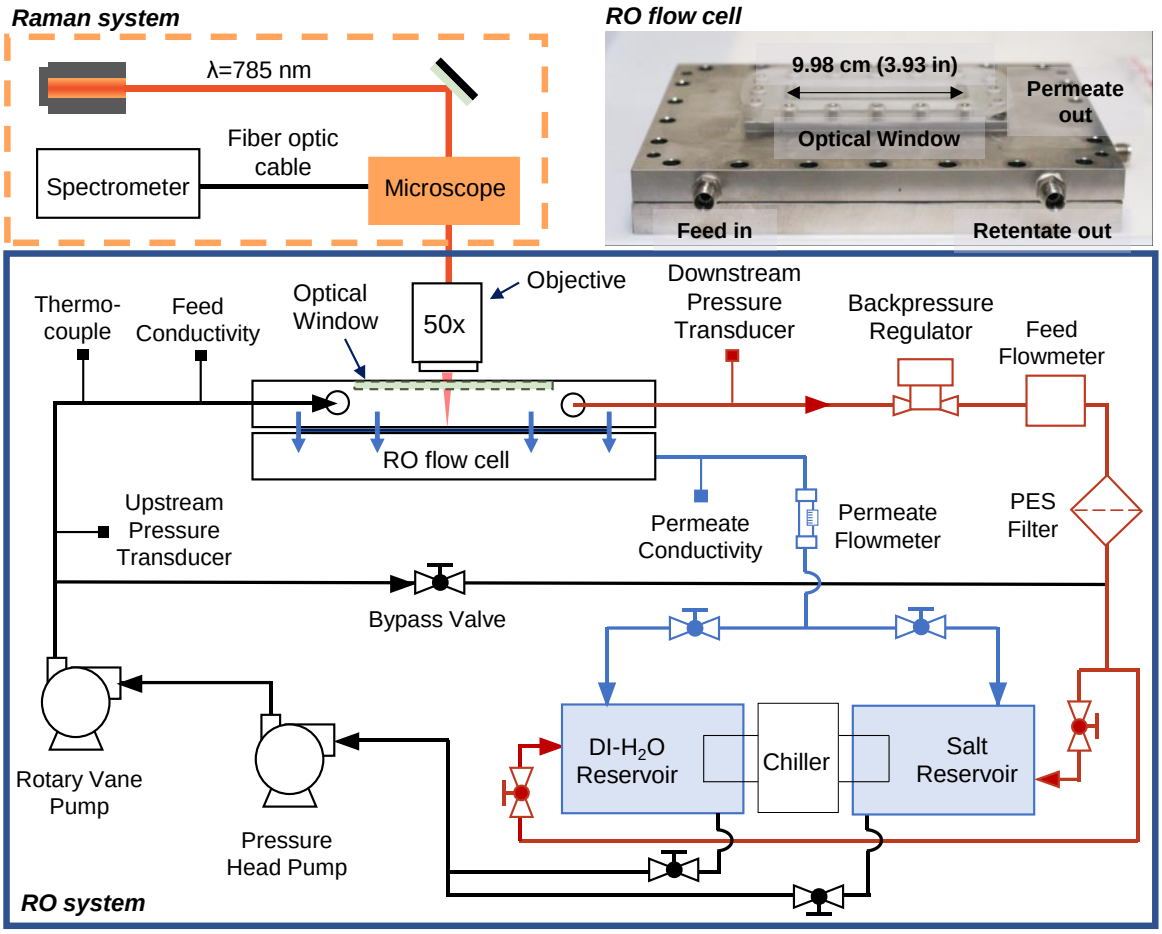


Figure 2-9. Schematic of Raman system (dotted orange outline), reverse osmosis system (solid blue), and photograph of reverse osmosis flow cell pictured with protective optical window cover. The optical window has dimensions of 3.23 cm× 9.98 cm, resulting in 6.98 cm of axial travel for the ~3.0 cm-diameter microscope objective.

Two feed tanks, one for DI water and the other for the prepared salt solution, were outfitted with feed intake valves and retentate return lines, allowing for RO operation in total-recycle mode and streamlined transitions between DI water and salt feeds. A thermocouple (TC-T-NPT-U-72, Omega) and chiller (T257P, Thermotek) were used to maintain constant feed temperatures during filtration. In-line conductivity probes measured the conductivity of the feed (EW-19500-65, Cole-Parmer) and permeate

streams (EW-19500-64, Cole-Parmer). Pressure transducers (PX191-300GV5, Omega) installed upstream and downstream of the flow cell, were used to monitor the feed channel pressure. A backpressure regulator (12-251B2-44AZ5-72, Neon) and a bypass valve (SS-1RS4, Swagelok) were used to manually set the applied feed pressure and volumetric flow rate at the start of all experiments. A turbine flow meter (TFM-LP07, Dwyer) measured the feed volumetric flowrate. All sensors were connected to a computer DAQ system (USB-6001, National Instruments), except for the permeate flux sensor, which was connected to the computer via an Arduino board (Arduino Uno R3). A 0.2 μm PES filter (CCS-020-C1B, Advantec) was installed in the retentate line to filter any large particulates.

# Chapter 3 Principles of Raman spectroscopy and Microscope Design

This chapter covers the basic principles of Raman spectroscopy and provides an overview of the Raman instrumentation used in this dissertation work. In general, spectroscopy is an analytical tool that stems from the broad study of interaction between a radiation source and matter. Valuable information can be extracted from the study of particular light-matter interactions (e.g., *excitation* of matter by light, matter *absorption* of light, and light *scattered* by matter).

Since the aim of the research was to use Raman spectroscopy to study mineral scaling on membranes during reverse osmosis (RO) desalination, the following chapters primarily focus on light scattered by molecules in the solid phase. Chapter 3 begins by introducing Raman scattering in gases/liquids (Section 3.1), followed by an overview of Raman scattering in solids (Section 3.4). The rationale for this organizational structure was that the principles of scattering by an individual, freely-oriented molecule (i.e., gases/liquids) would provide a generalized description of the Raman effect. This could then serve as the basis for understanding the more specific case of scattering by *many* molecules closely bound to each other in the fixed orientation of a solid.

## 3.1 Introduction to Raman Scattering

Consider an individual, freely-oriented molecule in a gaseous state. In the absence of a point charge, this molecule is electrically neutral because it has a positively charged nucleus surrounded by a cloud of negatively charged electrons of equal and opposite polarity. Then, when a point charge is placed on the electrically neutral molecule, the center of symmetry of the electron cloud changes. This asymmetric electron cloud is said to be in a ‘polarized’ state and is called an induced dipole. This electron cloud distortion process is known as polarization.

Polarizability is defined as the ease with which the molecule's electron cloud is distorted. Another way to think about polarizability is the tendency of the electron cloud to respond to a subjected electric field. The strength of the induced polarization, $\vec{P}$, is related to the incident electric field, $\vec{E}$, by the polarizability, $\alpha$:

$$\vec{P} = \alpha\vec{E}. \tag{3-1}$$

The incident electric field is an oscillating wave with an amplitude of $E_0$, and frequency $v_0$:

$$\vec{E} = \vec{E}_0 \cos(2\pi v_0 t). \tag{3-2}$$

Raman scattering occurs when an incident, oscillating electric field perturbs the electron cloud of the molecule, resulting in an oscillating induced electric dipole moment. In Equation 3-1, since $\vec{E}$ and $\vec{P}$ are vectors, the polarizability ($\alpha$), is a tensor. For this section, first consider a simplified case involving an isotropic molecule, for which the directions of $\vec{P}$ and $\vec{E}$ are the same. Consequently, $\alpha$ becomes a scalar quantity. With this simplification, and if the induced dipole is vibrating with a frequency (also known as a 'beat frequency'), $v_j$, the nuclear displacement, $Q_j$, of the molecule can be described by

$$Q_j = Q_j^{\circ} \cos(2\pi v_j t), \tag{3-3}$$

where $Q_j^{\circ}$ is the vibrational amplitude. The polarizability of oscillating dipole is a function of the nuclear displacement [59]. Here, a small vibrational amplitude allows the polarizability and displacement to be linearly related, resulting in:

$$\alpha = \alpha_0 + \left(\frac{\delta\alpha}{\delta Q_j}\right)_0 Q_j + \cdots, \tag{3-4}$$

where $\alpha_0$ is the polarizability of the molecule's nucleus at the equilibrium position, and likewise, the partial derivative $(\delta\alpha/\delta Q_j)_0$ is the rate of change of $\alpha$ with respect to the change in $q$, at the equilibrium position (displacement). Combining Equations 3-1 through 3-4, an expression for the strength of polarization is obtained for an oscillating induced dipole:

$$P = \alpha_0 E_0 \cos(2\pi v_0 t) + E_0 Q^\circ{}_j \left(\frac{\delta\alpha}{\delta Q_j}\right)_0 \frac{\cos(2\pi(v_0+v_j)t + \cos(2\pi(v_0-v_j)}{2}. \quad 3\text{-}5$$

The first term on the righthand side of the expression represents an oscillating induced dipole that radiates light at a frequency $v_0$, which was the frequency of the incident light (Rayleigh scattering). The second term represents an induced dipole that radiates light at a frequency of ($v_0$ + $v_j$) which represents anti-Stokes Raman scattering, and the third term represents Stokes Raman scattering at a frequency ($v_0$ – $v_j$).

An energy diagram helps to visualize the vibrational transitions of a molecule during Rayleigh and Raman scattering (Figure 3-1).

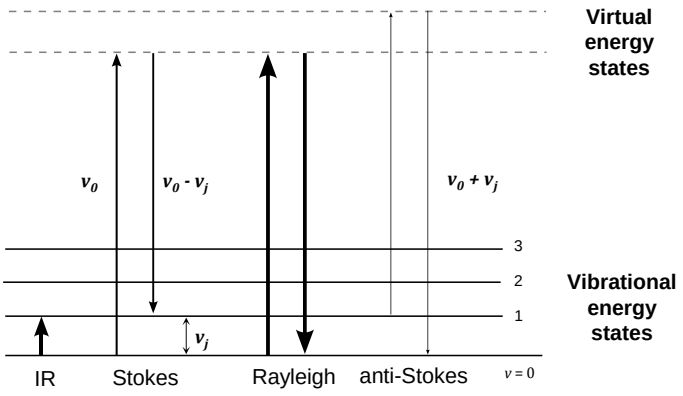


Figure 3-1. Energy levels for spontaneous (normal) Raman spectroscopy. Stokes Raman scattering is possible for molecules that are initially at a ground vibrational state before the light-matter interaction. Conversely, anti-Stokes Raman scattering is possible for molecules that are initially at an excited vibrational state.

Rotational transitions are generally associated with vibrational transitions and are mostly pertinent to molecules in the gas phase. Since there are no gas phases involved in the present work, discussions of rotational-vibrational (ro-vibrational) spectroscopy is not included in this chapter.

Since molecules are typically at a ground vibrational state, the Stokes transition is typically used to identify the chemical composition of the molecule, as the vibrational transition is unique to the molecular structure. In the Stokes transition, the scattered light has a lower energy (lower frequency or greater wavelength ) than the incident light. This difference in energy between the incident and scattered light is

termed the Raman shift (also known as the wavenumber) with units of $cm^{-1}$, given by the following relationship:

$$Raman\ \ shift\ [cm^{-1}] = 10^7 * \left(\frac{1}{\lambda_{ex}\ [nm]} - \frac{1}{\lambda\ [nm]}\right), \quad 3\text{-}6$$

where $\lambda_{ex}$ is the wavelength of the excitation (incident) laser source, and $\lambda$ is the wavelength of the Raman-shifted light. The Raman spectra of the membrane and mineral scaling species relevant to this work are summarized in Appendix A.

## 3.2 Raman-active Materials

In the past few decades, Raman spectral libraries have been established as internet-based open data sources, in an effort to make the data more accessible to the research community. One example is the RRUFF project, which provides high quality spectral data for thousands of mineral samples [60]. These databases illustrate the vast number of 'Raman active' materials/molecules, which are substances with vibrational modes that can be observed in a Raman spectrum. However, not all vibrational modes are Raman active, and the rules that govern Raman activity (or lack thereof) are commonly referred to as Raman selection rules.

Recall the specific, simplified case of an isotropic molecule that allowed $\alpha$ to be treated as a scalar quantity. In this case, the molecule was considered to be Raman active if the following were true:

$$\left(\delta\alpha/\delta Q_j\right)_0 = 0). \quad 3\text{-}7$$

In contrast, the more generalized case of the anisotropic molecule requires all three components of the fixed coordinate system (x, y, z), and $\alpha$ consequently becomes a tensor. Therefore, all the components of the polarizability tensor must be examined to determine Raman activity. The anisotropic molecule's induced dipole moment (Equation 3-1) can now be represented by a matrix equation:

$$\begin{bmatrix} P_x \\ P_y \\ P_z \end{bmatrix} = \begin{bmatrix} \alpha_{xx} & \alpha_{xy} & \alpha_{xz} \\ \alpha_{yx} & \alpha_{yy} & \alpha_{yz} \\ \alpha_{zx} & \alpha_{zy} & \alpha_{zz} \end{bmatrix} \begin{bmatrix} E_x \\ E_y \\ E_z \end{bmatrix}. \quad \text{3-8}$$

In spontaneous Raman scattering. the polarizability tensor is symmetric. Therefore, the off-diagonal components are related to each other: $\alpha_{xy} = \alpha_{yx}$, $\alpha_{yz} = \alpha_{zy}$, and $\alpha_{zx} = \alpha_{xz}$ [61]. This results in six distinct polarizability tensor components that are related to the characteristic normal modes of the molecule.

A polarizability ellipsoid is a three-dimensional surface whose center represents the electrical center of a molecule. Such an ellipsoid is commonly utilized to provide a helpful visualization of a molecule's polarizability tensor during vibration. Since the tensor is symmetric, it can be transformed to a new coordinate system of $x'$, $y'$, and $z'$ such that only the diagonal elements are nonzero. Using the transformed polarizability tensor in the new coordinate system, the polarizability ellipsoid is defined by the following [61]:

$$\frac{x'}{\left(\frac{1}{\sqrt{\alpha_{x'x'}}}\right)^2} + \frac{y'}{\left(\frac{1}{\sqrt{\alpha_{y'y'}}}\right)^2} + \frac{z'}{\left(\frac{1}{\sqrt{\alpha_{z'z'}}}\right)^2} = 1 \quad \text{3-9}$$

where $\alpha_{x'x'}$, $\alpha_{y'y'}$, and $\alpha_{z'z'}$ are the diagonal elements. Figure 3-2 [62] provides an example of changes in an ellipsoid during vibrations of the $CO_2$ molecule, showing three different normal modes ($v_1$, $v_2$, and $v_3$). Note a difference in the symbols utilized in the reprinted figure, where the nuclear displacement is represented by a lowercase $q$ instead of the uppercase $Q$ that was used in the rest of this dissertation. $+q$ and $-q$ represent the two extreme nuclear displacements.

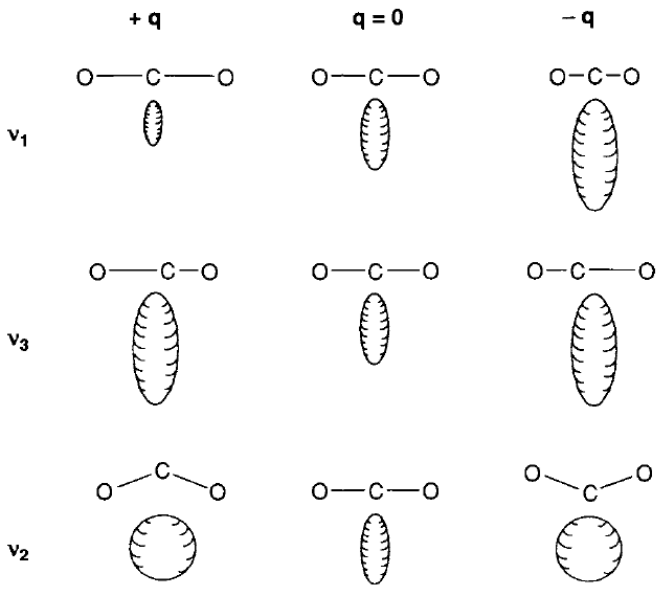


Figure 3-2. An illustration of changes in the polarizability ellipsoid of the $CO_2$ molecule during its three possible vibrational modes. (Reprinted with permission [62]. Copyright 2003 Elsevier Science.)

Let us examine the ellipsoids in each vibrational mode to determine whether or not it is Raman-active. In the $v_1$ and $v_3$ vibrational modes, the *size* of the ellipsoid changes for displacements $-q \rightarrow 0 \rightarrow +q$. In the $v_2$ vibrational mode, the *shape* of the ellipsoid changes for displacements $-q \rightarrow 0 \rightarrow +q$. However, the only Raman active vibrational mode is the $v_1$ vibrational mode. This is because the change in polarizability with respect to displacement *at equilibrium* must be nonzero. Figure 3-3 illustrates this by plotting polarizability ($\alpha$) as a function of displacement ($q$) from $-q$ to $+q$.

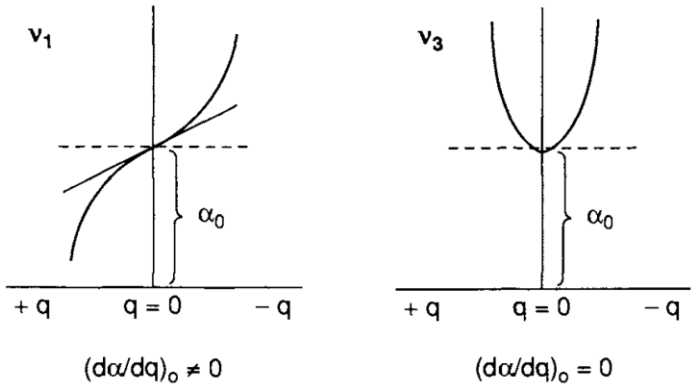


Figure 3-3. Polarizability ($\alpha$) is plotted as a function of displacement ($q$) from $-q$ to $+q$. When the slope is zero at $q = 0$, the vibration is Raman inactive, or forbidden. (Reprinted with permission [62]. Copyright 2003 Elsevier Science.)

We can understand why the $v_1$ vibrational mode is the only Raman-active mode by observing that $\left(\delta\alpha/\delta Q_j\right)_0 \neq 0$. In other words, the ellipsoids at the two extremes are different sizes. However, this is not the case for the $v_3$ vibrational mode where the ellipsoids at the two extremes are identical in size. Similarly, for the $v_2$ vibrational mode, the ellipsoids at the two extremes are identical in shape. Therefore, they are Raman inactive. In summary, a molecule is Raman active if either the size, shape, or orientation of the polarizability ellipsoid changes during vibration, such that the tensor $\left(\delta\alpha/\delta Q_j\right)_0 \neq 0$.

### 3.3 Raman Intensity Dependencies

In the previous section, the Raman active vibrational transitions were understood through the lens of classical mechanics (i.e., oscillations). However, to understand the intensity of Raman scattering, which is the magnitude of scattering, the *probability* of Raman active vibrational transitions must be included in the discussion using wavefunctions, a concept from quantum mechanics. A full discussion of the theory is is available elsewhere. Equation 3- presents without proof, the quantum-mechanical analogue of the classical expression for an induced electrical dipole moment ($P_{nm}$) [61,63]:

$$\overrightarrow{P_{nm}} = \left(\int \psi_m * \alpha\psi_n dQ\right)\vec{E} = \alpha_{nm}\vec{E}. \qquad 3\text{-}10$$

Here, $n$ and $m$ are the initial and final vibrational states of the molecule, respectively; $\psi_m$ and $\psi_n$ are the time-independent wavefunctions of the corresponding vibrational states; and as a reminder, $Q$ is the nuclear displacement during vibration. The scattering intensity ($I_{nm}$), averaged for all orientations of the molecule, is related to the square of the induced dipole moment in the general expression:

$$I_{nm} = N_n C(v_0 + v_{nm})^4 P_{nm}^2, \qquad 3\text{-}11$$

where, $N_n$ is the number of scattering molecules in initial state n, $v_{nm}$ is the frequency shift of the $n \rightarrow m$ vibrational transition, $C$ is a universal constant given by $64\pi^2/(3c^2)$, and $c$ is the velocity of light. Note that the intensity is proportional to the number of Raman scattering molecules ($N_n$) and the fourth power of the scattered light frequency, or approximately the fourth power of the incident light frequency.

Therefore, shorter incident wavelengths, or greater frequencies, give rise to higher Raman intensities [61]. Also, given that $P_{nm}^2 = \alpha_{nm}^2 E^2$, the intensity is proportional to the square of the molecule's polarizability ($\alpha_{nm}^2$) and the intensity of the incident light source ($E^2$) [61].

In practice, the Raman intensity is a measure of the number of photons, or counts, per second. However, this value changes from instrument to instrument, so relative intensities are more meaningful. Accordingly, the units of Raman intensity are typically presented as arbitrary units (au or a.u.) or omitted entirely. When describing Raman intensities, a particular parameter of interest is the Raman cross section, $\sigma_j$, also known as the scattering cross section. It is proportional to the intensity ratio of the incident and scattered light, and describes the probability that an incident photon will experience Raman scattering, with units of *cm$^2$/molecule* [64]:

$$I_R = I_0 \sigma_j D dz, \tag{3-12}$$

where $I_R$ is the measured intensity of Raman scattering, $I_0$ is the intensity of the incident laser, $D$ is number of scattering molecules per cubic centimeter, and $dz$ is the path length of the laser in the sample.

Finally, the polarization of the Raman scattered light can provide information about the scattering molecules. A polarizer and analyzer can be added to the Raman setup to determine intensity of light that is perpendicular or parallel to the incident polarization. The depolarization ratio, $\rho$, is the ratio between the two intensities:

$$\rho = \frac{I_{R\perp}}{I_{R\parallel}}, \tag{3-13}$$

where $I_{R\perp}$ and $I_{R\parallel}$ are the measured Raman intensities with perpendicular and parallel polarization relative to the incident laser polarization ( $\rho \cong 0 - 0.75$ for liquids and gases [64]). Lower values of $\rho$ indicate strongly polarized modes and larger values of $\rho$ correspond to strongly depolarized modes. Vibrations that preserve molecular symmetry (i.e., with spherical polarizability ellipsoids [62]) are known as *totally*

*symmetric* normal modes, with $\rho$-values generally close to 0. Asymmetric vibrations are related to strongly depolarizing modes, with corresponding $\rho$-values closer to ~0.75.

### 3.4 Raman Scattering by Solids

The Raman theory for the free molecule is applicable in low pressure gases and dilute solutions. In the solid and certain liquid states, the presence of intermolecular forces can introduce changes in the molecular vibrational modes. In other words, the incident laser source produces harmonic oscillations, not just in a single molecule, but also in neighboring molecules that constitute the solid material (lattice vibrations). In most cases, the spectral differences between the gas, liquid, and solid states range anywhere from several to hundreds of $cm^{-1}$ [65]. For example, in the case of the sulfate ($SO_4^{2-}$) ion, the $v_1$ vibrational mode increased from 981 to 1008 $cm^{-1}$ when the ion was incorporated into the lattice of calcium sulfate dihydrate, or gypsum ($CaSO_4 \cdot 2H_2O$) [66,67]. Nonetheless, the Raman bands of solids are still molecular in origin; any changes in the Raman spectra are determined by relevant intermolecular forces in the solid material.

It is now necessary to introduce the quantum unit of vibrational mechanical energy, which is the phonon. The vibrational frequencies of phonons can be categorized into two main branches [68]. In the acoustic branch, the wavelength of the phonon is large compared to the spacing of atoms in a lattice, so the vibrational wave propagates like a sound (acoustic) wave with relatively low frequency. In the optical branch, the vibrations have much higher frequencies and can thus couple with electromagnetic fields in the infrared region. In each branch, the vibrations can be further categorized by the direction of vibration: transverse and longitudinal modes move perpendicular and parallel, respectively, to the direction of wave propagation. Both optical and acoustic phonons can give rise to inelastic scattering, but Raman scattering deals with optical phonons.

When comparing the Raman spectra of solids to that of free molecules, there are three main differences to note. The first difference was already mentioned, namely, the changes in vibrational

frequencies and also potential changes in intensities. The second difference is the splitting of single Raman bands into two or more bands attributed to the removal of degeneracies when free molecules are incorporated into a solid environment. Finally, the third difference is the appearance of completely new low-wavenumber Raman bands, due to vibrations in the crystal lattice.

For solids with long range order (i.e., crystals), the depolarization ratio can provide information on the crystallographic orientation of the solid [69]. The intensity of Raman scattering by solids ($I$) still depends on the parameters mentioned for the free molecule: the number of scattering molecules and their polarizability, and the wavelength and intensity of the incident light. Additionally, $I$ is proportional to the following:

$$I \propto \left|\hat{e_i} \cdot \vec{R} \cdot \hat{e_s}\right|^2, \qquad 3\text{-}12$$

where, $\hat{e_i}$ and $\hat{e_s}$ are the unit vectors of the direction of the incident and scattered light, respectively. The Raman tensor, $\vec{R}$, is a symmetric tensor that is determined using the *nuclear site group analysis* method [65,70]. In brief, this method identifies the particular crystal structure and the location of the atoms in the unit cells to determine the symmetry of the crystal and its relevant Raman tensors. Rousseau et al. [71] provides a more detailed theory and a complete set of tables that can be used to determine relevant Raman tensors.

## 3.5 Advantages & Disadvantages of Raman Spectroscopy

The following are some of the advantages of using Raman spectroscopy for RO membrane scaling detection:

- Chemical fingerprinting
- Non-destructive and non-contacting
- Suitable for observation through transparent windows
- Sensitive to small changes in material structure

- Water-compatible (with the use of a Raman probe)

It is noted in the literature that Raman signals can be sensitive to ambient conditions of the material, such as temperature and pressure, because these conditions can also influence molecular vibrational modes in the material. The qualitative effects of ambient conditions on Raman spectra are documented in the literature [72,73]. For the presently applied range of RO operating conditions (pressures of ~1±0.3 MPa; temperatures of ~22–24°C) seem to have negligible effects on the Raman spectra of the membrane and foulants.

Some of the limitations of Raman spectroscopy for membrane scaling detection include:

- Interference of fluorescent background signals
- Low signal-to-noise ratios for some materials (spontaneous Raman)
- Quantitative analysis is difficult

Most of the light reflected from a material sample experiences Rayleigh scattering, in that the incident photons have the same energy before and after interaction with the material. In contrast, Raman scattering is a rarer occurrence: about 1 in $10^5$–$10^{10}$ photons are inelastically scattered [64,74]. Furthermore, in Section 3.1, it was shown that not all materials produce Raman scattering, as the probability of Raman scattering depends on a molecule's degree of polarizability ($\delta\alpha/\delta Q_j = 0$). Inorganic salts possess strong Raman cross-sections because of their long-range molecular order. Organic foulants can be more challenging to study using Raman spectroscopy because their fluorescence cross-sections can be as much as $10^{-14}$ times greater than their Raman cross-sections [75]. In other words, Raman signals of certain materials can be easily obscured by a large background signal comprised of fluorescence and noise. To further complicate matters, organic foulants tend to share the similar molecular bonds as polymer-based membranes resulting in low signal-to-noise ratios.

Still, there are ways to address these disadvantages, e.g., by employing Raman scattering with resonance or surface enhancement which have successfully overcome issues such as the obscuration of

Raman signals by background noise [51,76]. In the present work, spontaneous Raman scattering is used for real-time chemical detection and monitoring of membrane scaling. The successful aspects of the presented work achieved using only simplest version of the Raman-based technique (i.e., spontaneous Raman), demonstrates its potential for technological adoption on both research and industrial scales.

## 3.6 Microscope Design

### 3.6.1 *Renishaw Raman Microscope*

In Chapter 4, a Renishaw inVia Raman microscope was used to detect membrane scaling and scale removal. The RO flow cell was mounted on a high-load capacity, vertical translation stage (VAP4, Thorlabs), enabling Z-height adjustment during laser focusing on the membrane (Figure 3-4). The microscope objective (N-PLAN L50X, Leica; working distance of 8.2 mm) focused the beam to a spot size of ~3 μm (FWHM, Full Width at Half Maximum), and the incident power on the sample was ~20 mW of using a 785-nm laser excitation source (I0785SD0090B-IS1, Innovative Photonic Solutions).

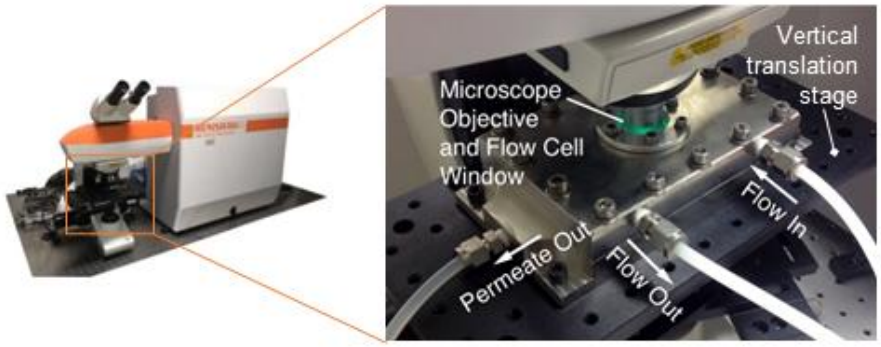


Figure 3-4. Integration of inVia Raman microscope and reverse osmosis flow cell [55].

For Raman data collection during scaling experiments, the microscope objective was aligned with the flow cell's optical window in using the microscope's white light source to guide the objective into the center of the window. Using the coarse adjustment knob on the vertical translation stage, the flow cell was raised so that the optical window cavity could accept the microscope objective, taking care to avoid collision. Once rough alignment was complete, the fine adjustment knob of the vertical translation stage

was used to raise the flow cell until the laser was focused onto the membrane surface. Finally, all stage adjustment knobs were locked into place to prevent any movement during Raman data collection, which would disturb the laser focus. To perform Raman scans on post-mortem scaled membrane samples, the samples were fixed on a glass slide and positioned under the microscope objective. The scan area and resolution were specified in the microscope's commercial software (WiRe 4.4), and scans were performed using a high-speed, optically encoded stage (MS30, Renishaw) featuring an 80 mm/s maximum travel speed, 112 mm × 76 mm range of travel, and a spatial resolution of 50 nm with a repeatability of 0.35 µm.

Raman data post-processing occurred in WiRe 4.4, including use of the cosmic ray removal tool (user defined cosmic ray threshold values) and baseline removal tool (utilizing a proprietary algorithm called Intelligent Fitting), which was used to remove the background fluorescence signal of the membrane. This is because the fluorescence signal tends to change over time due to effects such as photobleaching.

### 3.6.2 *In-house Raman Microscope*

The use of the commercial Raman microscope was suitable for a proof-of-concept demonstration of scaling detection on RO membranes. However, due to limitations on instrument availability and cost led to scaling experiments were designed to be completed within 3-6 h; supersaturated feed solutions were prepared to induce scaling within this relatively short timeframe. Accordingly, the design and fabrication of an in-house Raman microscope was justified, enabling a wider variety of scaling experiments including investigations in the use of different feed compositions and the time evolution of scaling progression, beyond initial Raman detection.

#### **3.6.2.1** Bill of Materials

A schematic of the Raman system is shown in Figure 3-5. The laser system constituted a narrow linewidth, 785-nm laser diode (FPV785S, Thorlabs), and laser and thermoelectric controller (TEC) controller (6305 ComboSource, Arroyo Instruments). The laser source was first directed through a laser

clean-up filter (LL01-785, Semrock). Silver mirrors (PF10-03-P01-10, Thorlabs) were used to reflect the light to a dichroic beamsplitter and a 25 mm × 35 mm shortpass dichroic mirror (DMSP650R, Thorlabs). A 50× objective (MUE21500, Nikon) with a working distance of 11 mm and 0.60 NA was used to focus the laser beam onto the sample with about 27 mW of optical power. The scattered light was guided to a longpass filter (RET792LP, Chroma) with an optical density (OD) of 6 for wavelengths <788 nm. This allowed light of wavelengths >785 nm to pass, effectively filtering out any Rayleigh scattered light. The remaining Raman scattered light was focused onto 0.1 NA, 105-µm diameter fiber (M96L02, Thorlabs) using a plano-convex lens with a focal length of 10 mm (LA1116-B, Thorlabs). The fiber was used to couple the Raman scattered light to the entrance slit of the spectrometer (Acton SP2500i, Princeton Instruments). The spectrometer featured a triple grating turret with 300 l/mm with 750-nm blaze wavelength (part number 1-030-750, Princeton Instruments), 600 l/mm with 1µm blaze wavelength (part number 1-060-1, Princeton Instruments), and 1200 l/mm with 850 nm blaze wavelength (part number unavailable) grating options to provide a variety of spectral ranges and resolutions. For the detector, a back-illuminated, deep-depletion charge coupled device (CCD) (PIXIS 100BR, Princeton Instruments) was used, which included a 1340 × 100 imaging array with 20 µm × 20 µm pixels (28.6 mm × 2 mm) and thermoelectric cooling to -75 °C to minimize dark current.

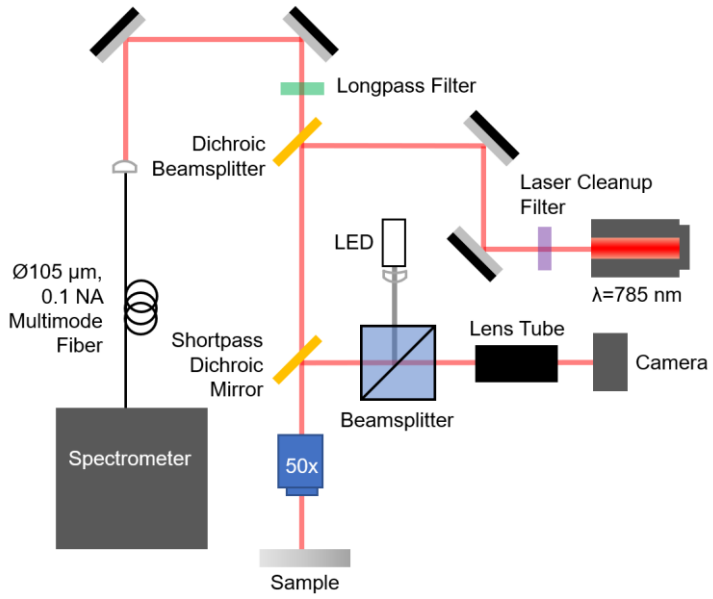

Figure 3-5. A schematic of the spontaneous Raman microscope. A 785-nm, narrow linewidth photodiode passed through a laser cleanup filter to filter out the Raman shifted wavelengths in the carrier fiber. The beam passed through the reflective sides of the dichroic beamsplitter and transmissive side of the short-pass dichroic mirror and is focused onto the sample by the microscope objective. The elastically and inelastically scattered light is redirected through the short-pass dichroic mirror, and a long-pass filter sorts out the Raman-shifted photons from the common beam path. These Raman-shifted photons are coupled into a 105-µm diameter, 0.1 NA fiber, which is connected to the entrance slit of the spectrometer. The spectrometer has a triple-grating turret featuring three different diffraction gratings (selection depends on desired spectral resolution). The diffracted light is projected onto a CCD detector thermoelectrically cooled to -75 °C to minimize background noise.

Finally, a USB 3.0 color camera (CM3-U3-50S5C-CS, Flir), collimated LED light source and driver (LEDD1B, Thorlabs) and 50:50 non-polarizing beamsplitter (BS013, Thorlabs) enabled illumination and visualization of the sample, as well as visualization of the laser beam during focusing.

#### **3.6.2.2** Choosing a laser source

The three standard excitation wavelengths used in Raman spectroscopy are 532 nm, 785 nm and 1064 nm. In order to select a suitable laser source, it is helpful to first characterize the fluorescent background of the samples that are to be measured, to assess the risk of any high fluorescence backgrounds that could potentially drown out the Raman signal. Fluorescence typically occurs with excitation wavelengths in the smaller, visible range (400-650 nm). Therefore, Raman measurement samples that have a high fluorescent background (such as organic foulants) could benefit from the use of greater excitation wavelengths. However, this would be at the expense of the intensity of the Raman signal, which is approximately inversely proportional to the fourth power of the excitation wavelength. Given that the primary materials in this work are inorganic crystals (low fluorescence) deposited on polymer membranes (moderate to high fluorescent background), the 785-nm laser source provided a suitable balance of strong Raman signals and reasonably low fluorescent background. This led to the selection of a single-frequency, 785-nm laser diode housed in a butterfly package that included an optical isolator, monitor diode, and thermoelectric controller/thermistor; the diode was mounted on a laser/thermoelectric controller for temperature management.

The operating current to optical power conversion (Figure 3-6) characterized using a photodiode power sensor (S130C, Thorlabs) matched with the conversion provided by the manufacturer, confirming that the assembled laser system was performing up to specifications.

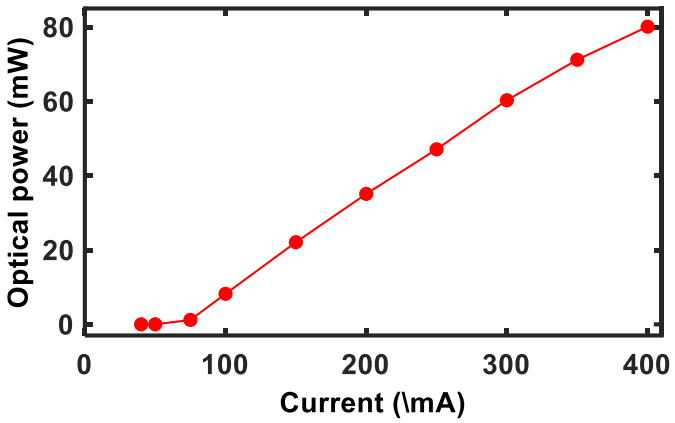


Figure 3-6. Conversion between operating current to optical output for the 785-laser diode.

Although the maximum rated operating current of the diode was 410 mA, the system was operated at currents no greater than 350 mA, corresponding to ~30 mW of incident power on the sample. This is because laser diodes can be extremely sensitive to excess operating current. To ensure the longevity of the laser source, especially for use in long-duration reverse osmosis experiments, the applied current must be increased/decreased gradually, such that the internal temperature sensor does not exceed 0.05 °C from the rated operating temperature (~20 °C).

Since an optical fiber was used to couple the Raman scattered light with the spectrometer, a laser clean-up filter was absolutely necessary to eliminate any Raman modes excited in the optical fiber and potential noise introduced by mode hopping, supersaturating the detector. The cleanup filter is typically already included in commercial turnkey systems.

**3.6.2.3** Spectrometer and detector

The spectrometer had a focal length of 500 mm and an aperture ratio of f/6.4 (68 mm × 68 mm gratings). An adjustable slit allowed for slit widths of 10 μm to 3 mm. During calibration of the Raman

system, a slit width of 20 μm was experimentally selected based on changes in the observed signal-to-noise ratios. Figure 3-7 provides the schematic of a general spectrometer/microscope body.

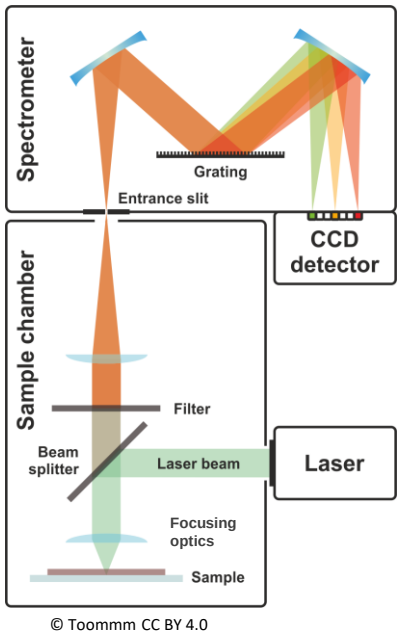


Figure 3-7. A schematic of a representative spectrometer/microscope assembly. The spectrometer has a Czerny Turner configuration, where light enters through the entrance slit, and is collimated onto the diffraction grating. The diffraction grating spatially separates the different wavelengths in the collimated light, and projects the separated light onto a mirror that finally focuses the light onto the CCD detector.

First, the fiber guided the Raman scattered light to the entrance slit of the spectrometer. At this point, the light is collimated onto the diffraction grating using a mirror. The diffraction grating spatially separates the different wavelengths in the collimated light, and projects the separated light onto a mirror that focuses the light onto the CCD detector.

Figure 3-8 shows a CCD image (middle) of ambient indoor lighting (no sample), illustrating how the light that passed through the entrance slit was spatially separated by the diffraction grating and projected onto the CCD detector. The image shows the spectral bands of the light from fluorescent bulbs that were installed in the microscope room (filled with argon gas).

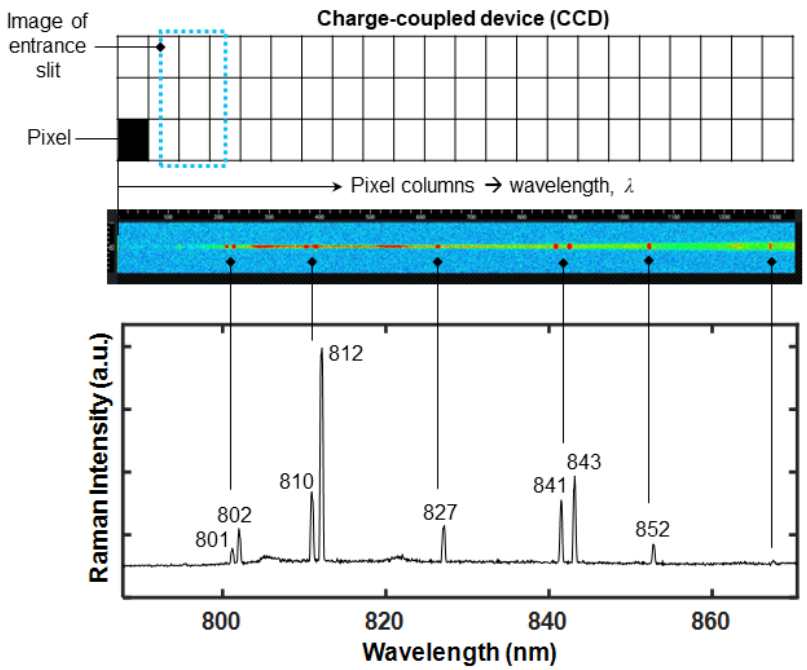


Figure 3-8. (top) The detector was a back-illuminated, deep-depletion charge coupled device (CCD) (PIXIS 100BR, Princeton Instruments), which included a 1340 × 100 imaging array with 20 μm × 20 μm pixels (total array size of 28.6 mm × 2 mm) and thermoelectric cooling to -75 °C to minimize dark current. (middle) An image was taken of ambient indoor light. The resulting CCD image shows the spectral bands of the fluorescent bulbs that were in the microscope room (filled with argon gas).

Diffraction grating selection depended on spectral resolution and range needs. Raman spectra of a reverse osmosis membrane obtained using three different diffraction gratings are shown in Figure 3-9. The finest-grooved grating (1200 lines per mm or lpmm), resulted in the highest spectral resolution (~1.8 $cm^{-1}$), the shortest spectral range (~400 $cm^{-1}$), and greatest amount of noise compared to the 300 and 600 lpmm gratings. Vibrational modes from ~100 to ~1400 $cm^{-1}$ [20,21,77] belong in the Raman spectra of both well-defined and amorphous mineral scales (e.g., calcium sulfate, calcium carbonate, calcium phosphate) relevant in RO desalination. Therefore, a spectral range of approximately 1300 $cm^{-1}$ was desired, and consequently, the ~400 $cm^{-1}$ range provided by the 1200 lpmm grating was deemed too narrow. The spectral resolution is directly proportional to the grating groove density, so the 300 lpmm grating provided a resolution of ~6 $cm^{-1}$. In the interest of studying crystalline polymorphs, which are solids with different crystal structures, this was not sufficient spectral resolution. For example, calcite, aragonite, and vaterite are the three main polymorphs of calcium carbonate, whose $v_1$ vibrational modes appear within ~5 $cm^{-1}$ of

each other (1086, 1085, and 1090 $cm^{-1}$, respectively). Consequently, a resolution of ~6 $cm^{-1}$ would not be able to resolve these differences in the calcium carbonate polymorph Raman spectra. Considering the tradeoff between spectral range and resolution, the 600 lpmm grating reasonably provided the required Raman specifications for the study of mineral scales.

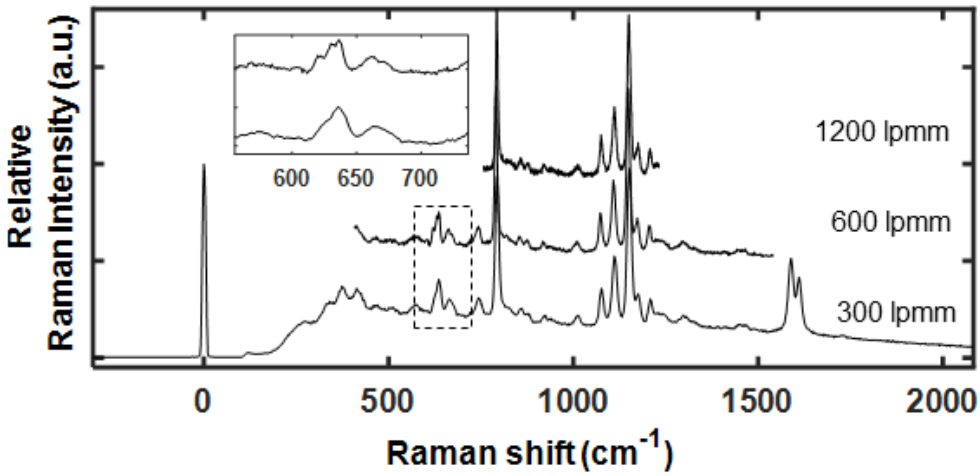


Figure 3-9. Raman spectra of a reverse osmosis membrane were obtained using three different diffraction gratings. The finest-grooved grating, 1200 lpmm (lines per mm), results in the highest spectral resolution, shortest spectral range, and greatest amount of noise compared to the 300 and 600 lpmm gratings. Selection of the grating depends on spectral resolution and range requirements.

#### **3.6.2.4** Calibration

The Raman system went through multiple iterations of beam alignment to maximize the coupling efficiency between the focusing lens and the optical fiber. Figure 3-10 is a representative Raman spectrum of a silicon wafer standard obtained after calibration, showing a high-SNR peak at 521.68 $cm^{-1}$, and a full width at maximum height (FWHM) of 3.6 $cm^{-1}$, which agreed with literature values [78]. This demonstrates that the in-house Raman microscope's performance was comparable to the commercial Raman system used in Chapter 4. Regular maintenance of the Raman system included collecting the Raman spectrum of a silicon wafer, to ensure that the signal-to-noise ratio remained approximately >150.

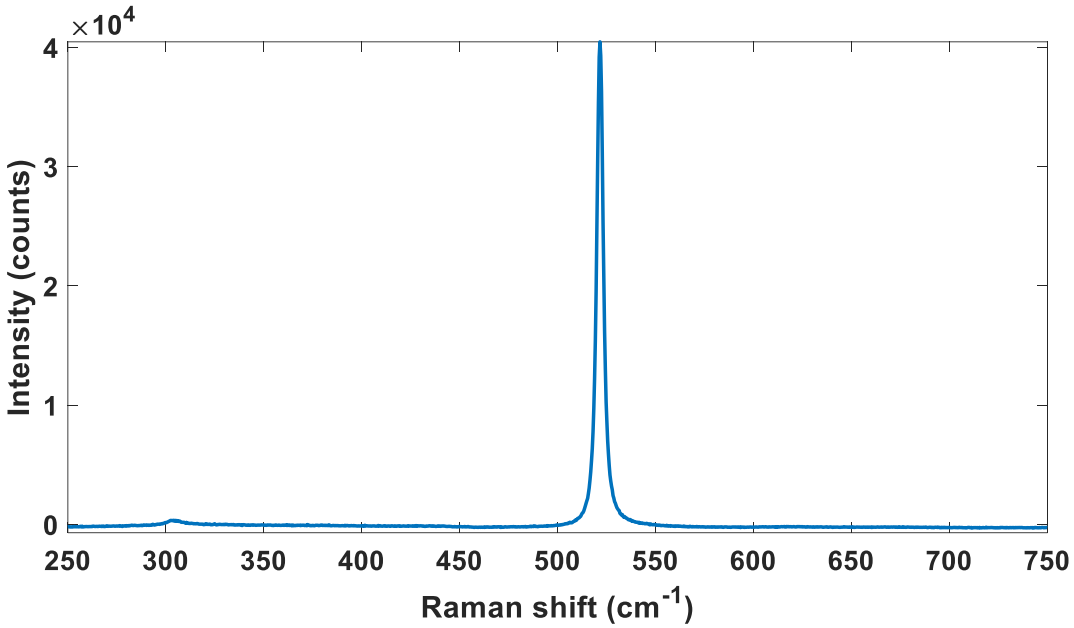


Figure 3-10. A silicon wafer was used to characterize the performance of the custom Raman system. A prominent peak at 521.68 $cm^{-1}$ with a FWHM of 3.6 $cm^{-1}$ is observed, which agrees with literature values [78]. This peak's high signal-to-noise-ratio demonstrates suitable calibration and performance of the Raman system, comparable to the commercial Raman system used in the experimental work in Chapter 4.

Increasing the acquisition time can lead to SNR improvements in spontaneous Raman spectroscopy. This is in part due to the decrease in the shot noise inherent to processes governed by Poisson statistics (random events) such Raman scattering [64]. To illustrate the effect of acquisition times on Raman SNR, Figure 3-11 shows three different normalized Raman spectra of a thin-film composite polyamide reverse osmosis membrane, for acquisition times of 1, 5, and 30 s.

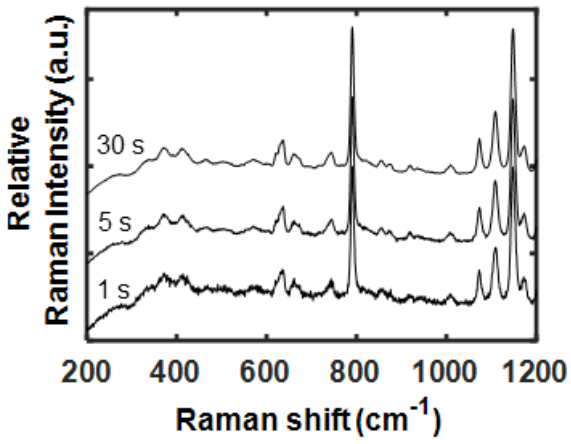


Figure 3-11. Longer acquisition times can lead to better signal-to-noise ratios.

Indeed, upon visual inspection, the greatest noise in the Raman signal is observed for the spectrum of shortest acquisition time (1 s). In the present work, real-time Raman signals of the mineral scales from reference scaling experiments and post-mortem inspection of the scaled membranes guided the selection of the acquisition times. Additionally, the selection of a ~10-20 s acquisition time range. for spectra provided sufficient SNR for early detection of calcium sulfate and calcium carbonate mineral scaling.

# Chapter 4 Real-time monitoring of calcium sulfate scale removal from RO desalination membranes using Raman spectroscopy

Chapter 4 is based on: "Real-Time Monitoring of Calcium Sulfate Scale Removal from RO Desalination Membranes Using Raman Spectroscopy," by D. J. Park, O. D. Supekar, A. R. Greenberg, J. T. Gopinath, and V. M. Bright. Published in *Desalination*, (2021) Vol. 497, p. 114736.

## 4.1 Abstract

Chemical characterization of scaling and removal processes was performed in real time via Raman spectroscopy in a bench-scale reverse osmosis (RO) system. A custom RO cross-flow cell was integrated with a Raman microscope objective, allowing for analysis of localized membrane scaling and scale removal. Permeate flux was also measured to provide a real-time metric for comparison. A commercial flat sheet, thin-film composite reverse osmosis (TFC RO) membrane was scaled using a calcium sulfate ($CaSO_4 \cdot H_2O$) feed solution. Upon $CaSO_4$ scale detection, the feed was switched to DI water, which served as a cleaning agent to remove the $CaSO_4$ scale from the membrane. In addition to the real-time local (Raman) and global (permeate flux) measurements, membrane samples were characterized post-mortem using Raman spectroscopy, gravimetric analysis, and scanning electron microscopy to provide important scaling and scale removal metrics. Results from real-time measurements indicated that changes in Raman intensity were a more sensitive indicator of local scale removal than changes in permeate flux, a standard cleaning performance metric; these findings were corroborated by the post-mortem analyses. Overall, the membrane cleaning experiments showed that Raman spectroscopy provided crucial real-time chemical composition and spatial distribution information, which can inform more effective antiscaling and cleaning strategies.

## 4.2 Introduction

The literature indicates that in general, membrane cleaning measures are most effective in the early stages of scaling before irreversible damage occurs [6]. It is also important to have access to chemical real-

time feedback as membrane cleaning ensues to assess how well the RO system is responding to the membrane cleaning. In particular, in complex feed waters, the timing, dosage, and chemical composition of the cleaning/antiscaling agents must be tailored to the multiple components in the feed water for optimal results [8]. Clearly, customization of the cleaning strategy would benefit from knowledge of the real-time chemical composition of the scale.

In addition, due to the spatial variation in membrane scaling caused by concentration polarization, a local detection technique is needed, because area-averaged metrics may provide delayed information about cleaning progress. In response to this critical need, a number of different methods of scaling/fouling detection have been developed. Ultrasonic time-domain reflectometry (UTDR) [8,15–18], electrical impedance spectroscopy (EIS) [19,20], Raman spectroscopy [21–23], visual observation techniques [24–26], streaming potentials [27,28], magnetic resonance [29] and X-ray imaging [30] are methods that have been used to study membrane fouling in real time. Many of these techniques have also been used to monitor membrane cleaning. For example, Uchymiak et al. [24] demonstrated scale detection and monitoring of scale removal using an ex-situ scale observation detector (EXSOD) in a bench-scale reverse osmosis flow cell. While each of these aforementioned techniques offer a different set of advantages and disadvantages, Raman spectroscopy uniquely provides real-time information regarding chemical composition of the scaling layer.

In this work, Raman spectroscopy is utilized for the first time to monitor scale removal from an RO membrane during desalination operating conditions. This is performed in real-time by monitoring changes in the intensity of the peaks corresponding to the chemical composition of the scalant under the Raman sensor. Here, incident photons from a laser focused onto the membrane surface through an optical window interact with optical phonons in the scale layer to generate inelastically scattered photons [31]. The energy difference between the incident and scattered photons, known as the Raman shift, is specific to the rotational and vibrational transitions of bonds in a molecule. The intensity of Raman shifts corresponding to the

scalant provides the means for chemical identification and relative quantification of the extent of the scaling.

We provide a detailed description of the application of Raman spectroscopy for monitoring the removal of $CaSO_4$ scale in a bench-scale RO system. An important component of the cleaning experiments conducted in this work is the comparison between the real-time Raman and permeate flux measurements, the latter constituting a commonly used indicator of membrane cleaning in commercial desalination plants [32]. While real-time changes in permeate flux are an indirect indicator of global scale deposition and removal, Raman spectroscopy provides a direct and chemically specific measurement of changes in a localized region. This initial study highlights the sensitivity and accuracy of the Raman technique and its capability to provide chemical information as a function of cleaning time and membrane location. Ultimately, the Raman methodology described here could lead to the development of improved membrane cleaning techniques.

## 4.3 Experimental Method

### 4.3.1 *Reverse osmosis system*

An RO cross-flow cell and supporting system were used to conduct the membrane cleaning experiments [53]. A schematic of the cross-flow cell is shown in Figure 4-1, and the system diagram is shown in Figure 4-2. The top and bottom components of the flow cell were constructed from 0.625-inch (1.59 cm) thick plates of stainless steel to withstand the high operating pressures. The top component featured an inlet (feed) port that injected pressurized feed into the flow cell and flushed the retentate through the outlet (retentate) port. The bottom component was fitted with a stainless-steel mesh to support the membrane. To allow for the real-time collection of Raman spectra, the flow cell featured an optical window that interfaces with a 50X microscope objective (N-PLAN L50x/0.50, Leica Germany) of the Raman microscope (inVia Reflex, Renishaw, Section 3.6.1). The flow cell was mounted on a custom stage with an

adjustable *z*-axis, and fixed *x*- and *y*- axes, and the center of the flow cell was aligned with the Raman microscope.

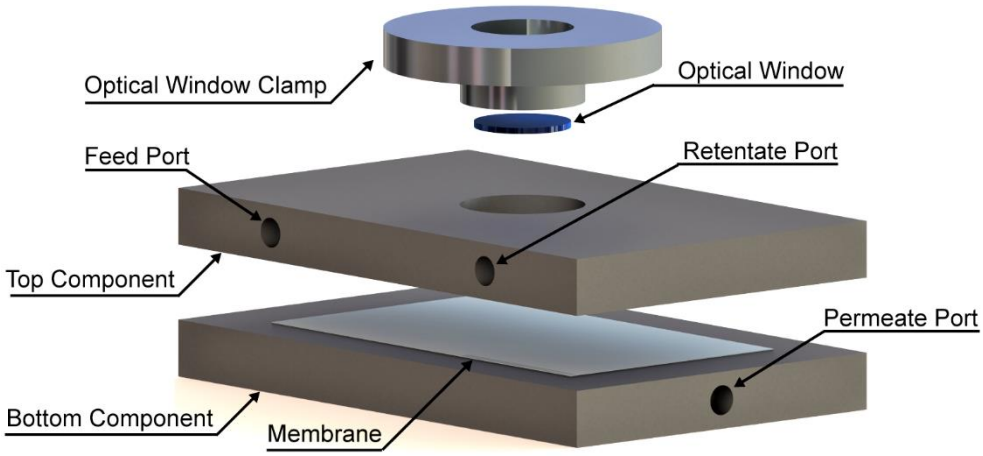


Figure 4-1. An exploded view of the RO flow cell is shown. The optical window accommodates the Raman microscope objective for real-time acquisition of Raman spectra during desalination. The top component houses the feed and retentate ports, while the bottom component includes the permeate port. The membrane is supported by a stainless-steel mesh on the permeate side.

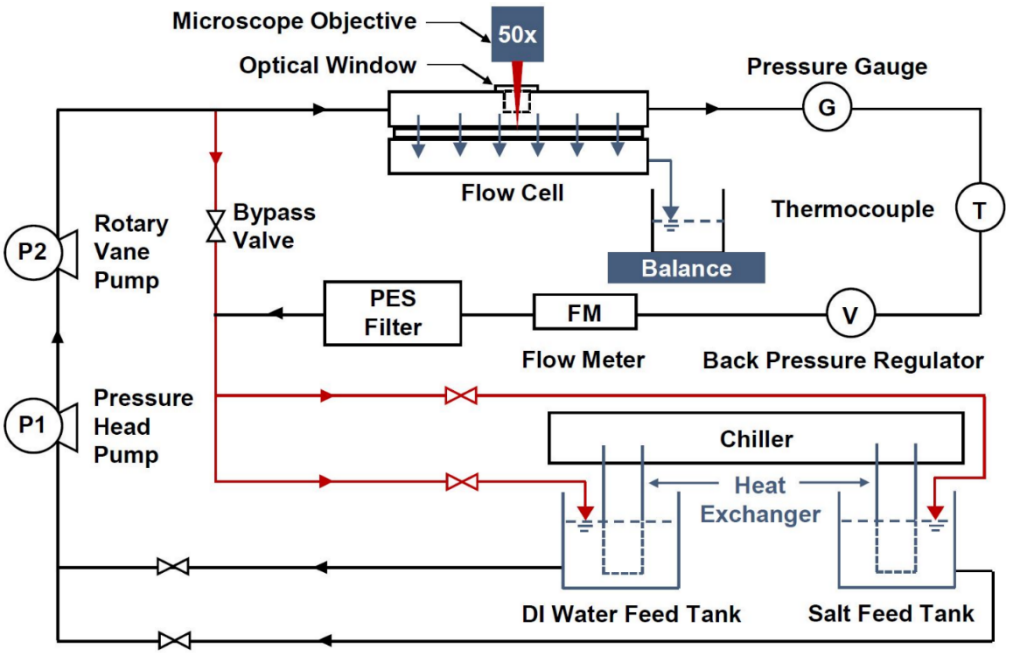


Figure 4-2. A diagram of the bench-scale RO system features two feed tanks with valves to facilitate the transition between membrane scaling and cleaning. Pressure, temperature, and flow rate were monitored and controlled using a pressure gauge and backpressure regulator, thermocouple and chiller, and flow meter and bypass valve, respectively.

A high-pressure rotary vane pump (TMFRSS051A, Fluid-o-Tech) circulated the feed to the flow cell, and a pressure head pump (3-MD-SC, Little Giant) was used to prevent cavitation. The retentate passed through a pressure gauge (100 Series, NoShok) and a backpressure regulator (12-251B2-44AZ5-72, Neon) was used to monitor and control the pressure in the flow cell. The retentate was also passed through a 0.2 μm polyether sulfone filter (CCS-020-C1B, 0.2 μm, Advantec) to filter particulates before it was circulated back into the salt feed tank. The temperature of the feed was monitored using a thermocouple downstream of the flow cell and controlled using a chiller (T257P, Thermotek). The bottom component of the flow cell features a port through which permeate water was collected in a beaker and its mass monitored with a precision balance (PNX-2002, American Weigh Scales). A flow meter (74C-234G041-421330, King) was used to monitor the flow rate, and a bypass valve (SS-1RS4, Swagelok) installed upstream of the flow cell was used for flow rate control. Commercial thin-film composite reverse osmosis (TFC RO) membranes (UTC-73HA, Toray) were used in all of the experiments.

### 4.3.2 *Experimental protocol*

The feed used to scale the membranes was a 1.8 g/L solution of calcium sulfate dihydrate (99% Reagent Plus, Sigma−Aldrich) in DI water. The scaling procedure followed that described in previous studies [53,55]. Typically, $CaSO_4$ cleaning is conducted using a series of acid and water washes to restore the permeate flux as quickly as possible [79,80]; however, for these experiments, DI water washes were deemed adequate for scale removal (cleaning). Before conducting the scaling and cleaning experiments, all membranes were pretreated by soaking in a solution of 300 ml DI water and 300 ml isopropanol for 30 min to remove any additives. The flow cell was cleaned with DI water and isopropanol, and the RO system was flushed with DI water for 30 min to remove residual scale and any contaminants before each experiment. Soaked membranes were placed in the flow cell and compacted in the RO system with a reservoir of DI water for ~15 h, at a temperature of 23.5 ± 0.5°C, pressure of 175 ± 1 psi (1.2 MPa), and volumetric flow rate of 15 ± 1 LPH. After compaction was completed, the Raman microscope objective was lowered into the optical window, and spectral acquisition was initiated for 15 min with DI water to collect baseline

Raman spectra on a compacted, clean membrane. To obtain a Raman signal, the z-height of the stage was adjusted to focus a 785 nm laser (I0785SR0090B-IS1, Innovative Photonic Solutions) on the membrane surface through the objective and optical window. Then, the feed was switched from DI water to calcium sulfate solution to initiate scale formation on the membrane.

A first series of experiments (intensity control) were conducted with the aim of simulating one scaling and cleaning cycle, whereby membranes were scaled so that the normalized $CaSO_4$ Raman peak intensity exceeded 50% and then cleaned until the $CaSO_4$ Raman peak intensity returned to baseline values (Tests 1–4). A second series of experiments (time control) were then conducted where membranes were scaled for 45 min and partially cleaned for 5 min to focus on monitoring the early stages of cleaning (Tests 5–7).

### 4.3.3 *Raman spectra analysis*

The Raman spectra of a clean TFC RO membrane is shown in Figure 4-3A. The peak at ~790 $cm^{-1}$ results from the C-H bond deforming in an out-of-plane benzene ring, the peaks at 1074 and 1108 $cm^{-1}$ are the result of symmetric and antisymmetric $SO_2$ stretching, respectively, and the peak at 1150 $cm^{-1}$ appears due to stretching of C-O-C bonds [81]. These are the major peaks observed in the Raman spectrum of polysulfone (PSf). The RO composite membranes are tri-layered with an ultra-thin polyamide layer, an intermediate micro-porous PSf layer, and a polyester support layer. Since the peak at 1150 $cm^{-1}$ is dominant, the entire Raman spectra was normalized to this peak. When $CaSO_4$ crystals, whose principal Raman peak occurs at 1008 $cm^{-1}$ [82], nucleate and grow on the membrane, the membrane and $CaSO_4$ peaks are superimposed (Figure 4-3B). Then, during membrane cleaning, as $CaSO_4$ dissolves and desorbs from the membrane, the peak at 1008 $cm^{-1}$ decreases (Figure 4-3) because the intensity of the peak is based on volume interactions between the incident photons from the laser and the material of interest ($CaSO_4$ scale).

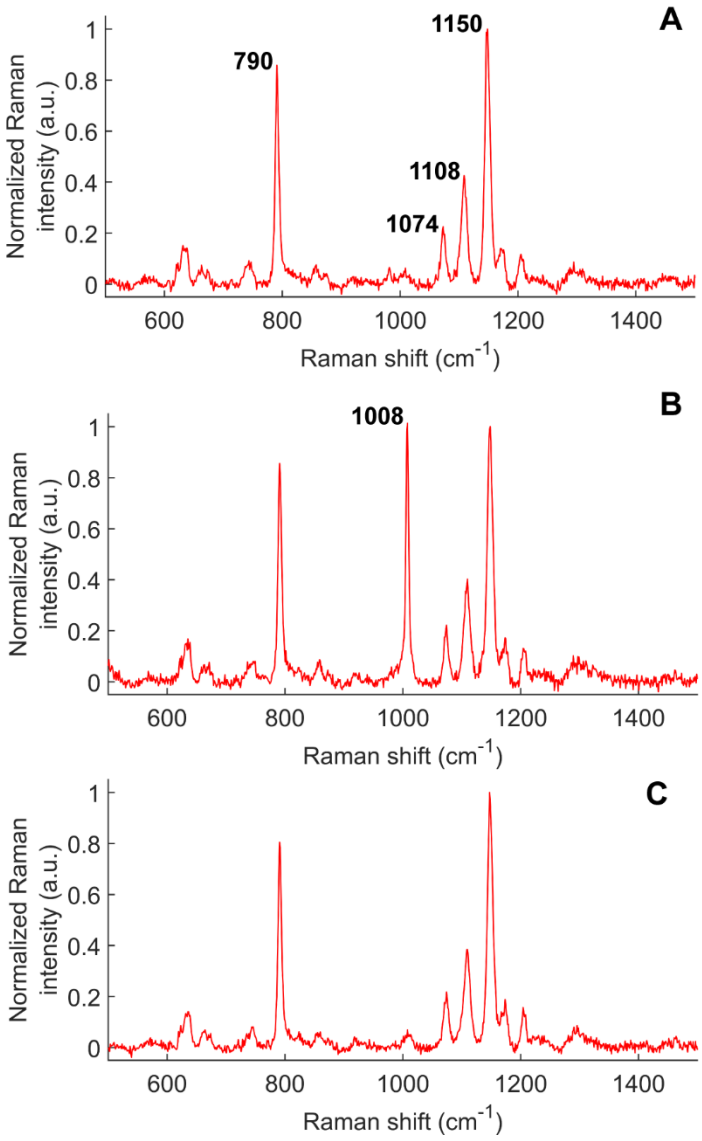


Figure 4-3. (A) Raman spectra of the TFC RO membrane before the onset of scaling with peaks at ~790 $cm^{-1}$ (C-H deformation), 1074 and 1108 $cm^{-1}$ ($SO_2$ symmetric and antisymmetric stretching), and 1150 $cm^{-1}$ (C-O-C stretching); (B) as $CaSO_4$ scale grows beneath the interrogated region of the membrane, a dominant peak appears at 1008 $cm^{-1}$; and (C) the $CaSO_4$ Raman peak intensity decreases as the membrane is cleaned with DI water.

### 4.3.4 *Post-mortem membrane characterization*

#### **4.3.4.1** Raman spectroscopy performed over a larger sampling area

Post-mortem characterization of partially cleaned membrane samples from Tests 5–7 was conducted to complement the real-time data and provide more insight into the performance of the Raman sensor during membrane cleaning. The membranes were cut into 4 $cm^2$ coupons from the upstream, center,

and downstream locations (Figure 4-4A). The center test coupon encompasses the location where real-time Raman measurements were made during the experiments.

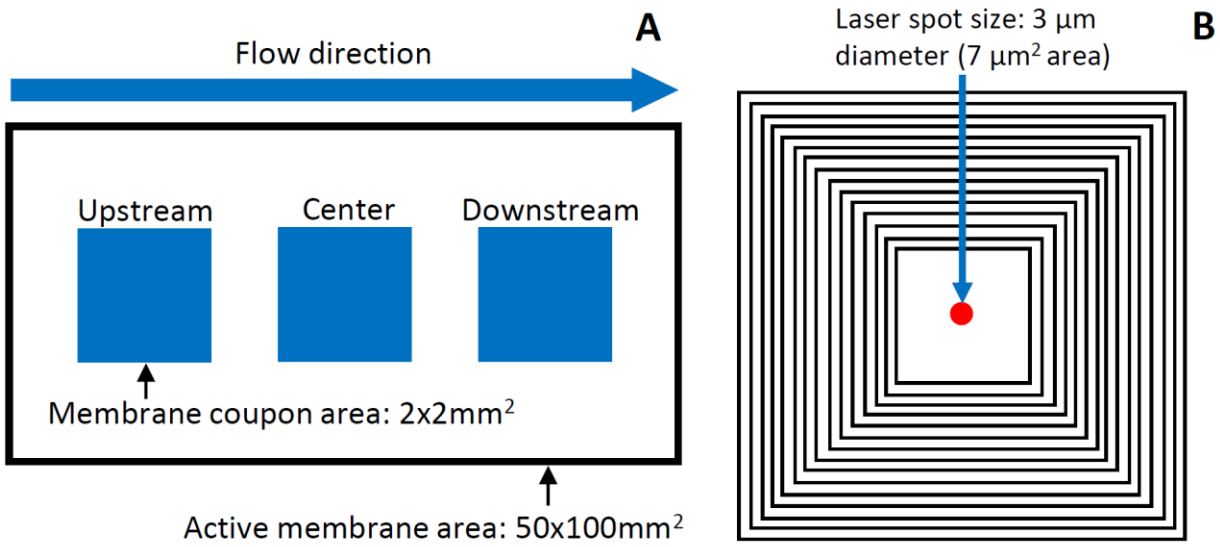


Figure 4-4. (A) Definition of upstream, center, and downstream locations on the membrane; and (B) For a Raman raster scan, the total sampled area was divided into subspaces to determine the relationship between Raman sampling area and detection capability.

During real-time detection, Raman data were acquired using a fixed Raman microscope objective that was lowered onto the optical window of the cross-flow cell. The resulting sampling area for this detection configuration is the spot size of the laser which is ~3 µm in diameter, or ~7 µm$^2$ in area [55]. Given that scaling does not form uniformly, and cleaning does not necessarily remove scaling in a uniform manner, it was desirable to increase the sampling area in order to investigate the relationship between the size of the area sampled and the likelihood of scale detection during/after cleaning. The custom Raman microscope stage used during the cleaning experiments was replaced with the microscope's original high-speed encoded stage, capable of moving the test coupons underneath the fixed microscope objective in precise increments. For data collection, the stage was programmed to perform a raster scan on the membrane coupon that underwent intensity-controlled cleaning, producing a dataset of 21 × 21 Raman spectra, each spectral acquisition with 50-µm spacing, spanning a total sampling area of 1 mm$^2$ (1000 µm × 1000 µm). For the membrane coupon that underwent time-controlled cleaning, a dataset consisting of 31 × 31 Raman

spectra, with 100-μm spacing between each spectral acquisition, spanning a total sampling area of 9 $mm^2$ (3000 μm x 3000 μm) was produced. During data processing, each spectral acquisition site was marked according to the presence or absence of $CaSO_4$ scale. The presence of scale is defined as a spectral acquisition site that features a Raman spectrum with a relative peak intensity of the dominant peak of $CaSO_4$ (1008 $cm^{-1}$) greater than 50% [53,55]. After identifying scale detection at each spectral acquisition site, the total sampled area in the raster scan was partitioned into square subspaces, starting at the center of the raster scan, which consisted of a single Raman spectrum. From the center of the raster scan, the length of the square subspaces consecutively increased by 100 and 200 μm for the intensity-controlled and time-controlled samples, respectively, until the largest subspace contained Raman spectra taken from the entire sampled area (Figure 4-4B).

**4.3.4.2** Gravimetric measurements

Gravimetric measurements of the membrane coupons were made using a microbalance (ME 235S, Sartorious), and dimensions of the coupons were measured using a digital caliper (DCLA 0605, VINCA). Gravimetric measurements of membrane coupons that underwent scaling and time-controlled cleaning were compared to that of virgin membrane coupons. The virgin membranes were soaked for 30 min in a 1:1 solution of isopropanol and DI water, and then dried before measurement.

**4.3.4.3** Microscopy and x-ray analysis

SEM (scanning electron microscopy) was conducted on membrane samples that underwent both intensity-controlled and time-controlled cleaning. After the gravimetric measurements were completed, the samples were sputter-coated with 9 nm of gold to prevent excessive charging during imaging. EDX (Energy dispersive X-ray spectroscopy) was conducted on membrane coupons that were cleaned 20+ min to determine whether any residual scale was present.

## 4.4 Results and Discussion

### 4.4.1 *Real-time metrics*

The peak intensity of $CaSO_4$ was recorded over the duration of each test to assess the performance of the Raman sensor in comparison to permeate flux, a standard membrane performance metric. After the pretreatment and compaction described in Section 4.3.2, each test began with an initial 15 min of DI water compaction to characterize the baseline value of the $CaSO_4$ Raman peak intensity before the salt feed is introduced. Membranes in the intensity-controlled tests (#1–4, Figure 4-5) were scaled until the $CaSO_4$ Raman peak intensity exceeded at least 50% [53,55] and were cleaned until the peak intensity returned to the baseline value (20+ min); membranes in the time-controlled tests (#5-7, Figure 4-6) were scaled for 45 min then cleaned for 5 min.

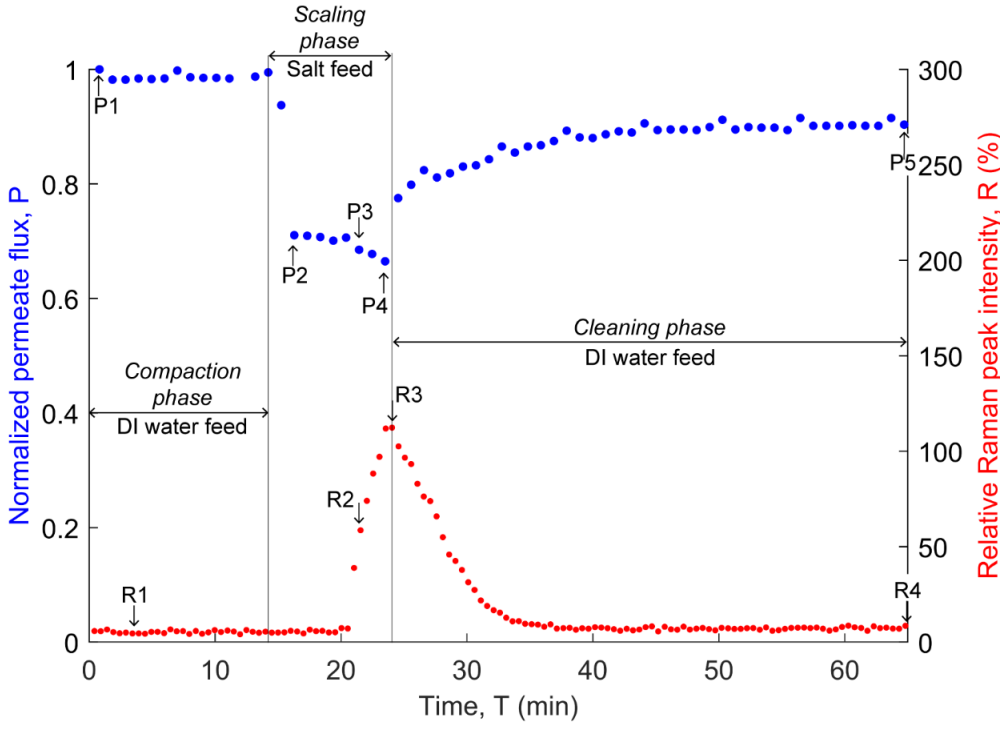


Figure 4-5. Representative intensity-controlled test result showing the three phases of each test and the permeate flux (P#) and Raman (R#) data points used to calculate test metrics. P1: Initial permeate flux; P2: Initial permeate flux with $CaSO_4$ feed; P3: Permeate flux at scale detection (R2); P4: Permeate flux at the end of scaling phase; P5: Permeate flux at the end of the test; R1: Initial baseline Raman peak intensity; R2: Scale detection threshold (at least 50% Raman peak intensity); R3. Raman peak intensity at cleaning initiation; and R4: Raman peak intensity at the end of the test.

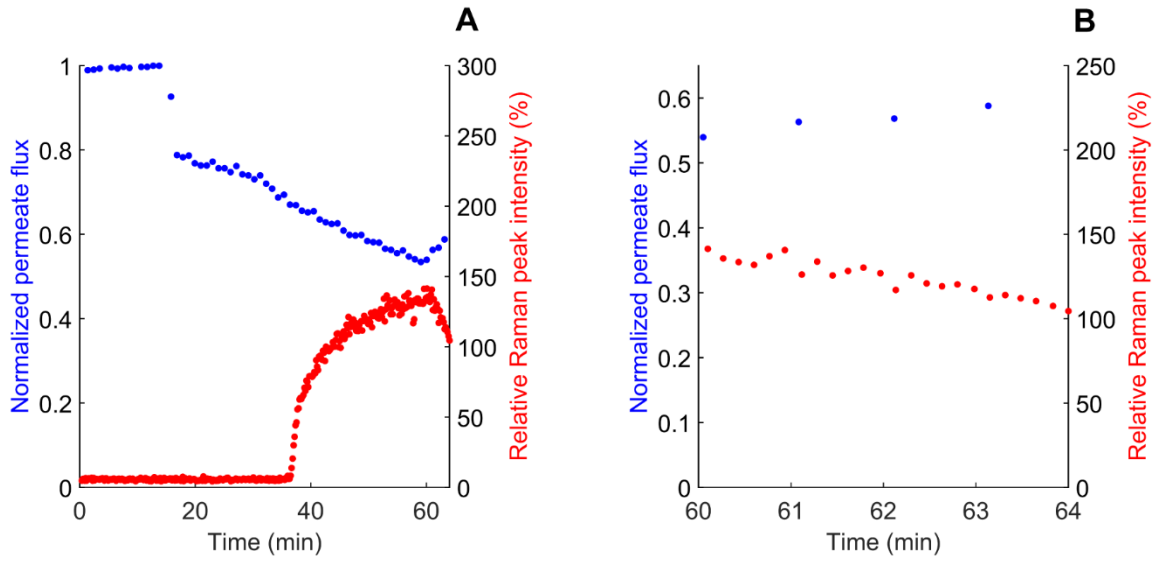


Figure 4-6. (A) From test 7, a representative progression of relative $CaSO_4$ Raman peak intensity is shown for a membrane that was scaled for 45 min and then partially cleaned for 5 min (time-controlled cleaning); corresponding permeate flux values were also determined. (B) The cleaning portion of test 7 is shown in more detail. A consistent, more pronounced decrease in relative Raman peak intensity for $CaSO_4$ is observed compared to the increase in permeate flux.

When the salt feed is introduced in both the intensity-controlled and time-controlled tests, the permeate flux initially decreases while the $CaSO_4$ Raman peak intensity remains at a baseline value. This initial decrease in permeate flux is primarily due to the increased osmotic pressure from the salt concentration in the feed solution. These two different responses to the increased feed concentration indicate that the $CaSO_4$ Raman peak intensity is not affected by concentration polarization. After the initial decline, the permeate flux continues to decrease due to the combined effects of concentration polarization, compaction, and scale formation. The sensitivity of the real-time Raman and flux measurements can be considered in the context of the degree of the respective changes and the time frame over which they occur. While permeate flux is sensitive to changes in concentration polarization, it does not provide clear information about the onset of scaling. In contrast, the $CaSO_4$ Raman peak intensity has been shown to be more sensitive to changes on the membrane surface than permeate flux for real-time detection of scaling via specific chemical and spatial information [53]. Despite some scatter in the data, this assertion is supported by the results presented in Table 4-1 that show low values of permeate flux decline relative to the 50% increase in the Raman peak intensity. The relatively high values of permeate flux decline at Raman

scale-detection exhibited in tests 2 and 7 may well reflect somewhat higher levels of scaling elsewhere in the membrane. The variation in time of scaling detection, which ranged from 6-30 min, is partly influenced by variations in initial permeate flux values during RO system operation. Since boundary layer concentration on the feed side of the membrane is related to permeate flux (along with other factors such as crossflow velocity, temperature and pressure) [38], scaling detection times for lower initial permeate fluxes tend to be longer because a lower flux leads to lower salt concentration on the feed side of the membrane.

Table 4-1. Results from the scaling phase of the experiments. The time of scaling detection was defined as the time taken from salt feed introduction to the time when the $CaSO_4$ peak reached at least 50% relative Raman peak intensity [53,55].

| Test # | Initial permeate flux during scaling [L/m²/h] | Time of scaling detection (min) | Duration of scaling (min) | Permeate flux decline at scale detection (%) |
|---|---|---|---|---|
| 1 | 69.6 | 15 | 16 | 4 |
| 2 | 73.9 | 27 | 31 | 18 |
| 3 | 80.4 | 7 | 9 | 3 |
| 4 | 84.1 | 6 | 6 | 3 |
| 5 | 64.1 | 30 | 45 | 4 |
| 6 | 67.0 | 10 | 45 | 3 |
| 7 | 72.4 | 23 | 45 | 12 |

The higher sensitivity in the response of the Raman sensor to scale formation compared to changes in permeate flux is also observed in the response to cleaning. The following test metrics are defined in Table 4-2 and calculated values presented in Table 4-3: cleaning time, permeate flux recovery at the end of cleaning, and $CaSO_4$ Raman peak intensity recovery at the end of cleaning. A sensitive method of monitoring membrane cleaning is desirable in enabling plant operators to quickly determine whether a cleaning or antiscaling regimen is lessening or worsening scale formation to avoid further damage to the membrane [83]. Results from the intensity-controlled cleaning experiments (tests 1–4) show that for a mean permeate flux recovery of 71.7 ± 1.7%, the corresponding mean Raman recovery is 99.0 ± 1.0%. For the time-controlled cleaning experiments (Tests 5–7), results show that for a mean permeate flux recovery of

14.0 ± 3.1%, the corresponding decrease in mean Raman peak intensity is 31.1 ± 7.1%. It should be noted that the permeate flux recovery is not only due to dissolution of scale by the DI water feed, but also a rapid, initial decrease in osmotic pressure when the feed is switched from salt to DI water. Therefore, the results show the higher sensitivity of the Raman response compared to the changes in permeate flux due to scale removal. Results from tests 1–4 show Raman recoveries greater than 95% that were achieved well before complete flux recovery, suggesting a more rapid, local Raman response to scale removal as compared to the permeate flux. However, it is also important to again note that the difference in the Raman and permeate flux responses to cleaning is also influenced by differences in the inherent characteristics of local and global measurements. The former reflects the conditions at a small, localized area while the latter considers the possibility of variable conditions across the entire active membrane surface area. This important consideration is addressed in Section 4.4.3.

Table 4-2. Permeate flux and relative $CaSO_4$ Raman peak intensity values defined in Figure 4-5 are used to calculate test metrics to enable comparison of permeate flux and Raman measurements during the cleaning experiments. P1: Initial permeate flux; P4: Permeate flux at the end of scaling phase; P5: Permeate flux at the end of the test; R1: Initial baseline Raman peak intensity; R3: Raman peak intensity at cleaning initiation; R4: Raman peak intensity at the end of the test; $T_{P4}$: Time at P4; $T_{P5}$: Time at P5.

| Test metric | Formula |
|---|---|
| Cleaning time (min) | $T_{P5} - T_{P4}$ |
| Permeate flux recovery at end of cleaning (%) | (P5 – P4)/(P1 – P4)*100 |
| Raman recovery (%) | (R3 – R4)/(R3 – R1)*100 |

Table 4-3. Values of the cleaning metrics for Tests 1–7. For the intensity-controlled experiments (Tests 1 – 4), the mean cleaning time was 64 ± 7 min; for the time-controlled experiments (Tests 5–7), the mean cleaning time was 5 ± 1 min.

| Test # | Start of cleaning, $T_{P4}$ (min) | End of cleaning, $T_{P5}$ (min) | Permeate flux recovery at $T_{R5}$ (%) | Raman recovery at $T_{R5}$ (%) |
|---|---|---|---|---|
| 1 | 32 | 91 | 69 | 97 |
| 2 | 48 | 118 | 73 | 100 |
| 3 | 24 | 89 | 73 | 98 |
| 4 | 21 | 78 | 70 | 99 |
| 5 | 60 | 64 | 17 | 23 |
| 6 | 61 | 65 | 15 | 33 |
| 7 | 60 | 65 | 11 | 37 |

### 4.4.2 *Post-mortem characterization*

Along with permeate flux recovery as a measure of membrane cleaning, post-mortem visual observation has also been employed [13, 15-17]. To provide additional comparison with the real-time Raman metrics, representative scanning electron microscopy (SEM) images of the upstream, center, and downstream membrane coupons from the intensity-controlled and time-controlled experiments are shown in Figure 4-7A and B, respectively. For the upstream, center, and downstream locations, the micrographs in Figure 4-7 indicate evidence of residual scale on the membrane cleaned for 20+ min while there is clear evidence of $CaSO_4$ scale remaining on the membrane cleaned for 5 min. These results are consistent with those in Fig. 5 and 6, which indicate that the Raman intensity under the sensor in the center of the membrane has clearly returned to or is very close to the baseline in the former and is well above the baseline value in the latter.

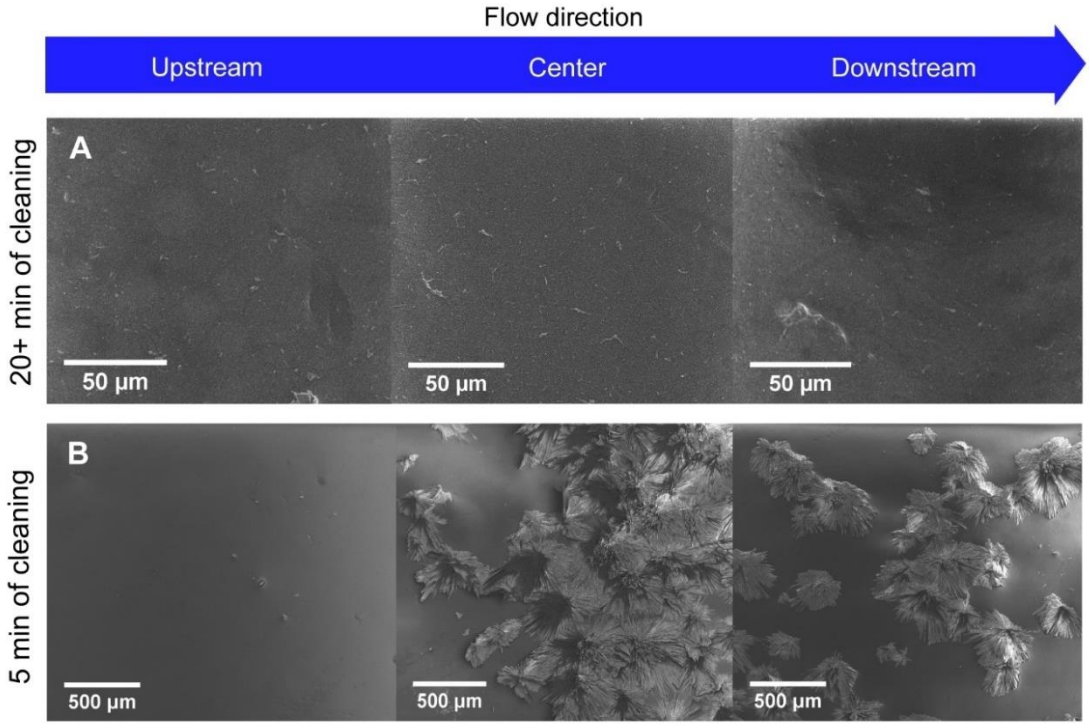


Figure 4-7. SEM images of upstream, center, and downstream membrane coupons from (A) membranes after more than 20 min of cleaning (intensity-controlled cleaning), and (B) membranes cleaned for 5 min (time-controlled cleaning). Membranes that underwent intensity-controlled cleaning show evidence of some residual scale, and membranes that underwent time-controlled cleaning show significantly more scale than those subjected to intensity-control cleaning.

Additional energy-dispersive X-ray spectroscopy (EDX) characterization of an upstream membrane coupon cleaned for more than 20 min (Figure 4-7A) shows trace amounts of calcium and sulfur, and an abundance of carbon and oxygen (Figure 4-8).

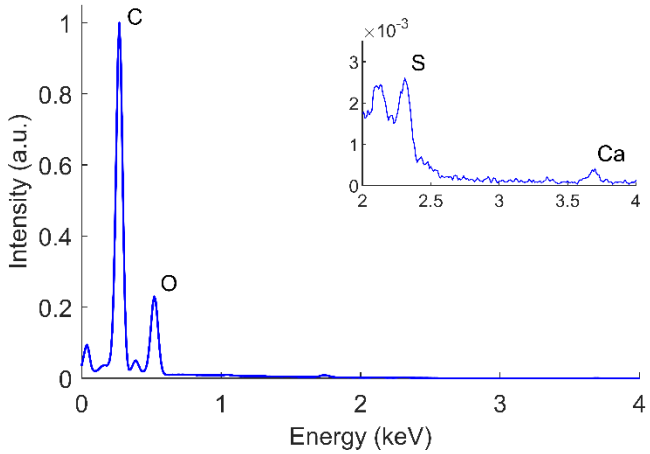


Figure 4-8. An EDX analysis is shown of an upstream membrane coupon taken from a scaled membrane cleaned for at least 20 min. The inset shows trace amounts of calcium and sulfur compared to the much larger carbon and oxygen peaks.

The sulfur and oxygen peaks may stem from either residual $CaSO_4$ scale or the PSf support, and the carbon peak stems from the TFC RO membrane. However, it is the trace amounts of calcium that strongly support that some small amount of residual scale was present in the corresponding micrograph (Figure 4-7A). These EDX results showing possible residual scale are consistent with the $CaSO_4$ Raman peak intensity not quite returning to the baseline value for two out of the four experiments (Tests 1–4; Figure 4-9). This result is consistent with findings by Uchymiak et al. [39] who monitored scale growth using a real-time visual technique during an experiment with subsequent scaling, scale dissolution, then rescaling phases. Uchymiak reports that after visually confirming the removal of scale and achieving complete permeate flux recovery, a higher surface crystal number density was observed on the rescaled membrane as compared to the initially scaled membrane. This indicates the possibility of incomplete scale removal even with complete permeate flux recovery and visual confirmation of cleaning. In comparison to visual techniques such as that employed by Uchymiak et al., Raman spectroscopy may provide improved accuracy and sensitivity when monitoring the extent of cleaning.

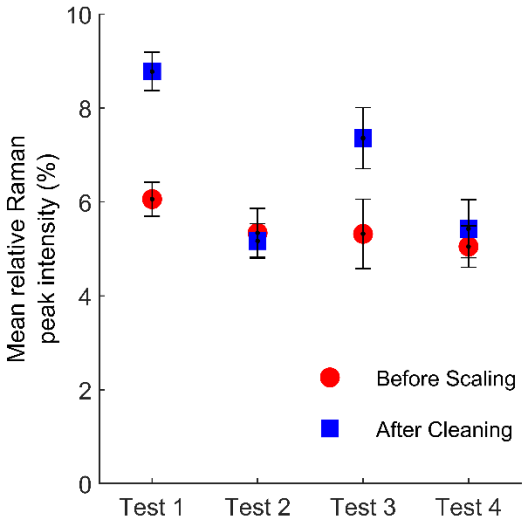


Figure 4-9. Comparison between mean relative $CaSO_4$ Raman peak intensity values before scaling and after cleaning for tests 1 – 4. The slight increase in the Raman intensity after cleaning in tests 1 and 3 suggests the presence of residual scale.

Gravimetric measurements were made on membranes from Tests 5–7 because they were partially cleaned and so had sufficient $CaSO_4$ scale available for analysis. After 5 min of cleaning, the mass of remaining $CaSO_4$ is greatest downstream and least in the upstream region (Figure 4-10). These results indicate the expected overall pattern of scale removal from the membrane during the initial stages of cleaning with DI water.

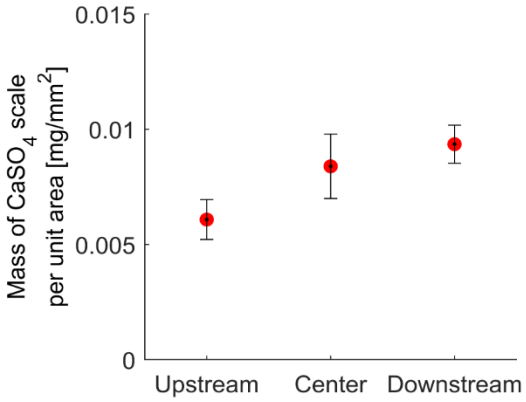


Figure 4-10. During scaling, scale formation is greater downstream due to effects of concentration polarization. Gravimetric measurements of upstream, center, and downstream membrane coupons from time-controlled cleaning experiments show a pattern of increased mass in the downstream region. These results suggest a relatively uniform removal of scale in the early stages of cleaning.

### 4.4.3 *Expanded Raman sampling area*

As previously noted, the Raman detection methodology for both scaling and cleaning utilizes point measurements. Specifically, the length scales of the Raman laser spot-size, $CaSO_4$ crystallites, and active membrane area are on the order of $10^{-3}$ mm (Figure 4-4B), $10^{-1}$ mm (Figure 4-7), and $10^{2}$ mm (Figure 4-4B), respectively. Clearly, the laser interrogates an area that is only a fraction of a $CaSO_4$ crystallite and an orders-of-magnitude smaller fraction of the entire membrane surface. In the present study, these length-scale differences require consideration of the possibility of a false negative during the real-time, fixed-point sampling of the membrane during cleaning, i.e., a no-scaling (clean) signal when scaling is still present at other nearby non-sampled locations. Thus, an alternate, post-mortem sampling strategy that could interrogate a larger portion of the membrane was explored. Raman raster scans spanning a total surface area of $1 \times 1$ mm$^2$ and $3 \times 3$ mm$^2$ were conducted for representative intensity-controlled and time-controlled cleaning, respectively. The raster scans consisted of discrete sampling points that were separated by 50 µm for coupons from intensity-controlled cleaning tests and 100 µm from the time-controlled cleaning tests. The raster scan for the intensity-controlled cleaning membrane sample was performed with a higher resolution of 50 µm spacing and smaller total area of $1 \times 1$ mm$^2$ compared to that of the time-controlled sample because other metrics, such as SEM imaging, indicated that negligible scale was present on the membranes cleaned via the intensity-control procedure. The percentage of sampled points indicating the presence of scale was determined as a function of sampled area (Figure 4-11). These analyses were conducted using representative membrane samples from the downstream location.

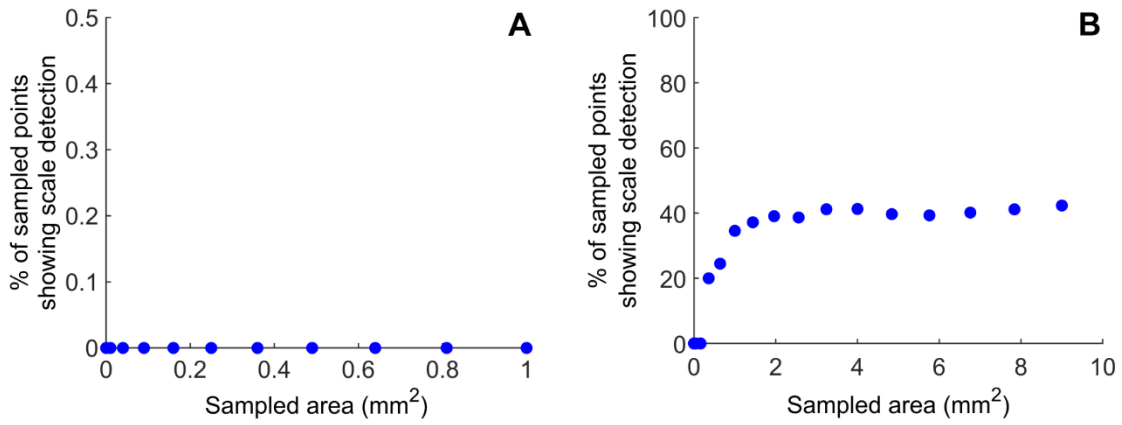


Figure 4-11. The percentage of Raman-sampled points indicating the presence of scale is determined for increasing subspaces of the sampled area from representative samples from (A) intensity-controlled, and (B) time-controlled cleaning. The membranes that underwent intensity-controlled cleaning show the absence of measurable scale (i.e. relative $CaSO_4$ Raman peaks in Raman spectra of sampled sites did not exceed detection threshold of 50%), independent of the area sampled. Membranes that underwent time-controlled cleaning show an initial increase in scale detection with increasing sampled area that becomes relatively constant at ~40%.

Results for the intensity-controlled tests (Figure 4-11A) indicate the absence of measurable scale independent of the area sampled. In the time-controlled cleaning analysis (Figure 4-11B), the percentage of sampled points that indicate scaling detection increases from a sampled area of about 7 $\mu m^2$ (laser spot-size area) to 9 $mm^2$ at which the scaling detection percentage becomes relatively constant at ~40%. The x-axes of Figures 12A and 12B both begin at 0% of sampled points showing scale detection because during post-mortem Raman raster scanning, the center of the scan does not precisely coincide with the location of the real-time point detection. The differences shown in Figure 4-11A and 11B are consistent with almost complete scale removal for the intensity-controlled cleaning and incomplete scale removal for the short, time-controlled cleaning. They also show that there may be an optimal sampling area during cleaning that is large enough to capture the spatial variation in scale distribution, but small enough to facilitate Raman sensor design such as required laser power and scanning speed. Additional factors that must be considered are the size and distribution of the scalant(s), cleaning protocol, and Raman detection thresholds. Overall, these results indicate the necessity to carefully consider sampling strategies and how they affect the accuracy of the real-time Raman scale-detection methodology. Comprehensive study of these aspects

comprises the next phase of the work, which we anticipate will provide insights for methodology optimization.

## 4.5 Conclusions and Future Directions

This study utilizes real-time Raman spectroscopy to quantify $CaSO_4$ scale removal during membrane cleaning in a bench-scale cross-flow RO system. The experiments consisted of an initial scaling phase followed by an in-situ cleaning phase. The prominent $CaSO_4$ Raman peak at 1008 $cm^{-1}$ consistently increased as scale formed and subsequently decreased as $CaSO_4$ dissolved during cleaning using DI water. Compared to the corresponding real-time permeate flux measurements, Raman spectroscopy was more responsive to local conditions during membrane cleaning. The real-time data are supported by microscopic, x-ray, and gravimetric post-mortem characterizations. In addition, post-mortem Raman analysis provided a basis for an improved real-time sampling strategy. A significant advantage of Raman spectroscopy is the ability to provide spatial and chemical information regarding scale formation and removal. Such real-time information could ultimately enable improved cleaning strategies and thus more efficient membrane-based desalination.

A limitation of the present work is the nonuniform channel height in the flow cell which provided different scaling conditions compared to the rest of the active membrane area. More details were reported in previous work [56]. To enable further investigation of the real-time chemical sensing capability of the developed Raman-based technique, next steps included redesigning the RO flow cell to feature a uniform channel height, as well as increasing the optical window to accommodate Raman detection at different positions along the membrane.

# Chapter 5 In-situ monitoring of calcium carbonate scale progression on reverse osmosis membranes using Raman spectroscopy

Chapter 5 is based on: "In-situ monitoring of calcium carbonate scale progression on reverse osmosis membranes using Raman spectroscopy," by D. J. Park, O. D. Supekar, A. R. Greenberg, J. T. Gopinath, and V. M. Bright. Submitted to *Desalination and Water Treatment.* In revision.

## 5.1 Abstract

Direct monitoring techniques of fouling in membrane-based filtration processes can be implemented as part of an effort to reduce the negative effects of membrane fouling. In particular, monitoring techniques with chemical characterization capability are crucial for the formulation of effective fouling prevention and mitigation strategies. In the present work, Raman spectroscopy was applied as an in-situ monitoring technique for calcium carbonate scaling on commercial reverse osmosis membranes. The bench-scale Raman monitoring system allowed for a qualitative chemical assay of the scaled membrane surface at sequential downstream and upstream axial positions. The time evolution of the downstream and upstream calcium carbonate Raman signal was evaluated with respect to computed values of local concentration at the membrane surface, revealing a statistically significant dependence ($p$<0.001). The real-time Raman data were bolstered by results of post-mortem analysis (scanning electron microscopy, gravimetric measurements, laser interferometry), which additionally revealed that the employed technique was capable of detecting crystals with characteristic lengths <50 μm. Preliminary evidence of polymorph detection was also presented with recommendations for improvements in the technique.

## 5.2 Introduction

In an effort to better understand fouling mechanisms and optimize the RO process, a portion of membrane research is dedicated to development of techniques for direct monitoring [8,10,43,48,51,52,84–

86] of membrane fouling. These techniques have been used to not only detect scaling in its early stages when remedial actions are most effective [24,33,85,87], but they have also been used to study the time evolution of membrane fouling, and gain insight into the mechanisms of fouling. However, the techniques used in these studies lacked chemical sensing capability, restricting their work to the use of simplified feeds. Understanding the time evolution of single-component scaling is still important for purposes of establishing a point of reference for scaling progression, yet without real-time chemical sensing capability, expansion of the work to multi-component feed investigations will likely be challenging, as the components may interact each other in ways that are undetectable using the already established techniques (visual observation, ultrasonic time-domain reflectometry).

In the present work, Raman spectroscopy is applied as an in-situ monitoring technique for membrane scaling. A Raman microscope was integrated with a custom bench-scale RO flow cell, outfitted with a long optical window. Given that scale progression on pressure-driven, crossflow filtration membranes is a function of axial position, the utilized experimental setup allowed for chemical detection of the scalant at downstream and upstream regions on the membrane using Raman spectroscopy. Crossflow filtration experiments were conducted, ensuring hydrodynamics reflective of more realistic RO operating conditions compared to dead-end filtration. Calcium carbonate was selected as a model scalant, which highlighted the Raman technique's ability to detect small crystals (<50 μm). The time evolution of the calcium carbonate Raman signal served as evidence of local progression of calcium carbonate scaling on RO membranes.

## 5.3 Experimental Method

Real-time, in-situ Raman data was collected for eight independent reverse osmosis experiments. The objective of each experiment was to demonstrate chemical detection of calcium carbonate scaling as well as compare the Raman data obtained from two different axial positions on the membrane (downstream vs upstream).

### 5.3.1 *Scaling experiments*

Membrane samples were cut from the same batch of thin-film composite reverse osmosis membranes (UTC-73HA, Toray), with each sample sized to an active membrane area of 17.5 cm × 12.5 cm (length × width). Undersaturated feed solutions were utilized to maintain scaling in the surface crystallization regime [88]. The bulk feed saturation index with respect to calcite was $SI_{Calcite} = log_{10}(IAP/K_{sp}) \approx -0.6$, where $IAP$ is the ionic activity product and $K_{sp}$ is the solubility product constant [89]. Feed solutions were prepared by combining 8 L of deionized (DI) water with 1.51 g $NaHCO_3$ (2.25 mM) and 1.33 g $CaCl_2$ (1.5 mM). Prior to conducting scaling experiments, the reverse osmosis (RO) system was flushed for several hours with DI water until conductivity readings reached ≤1 μS/cm. Each membrane sample was soaked in a 50% solution of isopropanol for 30 min to remove preservatives. Afterwards, the membrane was compacted (~12-15 h) with a fresh reservoir of DI water to minimize compaction contributions to permeate flux decline during the scaling experiments. The same RO operating conditions were applied in both the compaction and scaling phases. A volumetric flow rate of 25 L/h (crossflow velocity of 3.0 cm/s) was selected such that the flow in the channel remained laminar, resulting in a Reynolds number of ~63 with respect to the channel height as the characteristic length [88]. For the selected feed temperature of 24 °C and feed pressure of 1.03 MPa (150 psi), the initial permeate flux during scaling was 57.6 ± 6.3 L/m$^2$/h, which underscores the variability in membrane performance and operating conditions among replicate scaling experiments (Table 5-1).

Table 5-1. Summary of RO system operating parameters and permeate flux for scaling tests 1-8.

| Test # | RO system operating parameters | | | Membrane performance (L/m$^2$/h) | | |
|---|---|---|---|---|---|---|
| | Crossflow velocity (cm/s) | Pressure (MPa) | Temperature (°C) | Initial flux during scaling | Mean flux during downstream detection | Mean flux during upstream detection |
| 1 | 2.8 ± 0.0 | 1.057 ± 0.004 | 23.9 ± 0.1 | 58.6 | 55.6 | 50.5 |
| 2 | 2.8 ± 0.0 | 1.049 ± 0.005 | 23.7 ± 0.2 | 61.7 | 61.2 | 54.1 |
| 3 | 2.8 ± 0.1 | 1.050 ± 0.014 | 23.5 ± 0.1 | 59.7 | 59.7 | 50.7 |
| 4 | 3.0 ± 0.2 | 1.038 ± 0.007 | 24.7 ± 0.2 | 43.4 | 35.8 | 33.7 |
| 5 | 3.2 ± 0.1 | 1.062 ± 0.012 | 23.9 ± 0.2 | 55.6 | 51.4 | 45.5 |
| 6 | 2.9 ± 0.0 | 1.042 ± 0.003 | 22.3 ± 0.1 | 64.1 | 63.5 | 53.6 |
| 7 | 3.0 ± 0.0 | 1.073 ± 0.002 | 23.3 ± 0.3 | 60.5 | 59.8 | 50.0 |
| 8 | 2.8 ± 0.1 | 1.064 ± 0.007 | 23.7 ± 0.3 | 57.3 | 54.6 | 50.5 |

### 5.3.2 *Raman data collection*

The laser source employed was a narrow linewidth, 785-nm laser diode, and the beam was focused onto the sample using a 50X objective with ~27 mW of optical power incident on the sample (FPV785S, Thorlabs Inc). A 600 line/mm grating with a blaze at 1000 nm provided a spectral sampling of ~1 $cm^{-1}$/pixel. During the scaling experiment, all Raman spectra were acquired every 60 s with 10 s of integration time. All Raman data were preprocessed using the same procedures and parameters to avoid introducing artifacts [90]. Each spectrum was first baseline-corrected [91] to remove the fluorescent background signal, and cosmic rays were eliminated by linear interpolation. After baseline removal, all spectra were normalized by vector normalization to remove the effects of fluctuations in laser intensity and focus. Intensities of investigated Raman bands were expressed as ratios (%) to the most prominent RO membrane Raman band at 1150 $cm^{-1}$ (C-O-C stretching mode).

In each replicate scaling experiment, Raman detection was comprised of two parts, in which real-time Raman spectra were acquired downstream and upstream, in series (Figure 5-1).

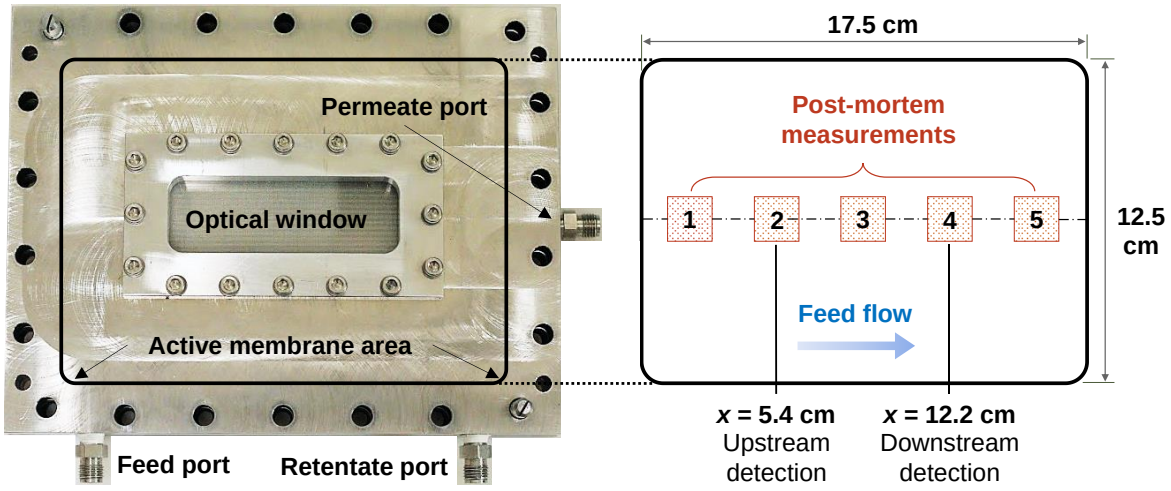


Figure 5-1. The active membrane area is schematically represented on the bench-scale flow cell (pictured on the left). Downstream Raman detection at $x$ = 12.2 cm is initiated first due to higher scaling propensity toward the channel exit. After completing downstream detection, the stage is moved to initiate upstream detection at x = 5.4 cm. To avoid edge effects, both downstream and upstream detection occurred at the center of the membrane, represented by the dotted centerline. The five square regions (1-5) represent membrane coupons that underwent post-mortem characterization, with the second and fourth squares encompassing the locations of upstream and downstream Raman detection, respectively.

Raman spectral acquisition was initiated during the last ~30-60 min of DI water compaction, when no calcium carbonate crystals on the membrane are expected due to prior system cleaning. This expectation is supported by observation of relatively constant permeate flux, where minimal flux decline is attributed to continued effects of membrane compaction. When the feed is switched to the salt solution, supersaturated levels of solute ions at the membrane surface, due to concentration polarization [28,92,93], provide conditions necessary for scaling. Downstream detection began first ($x$ = 12.2 cm) since early scaling crystals tend to form near the channel exit [22,92,94]. Raman detection of the scalant occurs when partial/full crystal dimensions overlap with the focal volume of the laser beam, causing an increase in the scalant Raman intensity.

In both the literature [95,96] and the present work, the dominant calcium carbonate polymorph is calcite, whose strongest internal vibrational mode ($V_1$) has been reported to occur at a Raman shift of 1086 $cm^{-1}$ [21,97]. In the recorded Raman data, the maximum intensity for the calcite Raman band typically occurred at 1086 $cm^{-1}$. Occasionally, maximum Raman intensities at 1087 $cm^{-1}$ were observed. The origin of the 1087 $cm^{-1}$ band was not certain, but a likely explanation is the use of a slightly deviated value for the excitation laser line, which is used to convert wavelengths (nm) of Raman-scattered light to wavenumbers ($cm^{-1}$). A deviation of ~0.06 nm (i.e., the current pixel resolution) in the specified laser line would offset all measured wavenumbers by ~1 $cm^{-1}$. Another possibility is the presence of trace impurities in the calcite scaling crystals [98,99]. For the present study, the calcite Raman signal was defined as the average of the intensities at 1086-1087 $cm^{-1}$, to allow for consistent processing of all Raman datasets. A spectral range of 400-1500 $cm^{-1}$ was specified for Tests 1–7, and for a final scaling test (Test 8), a spectral range of 100–1200 $cm^{-1}$ was specified to investigate proof-of-concept real-time detection of calcium carbonate polymorphs which exhibit distinct Raman bands at wavenumbers <400 $cm^{-1}$.

The criterion for downstream Raman detection of calcite was defined by a Raman intensity threshold value. The threshold value was obtained at approximately three standard deviations above the mean calcite Raman intensity, hereafter the calcite Raman signal, during membrane compaction.

Downstream detection ($x$ = 12.2 cm in Figure 5-1) was terminated and upstream detection ($x$ = 5.4 cm) initiated when the calcite Raman signal exceeded the threshold value. Since initial upstream detection began at a later stage of the scaling experiment, compared to initial downstream detection, there is a possibility of preexisting scaling crystals near or within the upstream laser focal volume. Thus, a secondary detection threshold value was established, defined as three standard deviations above the mean calcite Raman signal during the first 10 min of upstream detection. The secondary threshold value was used as criterion for termination of each scaling experiment. Additionally, the secondary threshold value enabled collection of sufficient data for determination of the time evolution of the calcite Raman signal, discussed in detail in the following section. The presented two-part Raman detection scheme used in this work allows for the investigation of earlier/downstream and later/upstream calcite scaling progression.

### 5.3.3 *Time evolution of calcite Raman signals*

In the present study, we report on the relationship between the time evolution of the calcite Raman signal and local progression of calcite scaling. Figure 5-2 shows a representative dataset comprised of real-time calcite Raman signals and permeate flux as a function of time, with the time evolution of the calcite Raman signal, i.e., the slope, represented schematically. The slope is given by Equation 3-1 where $RI(t_f)$ and $RI(t_i)$ are the calcite Raman intensity at the final and initial timestamp ($t_f$ and $t_i$, respectively) of the calcite Raman signal's time-evolution period.

$$m = \frac{RI(t_f) - RI(t_i)}{t_f - t_i} \qquad 5\text{-}1$$

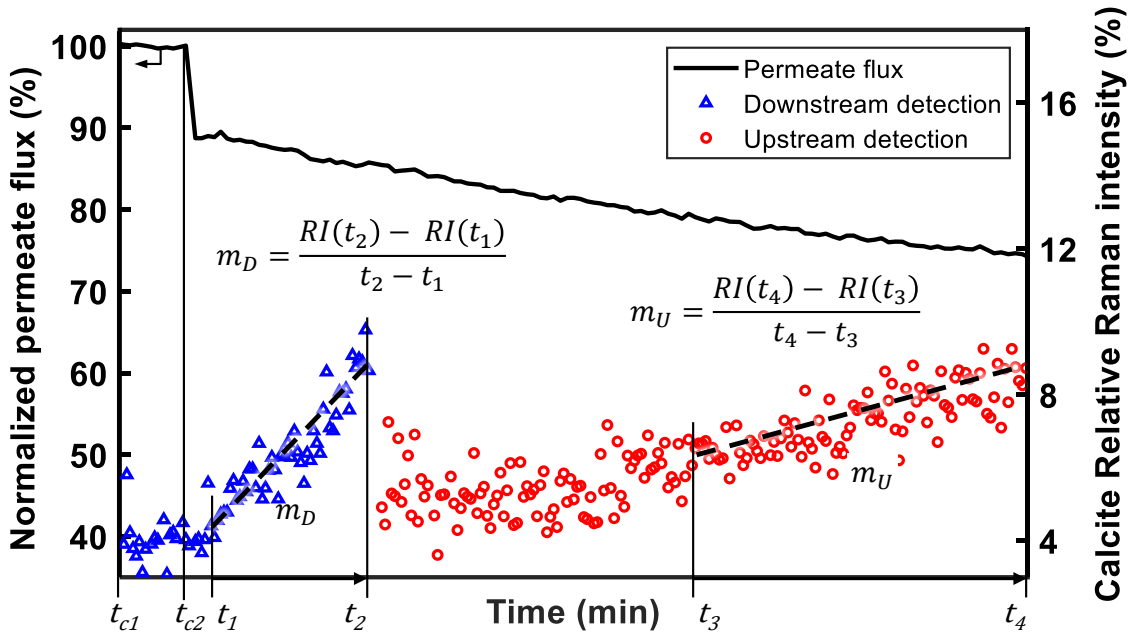


Figure 5-2. Representative dataset from a scaling experiment, showing normalized permeate flux and calcite relative Raman intensity over time. The time evolution of the calcite Raman signal is indicated by the dotted lines and calculated for time periods defined by the following timestamps ($t_{\#}$): $t_{c1}$: Start of membrane compaction phase; $t_{c2}$: End of membrane compaction phase; $t_1$: Start of downstream Raman time evolution; $t_2$: End of downstream Raman time evolution; $t_3$: Start of upstream Raman time evolution; $t_4$: End of Raman upstream time evolution.

The time evolution of the calcite Raman signal during compaction is expected to be zero (Eq. 5-2) since Raman spectra acquired during this period reflect Raman bands of only the RO membrane, whose chemical composition is assumed to remain constant:

$$m(t_f = t_{c2}, t_i = t_{c1}) \approx 0 \qquad 5\text{-}2$$

When the feed is switched to the salt solution and scaling initiates at the detection site, the calcite Raman signal exhibits a steady increase. The downstream and upstream Raman time evolutions of calcite were obtained by identifying the periods during which the mean and slope of the calcite Raman signal experienced an abrupt change.

### 5.3.4 *Post-mortem characterization*

The measured real-time data were complemented by post-mortem characterization of membrane samples from Tests 1–8. Scaled membranes were cut into 2 cm × 2 cm coupons from five locations along

the direction of feed flow (Figure 5-1). Gravimetric analysis was conducted by weighing the membrane coupons using a microbalance and measuring the dimensions of the coupons using a digital caliper. SEM (scanning electron microscope) images of the membrane coupons provided length-scale estimates of the calcium carbonate crystals. These estimates were obtained using image processing packages available in Fiji [100]. The heights of calcium carbonate crystals were measured using a laser interferometer. For SEM imaging and laser interferometry, membrane coupons were coated with ~2 nm of platinum prior to analysis.

### 5.3.5 *Estimation of local saturation indices*

Comparison of the time evolution of calcite Raman signals across replicate scaling experiments requires careful consideration of the inherent variability in membrane performance, RO system operating parameters, and spatiotemporal dependencies of local scaling conditions. Estimation of local saturation indices (SI) at the membrane surface can be used to streamline this variability, by serving as a comparison metric that accounts for different axial position and experimental conditions which, in turn, result in different concentration levels at the membrane wall. The membrane wall concentration profile is often expressed using the concentration polarization modulus (*CP*) [101], which normalizes the solute ion concentration at the membrane wall ($C_m$) to that in the bulk feed ($C_b$). This concentration polarization modulus is represented by an analytical solution derived from classical one-dimensional film theory [45,94] (Eq. 5-3).

$$CP = \frac{C_m - C_p}{C_b - C_p} = \frac{\pi_m}{\pi_b} = (1 - R) + R \cdot exp\left(\frac{J_v}{k_m}\right) \quad 5\text{-}3$$

Salt rejection ($R$) was assumed to be 1 (complete solute rejection). Consequently, permeate concentration ($C_p$) was approximated to be 0, which corresponded to a lower limit estimate of the *CP* modulus. $\pi_m$ and $\pi_b$ are the osmotic pressures at the membrane wall (feed side) and bulk solution, respectively; $J_v$ is the local permeate flux and $k_m = D/\delta$ is the local mass-transfer coefficient, which is a ratio of the salt diffusion coefficient ($D$) and the boundary layer thickness ($\delta$). The permeate flux is given

by Equation 5-4 [102] which relates permeability of the membrane ($L_p$), applied feed pressure ($P$), and osmotic pressure at the membrane wall.

$$J_v = L_p(P - \pi_m) \quad 5\text{-}4$$

In Equation 5-5, the Sherwood number ($Sh$) obtained from the Graetz solution [45,101,102] is used to couple fluid flow with mass transfer in a thin rectangular channel, as a function of axial position ($x$).

$$Sh = \frac{k_m d}{D} = 1.85\left(Re \cdot Sc \cdot \frac{2d}{x}\right)^{\frac{1}{3}} \quad 5\text{-}5$$

The Sherwood number considers the flow cell geometry (hydraulic diameter, $d$); the Reynolds number ($Re = Ud/\nu$), which includes the crossflow velocity ($U$) and kinematic viscosity of the feed solution ($\nu$); as well as the Schmidt number ($Sc = \nu/D$) which describes solute properties. The concentration profile at the membrane wall was estimated by computing the Sherwood number at discretized values of axial position [45]. A boundary condition of $CP(x = 0\text{ cm}) = 1$ was assumed (i.e., no concentration polarization) because the permeate flux at the channel entrance is assumed to be zero. Figure 5-3 presents the computed CP modulus, boundary layer thickness, and permeate flux profiles as a function of nondimensional axial position ($x/L$, $L$=17.5 cm) for Tests 1-8, using experimentally determined inputs of mean crossflow velocity, pressure, temperature, and initial permeate flux values ($J_{v0}$) (Figure 5-3).

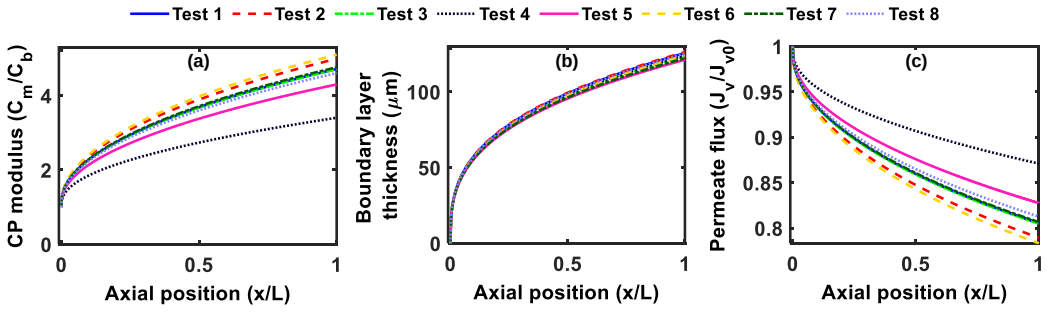


Figure 5-3. (a) The concentration polarization (CP) modulus, (b) boundary layer thickness, and (c) normalized permeate flux was computed as a function of axial position [45]. Concentration at the membrane wall increases with increasing axial position [101].

According to the computed CP modulus and boundary layer thickness profile for each test, both the concentration of scaling ions and the boundary layer thickness are observed to increase with increasing axial position ($x/L \rightarrow 1$). Additionally, the variability in scaling conditions across Tests 1-8 is depicted by the distinct CP modulus and permeate flux profiles of each test.

For the estimation of the local saturation index, the CP modulus was computed using the known value of the bulk feed concentration and estimates of the CP modulus at the upstream ($x$ = 5.4 cm) and downstream ($x$ = 12.2 cm) Raman detection regions. For simplicity, only major scaling ions ($Ca^{2+}$, $CO_3^{2-}$) were considered in the estimation of saturation indices with respect to calcite ($SI_{calcite}$), using PHREEQC Interactive 3.7.0 software [89].

## 5.4 Results and Discussion

### 5.4.1 *Raman monitoring of RO membrane*

The Raman spectrum of the RO membrane exhibits Raman bands at 740, 792, 1073, 1110, and 1149 $cm^{-1}$, which were identified as belonging to the polysulfone layer of the RO membrane in previous work [56]. In the present study, the thin-film composite polysulfone/polyamide (PSF/PA) layer of a virgin sample of the RO membrane was peeled off using masking tape to reveal the nonwoven polyethylene terephthalate (PET) support layer. Each layer was fixed on a glass slide and analyzed in vitro using the Raman microscope (Figure 5-4). The PET Raman bands at 281, 303, 634, and 861 $cm^{-1}$ [103] were also observed in the real-time Raman spectrum of the RO membrane during compaction. Raman observation of support layers is possible, depending on the level of defocus of the Raman laser beam [104]. In the subsequent discussion of calcium carbonate Raman data, it is important to note the influence of the PET support layer given that calcium carbonate polymorphs exhibit Raman bands that may overlap with those of the PET layer (e.g., 281 and 301 $cm^{-1}$ for the calcite and vaterite polymorphs, respectively).

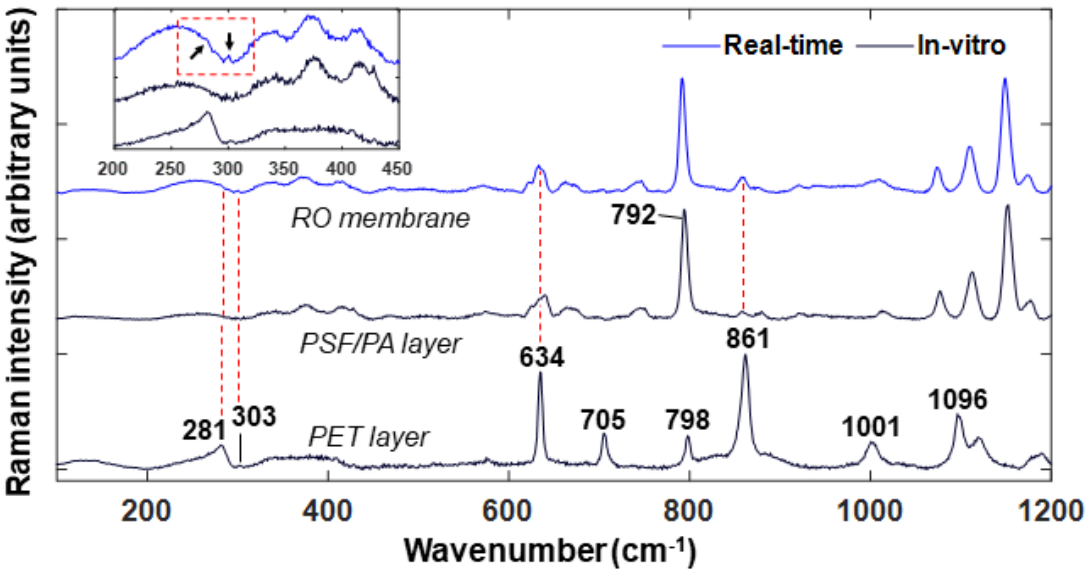


Figure 5-4. In vitro Raman spectra of the polyethylene terephthalate (PET) non-woven support layer and the polysulfone support/polyamide (PSF/PA) layer compared to a real-time Raman spectrum of the reverse osmosis membrane during compaction in Test 8.

Since the aim of the present work is to correlate the time evolution of calcite Raman signals to the progression of calcite scaling on a RO membrane, it is important to avoid potential misinterpretation of calcite Raman signal growth. Previous gypsum scaling studies [53,55], which used the same RO membrane and a laser beam of similar spot size, showed that during initial Raman detection of gypsum scale, the increase in the gypsum Raman signal could be sudden or gradual. However, the time evolution of the gypsum Raman signal does not reliably translate to scaling dynamics, in part, due to the length-scale mismatch between the laser focal volume and the interrogated gypsum crystal. Consider for example, a gypsum crystal that nucleates close to, but still outside the focal volume of the laser beam. As the gypsum crystal grows into a larger crystal rosette (~$10^2$–$10^3$ μm in diameter [88,105]), a portion of the peripheral crystal may suddenly overtake the focal volume of the laser beam. Crystal obstruction of the membrane surface at the detection site would simultaneously result in a decrease in the membrane Raman signal and a rapid increase in the gypsum Raman signal over a short time period, i.e., $m >> 1$. However, this rapid increase in the gypsum Raman signal does not necessarily translate to correspondingly rapid scaling on the membrane surface, illustrating a possible concern in utilizing too-small Raman sampling areas. Therefore,

for the present study of calcite scaling progression, such potential decreases in the RO membrane Raman signals were investigated.

The RO membrane band at ~792 $cm^{-1}$ (out-of-plane bending of the C-H bond in the benzene ring) was selected for study to avoid including potential Raman signal contributions from calcium carbonate. An additional DI water feed experiment was conducted using the same preconditioning and Raman spectral acquisition procedures described for the other scaling experiments. Raman data for the DI feed experiment and a representative calcium carbonate scaling experiment is shown in Figure 5-5.

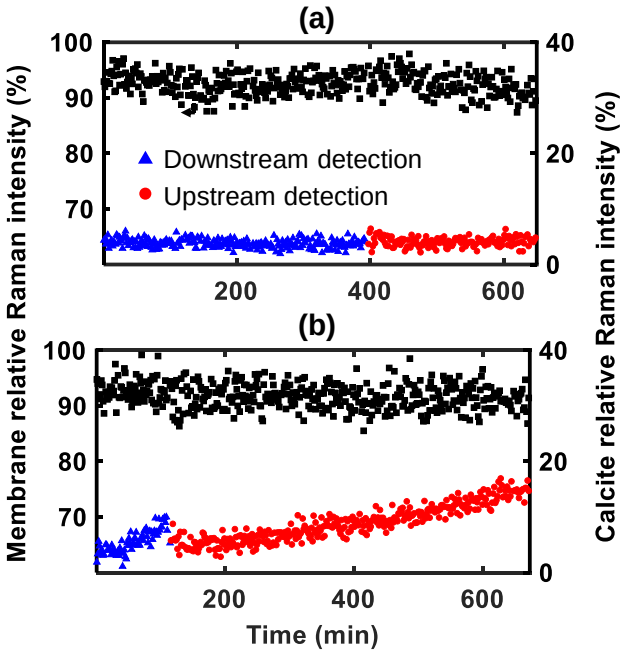


Figure 5-5. No sustained trends are observed for the 792 $cm^{-1}$ membrane Raman signal from the (a) deionized (DI) water feed experiment and (b) representative calcium carbonate scaling experiment. The calcium carbonate Raman signal remained constant for the DI water feed experiment and consistently increased for the calcium carbonate scaling experiment.

For the DI feed experiment (Figure 5-5a), a slight initial decrease in the membrane Raman signal (~4%) is detected at the start of both downstream and upstream observation. Despite background removal in data preprocessing, this is likely due to decreases in the fluorescent background over time, which was consistently observed in the last 30-60 min of compaction in the other scaling experiments. Overall, no consistent trends are observed in the time evolution of the 792 $cm^{-1}$ Raman signal during the DI feed

experiment, serving as a standard of comparison and confirming the absence of false positive calcium carbonate detection [106]. For a representative scaling experiment (Figure 5-5b), no discernable changes in the membrane Raman signal were observed, even while the calcite Raman signal consistently increased over time.

The relatively steady 792 $cm^{-1}$ band Raman signal over the duration of the scaling experiment, serves as evidence that the increase in the calcite Raman signal was due to a gradual growth of calcite scale on the membrane surface, rather than the misleading effect of a length-scale mismatch between the Raman sampling area and scaling crystals.

### 5.4.2 *Scaling crystal characteristic length*

Due to the previously noted importance of length-scale matching between the Raman sampling area and scaling crystals, it was necessary to identify a critical length-scale in the current membrane system. We refer to this critical length-scale as the crystal characteristic length, which was defined as the longest measured diagonal of a calcite crystal face. SEM image analysis of representative scaled membrane samples showed crystal characteristic lengths predominantly ranging from 20–50 µm. For example, the double arrow in Figure 5-6b shows a crystal characteristic length of ~30 µm. For the same membrane samples, laser interferometry measurements indicated representative crystal heights of ~10 µm.

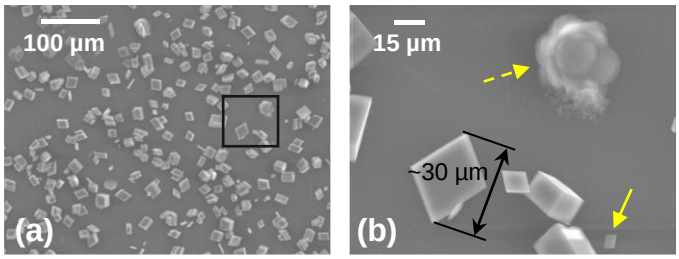


Figure 5-6. SEM images of representative calcium carbonate scaling crystals with characteristic lengths of ~20–50 µm (a) from the region of upstream Raman observation ($x$ = 5.4 cm). Higher magnification image of the region indicated by the rectangle is shown in (b), where the double arrow depicts an example of a characteristic length measurement. A small calcite crystal with a characteristic length of ~5 µm (yellow solid arrow) and a hexagonal-plate vaterite [107] polymorph (yellow dashed arrow) are also observed.

Overall, the characteristic length range of the calcite crystals was somewhat larger than the laser beam spot size of ~3 μm (FWHM, full width at half maximum) whereas the crystal heights were similar to the laser beam depth of focus (~9 μm). Given that the crystal characteristic length measurements were taken from samples that underwent 9–30 h of scaling and that Raman detection of calcium carbonate occurred as early as 30–60 min into the scaling experiment, calcium carbonate crystals were likely much smaller during the initial stages of scaling. This is substantiated by post-mortem observation of calcite characteristic lengths as small as ~5 μm (Figure 5-6b). Moreover, Raman detection of calcium carbonate scaling crystals <50 μm in characteristic length demonstrates the high spatial resolution of the technique.

### 5.4.3 *Raman monitoring of calcium carbonate scaling*

#### **5.4.3.1** Calcium carbonate polymorphs

Calcium carbonate is an inorganic crystal comprised of calcium and carbonate ions. Raman bands of calcium carbonate due to its internal vibration modes ($\nu_{1\ldots n}$) are attributed to vibrations within the ionic species. Additionally, these ionic species can be arranged into different lattice structures, resulting in three main polymorphs that exhibit different Raman bands arising from lattice vibrations (<400 $cm^{-1}$). For example, aragonite and vaterite, two other polymorphs of calcium carbonate, with $V_1$ vibrational modes occurring at 1085 $cm^{-1}$, and 1090 and 1075 $cm^{-1}$ respectively [21,97], have also been observed in scaling studies [96,108]. However, to verify the exact calcium carbonate polymorph, Raman bands attributed to lattice structure are typically measured. For this reason, in Test 8 (Figure 5-7), Raman data were collected with a spectral range of 100–1200 $cm^{-1}$ to investigate whether it was possible to distinguish calcium carbonate polymorphs in real time. During both downstream and upstream detection, the 1087 $cm^{-1}$ band was observed, suggesting Raman detection of a calcite polymorph. As for the observed Raman band at 281 $cm^{-1}$, due to its low signal-to-noise ratio, it is difficult to confirm whether the band is due to lattice vibration of calcite [21] or the PET layer of the membrane.

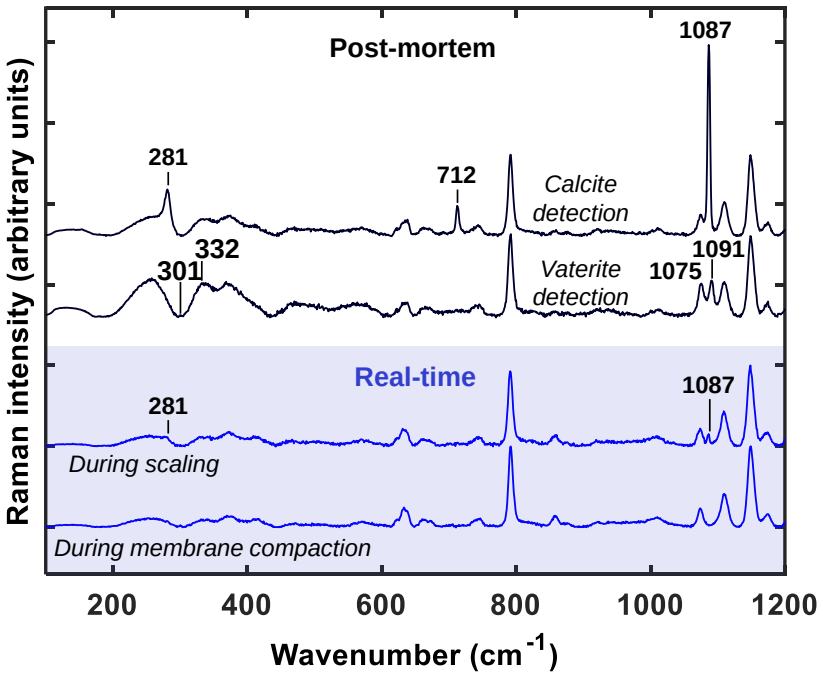


Figure 5-7. Representative real-time vs post-mortem Raman spectra. A real-time Raman spectrum of the reverse osmosis membrane during membrane compaction (Test 8) shows an absence of calcium carbonate Raman signals. A Raman spectrum acquired during scaling suggests detection of a calcite polymorph due to the appearance of the 1087 and 281 $cm^{-1}$ bands. Post-mortem Raman spectra of Test 8's scaled membrane suggest the presence of the vaterite and calcite polymorphs, with lattice Raman bands at 301 and 332 $cm^{-1}$, and 281 $cm^{-1}$, respectively.

SEM images (Figure 5-6) confirmed a majority of rhombic calcite polymorphs and a few hexagonal plate vaterite crystals. Given the dominance of calcite, detection of other polymorphs did not occur in real-time. Thus, polymorph detection was carried out via post-mortem Raman measurements of scaled membrane samples. Raman bands at 301, 332, 1075, and 1090 $cm^{-1}$ [97,109] confirmed the presence of vaterite polymorphs on the Test 8 membrane sample. However, the challenge of weak signal-to-noise ratios still remained, due to the less-ordered crystalline form of vaterite compared to that of calcite [110]. Despite these limitations, the present work indicates the potential of the technique to distinguish polymorphs of calcium carbonate, which is critical in the investigation of scaling dynamics of single and multiple component feed solutions. Depending on the properties of the feed solution such as ionic strength, ratio of scaling ion concentrations, and the presence of additional components in the feed water [111,112], the pathways to $CaCO_3$ crystallization are broad, resulting in initial polymorphs which can evolve over time into other polymorphs. Additionally, since co-precipitation is a common occurrence in industrial water

systems [113], crystallization pathways can be even further confounded. The initial results presented here suggest that such complexities can be studied in real-time with improvement of Raman signal-to-noise ratios.

#### **5.4.3.2** Local calcite scaling progression

Metrics of solute supersaturation at the membrane wall are usually reported in bench-scale scaling studies because scaling rates are related to supersaturation levels [85,88,105,114]. According to classical nucleation theory [25,115,116], crystallization is comprised of nucleation and growth mechanisms. Either homogenous or heterogeneous crystal nucleation can occur when clusters of scaling ions aggregate to a stable, critical size. The heterogeneous nucleation mechanism is likely favored in the present membrane system, considering that heterogenous nucleation is most commonly reported for RO systems [43,117,118] and homogenous nucleation only occurs at extremely high levels of supersaturation [118,119]. Once stable nuclei are established, their continued growth depends on the degree of supersaturation, where growth rate increases with increasing supersaturation [115,120]. If the increase in the calcite Raman signal over time is attributed to the local volumetric growth of calcium carbonate scale at the detection site, it is reasonable to expect greater magnitudes of the calcite Raman signal time evolution, $m$, for greater local supersaturation levels. A summary of the time evolution of calcite Raman signals is presented in Figure 5-8.

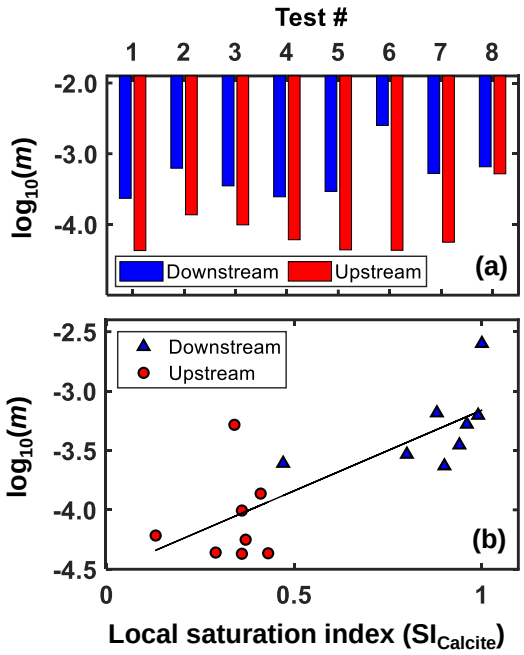


Figure 5-8. (a) The time evolution of the calcite Raman signal (*y*-axis) is summarized for Tests 1-8 (top x-axis). For each test, downstream m values were found to be consistently greater than upstream counterparts by about an order of magnitude. (b) The time evolution of the calcite Raman signal evidenced a statistically significant dependence on the local saturation index; fitted regression line (black) with $p<0.001$.

In Figure 5-8a, downstream *m* values were found to be consistently greater than upstream counterparts by about an order of magnitude. This can be explained by boundary layer theory which describes higher concentrations of solute ions at the downstream membrane wall, causing greater scaling propensity in this region. This result was predicted by the computed CP modulus profiles and supported by post-mortem gravimetric analysis (Figure 5-9), which showed a clear increase in calcium carbonate mass per area with increasing axial position.

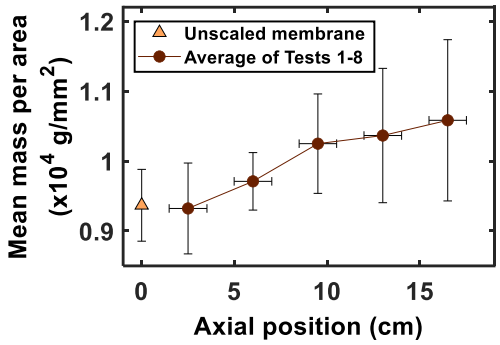


Figure 5-9. Post-mortem gravimetric analysis. An increase in mean calcium carbonate mass per area with increasing axial position confirms the presence of higher supersaturation levels towards the downstream region ($x \rightarrow 17.5$ cm). *y*-axis error bars are large due to significant variation in scale coverage between Tests 1-8. *x*-axis error bars represent the width of each membrane coupon (2 cm).

In Figure 5-8b, *m* values are plotted for downstream and upstream observation from the eight replicate $CaCO_3$ scaling tests, resulting in a total of 16 data points. Generally, the expected trend is observed across all scaling experiments, such that there is a statistically significant dependence of *m* on local $SI_{calcite}$ values ($p<0.001$). Strong literature evidence of scaling dependence on supersaturation levels [115,119,121,122] supports the observed relationship between *m* and $SI_{calcite}$. Changes in Raman signals over time appear to be a useful metric for comparisons of local scaling progression within a membrane sample (i.e., downstream vs upstream) and across different membrane samples.

## 5.5 Conclusions and Future Directions

This study employs the time evolution of the calcite Raman signal as a useful metric for chemical comparison of local scaling progression within and across different membrane samples. The time evolution of the calcite Raman signal is represented by a simple rate of change, i.e., slope, of the calcite Raman signal

over time. A bench-scale plate-and-frame reverse osmosis (RO) flow cell was outfitted with a long optical window to compare downstream and upstream calcite Raman signal time evolution under realistic hydrodynamic conditions. Results demonstrated a statistically significant dependence of the time evolution of the calcite Raman signal with increasing values of the local saturation index. Additionally, in each scaling experiment, the time evolution of the calcite Raman signal during downstream detection consistently exceeded that of upstream detection. Post-mortem gravimetric analysis agreed with the observed real-time Raman behavior, indicating that the Raman-based technique successfully responded to the spatial progression of calcium carbonate membrane scaling.

In-vitro Raman detection of the vaterite and calcite polymorph showed that real-time detection of calcium carbonate polymorphs was possible if the signal-to-noise ratios of the lattice-mode Raman bands can be improved. This capability would be an important asset in the direct observation of scaling progression, especially in the study of multicomponent scaling dynamics, which requires consideration of any interaction effects that can complicate crystallization pathways of inorganic foulants.

Spectral data generally require careful interpretation due to the presence of potential artifacts. Thus, progression of the RO membrane band at 792 $cm^{-1}$ was studied because any changes in the laser focal plane or obstruction of the membrane substrate would affect the Raman spectrum of the substrate. The RO membrane Raman signal remained relatively constant throughout the scaling experiment despite a steady increase in the calcite Raman signal. This result suggests that the steady increase in the calcite Raman signal was caused by actual calcite volumetric growth, gradual enough to leave the Raman signal of the interrogated substrate undisturbed. Post-mortem imaging of the scaling crystals further supported this finding. Matching the characteristic lengths of the sampling area and crystallite was identified as an important aspect of the Raman sampling strategy.

The demonstrated ability to study high-resolution, single-component scaling progression with chemical identification is an important step towards developing the in-situ Raman monitoring technique for expanded studies of multicomponent scaling detection. Consequently, real-time multicomponent scaling

detection comprises the next phase of work, which will require a modified sampling strategy, in order to better match the characteristic lengths of the sampled area with the detected crystallites.

# Chapter 6 Real-time detection of multiple component scaling on reverse osmosis desalination membranes

Chapter 6 is based on: "Real-time detection of multiple component scaling on reverse osmosis desalination membranes," by D. J. Park, O. D. Supekar, A. R. Greenberg, J. T. Gopinath, and V. M. Bright. In preparation.

"Real-Time Detection of Early-Stage Calcium Sulfate and Calcium Carbonate Scaling Using Raman Spectroscopy," by O. D Supekar, D. J. Park, A. R. Greenberg, J. T. Gopinath, and V. M. Bright. Published in *Journal of Membrane Science,* (2020) Vol. 596, p. 117603.

## 6.1 Abstract

Improved operation, maintenance, and longevity of reverse osmosis (RO) desalination systems requires an understanding of the kinetics and mechanisms of scale formation. In-situ monitoring techniques can provide the means for early scaling detection, in addition to better understanding of important scaling mechanisms. In this work, calcium sulfate and calcium carbonate scaling on reverse osmosis membranes were chemically detected in real-time using Raman spectroscopy.

Raman sampling strategy plays a critical role in producing accurate, representative detection results. Three different sampling strategies are presented, including single-point sampling, manual multi-point sampling, and automated multi-point sampling. The performance of these different sampling strategies was evaluated by comparing the Raman detection times to concurrent values of flux decline as a standard metric of comparison. The automated multi-point sampling strategy provided the best performance, with detection of calcium sulfate and calcium carbonate at permeate flux values as low as 0.4% and 0.5%, respectively. Post-mortem characterization provided estimates of scaling crystal characteristics such as mean crystal size, surface coverage, and crystal number density. The limitations of the single-point detection results suggested that the crystal voids (i.e., scale-free zones) could be as important as the characteristics of the crystals themselves in obtaining accurate detection metrics. A spatial point pattern analysis tool known as Ripley's *K* Function was used to compare quantitative differences in

spatial uniformity between calcium sulfate and calcium carbonate scaling crystals. These results suggested that in addition to crystal characteristics, the distribution of the scaling crystals was an important criterion in optimizing the Raman sampling strategy. The ability to identify the chemical composition of different scaling crystals including their polymorphs was identified as an important step toward better understanding of the crystallization pathways of multi-component feed streams used in seawater and brackish water RO desalination.

## 6.2 Introduction

Real-time chemical sensing is a crucial aspect of in-situ monitoring since the success of many scale-control measures depends on accurate identification of the chemical composition of the deposited scales. Despite its importance, this critical capability is not addressed by well-researched real-time techniques, such as visual observation (VO) [40,88,105], ultrasonic time-domain reflectometry (UTDR) [33,34,44], magnetic resonance imaging (MRI) [84,123], and electrical impedance spectroscopy (EIS) [47,124,125]. As a workaround, membrane autopsies are commonly employed to identify the chemical composition and severity of membrane scaling [126,127]. Autopsies, though they provide useful diagnostic information, cannot provide real-time feedback, and oftentimes fail to reflect the actual scaling potential of the feed. This is because the autopsies are typically conducted after the use of remediation measures (e.g., cleaning) that can alter the composition and structure of the fouling layer.

With regards to bench-scale experiments pertaining that support fundamental membrane scaling research, investigations are usually limited to single-component scaling, despite the high likelihood of altered membrane scaling behavior in the presence of multiple solute ions (components) [95,105,128,129]. This missing aspect can, in part, be attributed to the lack of real-time chemical identification. Furthermore, multi-component scaling studies that have been reported in the literature generally lack the hydrodynamics of realistic RO processes [128] because they utilize dead-end filtration setups or stirred-cell reactors [130,131], or focus on stainless steel heat exchangers which clearly have different properties from polymer RO membranes [132].

Raman spectroscopy is capable of real-time chemical sensing, and is a more recent in-situ monitoring technique that has been employed to detect vanillin on ultrafiltration (UF) membranes [52,133], bacteria on microfiltration (MF) membranes [51], and single-component scalants on RO membranes [53,55,56]. The distinctive chemical identification capability of Raman spectroscopy offers the opportunity to better understand multi-component scaling behavior during RO desalination. In the present work, a Raman microscope with a static (fixed) objective is integrated with a specially designed bench-scale RO crossflow cell mounted on a movable stage. Replicate scaling experiments are conducted, during which real-time Raman data and permeate flux are simultaneously recorded. Since permeate flux decline is a commonly used metric of membrane performance, it provides a key benchmark to which Raman data can be compared. The experiments conducted utilize model feed solutions containing precursors for calcium sulfate and calcium carbonate scale formation. This work also aimed to identify sampling specific parameters to consider in an optimized Raman sampling strategy, understand their influence on the performance of the Raman sensor. Since representative, accurate scaling detection is a key component of this work, the performance of different Raman sampling strategies is evaluated.

## 6.3 Experimental

This chapter includes the results of Raman detection for 10 independent, two-component scaling experiments. A preliminary multi-component scaling experiment (Test 0) was conducted using a single-point Raman sampling strategy. The remaining experiments were conducted in two series, using a multi-point, sequential Raman sampling strategy. Series I (Tests 1–3) were performed using manual stage movement (manual sampling) and Series II tests (Tests 4–9) were performed with motorized stage movement (automated sampling).

### 6.3.1 *Feed solutions*

Feed solutions were prepared to include precursors of both calcium sulfate and calcium carbonate scaling. To prepare the salt solutions, calcium sulfate dihydrate ($CaSO_4 \cdot 2H_2O$, ReagentPlus, ≥99%, Sigma Aldrich) was first added to deionized water and mixed for ~12 h. Since calcium chloride ($CaCl_2$, anhydrous,

powder, ≥97%, Sigma Aldrich) has a significantly higher solubility than calcium sulfate dihydrate, calcium chloride was added to the $CaSO_4$ salt solution following the calcium sulfate dihydrate. To avoid premature precipitation of $CaCO_3$ during synthesis of the salt solution, sodium bicarbonate ($NaHCO_3$, 99+%, extra pure, Acros Organics) was added to the feed solution at the start of the scaling experiment [106].

### 6.3.2 *Experimental procedure*

Details of the RO flow cell, system, and experimental procedure for Test 0 can be found in Supekar and Park et al. [55]. Figure 6-1 shows the reverse osmosis (RO) system and Raman system used to conduct Tests 1–9. The bench-scale RO flow cell was described in detail in Section 2.5.2.and the details of the in-house Raman microscope are provided in Section 3.6.2.

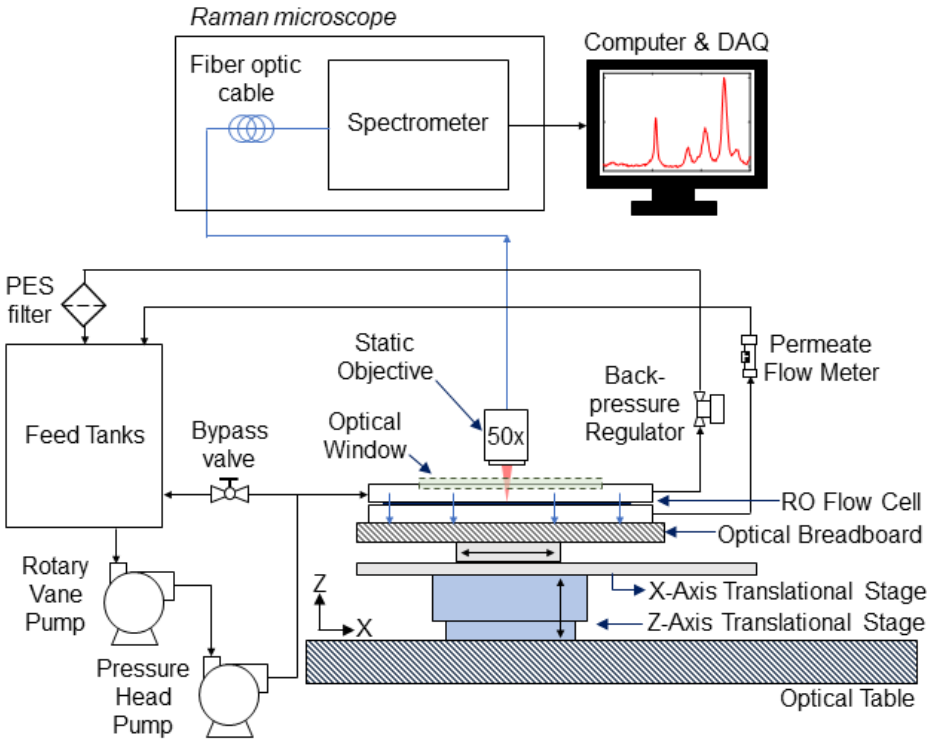


Figure 6-1. RO system schematic. The plate-and-frame reverse osmosis (RO) flow cell features a rectangular optical window that interfaced with a static (fixed-coordinate) Raman microscope objective. The position of the RO flow cell with respect to the Raman laser beam was adjusted using manual translational stages for Series I tests and a motorized stage for Series II tests. The flow cell/stage assembly was bolted to an optical table to minimize any environmental noise.

Prior to initiating the scaling experiments, the system was cleaned via 2-3 cycles of deionized water flushes until conductivity readings sustained values <1 μS/cm for at least 30 min. In some cases, this could not be achieved within the 2–3 cycles of deionized water flushes and thus, a system flush of <1% hydrogen peroxide was followed by two additional cycles of deionized water flushes. A commercial reverse osmosis membrane (Toray UTC-73HA) with an active membrane area of 12.5 cm × 17.5 cm was used for all experiments. The membrane stock rolls were stored in a plastic bag with DI water to prevent dry out. Prior to each scaling experiment, the utilized membrane was cut to size from a stock roll and soaked in a 50% solution of isopropanol for at least 30 min and then rinsed with DI water. The membrane was then compacted at 1 MPa with DI water for 12 to 15 h.

An inline 0.2 μm PE filter and prior system cleaning minimized the deposition of loose scaling crystals formed in the bulk feed or released from any buildup in the RO system. These measures have been reported to successfully minimize bulk crystallization in bench-scale scaling experiments [22]. In-line pressure, flow, and temperature sensors were monitored using a data acquisition system. Operating conditions were recorded approximately every minute during both the compaction and the scaling phases of the experiments.

During the scaling phase, the prepared feed solution was stored in a temperature-controlled tank (23.5 ± 0.5°C) and pumped into the flow cell at a volumetric flow rate of 25 L/h (crossflow velocity of ~3.0 cm/s). To fix the transmembrane pressure and flow rate of the feed stream, the backpressure regulator and bypass valve were iteratively adjusted until desired conditions were obtained. The transmembrane pressure varied from 1.05 to 1.25 MPa (~150 to 180 psi) to maintain a constant initial permeate flux between replicate scaling experiments.

Table 6-1 summarizes the RO system operating parameters and feed compositions that were applied during testing (Tests 0–9). The feed composition and initial flux parameter combinations were selected to accelerate both calcium sulfate and calcium carbonate scaling due to time constraints on the use of the

shared facility, commercial Raman microscope (Section 3.6.1). The pH of the feed solution was estimated using pH test strips. The feed pH at the beginning of the experiment was ~7, and the feed pH at the end of the experiment was ~6.

Table 6-1. Summary of mean RO system operating parameters and membrane performance (according to permeate flux) for scaling tests 0–9

| | RO System Operating Parameters | | | | Feed Composition (mM) | | |
|---|---|---|---|---|---|---|---|
| | Mean pressure (MPa) | Mean crossflow velocity* (cm/s) | Mean temperature (°C) | Initial flux (L/m$^2$/h) | $CaSO_4 \cdot 2H_2O$ | $CaCl_2$ | $NaHCO_3$ |
| Tests 0 | 1.20 ± 0.01 | 4.2 ± 0.3 (94) | 23.5 ± 0.5 | 55.5 ± 0.5 | 8.4 | 1.7 | 2.0 |
| Tests 1–3 | 1.09 ± 0.04 | 2.9 ± 0.3 (65) | 23.2 ± 0.3 | 48.5 ± 0.2 | 8.4 | 1.7 | 2.0 |
| Tests 4–9 | 1.23 ± 0.02 | 3.2 ± 0.2 (72) | 24.2 ± 0.5 | 36.6 ± 1.6 | 10.5 | 3.4 | 4.0 |

* Reynolds number indicated by the parentheses

Test 0 was performed using the RO system and flow cell described in Section 4.3.1. The RO system operating parameters are included in Table 6-1. Note that the feed composition for Test 0 was the same as that of Tests 1–3.

### 6.3.3 *Raman data acquisition*

A Raman spectral range of 100–1300 cm$^{-1}$ was selected to capture the Raman bands of the scaling species relevant in this work (Table 6-2). There are several different polymorphs that can form in the calcium sulfate ($CaSO_4$) and calcium carbonate ($CaCO_3$) crystal systems. The most stable form of calcium sulfate is gypsum ($CaSO_4 \cdot 2H_2O$), which has a strong $\nu_1$ vibrational mode at a Raman shift of 1008 cm$^{-1}$ [20]. The most stable polymorph of calcium carbonate is calcite, whose strongest vibrational mode occurs at a Raman shift of 1086 cm$^{-1}$ [21,97]. The two other polymorphs of calcium carbonate, namely aragonite and vaterite, have also been observed in other calcium carbonate scaling studies [96,108], with $\nu_1$ vibrational modes at 1085 and 1075/1090 cm$^{-1}$, respectively.

Table 6-2. Raman bands of relevant scaling species in RO desalination.

| Ref. | Species | Raman bands ($cm^{-1}$) | Assignment |
|---|---|---|---|
| [82,134,135] | $CaSO_4 \cdot 2H_2O$ | 1008 | $v_1$ mode (symmetric stretching) |
| [82,134] | $CaSO_4 \cdot 2H_2O$ | 414, 493 | $v_2$ mode (symmetric bending) |
| [82,134,136] | $CaSO_4 \cdot 2H_2O$ | 1135 | $v_3$ mode (antisymmetric stretch) |
| [82,136] | $CaSO_4 \cdot 2H_2O$ | 619, 670 | $v_4$ mode (antisymmetric bending) |
| [137] | $SO_4^{2-}$ | 981 | $v_1$ mode (symmetric stretching) |
| [109,138] | $CaCO_3$ (calcite) | 1086 | $v_1$ mode (symmetric stretching) |
| [139] | $CaCO_3$ (calcite) | 155, 281 | Lattice vibration |
| [21,138] | $CaCO_3$ (aragonite) | 1085 | $v_1$ mode (symmetric stretching) |
| [109] | $CaCO_3$ (aragonite) | 152, 205 | Lattice vibration |
| [109] | $CaCO_3$ (vaterite) | 1075, 1090 | $v_1$ mode (symmetric stretching) |
| [109] | $CaCO_3$ (vaterite) | 105, 301 | Lattice vibration |

For Test 0, a commercial Raman microscope (inVia Reflex, Renishaw) was integrated with the optical window positioned in the center of the flow cell. The laser beam (I0785SR0090B-IS1, Innovative Photonic Solutions) had a wavelength of 785 nm and incident power of ~20 mW and was focused onto the surface of the membrane through a microscope objective (N-PLAN L50x/0.50, Leica Germany).

For Tests 1–9, a lab-assembled Raman microscope (Section 3.6.2) was used to acquire the real-time Raman data. The incident power on the sample was ~27 mW. Raman data preprocessing included baseline removal to subtract the fluorescent background, cosmic ray removal, and vector normalization to account for power fluctuations. Next, the spectral intensity values were normalized again, this time to the membrane's C-O-C stretching band at 1150 $cm^{-1}$ (most prominent membrane Raman band), hereafter referred to as the relative Raman intensity. Raman detection was defined to occur when the relative Raman intensity of the scalant Raman band exceeded a threshold value of two standard deviations above the mean relative intensity value during compaction in DI water. This was to ensure that noisy scalant Raman signals were not taken as positive detection events.

For Test 0, the employed Raman strategy were fixed, single-point sampling. For Tests 1-9, two different sequential, multi-point sampling strategies were tested. All three sampling strategies utilized a fixed laser beam with a spot size of ~3 µm (Full Width at Half Maximum).

**6.3.3.1** Single-point sampling

In Test 0, the microscope objective of the commercial Raman microscope was focused on the membrane surface through an optical window positioned in the center of the flow cell. After a multi-hour membrane compaction phase, the scaling experiment was initiated by switching the feed to the mixed salt solution, accompanied by real-time Raman spectra acquisition and permeate mass measurements. The Raman detection site remained static throughout the entire duration of the scaling experiment.

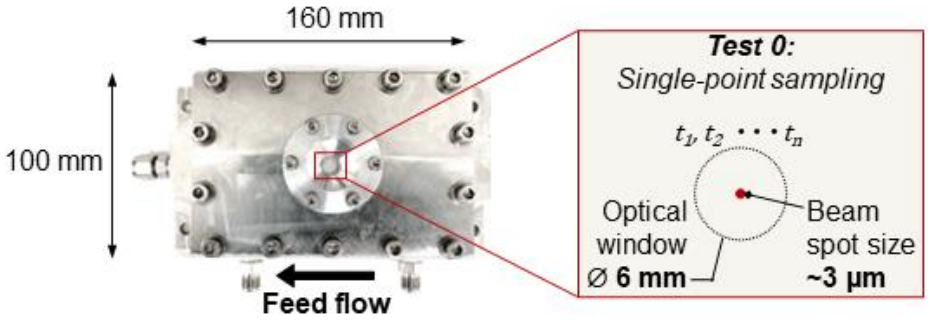


Figure 6-2. The reverse osmosis flow cell (left) and schematic of single-point detection (right). The Raman detection site remained static throughout the entire duration of the scaling experiment. Single-point sampling occurred at time $t_1$ to $t_n$ where $n$ was the total number of acquired Raman spectra.

**6.3.3.2** Manual, multi-point sampling

In Series I experiments (manual sampling, Tests 1–3), Raman data were recorded using a multi-point sampling strategy where the RO flow cell position was adjusted using manual *x*- and *y*-axis translation stages. Upon calcium sulfate and/or calcium carbonate detection, or after 10 min of no detection (whichever occurred first), the flow cell position was modified to a new, random position within a 2 mm × 2 mm area within the optical window of the flow cell (Figure 6-3).

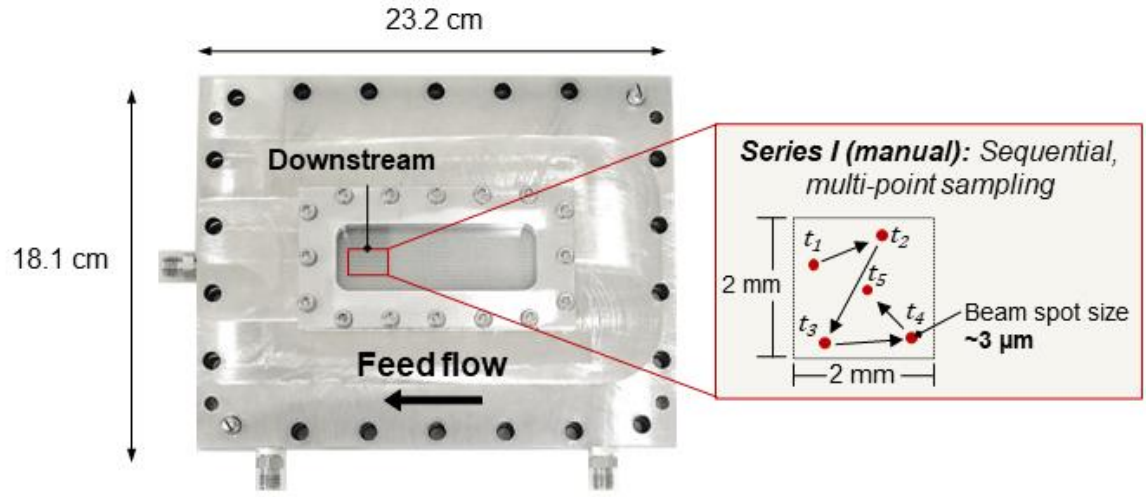


Figure 6-3. The reverse osmosis flow cell (left) and schematic of manual, multi-point detection (right). Manual *x*- and *y*-axis translational stages were adjusted to reposition the flow cell in the downstream location for real-time Raman detection. Time $t_1$ represented the time at which the Raman detection began at the first point, $t_2$ represented the time at which Raman detection began at the second point, and etc.

At each detection location, Raman spectra were acquired with 20 s of exposure. The experiment was terminated when both salts were detected in at least one location (Tests 1–3).

**6.3.3.3** Automated, multi-point sampling

In Series II experiments (automated sampling, Tests 4–9), a motorized linear stage (X-LSM150A, Zaber) with a resolution of 0.05 µm was used to automate linear movement of the RO flow cell (Figure 6-4). In these experiments, downstream Raman data were recorded for the first two hours, and subsequent upstream Raman data were recorded for the next two hours, for a total scaling duration of four hours (Tests 4–9). Raman spectra were acquired with two averaged scans with 10 s of exposure.

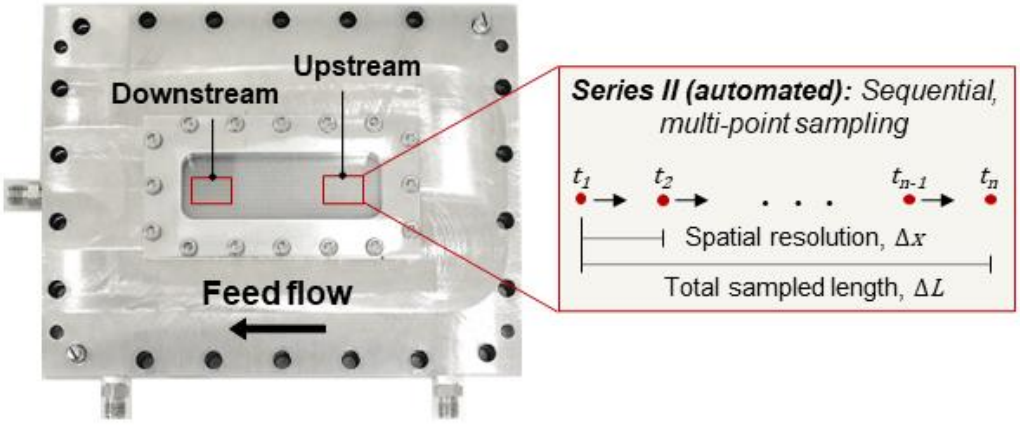


Figure 6-4. The reverse osmosis flow cell (left) and schematic of automated, multi-point sampling (right). A motorized *x*-axis stage allowed for sequential, linear Raman sampling along a predefined sampling length ($\Delta L$) with increments of the predefined spatial resolution ($\Delta x$). Time $t_1$ represented the time at which Raman data was obtained at the first sampled point, and time $t_2$ represented the time at which Raman data was obtained at the second sampled point. Time $t_n$ represented the time at which Raman data was obtained at the last sampled point, in a series of *n* points.

### 6.3.4 *Post-mortem characterization*

After the completion of each scaling experiment, the RO membrane was promptly removed from the flow cell and dried in ambient air. Test 0's membrane coupon measured 1 cm × 1 cm. Test 1–9 coupons were cut into coupons of 1 cm × 3 cm such that the coupons incorporated the regions of real-time Raman detection (Figure 6-5). Post-mortem characterization of the prepared membrane coupons was conducted to complement the real-time data and provide more insight into the performance of the Raman sensor during $CaSO_4$ and $CaCO_3$ detection.

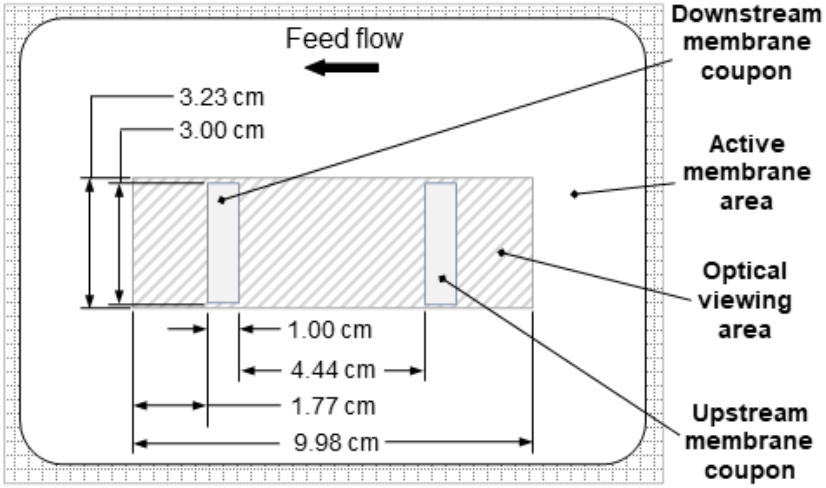


Figure 6-5. After the scaling experiment was terminated, the membranes were removed from the flow cell in under ~5 min and dried in ambient air. Once dry, 3 cm × 1 cm coupons were cut to size from the downstream and upstream regions, such that the coupons incorporated the regions of real-time Raman detection. These coupons initially underwent gravimetric analysis, due to the sample coating required for scanning electron microscopy.

#### **6.3.4.1** Gravimetric measurements

The mass of the scaled membrane coupons (Tests 1–9) was measured using a microbalance (ME 235S, Sartorious). The mass measurements were normalized to the dimensions of the coupons, measured using a digital caliper (DCLA 0605, VINCA). Gravimetric measurements of the scaled membranes were compared to that of virgin membrane coupons. The virgin membranes underwent the same pretreatment as the scaled membranes, which included a 30-min soak in a solution of 50% isopropanol and 12–15 h period of compaction at 1 MPa in DI water.

#### **6.3.4.2** Microscopy and X-ray analysis

After completing the gravimetric measurements described in Section 6.3.4.1, the prepared membrane coupons were sputter-coated with ~4–6 nm of platinum to prevent charging during scanning electron microscopy (SEM) and energy dispersive x-ray spectroscopy (EDS). EDS was performed on calcium sulfate crystals and polymorphs of calcium carbonate to confirm their chemical composition.

SEM images were processed using Fiji software [100] to extract various metrics regarding membrane surface coverage by both calcium sulfate and calcium carbonate crystals. These metrics

included: the percentage of the membrane surface coverage by scaling crystals, mean diameters of the scaling crystals, and distribution statistics. The images were first converted to 8-bit images and a thresholding procedure was employed to mark the scaling crystals with black pixels and membrane background with white pixels. Subsequently, the calcium sulfate crystals were differentiated from calcium carbonate crystals using a size and shape thresholding procedure. This enabled the calculation of the percentage area coverage, sizes, and centroids of the $CaSO_4$ and $CaCO_3$ particles.

## 6.4 Results and Discussion

This section begins with the detection results of a preliminary multiple component scaling experiment (Test 0) with fixed-coordinate, single-point Raman sampling to motivate subsequent multi-component scaling experiments using multi-point, sequential Raman sampling. To minimize any confusion with multi-point sampling, multi-component scaling is referred to as two-component scaling, with calcium sulfate and calcium carbonate as the two salts under investigation as they are commonly encountered scalants. Series I experiments (Tests 1–3) were conducted using manual stage movement (manual sampling) and Series II tests (Tests 4–9) were conducted using automated stage movement (automated sampling). The performance of the various sampling strategies was evaluated by comparing the Raman detection times of calcium sulfate and calcium carbonate with concurrent values of permeate flux decline at the time of Raman detection.

### 6.4.1 *Real-time Raman detection*

#### **6.4.1.1** Single-point sampling

As a preliminary investigation of two-component scaling detection, a commercial Raman microscope with a fixed-coordinate laser beam was used to collect real-time Raman data from a central position on the RO membrane. Permeate flux decline at the time of downstream Raman detection of gypsum (calcium sulfate) and calcium carbonate, termed the detection flux decline, was used to gauge the performance of the Raman sensor. Lower detection flux decline values were classified as more sensitive

detection events, i.e., better sensor performance. Conversely, higher values of detection flux detection were taken to suggest that the Raman sampling strategy was nonoptimal.

According to the Raman data shown in Figure 6-6, only gypsum ($CaSO_4 \cdot 2H_2O$), with a Raman band at 1008 $cm^{-1}$ was detected at 228 min of measurement, corresponding to a detection flux decline of 22.8%. Even considering the expected ~2–9% of the detection flux decline attributed to only membrane compaction [55], this result does not provide improved detection sensitivity compared to standard metrics of membrane performance, such as permeate flux and salt rejection. The calcium carbonate Raman signal remained at initial baseline values throughout the duration of the experiment, which indicated a negative detection result. Figure 6-6 shows the permeate flux and calcium sulfate Raman signal as a function of time. In post-mortem SEM and EDS characterization, the presence of both scaling crystals on the membrane surface was confirmed. Calcium carbonate would have been detected by Raman sensor if it had deposited at the detection site, but there was a ~1 order-of-magnitude difference in crystal size between the gypsum (~100 μm) and calcium carbonate (~10 μm) crystals, in addition to greater surface coverage by calcium sulfate scale. In addition, the laser beam spot size was ~3 μm (full width at maximum height). This suggests that, with such a small detection area, the probability of detecting large gypsum (calcium sulfate) with the fixed-coordinate Raman laser beam was more likely.

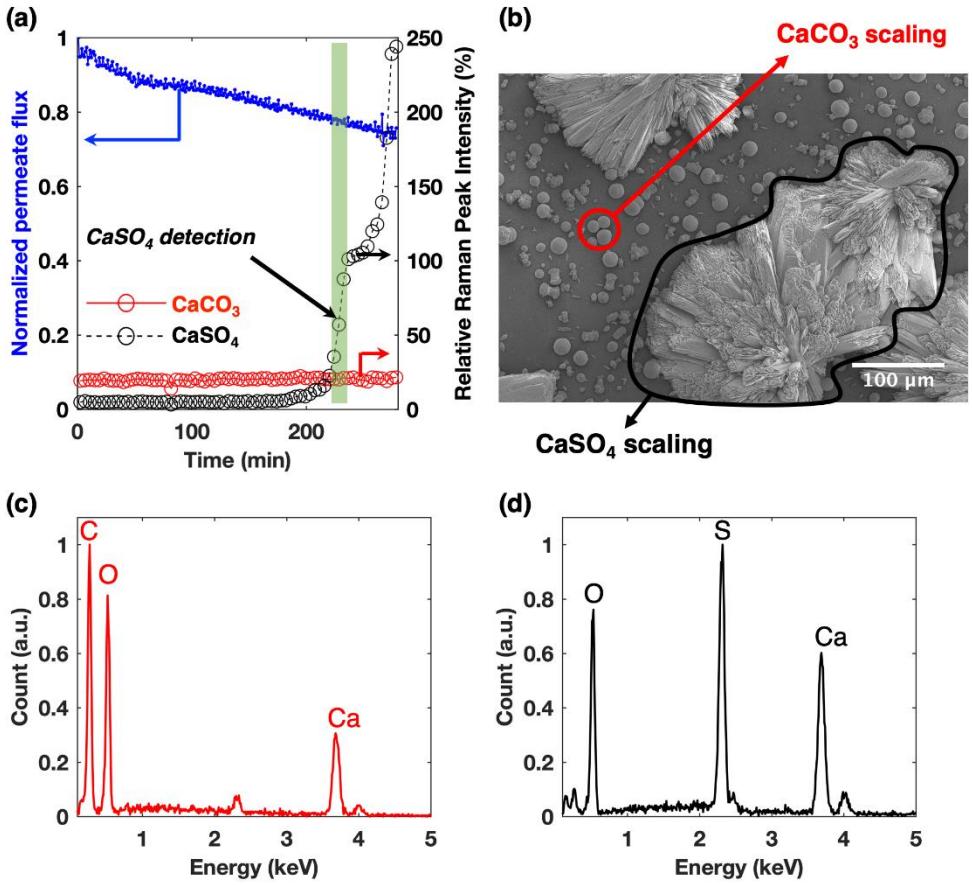


Figure 6-6. Real-time (a) permeate flux and Raman signal intensity for $CaSO_4$ and $CaCO_3$ Raman detection; (b) SEM image from Test 0 showing $CaSO_4$ and $CaCO_3$ scaling morphology in a location near, but not under the sensor; (c) and (d) corresponding EDS spectra for $CaCO_3$ and $CaSO_4$, respectively [55].

Replicate multi-component scaling detection attempts produced similar results with only calcium sulfate detection. This result demonstrates that the employed fixed, single-point Raman sampling strategy was limited by spatial factors, namely, differences between (i) the laser beam spot size and the scaling crystals size and (ii) nonuniformity in the deposition pattern of each scalant. For instance, a significantly larger laser beam spot size (detection area) or a uniform, crystalline scaling layer could increase the success rate of the Raman sensor, but the former would require considerably more laser power and the latter would restrict the applicability of the sensor to fewer cases such as silica scaling which can deposit on membranes in the form of a widespread and uniform silica gel film [140].

The degree to which the sampled area is representative of the membrane scaling condition is a crucial element in the present development of the Raman-based, in situ monitoring technique, and the gypsum-only detection result was not appropriately representative. Consequently, although the utility of a high spatial-resolution technique is recognized, it is clear that localized information for a *greater* sampling area would provide more accurate and useful results.

In implementing a greater sampling area, tradeoffs between factors such as microscope design, incident laser power, and spectral acquisition time must be considered. For example, the time it takes to obtain the Raman data should reasonably match the temporal resolution of membrane scale progression, so a greater sampling rate is more desirable. However, this comes at the expense of the signal-to-noise ratio (SNR) of the spectral bands, since the present spontaneous Raman system depends on longer acquisition times to improve the SNR, mainly by decreasing the shot noise inherent to processes governed by Poisson statistics (random events) such as Raman scattering [64]. Therefore, in the subsequent multi-point Raman sampling experiments, it was important to weigh the tradeoffs between laser power, acquisition time, and sampling area/resolution when selecting a suitable Raman sampling strategy that would increase the Raman sensor's success in two-component scaling detection.

#### **6.4.1.2** Manual, multi-point sampling

In Series I experiments (Tests 1–3 in Tables 4-3 and 4-4), a multi-point sampling strategy was tested with a custom-built Raman microscope, which featured a fixed-coordinate laser beam. An RO flow cell with a larger optical window and manual translation stages allowed for movement of the Raman detection site on the membrane by simultaneously adjusting the X-axis translation stage and Y-axis translation stage within a 2 mm × 2 mm area. Detection remained in the specified area with the aid of an acrylic stencil that acted as stops for the microscope objective's position.

Results for gypsum and calcium carbonate Raman detection are summarized in Table 6-3. Gypsum was detected at 100±53 min of measurement and calcium carbonate (calcite) was detected at 161±18 minutes. Flux decline at the time of calcium sulfate and calcium carbonate Raman detection was 13±10%

and 22±3%, respectively. Although these results are improved from the Test 0 result in that both scalants were detected in real-time, in general, sensitive detection with respect to permeate flux decline was not demonstrated, considering that a flux decline of 10–15% typically warrants remediation measures [141]. There was one instance of early detection, during Test 1, where gypsum detection occurred at a flux decline of only 1%, however, consistency in early detection is an important objective of the technique.

Table 6-3. Summary of Series I Raman detection times for $CaSO_4$ membrane scaling, as compared to the permeate flux decline at the time of Raman detection.

| | **$CaSO_4$ Detection** | | **Characterization of $CaSO_4$ Crystals** | | |
|---|---|---|---|---|---|
| | **Raman Detection Time** | **Permeate Flux Decline*** | **Mean Crystal Size** | **Crystal Number Density** | **Surface Coverage** |
| | **min** | **%** | **μm** | **#/cm²** | **%** |
| Test 1 | 39 | 1 | 315 ± 222 | 6 | 72 |
| Test 2 | 127 | 20 | 145 ± 101 | 18 | 44 |
| Test 3 | 133 | 18 | 152 ± 119 | 10 | 61 |

*At the time of Raman detection

Table 6-4. Summary of Series I Raman detection times for $CaCO_3$ membrane scaling, as compared to the permeate flux decline at the time of Raman detection.

| | **$CaCO_3$ Detection** | | **Characterization of $CaCO_3$ Crystals** | | |
|---|---|---|---|---|---|
| | **Raman Detection Time** | **Permeate Flux Decline*** | **Mean Crystal Size** | **Crystal Number Density** | **Surface Coverage** |
| | **min** | **%** | **μm** | **#/cm²** | **%** |
| Test 1 | 170 | 19 | 9.1 ± 3.0 | 836 | 6 |
| Test 2 | 141 | 24 | 9.1 ± 3.4 | 643 | 5 |
| Test 3 | 174 | 24 | 9.7 ± 4.6 | 340 | 3 |

*At the time of Raman detection

A final critique of the manual sampling strategy is that calcium carbonate Raman detection regularly occurred after gypsum detection. However, it was hypothesized that this result inaccurately portrayed the induction time of calcium carbonate scale formation. This hypothesis was suggested by post-mortem observation of the calcium carbonate scaling crystals. If calcium carbonate deposition truly occurred after gypsum deposition, the expectation is that the calcium carbonate crystals would have been much smaller than the observed ~10–15 μm, especially since the experiment was terminated shortly after their detection. The gypsum twinning observed in the SEM images further supports this hypothesis because

the twinned formations rely on calcium carbonate surfaces as nucleation sites, suggesting that an initial layer of calcium carbonate crystallites deposited early in the scaling experiment.

The reason for late calcium carbonate detection could be due to low Raman SNR caused by the comparably small sizes of the crystals and the Raman laser beam spot size (~3 μm). The strength of the Raman signal is influenced by various factors, one of which is laser-sample volume interaction [142]. While the high sensitivity of the Raman sensor to trace amounts of scale was noted in Chapter 4, Raman signals may suffer from reduced volume interaction with small crystals. It is also important to mention that the beam spot size was small enough to fit in the gaps between the calcium carbonate crystals, which would result in a negative detection result. Although real-time detection of both calcium sulfate and calcium carbonate was demonstrated, results indicated that randomized, manual sampling was an inefficient sampling strategy, exacerbated by the use of a small laser beam spot size and crystals of varied length-scales. It follows that a more systematic sampling approach could be suitable for more consistent, representative detection. Therefore, an automated sampling approach was proposed as a second multi-point sampling strategy.

#### **6.4.1.3** Automated, multi-point sampling

In the automated, multi-point sampling strategy (Series II tests), the same fixed-coordinate Raman system was integrated with a motorized stage programmed to move linearly, so that multiple points could be sampled in series, along the direction of feed flow. The selection of the total sampled length ($\Delta L$ in Figure 6-4) and spacing ($\Delta x$) between sampled points ($\Delta L/\Delta x$) (spatial resolution) was informed by the distances between the largest scaling species and the smallest scaling species, respectively. According to Series I membrane samples, gypsum was the larger scaling species with crystal distances that were on the order of millimeters, and calcium carbonate was the smaller scaling species, with crystal spacings on the order of 10's of microns. Therefore, a total sampled length ($\Delta L$) of 4.5 mm was selected. Since the goal is to minimize the total time taken to complete a full cycle of multi-point sampling in early scaling stage, the minimum Raman acquisition time was first determined. A 10 s acquisition time was selected with two

accumulations (averaged spectra) as a means to improve SNR, and an additional ~20 s was added to the sampling time to provide ample time for data acquisition and storage. Based on a goal of <5 min for the total sampling cycle time ($\Delta L/\Delta x \times 30$ s), a spatial resolution of 0.5 mm was selected, resulting in 10 total points per sampling cycle.

Table 6-5 and Table 6-6 summarize the results for downstream Raman detection (Figure 4-5) for calcium sulfate and calcium carbonate, respectively.

Table 6-5. Series II results for downstream Raman detection of gypsum, permeate flux decline at the time of Raman detection, and post-mortem characterization of scaling crystals.

| | **Real-time $CaSO_4$ Detection** | | **Post-mortem Characterization of $CaSO_4$ Crystals** | | |
|---|---|---|---|---|---|
| | **Raman Detection Time** | **Permeate Flux Decline*** | **Mean Crystal Size** | **Crystal Number Density** | **Surface Coverage** |
| | **min** | **%** | **μm** | **#/cm²** | **%** |
| Test 4 | 59 | 2.1 | 152 ± 104 | 14 | 35 |
| Test 5 | 124 | 10.8 | 156 ± 146 | 13 | 39 |
| Test 6 | 19 | 0.4 | 136 ± 95 | 7 | 18 |
| Test 7 | 133 | 13.8 | 155 ± 83 | 13 | 47 |
| Test 8 | 94 | 9.6 | 241 ± 147 | 10 | 39 |
| Test 9 | 63 | 4.2 | 170 ± 99 | 11 | 23 |

*At the time of Raman detection

Table 6-6. Series II results for downstream Raman detection of calcium carbonate, permeate flux decline at the time of Raman detection, and post-mortem characterization of scaling crystals.

| | **Real-time $CaCO_3$ Detection** | | **Post-mortem Characterization of $CaCO_3$ Crystals** | | |
|---|---|---|---|---|---|
| | **Raman Detection Time** | **Permeate Flux Decline*** | **Mean Crystal Size** | **Crystal Number Density** | **Surface Coverage** |
| | **min** | **%** | **μm** | **#/cm²** | **%** |
| Test 4 | 95 | 5.0 | 8.1 ± 7.5 | 2521 | 11 |
| Test 5 | 26 | 0.5 | 11.9 ± 6.2 | 1426 | 13 |
| Test 6 | 40 | 1.4 | 13.2 ± 6.8 | 1682 | 15 |
| Test 7 | 28 | 8.1 | 13.9 ± 5.9 | 1179 | 15 |
| Test 8 | 52 | 3.8 | 14.5 ± 6.3 | 1315 | 16 |
| Test 9 | 124 | 2.3 | 13.1 ± 6.7 | 1935 | 15 |

*At the time of Raman detection

Downstream Raman sampling resulted in calcium sulfate and calcium carbonate detection at an average flux decline of 7 ± 5% and 4 ± 3%, respectively. Calcium carbonate detection in the present sampling strategy significantly improved from Series I detection (19–24% detection flux decline). The

lower values of flux decline (<10–15% permeate flux decline) at the time of Raman detection suggest improved early detection capability of the modified sampling strategy. After two hours of downstream Raman detection, the automated sampling strategy was translated to the upstream detection location. This time period was based on the longest downstream Raman detection time observed for calcium sulfate and calcium carbonate scaling in early reference experiments. The time taken for upstream Raman detection would signify whether membrane scaling was in its early or late stages, with a longer detection time signaling an earlier stage. The upstream Raman detection results are shown in Table 6-7 and 6-8. It should be noted that upstream Raman detection times and concurrent values of flux decline are reported with respect to the start of upstream detection.

Upstream Raman detection of calcium sulfate and calcium carbonate scaling occurred at a mean flux decline of 3 ± 5% and 1 ± 3%, respectively. These low values of permeate flux decline Raman detection suggest that by the time upstream detection initiated at the two-hour mark, scale had already progressed upstream.

Table 6-7. Series II results for upstream Raman detection of gypsum, permeate flux decline at the time of Raman detection, and post-mortem characterization of scaling crystals.

| | **Real-time $CaSO_4$ Detection** | | | | **Post-mortem Characterization of $CaSO_4$ Crystals** | | |
|---|---|---|---|---|---|---|---|
| | **Raman Detection Time[1]** | | **Permeate Flux Decline*** | | **Mean Crystal Size** | **Crystal Number Density** | **Surface Coverage** |
| | **min** | | **%** | | **µm** | **#/cm²** | **%** |
| Test 4 | 8 | (145) | 1.9 | (14) | 198 ± 0 | 14.4 | 18.0 |
| Test 5 | 2 | (133) | 0.3 | (13) | 150 ± 106 | 3.7 | 3.1 |
| Test 6 | - | - | - | | 139 ± 95 | 0.1 | 0.2 |
| Test 7 | 1 | (155) | 0.4 | (17) | 120 ± 64 | 11.2 | 29.5 |
| Test 8 | 88 | (226) | 11.9 | (26) | 241 ± 147 | 1.7 | 1.2 |
| Test 9 | 4 | (185) | 0.8 | (22) | 37 ± 36 | 9.6 | 21.3 |

[1]With respect to the start of upstream Raman detection
*At the time of Raman detection
( ) – With respect to salt feed introduction time

Table 6-8. Series II results for upstream Raman detection of calcium carbonate, permeate flux decline at the time of Raman detection, and post-mortem characterization of scaling crystals. The values in the parentheses are the values with respect to the start of the scaling experiment.

| | Real-time $CaCO_3$ Detection | | | | Post-mortem Characterization of $CaCO_3$ Crystals | | |
|---|---|---|---|---|---|---|---|
| | Raman Detection Time[1] | | Permeate Flux Decline* | | Mean Crystal Size | Crystal Number Density | Surface Coverage |
| | min | | % | | μm | #/cm² | % |
| Test 4 | 45 | (183) | 6.9 | (18) | 9.6 ± 6.5 | 3240 | 34 |
| Test 5 | 1 | (132) | 0.3 | (18) | 9.5 ± 5.8 | 3180 | 31 |
| Test 6 | 3 | (154) | 0.3 | (13) | 10.3 ± 5.7 | 2060 | 22 |
| Test 7 | 0 | (159) | 0.0 | (17) | 13.3 ± 7.0 | 1480 | 26 |
| Test 8 | 0 | (141) | 0.0 | (16) | 12.1 ± 5.5 | 2230 | 31 |
| Test 9 | 0 | (181) | 0.1 | (20) | 12.7 ± 6.5 | 2170 | 35 |

[1]With respect to the start of upstream Raman detection
*At the time of Raman detection
( ) – With respect to salt feed introduction time

Reflecting on the inherent variability of membrane scaling, upstream detection of gypsum in Test 6 was not observed and gypsum detection in Test 8 took about four times longer than the mean upstream detection time of ~21 min. Both results were likely due to a low gypsum surface coverage of 0.2 and 1.2%, respectively, which decreased the likelihood of overlapping deposited crystal and detection sites.

Overall, these results show the Raman sensor's ability to sensitively detect both calcium sulfate and calcium carbonate salts in real-time. Continued improvement of the technique would recommend its use in studies of mixed salt precipitation which is still not well understood due to general lack of real-time chemical sensing capability.

### 6.4.2 *Gravimetric analysis*

In bench-scale RO flow cells, the greater concentration polarization effects at downstream membrane surfaces, in contrast to upstream surfaces, serve as a greater source of scaling ions for scale formation. Thus, the severity of scaling is typically greatest at the channel exit (downstream). This expected result is supported by the gravimetric measurements in Figure 6-7. These data suggest that the scale progression from downstream to upstream locations was similar to that of single-component scaling [31,56] with greater deposited mass downstream. The measured scaling crystal mass per area ($g/mm^2$) increases with increasing normalized axial position ($x/L$, where $x$ represents the axial position at the membrane from

the feed inlet along the flow direction and $L$ is the length of the membrane). The downstream mean mass per area was 16 ± 2 % and 14 ± 9 % greater than the upstream values for Series I coupons (Tests 1–3) and Series II coupons (Tests 4–9), respectively. The mass per area of coupons from Test 6 did not show marked changes with increasing axial position. This result is unexpected but could reflect the inherent variability within each membrane sample, as evidenced by the standard deviation for the mass per area (~$0.5 \times 10^{-4}$ g/mm$^2$) of an unscaled membrane coupon.

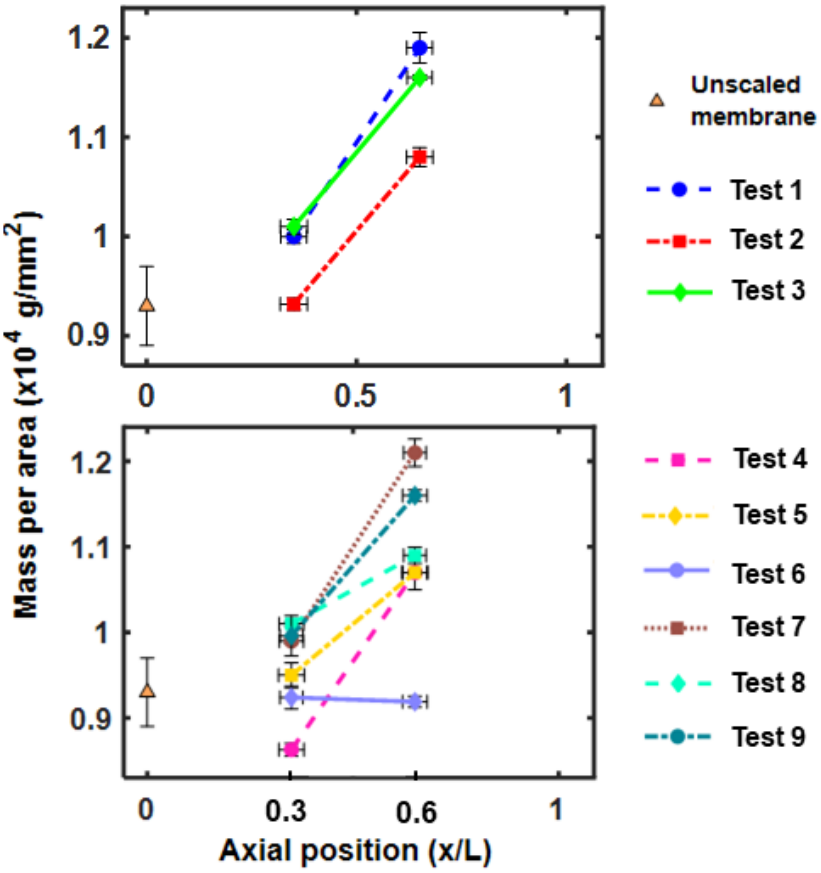


Figure 6-7. Post-mortem gravimetric analysis from Tests 1-9. Upstream gravimetric measurements are shown for x/L = 0.3 and downstream values are shown for $x/L$=0.6.

### 1.1.1 *Post-mortem confirmation of two-component scaling*

Figure 6-8 shows SEM images from Series I (manual sampling) and Series II (automated sampling) representative post-mortem membrane coupons. The presence of calcium sulfate and calcium carbonate scaling crystals was visually confirmed for both test series.

Calcium carbonate can form three main polymorphs, which are crystals that have the same chemical composition, but a differing arrangement of lattice ions. The arrangement of the lattice ions results in different crystal morphologies and solubilities [143]. The upstream and downstream Series I calcium carbonate scaling crystals were predominantly spherical vaterite [144]. Upstream and downstream Series II calcium carbonate crystals appear to exhibit a wider variety of shapes and sizes, including spherical vaterite, football-shaped calcite [144], and peanut-like calcite and aragonite [145] (also reported as "broccoli" aragonite [146]).

Calcium sulfate crystals are observed to belong to a monoclinic crystal system with a rosette-like growth pattern, indicating that gypsum ($CaSO_4 \cdot 2H_2O$) is the dominant calcium sulfate polymorph [22,88,108,147,148]. The fact that gypsum crystals presented themselves as rosettes serves as evidence that surface crystallization was the main scaling mechanism [23], as gypsum membrane scaling by bulk crystallization and subsequent deposition lacks this rosette-like form and instead appears to be a loose cake layer of gypsum rods or needles [149].

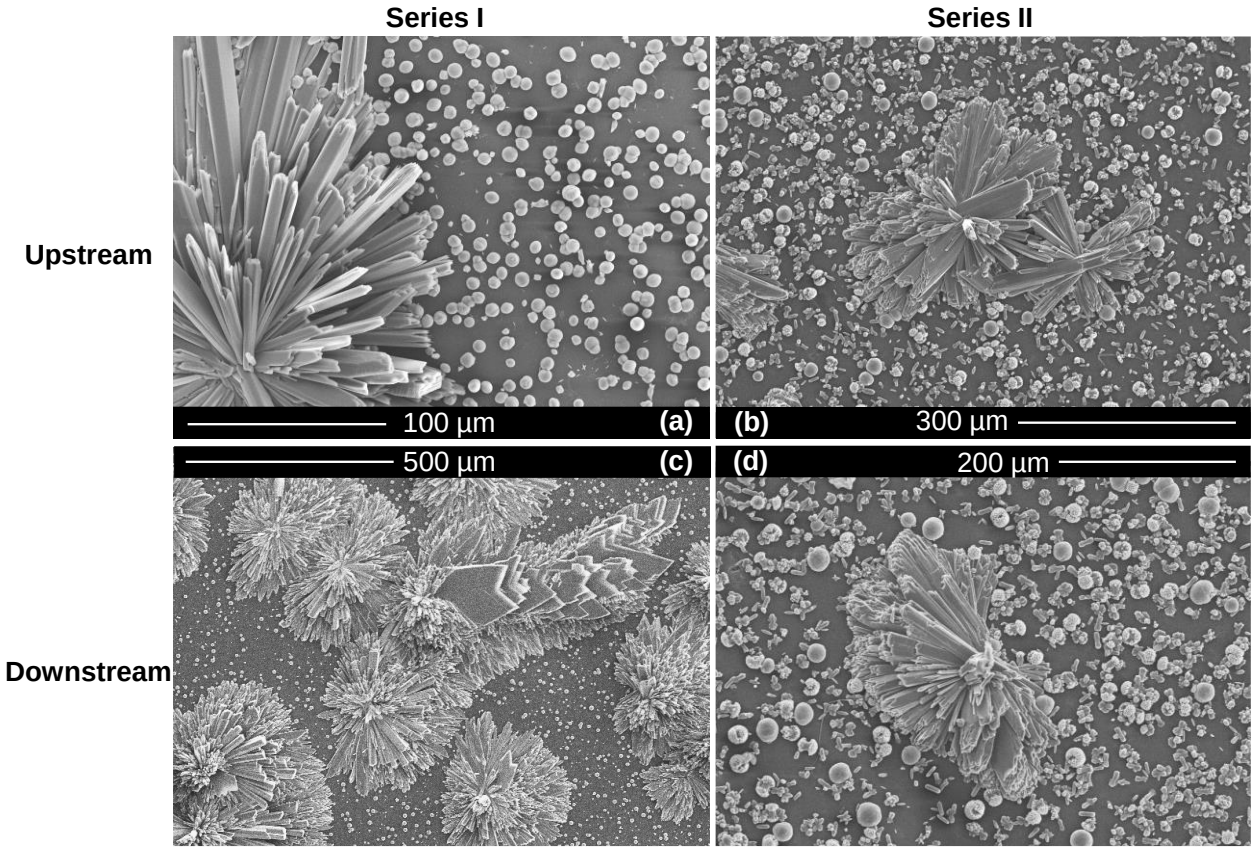


Figure 6-8. SEM images of calcium sulfate and calcium carbonate crystals from the following representative post-mortem membrane coupons: (a) Series I experiment upstream, (b) Series II upstream, (c) Series I downstream, and (d) Series II downstream.

Long gypsum rods with a high aspect ratio (length/width), emanating from a common core, constituted the representative Series I upstream rosette depicted in Figure 6-8a, whereas the features of the representative Series II upstream and downstream gypsum rosettes were more plate-like (Figure 6-8b,d). The bicarbonate to sulfate ratio in the Series II bulk feed solution was ~62% greater than that of Series I. A greater bicarbonate ($HCO_3^-$) presence during gypsum growth may have favored the formation of these plate-like rosettes. Indeed, Rahardianto et al. [105] suggested that the adsorption/desorption of foreign ions could influence the growth kinetics of the gypsum rosettes formed during bench-scale experiments. The decrease in the growth rates was attributed to the fact that when foreign ions adsorb on the crystal surface, they must also desorb prior to further gyspum growth [150]. They reported as much as a 63% decrease in gypsum

growth rate and 78% decrease in membrane surface coverage with the addition of 7.81 mM $HCO_3^-$ in the gypsum feed solution, but the morphology of the gypsum scale was not reported in detail.

Interestingly, in the Series I downstream SEM image (Figure 6-8c), a trailing tail of platelets can be observed, nestled between the typically present gypsum rosettes. These particular platelets could be swallow-tail twins or Monmatre twins [151], which results from gypsum nucleation on a preexisting calcite surface and subsequent epitaxial growth [152]. In the formation of gypsum twins, dissolution of calcite (host crystal) provides calcium ions for the growth of the gypsum (guest crystal). This could mean that whereever the twinning of gypsum is observed, calcium carbonate was initially present.

#### **6.4.2.1** Polymorph detection

Antiscalant formulations have been reported to be related to the structure of scaling crystals. For instance, polyvinyl sulfonate was found to inhibit the calcium sulfate dihydrate phase, while polyglutamic acid more effectively inhibited calcium sulfate hemihydrate [153]. For calcium carbonate, a commonly utilized scale-control technique is to increase the pH of the feed which effectively increases the solubility limit of the calcium carbonate. Calcite, the most stable polymorph of calcium carbonate, is typically the least soluble in water. In contrast, vaterite or aragonite, the less stable polymorphs are more soluble in water [154,155]. Since high pH levels can induce other types of scaling, knowledge of the dominantly deposited polymorph may be particularly useful in RO desalination, influencing membrane cleaning decisions and ultimately enabling optimization of scale-control strategies.

One way to differentiate polymorphs in the Raman data is to study the lattice Raman bands occurring <400 $cm^{-1}$ for calcium carbonate. However, these lattice bands can exhibit low signal to noise ratios (Chapter 5), making it difficult to distinguish background noise from potential lattice Raman vibrations. Alternatively, the $v_1$ vibrational modes of the polymorphs could be studied, but all the $v_1$ vibrational modes fell within a short spectral range of ~5 $cm^{-1}$ (1085–1090 $cm^{-1}$), with spacings of a few $cm^{-1}$, which could result in overlapping $v_1$ vibrational modes. Therefore, a finer spectral resolution may be able to resolve these closely occurring Raman bands. As a rule of thumb, at least 3 pixels are needed to

resolve Raman bands of a certain peak width or peak spacing; therefore, a spectral resolution of ~0.7cm$^{-1}$/pixel (2 cm$^{-1}$/3 pixels) was a reasonable starting point. The Raman spectral resolution was increased from ~0.9 to ~0.4 cm$^{-1}$/pixel using a 1200 line/mm grating for a separate scaling experiment that was not included in the series due to improper RO system cleaning. Figure 6-9 shows an example of a Raman spectrum obtained using the finer spectral resolution (1200 line/mm grating). Here, two smaller peaks at 1086 and 1090 cm$^{-1}$ can be observed, suggesting the presence of calcite and vaterite.

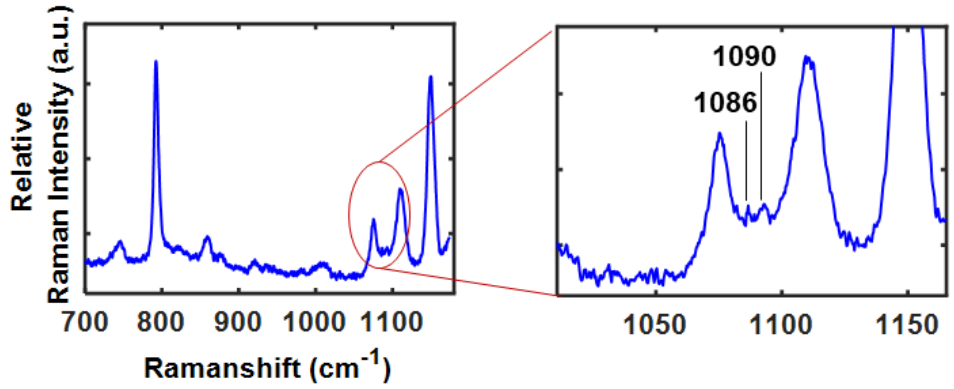


Figure 6-9. A broad band spanning 1085 to 1090 cm$^{-1}$ was observed during upstream detection. To resolve the broad band into finer distinct bands, the spectral resolution was increased by using a 1200 lines per mm grating during the last segment of upstream detection (~0.5 cm$^{-1}$/pixel).

Amorphous calcium carbonate (ACC) is a metastable phase of calcium carbonate which has a Raman band at ~1080 cm$^{-1}$. Although this band overlaps a membrane Raman band occurring at 1073 cm$^{-1}$, a widening of the 1073 cm$^{-1}$ was occasionally observed during detection (Figure 6-10b).

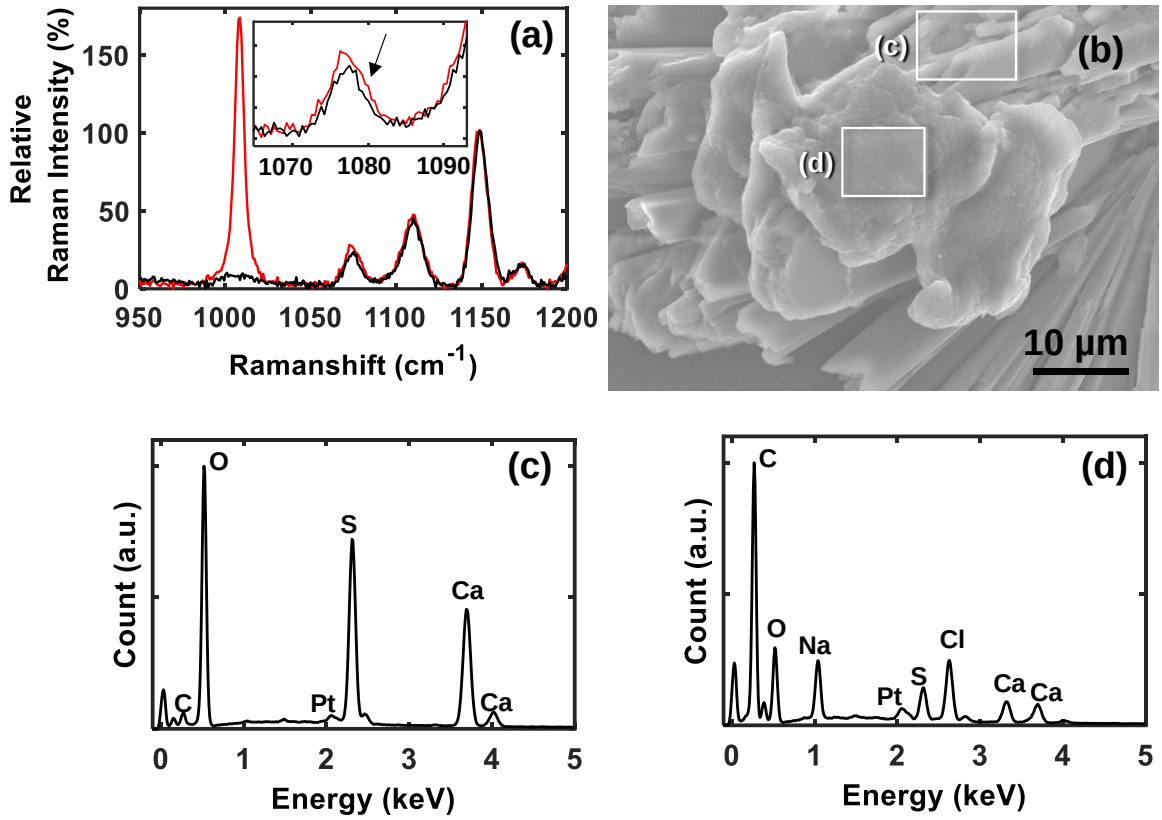


Figure 6-10. (a) The presence of amorphous calcium carbonate (ACC) on gypsum was suggested by the real-time Raman data and further investigated by (b) SEM imaging and EDS analysis on (c) a suspected deposit of ACC and (d) gypsum as a means of comparison. EDS results supported that the amorphous deposit was ACC. Platinum was additionally identified in (c, d) due to sample preparation prior to SEM imaging. The presence of sodium and chloride was likely caused by residual feed solution on the membrane sample prior to removal from the flow cell.

Furthermore, amorphous masses have been observed in representative SEM images of the detected scales. To investigate this further, EDS analysis was performed on one such example of an amorphous mass (Figure 6-10c,d). The greater ratio of carbon (C) to sulfur (S) atoms from the amorphous region strongly identification as amorphous calcium carbonate rather than, for example, a deformed gypsum crystal. These results ultimately clearly demonstrate the potential of the Raman sensor for distinguishing not only chemical composition, but also inferring the crystal structure of the scale particles. The latter could enhance scale control techniques during RO desalination.

### 6.4.3 *Scaling crystal characteristics*

Representative detection was identified an pivotal design criterion for the Raman methodology. Given that conditions on the membrane surface change as a function of time, the fraction of precipitates sampled can only be a small percentage of the total deposition mass. Thus, an important consideration in the interpretation of the local data is the degree to which the sample appropriately represents the condition of the larger surrounding membrane area. This judgement depends on an understanding of scaling crystal characteristics, including surface coverage and number density, size, and distribution of the crystals. Thus, SEM images were processed using Fiji software [100] using a standardized imaging processing procedure to extract additional quantitative information regarding the scaling crystals. The images in Figure 6-11 and Figure 6-12 were obtained from the same membrane coupons used for gravimetric analysis (Section 6.4.2).

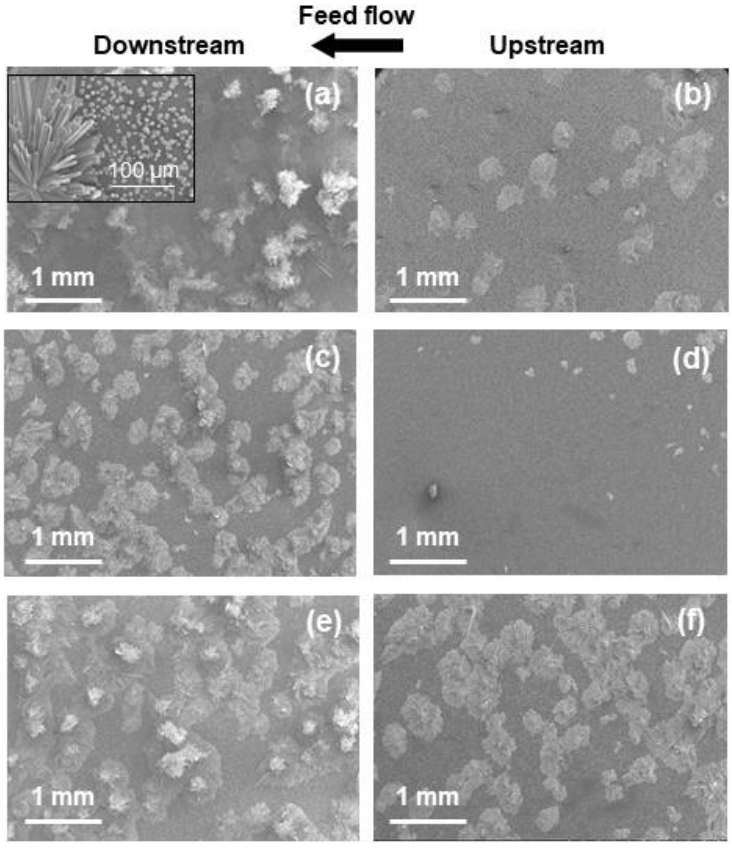


Figure 6-11. (a, c, e) Representative Raman-detected calcium sulfate (gypsum) and calcium carbonate (mostly vaterite) crystals from downstream Series I Raman detection (Tests 1–3). (b, d, f) SEM images for upstream membrane coupons are also shown, but note that real-time Raman detection was not performed in these regions due to the Series I focus on a proof-of-concept demonstration of multi-point sampling.

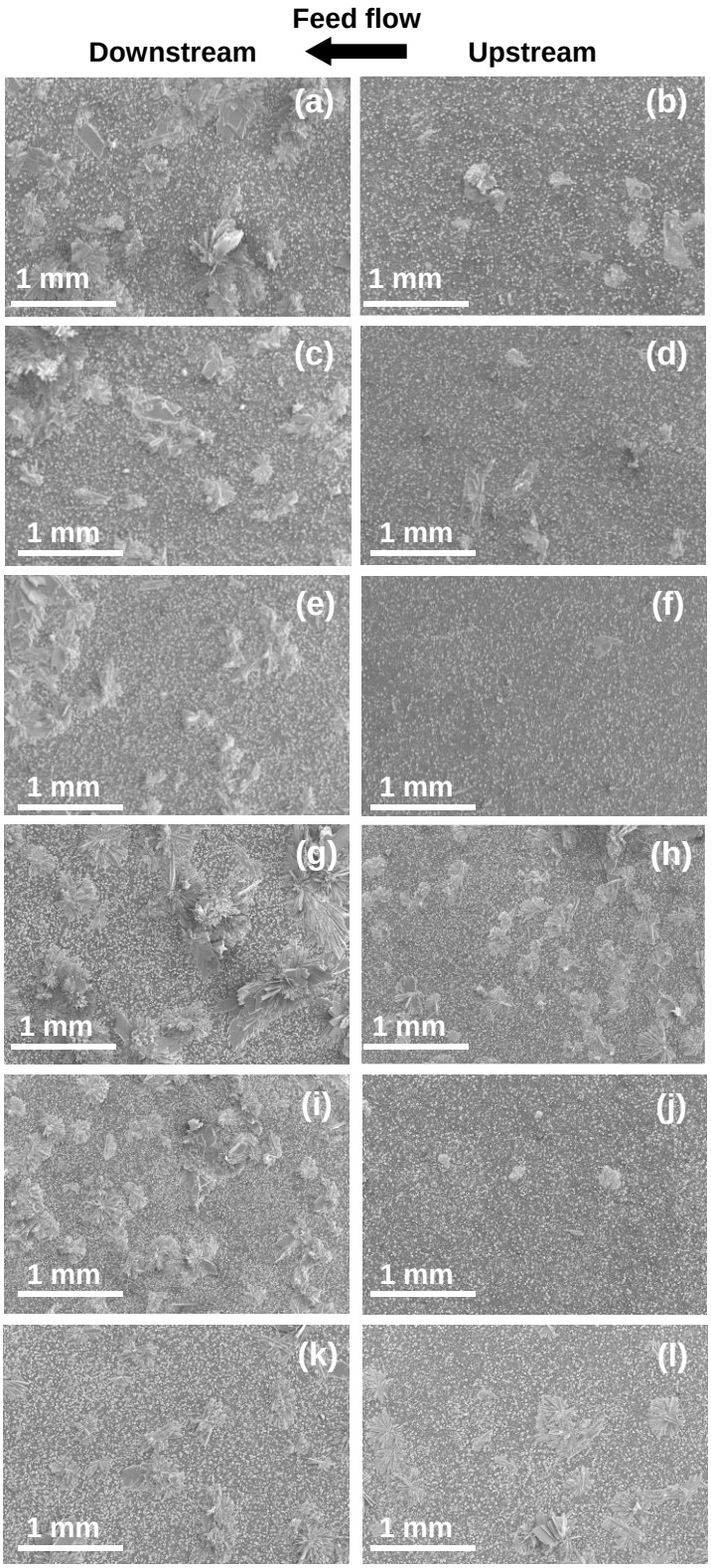


Figure 6-12. Representative calcium sulfate (gypsum) and calcium carbonate (calcite, vaterite, and aragonite) crystals from downstream and upstream Series II Raman detection (Tests 4–9).

### **6.4.3.1** Mean crystal size

Image processing generated crystal area measurements that were used to approximate the crystal size as the diameter of a circular crystal (Figure 6-13). The circular crystal assumption was applied to both gypsum and calcium carbonate scaling crystals, and a ~1 order-of-magnitude difference was observed between the mean crystal size of gypsum and calcium carbonate.

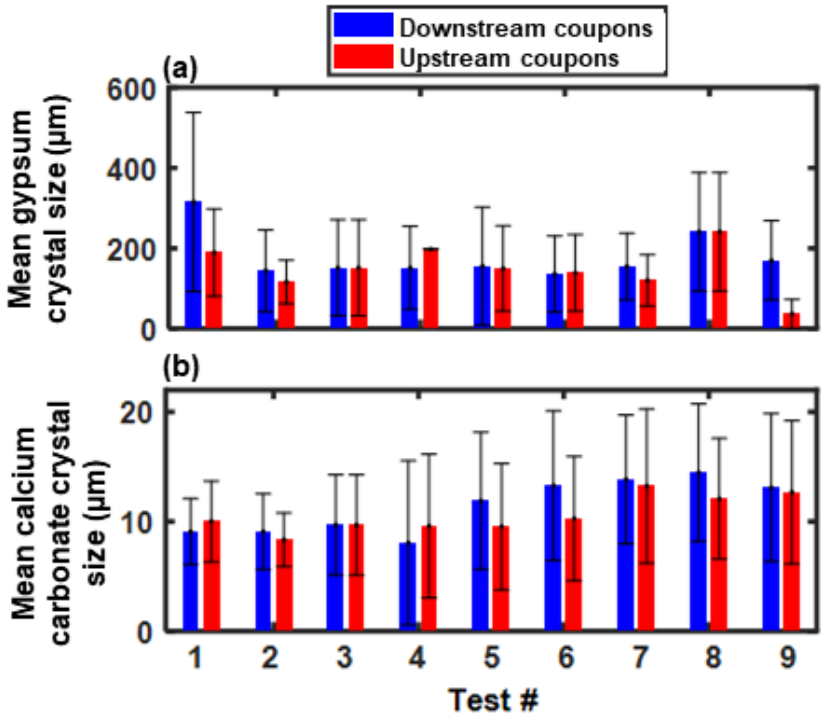


Figure 6-13. Comparison of downstream and upstream mean crystal sizes of (a) gypsum and (b) calcium carbonate scaling crystals. The error bars represent two standard deviations in crystal sizes measured from each membrane coupon, and the upstream error bar for gypsum's mean crystal size in Test 4 was zero since only one crystal was present on the SEM image.

The mean crystal size of gypsum for Tests 1, 2, 5, 7, and 9, is observed to be greater for downstream coupons. The onset of scaling typically begins downstream for crossflow RO, where a heightened concentration polarization effect, i.e., greater supersaturation levels, can encourage earlier salt precipitation. In crossflow RO, a greater concentration polarization effect at downstream membrane surfaces (compared to upstream surfaces) provides higher supersaturation levels of scaling ions, which are a necessary

prerequisite of salt precipitation. These downstream crystals can continue to grow given sufficient concentrations of scaling ions, but as the availability of scale-free surface area diminishes, scaling progresses further upstream. Given the difference in growth times, upstream crystals can be smaller than downstream crystals, but this was not the case for the mean gypsum crystal sizes from Tests 3, 6, and 8, whose downstream and upstream values are about equal. The slowed growth kinetics of the downstream crystals can be attributed to not only a shortage of scale-free surface area [85], but also potential decreases in the concentration polarization effect caused by existing crystals that locally block or reduce permeation [101].

In contrast to the gypsum crystals, the mean calcium carbonate crystal sizes did not consistently follow a pattern. SEM images of Series I membrane coupons (Figure 6-8a,c) showed spherical vaterite as the dominant calcium carbonate polymorph. In comparison, Series II membrane coupons show varied polymorphs of different sizes (i.e., stages of crystal growth). Figure 6-14 shows a histogram of crystal sizes from Test 4, which exhibited a multimodal distribution for both upstream and downstream crystals.

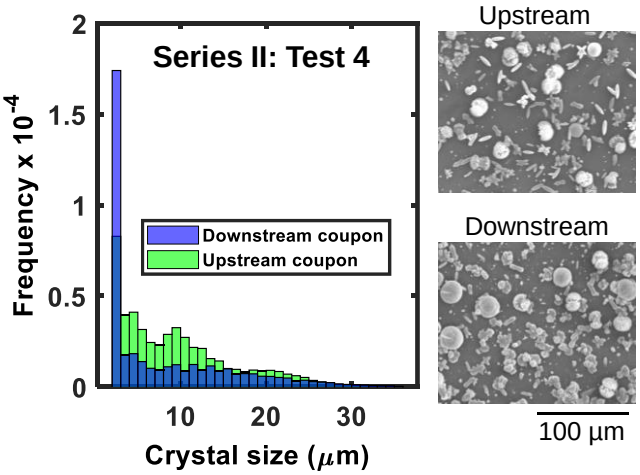


Figure 6-14. Test 4 exhibits a multimodal distribution for downstream and upstream calcium carbonate crystals.

A greater number of small crystals were observed downstream. The smallest bin range (2–3 μm) for the downstream crystals had a frequency nearly double that of the upstream crystals, explaining the slightly lower downstream mean crystal size of Test 4 (Figure 6-13). The general relationship between supersaturation level and crystal nucleation/growth indicates that nucleation is increasingly favored over crystal growth with increasing supersaturation [150]. This is consistent with the greater number of small crystals observed in the downstream SEM image, where supersaturation was higher at the membrane surface as compared to upstream locations.

#### **6.4.3.2** Membrane surface coverage and number density

Two-component detection results from Test 0 identified surface coverage as one of the main reasons for gypsum-only detection. Therefore, the surface coverage of the membrane by gypsum and calcium carbonate scale are shown for Tests 1–9 in Figure 6-15. Gypsum scale coverage was consistently greater downstream as compared to the upstream coupons (Figure 6-15a). In contrast, upstream surface coverage by calcium carbonate was generally greater than downstream coverage (Figure 6-15b).

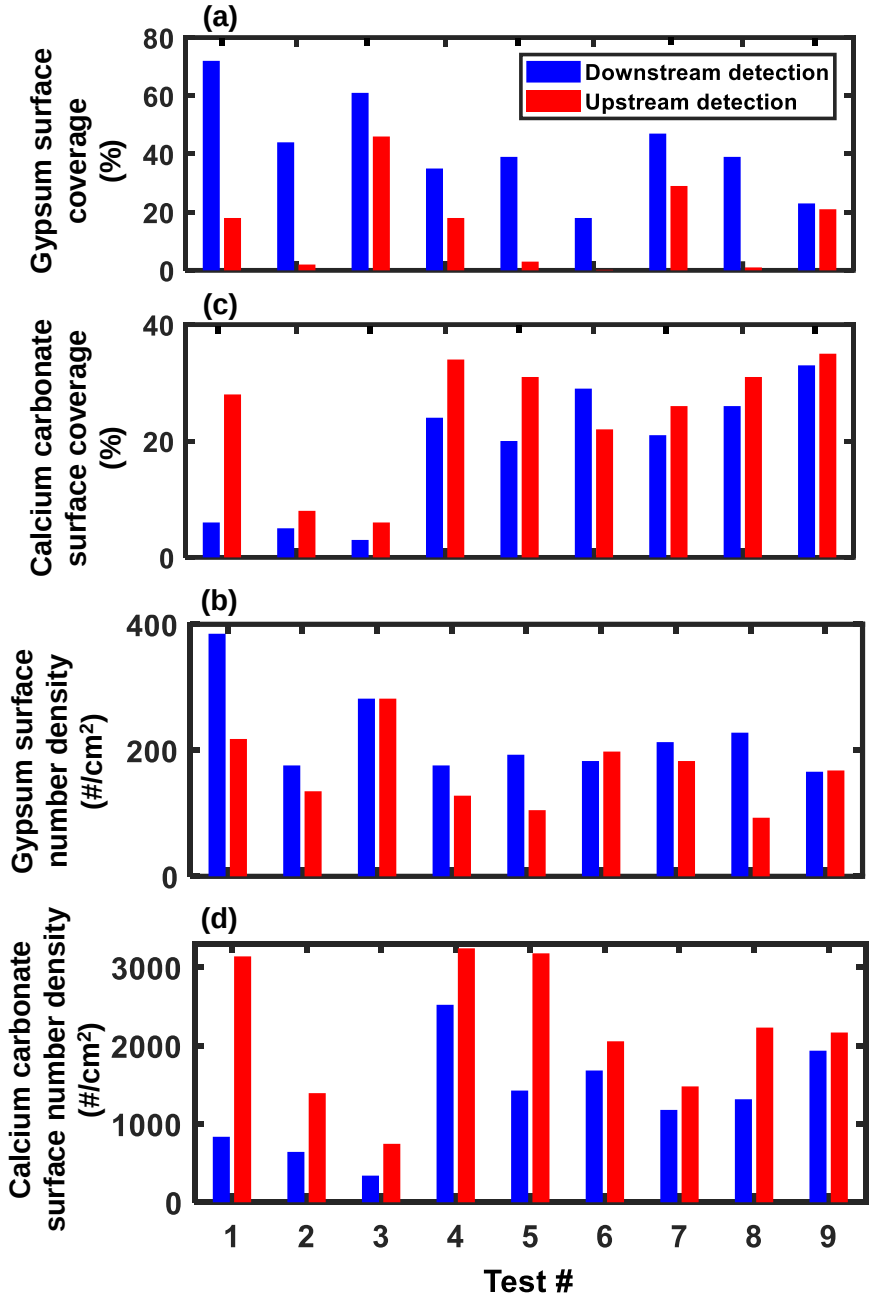


Figure 6-15. Upstream and downstream comparison of surface coverage (%) for (a) gypsum crystals and (b) calcium carbonate crystals; surface number density (#/cm$^2$) for (c) gypsum crystals and (d) calcium carbonate crystals.

Test 6 was the only exception in which downstream calcium carbonate surface coverage exceeded upstream coverage. Test 6 also had the least amount of downstream gypsum surface coverage. Upon closer inspection, it appeared that the order-of-magnitude larger, downstream gypsum crystals monopolized the

available scale-free membrane area for all of the tests except in Test 6. In the study of expanded multi-component membrane scaling/fouling, it will be important to identify which components are the most dominant in size.

In addition to membrane surface coverage, the crystal surface number density, termed crystal SND by Uchymiak et al. [88], was estimated for each membrane coupon. The crystal SND is defined as the number of scaling crystals per unit of membrane area (Figure 6-15c,d). For the gypsum crystals, downstream crystal SND exceeded upstream crystal SND values except for Tests 3, 6, and 9, in which downstream and upstream values were nearly equal. Once again, the opposite trend was observed for calcium carbonate crystal SND, in which upstream values exceeded downstream values. The available, scale-free, membrane surface area is an important factor in the estimation of both surface coverage and crystal SND. For surface area metrics such as average size and crystal SND, crystals that occupy a larger area will tend to dominate finite membrane surface areas, thus influencing the surface area metrics of the smaller crystals, and subsequently, their chances of real-time detection.

### 6.4.4 *Distribution of scaling crystals*

The false negative calcium carbonate detection result in Test 0 (Section 6.3.3.1) was thought to result from nonuniform gaps (spacing) between the scaling crystals. This is consistent with the post-mortem SEM images of the scaled membranes which showed high variability and nonuniformity in the crystal distribution patterns, not only within an imaged area, but also between membrane coupons of the same sample as well as coupons from different scaled membrane samples. This result is further supported from the work of Benecke et al. [148] who investigated the reproducibility of gypsum scaling in replicate experiments. Despite tight control of operating conditions between each replicate experiment, a variability in local membrane performance such as salt rejection and pure water permeability was cited as one of the reasons for highly variable results across replicate scaling experiments.

It is clear that the particular arrangement (uniformity vs nonuniformity) of these scale-free zones poses a challenge for any local measurement technique, including Raman sampling. Thus, it was

hypothesized that a more uniform distribution of scaling crystals would lower the probability of false negative detection because uniformity in scale deposition would minimize large expanses of scale-free voids. A literature review of heterogeneous scaling indicated that scale deposition nonuniformity was typically discussed in only a qualitative manner. Thus, a more quantitative methodology is necessary, not only in the development of the present Raman sensor, but for local measurement techniques in general. This section attempts to quantify the nonuniformity in scale deposition using Ripley's *K* Function, which is a statistical metric that predicts whether or not a spatial point pattern of interest is governed by a random process.

**6.4.4.1** Background on Ripley's K Function

The K Function is a useful tool with widespread applications in many fields such as geographic information systems [156], manufacturing processes [157], and cellular biology [158]. This statistical technique is also known as a second moment analysis because it describes the variance of the point pattern by quantifying the expected number of additional random points between two points separated by a distance *r*, given by [157]:

$$K(r) = \frac{\text{Exp[number of additional points within distance } r \text{ of a randomly selected point]}}{\lambda}, \qquad 6\text{-}1$$

where, λ is the intensity (or density) of points in a space of $r$ (radius). $K(r)$ is an interpoint distribution function with the behavior $K(r) \rightarrow \infty$ as $r \rightarrow \infty$. *K* Function values for completely random point patterns (known as complete spatial randomness) should approach the theoretical *K* Function resulting in $K_{theoretical}(r) \rightarrow \pi r^2$. Furthermore, $K(r) > \pi r^2$ describes a point pattern that shows statistically significant clustering while $K(r) < \pi r^2$ describes a more regular (uniform) distribution.

In practice, the calculated *K* Function for a point pattern of interest is accompanied by the theoretical *K* Function ($\pi r^2$) and a confidence interval. The purpose of the confidence interval is analogous to the error bars on a graph, but instead of the calculation of a mean and standard deviation, a user-specified number of randomly generated spatial point patterns serve as input parameters for the calculation of *n*

generated random spatial point patterns (permutations). Comparison of these three functions allows for conclusions based on statistical significance regarding a pattern's clustering or dispersion tendencies. For any subset of interpoint distances, *r*, if the calculated *K* Function falls outside the theoretical and permutation *K* Functions, statistically significant clustering and regularity (above and below the confidence interval, respectively).

A normalization of the *K* Function, known as the *H* Function has been used in the literature to determine the organization and size of cluster characteristics [159]. The *H* function is given by the following:

$$H(r) = \sqrt{K(r)/\pi} - r \qquad 6\text{-}2$$

Since the H Function is normalized to *r*, $H_{theoretical}(r) \rightarrow 0$, $H_{theoretical}(r) > 0$ indicates clustering (nonuniformity), and $H_{theoretical}(r) < 0$ indicates regularity (uniformity). The spatial point patterns of calcium sulfate and calcium carbonate were extracted from both downstream and upstream membrane coupons using Fiji. The *K* and *H* Functions were calculated for point patterns of calcium sulfate and calcium carbonate using an R package [160] and an isotropic correction was applied to the *K* Function to minimize the bias introduced by evaluating a finite spatial point pattern

**6.4.4.2** Results of gypsum point pattern analysis

A downstream and upstream gypsum spatial point pattern from Test 1 (Figure 6-16). Greater *H* Function values for the upstream point pattern are immediately evident, indicating a higher degree of clustering.

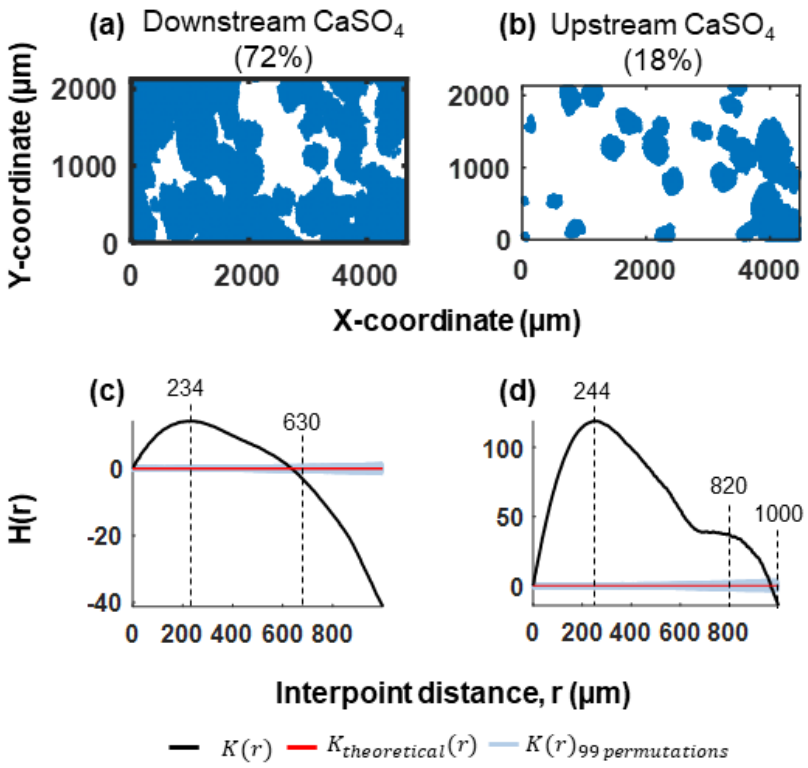


Figure 6-16. The spatial point pattern for (a) downstream and (b) upstream gypsum crystals from Test 1 were used to generate each pattern's H Function. (c) For the downstream gypsum point pattern, a cluster diameter of 234 µm is represented by the maxima and an x-intercept of 630 µm represents the distance between the clusters. (d) For the upstream point pattern, the two local maxima at 244 and 820 µm represent two different cluster diameters and a cluster distance of 1000 µm.

The interpoint distance for which a local maximum in the *H* function is observed, (e.g., $r$=234 and 580 µm in Figure 6-16c and $r$=244 and 820 µm in Figure 6-16d) represents a critical length-scale where the increasingly clustering behavior of the point pattern (i.e., an increase in the *H* values, away from uniform distribution) slows down and remains constant for a brief moment, before progressing down towards complete spatial randomness. This critical length-scale, in other words, could quantify the interpoint distances for which the greatest amount of aggregation occur in a point pattern. In the literature, Ripley's *K* Function (and its normalized forms, *H*, and *L* Functions) has been used to identify the domain or cluster size of proteins [158,159,161]. In this chapter, the domain size will be defined as the cluster diameter, $D_{cluster,gypsum}$.

Interestingly, from scaling crystal characterization, the mean crystal size of the downstream and upstream crystals was estimated to be 315±222 and 189±109 μm, respectively. Among the identified cluster diameters for downstream and upstream gypsum point patterns, the smaller cluster diameters ($D_{cluster,gypsum}$ = 234 and 244 μm, respectively) fall within the range of mean crystal size measured in this work. However, the larger cluster diameters ($D_{cluster,gypsum}$ = 580 and 820 μm, downstream and upstream, respectively) lie outside the range of estimated mean crystal size. This could occur because the cluster diameter includes the various crystal voids that constitute the cluster. In fact, in the protein domain size studies mentioned earlier, a commonly cited limitation was that the *K* Function protein domain analysis was susceptible to noise introduced by domain interactions and low point density inside the clusters. The gypsum point patterns did not appear to suffer from low point density when qualitatively compared to the reported protein point patterns. As for the noise limitation caused by domain interaction, this is undesirable for protein cluster studies given that the objective is to achieve accuracy in the measurement of a single cluster. However, for the purposes of the present work, this limitation may turn out to be a strength of the *K* Function.

Importantly, cluster diameter could be a more useful metric than mean crystal size or surface crystal number density when considering the selection of more optimal Raman sampling parameters. This is because the cluster diameter, $D_{cluster,}$ could allow for the treatment of a group of gypsum crystals as one entity, resulting in a sampling resolution that can be relaxed ($\Delta x > D_{cluster,gypsum}$), since one successful gypsum detection event suffices for early detection purposes (vs multiple gypsum detection events within a gypsum cluster). Furthermore, the ability to relax the sampling resolution could mitigate long sampling cycle times, which are inversely proportional to the sampling resolution ($\Delta L/\Delta x$). Thus, more areas could be sampled in the same time interval.

As a final remark on gypsum point patterns, the *H* values in Figure 6-16d and c are both observed to cross the *x*-axis towards increasingly negative values at *r*=630 and 1000 μm for downstream and upstream patterns, respectively. This indicates that the *x*-intercepts mark the transition from clustering to increasing uniformity in the point pattern. This can be understood from a statistics viewpoint, where a larger sample

size can decrease sampling error and increase the power of a statistical test. In a similar fashion, a larger interpoint distance, *r*, could increase the regularity in a point pattern and thereby decrease its irregularity. Therefore, it is hypothesized that the *x*-intercept of the *H* function may be an indicator of the intercluster distance, $L_{cluster,\ gypsum}$. In application, the intercluster distance could inform the selection of total sampled length ($\Delta L$), in which $\Delta L > L_{cluster,\ gypsum}$. Here, the goal would be to minimize sampling in locations that are absent of gypsum clusters (i.e., crystal voids).

**6.4.4.3** Results of calcium carbonate point pattern analysis

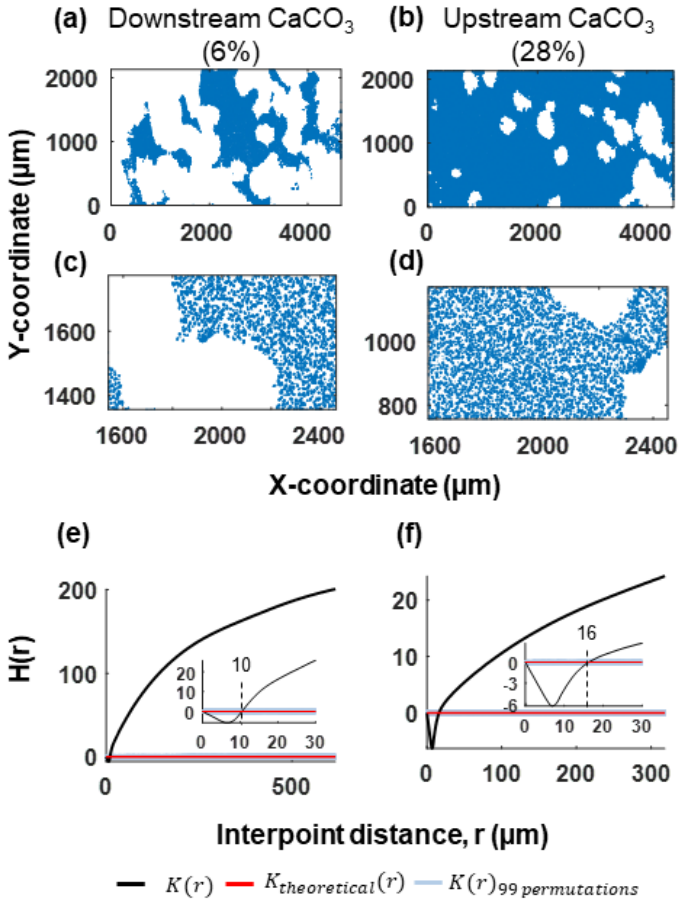


Figure 6-17. The spatial point pattern for (a, c) downstream and (b, d) upstream calcium carbonate crystals were used to generate each pattern's *H* Function. (e) The downstream point pattern exhibited uniformity at an interpoint distance of 0–10 µm. For >10 µm, a higher degree of nonuniformity, likely introduced by greater gypsum scale coverage, was observed compared to the (f) upstream point pattern. The transition from uniform to nonuniform distribution occurred around an interpoint distance of 16 µm.

For the calcium carbonate point patterns (Figure 6-17a-d), interpoint distances, $r$, from $0 < r < 10$ and $0 < r < 16$ μm for downstream and upstream point patterns, respectively, showed uniform distribution (Figure 6-17e, f). These ranges in $r$ values were similar to the estimated mean calcium carbonate crystal sizes (5–20 μm). For $r > \sim 20$, both downstream and upstream $H$ values increased significantly, showing clustering effects. This was an unexpected result, given that the calcium carbonate point patterns visually appeared more uniformly deposited than the gypsum crystals. However, closer examination of the SEM images of calcium carbonate crystals reveals that clusters of anywhere from 2 to 10 crystals can be identified. This result indicates that the use of a quantitative methodology may overcome potential biases in qualitative estimates of crystal distribution.

Overall, the downstream point pattern exhibits greater $H$ values (>100 compared to >20 upstream), perhaps due to greater surface coverage by gypsum scale. These results, although limited, suggest that the magnitude of the $H$ Function could be used to gauge the extent of calcium carbonate pattern 'interruption' by the more ubiquitous gypsum crystals, where greater $H$ values would imply greater interruption. In contrast to the sampling recommendations made for gypsum clusters ((i) $\Delta L > L_{cluster,gypsum}$ and (ii) $\Delta x > D_{cluster,gypsum}$), here, the more optimal sampling parameters could be to select $\Delta x < L_{cluster,gypsum}$ to ensure that the patches of calcium carbonate scale are not missed during Raman sampling.

## 6.5 Conclusions

This portion of the work focused on characterizing the Raman sensor's response to multi-component scaling during reverse osmosis desalination. Gypsum and calcium carbonate scale were both detected in real-time during bench-scale reverse osmosis desalination experiments. A Raman microscope's static (fixed-coordinate) objective was integrated with a bench-scale RO crossflow cell mounted on a movable stage to enable multi-point Raman sampling during desalination. Replicate scaling experiments were conducted and real-time Raman data and permeate flux were recorded as a standard metric of comparison. Although local monitoring techniques may provide higher sensitivity to early onset scaling compared to global metrics such as permeate flux, more localized measurements also run the risk of

providing false negative detection results due to unrepresentative sampling. Thus, the performance of different Raman sampling strategies was compared since representative, accurate scaling detection is a crucial aspect in the development of in-situ monitoring techniques.

A preliminary single-point sampling strategy resulted in gypsum-only detection, demonstrating that large crystals such as gypsum were more easily detected than smaller crystals such as calcium carbonate. The use of a laser beam spot size that was smaller than the present scaling crystal voids was also identified as the cause of false negative detection results. A manual, multi-point sampling strategy was subsequently employed to increase the chances of detecting both small and large scales. Successful detection of both scaling crystals occurred, but inconsistently, and at flux decline values of up to 24%. Thus, a final, more systematic approach was utilized in the final sampling approach, with an automated, multi-point sampling strategy. In these results, flux decline as low as 0.4% and 0.5% was observed at the time of gypsum and calcium carbonate Raman detection, respectively. This supported the Raman sensor's early detection capability and potential utility as a real-time decision-making tool during desalination plant operation.

Post-mortem scanning electron microscopy of scaled membrane coupons confirmed the presence of both types of scaling crystals, where the gypsum polymorph primarily featured a rosette structure consisting of rods and plates, and where calcium carbonate presented a more varied morphology depending on the polymorph. Gravimetric results demonstrated that the mass of deposited scales for two-component scaling followed the same behavior as that for single-component scaling, with greater mass per area on downstream coupons. Scaling crystal characteristics, such as average size, surface coverage, and surface number density were estimated, revealing that gypsum crystals were approximately an order of magnitude larger in diameter, assuming round crystal shapes. Downstream crystals were larger than upstream crystals for gypsum scale, but a less consistent trend was observed for calcium carbonate due to the variability in polymorphs and their corresponding shapes and size. Results also suggested that the surface coverage of the smaller scaling crystal was reduced due to the presence of the larger, dominant crystal, which in turn decreased chances of detection.

In addition to scaling crystal characteristics, the particular distribution pattern of the scaling crystals was suggested as an important parameter in an optimized Raman sampling strategy. A spatial point analysis was conducted on the SEM images of scaled membrane coupons from Test 1, showing that deposited gypsum crystals exhibited significant clustering on all length-scales. Calcium carbonate had tendency for statistically significant regularity (i.e., uniform distribution) of lengths ~10–15 μm but switched over to clustering at greater length-scales, likely due to interruption in their point pattern by the gypsum crystals. Two new crystallite metrics were suggested, the cluster diameter ($D_{cluster}$) and the intercluster distance ($L_{cluster}$), for consideration in a more optimized sampling strategy.

Since scale-control measures are sensitive to the chemical composition of the deposited scales, the ability to obtain real-time chemical information is critical for optimal timing and dosing of antiscaling/cleaning agents. Overall, the presented methodology for real-time chemical sensing using Raman spectroscopy is an important step in the optimization of scale control techniques as well as early detection of membrane scaling during filtration of complex feed waters.

### 6.5.1 *Future directions based on Series II results*

**Maintaining laser focus throughout multi-point sampling**: For calcium carbonate, the Raman detection time in Test 4 was an outlier for calcium carbonate detection, possibly due to a high detection threshold value caused by significant fluctuations in the baseline calcium carbonate Raman signal during compaction. These fluctuations were likely due to poor focusing throughout the automated sampling cycle. Figure 6-18a shows raw Raman data from sequentially sampled points during membrane compaction of Test 4. The raw Raman spectrum from $x$ = 59.0 mm has the lowest background signal (~3000 a.u.) and the spectrum from $x$ = 63.5 mm was the noisiest spectrum with the highest background signal (~5800 a.u.).

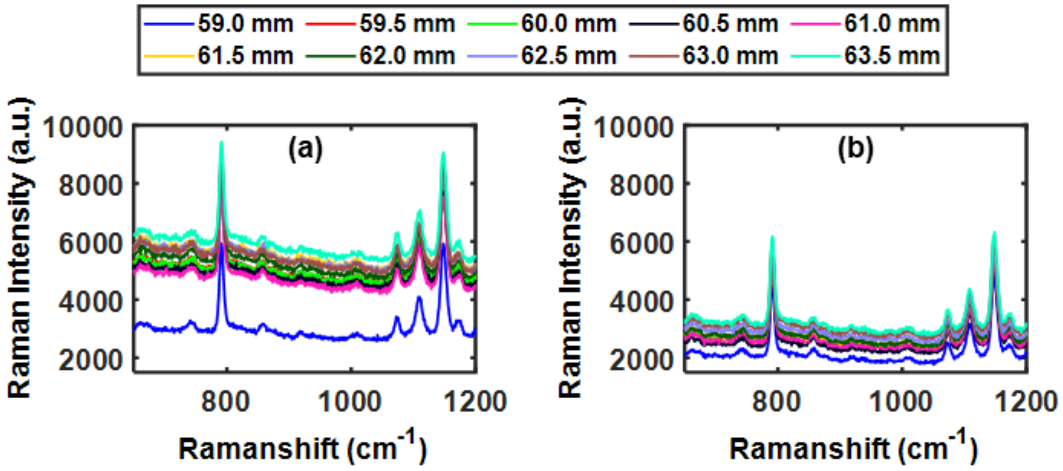


Figure 6-18. Raw Raman spectra (no baseline removal) from downstream axial positions at (a) 7 min acquisition and (b) 1 h since the start of Raman acquisition.

Over time, the difference in background signal between sampled points is nearly halved, but still evident (Figure 6-18a). This decrease in the background signal could have been caused by photobleaching [162,163] which has been reported for polymeric materials [164]. The most dramatic effects of possible photobleaching subsided within ~1 h, yet the persisting difference in background signals suggests that the laser focus varied nontrivially between sampled points. For membrane scaling detection, laser beam defocus can reduce the signal-to-noise (SNR) ratio of the scalant Raman bands. Generally, for larger crystalline species such as gypsum, the gypsum Raman signal is still strong enough to be detected despite a dominant membrane Raman signal and reduced SNR. However, detection of smaller crystalline species like calcium carbonate could become more difficult to confirm, resulting in late detection such as the upstream calcium carbonate detection result in Test 4. Techniques for filtering defocused light should be investigated to overcome this limitation.

**Repeatability of laser beam position**: Previous work in Chapter 5 showed the potential use of the Raman sensor in studies of scaling kinetics. To study the time evolution of the scalant Raman signals in the present work, the laser beam would need to be at the same exact location over the many sampling cycles. If the laser beam position drifted even the slightest distance, the relative Raman peak intensity would be

affected because the contents/degree of the Raman volume interaction would change. To illustrate a possible risk, a decrease in the Raman signal may be misinterpreted as crystal dissolution, when in fact it was simply caused by a gradual drift in the position of the flow cell, away from the detected crystal.

Since the present work was focused on establishing a proof-of-concept for real-time, two-component Raman detection, repeatability of detection site positioning was not considered a critical factor. Still, this function is important in better understanding the kinetics of membrane scaling, especially of natural feed waters that contain many scaling/fouling components. According to the motorized stage manufacturer specifications, spatial repeatability was <3 µm which is considered significant with respect to the length-scale of incipient scaling crystals. The repeatability of laser beam positioning (i.e., motorized-stage positioning) was investigated by comparing the raw Raman spectra obtained over time at the same axial position during membrane compaction (Figure 6-19). If there were any spatial drift occurring over time at a given location, the raw Raman data could reveal spectral differences such as the changes in background signal observed in Figure 6-18. Figure 6-19 shows the raw Raman spectra at the axial position, $x$ = 59.5 mm, after being repositioned every 7 min for ~35 min.

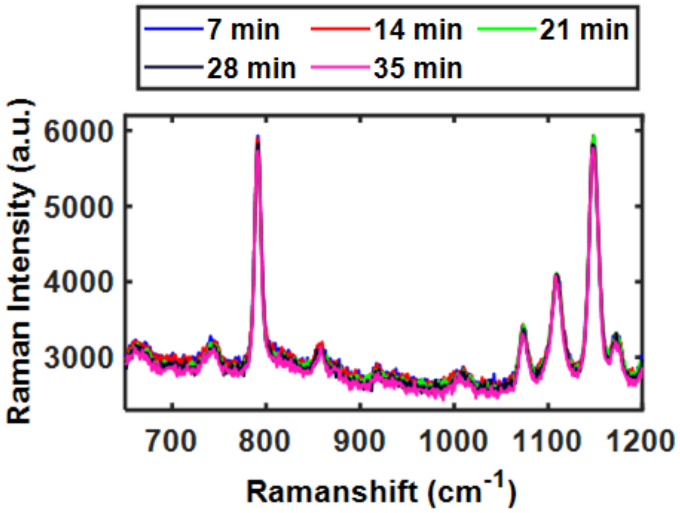


Figure 6-19. Raw Raman spectra (no baseline removal) from $x$ = 59.5 mm at different time stamps to examine the repeatability of the motorized stage position.

The observed intensity shifts are relatively low (<200 a.u.), indicating reasonable performance in position repeatability. Nevertheless, any investigation of scaling kinetics requires a different microscope design that allows for simultaneous, multi-point sampling (e.g., using a fiber optic bundle) instead of sequential, multi-point sampling, and a second real-time measurement such as visual imaging to validate the Raman data.

# Chapter 7 Conclusions and Future Directions

Chapter 2 presented a critical review of the literature surrounding in-situ monitoring techniques in membrane-based desalination processes. The current chapter aims to locate where the present dissertation work stands in the existing body of work by providing a summary and interpretation of results.

Membrane performance is commonly monitored using global metrics such as permeate flux and salt rejection. These metrics represent the overall membrane module's scaling conditions, so they lack the spatial resolution required to detect scaling in its early stages. Therefore, local or in-situ monitoring techniques could provide improved resolution for detection of scaling onset.

Additionally, these techniques could serve important roles beyond early detection during plant operation—particularly, in membrane scaling research (e.g., research and development of scaling mitigation and control techniques). The literature review of in-situ monitoring techniques presented in Section **Error! Reference source not found.** revealed an absence of real-time chemical identification capability. Without real-time chemical sensing, the research is often limited to the use of simplified feeds. Due to component interactions in complex feed waters [105,113,129], the scaling behavior of a single salt may change in the presence of other scalants, and as a result, scaling scale-control techniques developed using simple feed compositions may transfer poorly to full-scale applications. Indeed, in-situ monitoring techniques are useful for their ability to assess *if* scaling is present and *when* onset occurs but given that scaling control and mitigation techniques are highly chemistry specific, they should also identify the chemical composition of the deposited scales.

Hence, a Raman-based methodology was developed for early detection and monitoring scaling of reverse osmosis membranes. The developed methodology provided real-time chemical sensing of membrane scaling in a bench-scale RO crossflow cell and sensor performance was evaluated by comparisons to permeate flux, a commonly utilized indicator of membrane scaling. Attributed to the lack

of real-time chemical sensing capability, the majority of the fouling studies have been limited to scaling of a single scaling species/component. Thus, a more in-depth understanding of scaling mechanisms involving multiple species/components has been unavailable. As it is commonplace for multiple components to foul the membrane simultaneously [12], the specific aim of the dissertation work was to demonstrate both single-component and multiple-component scaling detection using the developed Raman sensor.

## 7.1 Summary of Findings and Conclusions

This section summarizes each chapter's main findings and provides conclusions based on the findings and research questions/sub-questions posed in Section 1.2.3.

### 7.1.1 *Raman detection of single-component scaling*

#### **7.1.1.1** Detection of scale deposition and removal

Chapter 4 aimed to characterize and compare the Raman and permeate flux response to membrane scaling/removal. A $CaSO_4$ solution as the model feed and deionized water was the representative cleaning agent. Results of Raman scaling detection showed generally low values of flux decline relative to the 50% increase in the $CaSO_4$ Raman peak intensity. In response to the introduction of deionized water cleaning agent, the $CaSO_4$ Raman peak intensity systematically decreased (**RQ 4**) and returned to its initial baseline values more quickly than the recovery of the permeate flux, illustrating the utility of the Raman sensor during membrane cleaning when timely feedback is needed to confirm cleaning progress. The real-time data were supported by microscopic, x-ray, and gravimetric post-mortem characterizations. Additionally, a larger-area Raman scan (**RQ 6**) of the post-mortem scaled/cleaned membrane samples elucidated the relationship between sampling area and Raman detection representativeness, where increasing the sampling area beyond ~2 $mm^2$ resulted in marginal improvements in Raman detection. This suggested that there was an optimal minimal sampling area that could still provide representative information about the state of cleaning on the RO membrane. Overall, it was found that a significant advantage of Raman spectroscopy is the technique's ability to provide spatial (local) and chemical information regarding scale formation and removal (**RQ 3**).

The real-time, local, chemical sensing attributes of the Raman sensor are particularly important in full-scale cleaning procedures. Presently, membrane autopsies are commonly performed to learn more information the scaling/fouling layer, including the composition of the deposited scalants/foulants, their location, and severity [19,165]. However, membrane autopsy is a destructive process that only shows the module conditions from a single point in time, so assessing the temporal progression of cleaning procedures poses a significant challenge. As for chemical compositional analysis, energy-dispersive x-ray spectroscopy (EDS) is a chemical analysis technique commonly used to obtain elemental composition information of the deposited scalants/foulants on the membrane module. However, the fouling layers are often amorphous sludge-like layers and identification of the foulants is often based on the elements that are most prominent in the EDS data. This can result in the dismissal of relatively trace amounts of elements that may have been instrumental in the overall fouling progression on the RO membrane. The simple gypsum deposition and removal experiments conducted in this chapter can be applied to confirm or expose the assumptions that are commonly made regarding membrane scaling/fouling, due to a lack of real-time sensing capability.

#### **7.1.1.2** Time evolution of membrane scaling

Chapter 5aimed to evaluate the time evolution of the calcite Raman signal as a potential metric for chemical comparison of local scaling progression within (as a function of axial position) and across different membrane samples (**RQ 4**). Real-time permeate flux and Raman data were recorded at a downstream and upstream location, in series. A time evolution of the calcite Raman signal was represented by a simple rate of change, i.e., systematic increases, of the calcite Raman signal over time. Generally, the rate of change, or slope, of the calcite Raman signal increased with increasing local saturation indices at the membrane wall, and the slope of the calcite Raman signal during downstream detection consistently exceeded that of upstream detection, suggesting faster scaling progression downstream due to greater supersaturation levels (**RQ 5**). In addition to the time evolution of the calcite Raman signal, the time evolution of the *RO membrane's* Raman signal suggested that the steady increase in the calcite Raman signal was caused by actual calcite volumetric growth, slow enough to leave the Raman signal of the

interrogated substrate undisturbed. Post-mortem imaging of the calcite crystals further supported this finding. Matching the characteristic lengths of the Raman sampling area and crystallite was additionally identified as an important aspect of the time evolution studies, explaining why the present microscope design, with a ~3 μm beam spot size, was unsuitable for studies of gypsum scaling progression, whose crystals are at least an order-of-magnitude larger. Post-mortem gravimetric analysis agreed with the observed real-time Raman behavior, indicating that the Raman-based technique successfully responded to progression of calcium carbonate membrane scaling. In-vitro Raman detection of the vaterite and calcite polymorph showed that real-time detection of calcium carbonate polymorphs was possible if the signal-to-noise ratios of the lattice-mode Raman bands can be improved. This capability would be an important asset in the direct observation of scaling progression.

Similar calcium carbonate scaling studies have utilized methods such as characterization of the feed solution ($Ca^{2+}$ concentration, pH, turbidity) [34,39] and post-mortem SEM imaging [32,34] to draw conclusions about incipient scaling and scaling rates. However, feed characterization does not provide information regarding the location of scalant deposition, which is crucial information for foulants that form nonuniformly, such as inorganic scales. Furthermore, though post-mortem SEM images can provide the spatial resolution necessary to study small incipient calcium carbonate crystals, it is difficult to implement in real-time due to the required high vacuum environment and relatively higher costs. Other real-time visualization methods have been demonstrated using high-resolution cameras and strategic lighting, however, the majority of the studies are dedicated to calcium sulfate scaling due to the larger, therefore more easily detectable, gypsum crystals. Due to these challenges, real-time observation techniques are not as readily available for calcium carbonate. The Raman sensor offered both the high spatial resolution necessary to detect smaller crystals (20─50 μm) and chemical sensing for real-time detection of calcium carbonate scaling on RO membranes (**RQ 3)**.

Overall, the demonstrated ability to study high spatial resolution, single-component scaling progression with crucial chemical identification is an important step for understanding how for developing

Raman methodology for detection of multi-component scaling progression. The use of the Raman-based detection methodology in expanded time evolution studies of multi-component feeds could be used to develop more effective scale mitigation strategies, improvement of predictive scaling models, and overall optimization of RO processes.

### 7.1.2 *Raman detection of multi-component scaling*

Chapter 6 aimed to demonstrate real-time Raman detection of two-component scaling using calcium sulfate and calcium carbonate as model scalants (components) (**RQ 2**). With a single-point Raman sampling strategy, only the Raman peak for $CaSO_4$ was consistently detected even though SEM images and energy dispersive X-ray spectroscopy confirmed both $CaSO_4$ and $CaCO_3$ scaling on the membrane. This limitation of a point detection system can be overcome by expanding the area of Raman detection.

Raman spectroscopy was used to detect both gypsum and calcium carbonate scale in real-time during bench-scale reverse osmosis desalination experiments. Raman detection times were compared between downstream and upstream locations (**RQ 5**), and to concurrent values of flux decline, suggesting early detection capability. Although local monitoring techniques may provide higher sensitivity to early onset scaling compared to global metrics such as permeate flux, more localized measurements run the risk of providing false negative detection results due to unrepresentative sampling. The general dimensions of the two scaling components and the Raman laser beam spot size were identified as important considerations in the selection of Raman sampling parameter that would enable more representative, accurate detection. Moreover, statistical tests (Ripley's *K* Function) conducted on the distribution of the scaling crystals revealed the cluster diameter and intercluster distance of gypsum crystals could be characterized. This could be a more useful metric than the mean crystal size and surface crystal number density in the selection of more optimal Raman sampling parameters. Two new crystal characteristics were extracted from the *K* Function analysis of gypsum and calcium carbonate crystal point patterns: the cluster diameter of gypsum, $D_{cluster,gypsum}$, and the intercluster distance of gypsum, $L_{cluster,gypsum.}$ From these additional crystal

characteristics, some recommendations/observations were provided in the context of a more optimized Raman sampling strategy.

For gypsum Raman detection:

(i) $\Delta x > D_{cluster,gypsum}$

The sampling resolution can be relaxed, or increased, since one successful gypsum detection event is sufficient for early detection purposes.

(ii) $\Delta L > L_{cluster,gypsum}$

Selecting a total sampled length ($\Delta L$) that is greater than gypsum's intercluster distance could minimize sampling in crystal voids (i.e., false negative Raman detection).

For calcium carbonate Raman detection:

(i) $\Delta x < L_{cluster,gypsum}$

Due to the greater degree of calcium carbonate scaling 'interruption' by the more dominant gypsum scaling crystals, a shorter sampling resolution could ensure that patches of calcium carbonate scale are not overlooked during real-time detection.

The two Raman sampling parameters discussed in detail were the total sampled length ($\Delta L$) and sampling resolution ($\Delta x$). However, there are other sampling parameters that can be adjusted. Two potential methods of increasing the sampling area without introducing any moving parts (e.g., motorized stage) could be increasing the beam spot size by changing the magnification of the microscope objective or the use of a multi-core optical fiber that would effectively split a multimode laser beam into a circular or linear pattern that spans a greater detection area. A more sophisticated version of the automated sampling strategy (which provided a sequential line scan) would be to incorporate laser scanning microscopy and cover a two-dimensional sampling area. Nevertheless, independent from the particular choice of Raman instrumentation and microscope design, the two new crystallite metrics that were defined in this section, the cluster diameter

($D_{cluster}$) and the intercluster distance ($L_{cluster}$), could be characterized for other problematic scaling components in seawater and brackish water, allowing for expanded application of the technique.

In RO desalination, natural feed waters contain numerous fouling components that interact with one another. Residual pretreatment chemicals, antiscalants, and cleaning chemicals can add further complexity to the system, making it difficult to optimize remediation measures. Scale-control techniques are highly sensitive to the chemical composition of the deposited scales, which dictates the optimal timing and dosing of antiscaling/cleaning agents. Therefore, real-time chemical sensing is a crucial aspect of in-situ monitoring since incorrect selection and delivery of these chemical agents can exacerbate membrane scaling. In this chapter, by incorporating a multi-point sampling strategy during real-time Raman detection of membrane scaling, the sensor was able to cover a larger area that was still localized and able to provide a sensitive response to membrane scaling compared to permeate flux decline. Therefore, this works serves as an important step in the optimization of scale control techniques in RO desalination. The scaling detection results achieved using the simplest form of Raman spectroscopy (i.e., spontaneous Raman) demonstrated the potential for the work to be technologically adopted in fields of both research and industry.

## 7.2 Future Directions

The ultimate goal of the presented work will be to test the developed Raman sensor on natural or artificial seawater or brackish water feed solutions. This requires continued optimization of the Raman sampling strategy. Two new metrics that could describe scaling crystal characteristics were suggested in Chapter 6: the cluster diameter and intercluster distance of scaling crystals. It was hypothesized that these additional metrics could inform a better selection of a total sampled length (or an area), and sampling resolution. Thus, the next step would be to test the recommended parameters in a series of two-component of multi-component feed solutions. This would require further literature review on which relevant scalants/foulants have active Raman cross sections as well as upgrades to the present Raman microscope setup, such as two-dimensional scanning or the use of multi-core optical fiber/multimode laser source. Additionally, characterization of the feed water such as turbidity, pH, and calcium ion/divalent ion

measurements could provide further critical insight that would serve to validate the Raman data or suggest areas of improvement.

Furthermore, the completed work comprised the early stages of the Raman sensor development for scaling detection on reverse osmosis membranes. Thus, the design of the experiments were focused on necessary, but simplified, bench-scale demonstrations of real-time Raman detection of membrane scaling that illustrated the potential impact of the technique on a larger scale. Therefore, the next step is to focus on mechanistic scaling/fouling detection investigations that would more directly translate to improvements in scale control and overall desalination plant maintenance and operation. An important characteristic of mechanistic investigations is a factorial design of experiment with replication. Due to the stochastic nature of membrane scaling, replication is a critical part of determining real effects from experimental variability. However, a factorial design of experiment could result in an unreasonably high number of experiments. Thus, in the design of more mechanistic multi-component scaling/fouling studies, it is recommended that initial sensitivity tests are conducted to identify the most important or influential operating conditions and feed compositions.

# References


[1] Christiano, A., and Neimand, A., 2018, "The Science of What Makes People Care," Stanford Social Innovation Review, **16**(4), pp. 26–33.

[2] Lee, Y.-G., Kim, S., Shin, J., Rho, H., Lee, Y., Kim, Y. M., Park, Y., Oh, S.-E., Cho, J., and Chon, K., 2020, "Fouling Behavior of Marine Organic Matter in Reverse Osmosis Membranes of a Real-Scale Seawater Desalination Plant in South Korea," Desalination, **485**, p. 114305.

[3] Fritzmann, C., Löwenberg, J., Wintgens, T., and Melin, T., 2007, "State-of-the-Art of Reverse Osmosis Desalination," Desalination, **216**(1–3), pp. 1–76.

[4] Song, Y., Gao, X., and Gao, C., 2013, "Evaluation of Scaling Potential in a Pilot-Scale NF–SWRO Integrated Seawater Desalination System," Journal of Membrane Science, **443**, pp. 201–209.

[5] Oh, H.-J., Choung, Y.-K., Lee, S., Choi, J.-S., Hwang, T.-M., and Kim, J. H., 2009, "Scale Formation in Reverse Osmosis Desalination: Model Development," DESALINATION, **238**(1–3), pp. 333–346.

[6] Rahardianto, A., Shih, W.-Y., Lee, R.-W., and Cohen, Y., 2006, "Diagnostic Characterization of Gypsum Scale Formation and Control in RO Membrane Desalination of Brackish Water," Journal of Membrane Science, **279**(1), pp. 655–668.

[7] Goh, P. S., Lau, W. J., Othman, M. H. D., and Ismail, A. F., 2018, "Membrane Fouling in Desalination and Its Mitigation Strategies," Desalination, **425**, pp. 130–155.

[8] Chen, J. C., Li, Q., and Elimelech, M., 2004, "In Situ Monitoring Techniques for Concentration Polarization and Fouling Phenomena in Membrane Filtration," Advances in Colloid and Interface Science, **107**(2), pp. 83–108.

[9] Sim, L. N., Chong, T. H., Taheri, A. H., Sim, S. T. V., Lai, L., Krantz, W. B., and Fane, A. G., 2018, "A Review of Fouling Indices and Monitoring Techniques for Reverse Osmosis," Desalination, **434**, pp. 169–188.

[10] Li, J., Hallbauer, D. K., and Sanderson, R. D., 2003, "Direct Monitoring of Membrane Fouling and Cleaning during Ultrafiltration Using a Non-Invasive Ultrasonic Technique," Journal of Membrane Science, **215**(1), pp. 33–52.

[11] Hu, Z., Antony, A., Leslie, G., and Le-Clech, P., 2014, "Real-Time Monitoring of Scale Formation in Reverse Osmosis Using Electrical Impedance Spectroscopy," Journal of Membrane Science, **453**, pp. 320–327.

[12] Matin, A., Rahman, F., Shafi, H. Z., and Zubair, S. M., 2019, "Scaling of Reverse Osmosis Membranes Used in Water Desalination: Phenomena, Impact, and Control; Future Directions," Desalination, **455**, pp. 135–157.

[13] Osada, Y., and Nakagawa, T., 2014, *Membrane Science and Technology*, CRC Press, Boca Raton.

[14] Baten, R., and Stummeyer, K., 2013, "How Sustainable Can Desalination Be?," Desalination and Water Treatment, **51**(1–3), pp. 44–52.

[15] Boerlage, S., 2012, "Research Measuring Seawater and Brine Salinity in Seawater Reverse Osmosis."

[16] Greenlee, L. F., Lawler, D. F., Freeman, B. D., Marrot, B., and Moulin, P., 2009, "Reverse Osmosis Desalination: Water Sources, Technology, and Today's Challenges," Water Research, **43**(9), pp. 2317–2348.

[17] Boerlage, S. F. E., 2012, "Measuring Salinity and TDS of Seawater and Brine for Process and Environmental Monitoring—Which One, When?," Desalination and Water Treatment, **42**(1–3), pp. 222–230.

[18] Koo, C. H., Mohammad, A. W., Suja', F., and Meor Talib, M. Z., 2012, "Review of the Effect of Selected Physicochemical Factors on Membrane Fouling Propensity Based on Fouling Indices," Desalination, **287**, pp. 167–177.

[19] Jiang, S., Li, Y., and Ladewig, B. P., 2017, "A Review of Reverse Osmosis Membrane Fouling and Control Strategies," Science of The Total Environment, **595**, pp. 567–583.

[20] Prieto-Taboada, N., Gómez-Laserna, O., Martínez-Arkarazo, I., Olazabal, M. Á., and Madariaga, J. M., 2014, "Raman Spectra of the Different Phases in the CaSO4–H2O System," Anal. Chem., **86**(20), pp. 10131–10137.

[21] Carteret, C., Dandeu, A., Moussaoui, S., Muhr, H., Humbert, B., and Plasari, E., 2009, "Polymorphism Studied by Lattice Phonon Raman Spectroscopy and Statistical Mixture Analysis Method. Application to Calcium Carbonate Polymorphs during Batch Crystallization," Crystal Growth & Design, **9**(2), pp. 807–812.

[22] Shih, W.-Y., Rahardianto, A., Lee, R.-W., and Cohen, Y., 2005, "Morphometric Characterization of Calcium Sulfate Dihydrate (Gypsum) Scale on Reverse Osmosis Membranes," Journal of Membrane Science, **252**(1–2), pp. 253–263.

[23] Lee, S., 2000, "Effect of Operating Conditions on CaSO4 Scale Formation Mechanism in Nanofiltration for Water Softening," Water Research, **34**(15), pp. 3854–3866.

[24] Antony, A., Low, J. H., Gray, S., Childress, A. E., Le-Clech, P., and Leslie, G., 2011, "Scale Formation and Control in High Pressure Membrane Water Treatment Systems: A Review," Journal of Membrane Science, **383**(1–2), pp. 1–16.

[25] Van Driessche, A. E. S., Stawski, T. M., Benning, L. G., and Kellermeier, M., 2017, "Calcium Sulfate Precipitation Throughout Its Phase Diagram," *New Perspectives on Mineral Nucleation and Growth: From Solution Precursors to Solid Materials*, A.E.S. Van Driessche, M. Kellermeier, L.G. Benning, and D. Gebauer, eds., Springer International Publishing, Cham, pp. 227–256.

[26] Gilron, J., and Hasson, D., "MEMBRANES: FLUX DECLINE MECHANISM," p. 10.

[27] Brian, P. L. T., 1965, "Concentration Polar Zation in Reverse Osmosis Desalination with Variable Flux and Incomplete Salt Rejection," Ind. Eng. Chem. Fund., **4**(4), pp. 439–445.

[28] Zhang, Z., Bright, V. M., and Greenberg, A. R., 2006, "Use of Capacitive Microsensors and Ultrasonic Time-Domain Reflectometry for in-Situ Quantification of Concentration Polarization and Membrane Fouling in Pressure-Driven Membrane Filtration," Sensors and Actuators B: Chemical, **117**(2), pp. 323–331.

[29] Nam, J.-W., Park, J.-Y., Kim, J.-H., Kwon, S., Chon, K., Lee, E.-J., Kim, H.-S., and Jang, A., 2014, "The Evaluation on Concentration Polarization for Effective Monitoring of Membrane Fouling in Seawater Reverse Osmosis Membrane System," Journal of Industrial and Engineering Chemistry, **20**(4), pp. 2354–2358.

[30] Shih, W.-Y., Rahardianto, A., Lee, R.-W., and Cohen, Y., 2005, "Morphometric Characterization of Calcium Sulfate Dihydrate (Gypsum) Scale on Reverse Osmosis Membranes," Journal of Membrane Science, **252**(1–2), pp. 253–263.

[31] Benecke, J., 2018, "Gypsum scaling during reverse osmosis desalination − characterization and effects of natural organic matter," TUHH Universitätsbibliothek.

[32] Uchymiak, M., Bartman, A. R., Daltrophe, N., Weissman, M., Gilron, J., Christofides, P. D., Kaiser, W. J., and Cohen, Y., 2009, "Brackish Water Reverse Osmosis (BWRO) Operation in Feed Flow Reversal Mode Using an Ex Situ Scale Observation Detector (EXSOD)," Journal of Membrane Science, **341**(1–2), pp. 60–66.

[33] Lu, X., Kujundzic, E., Mizrahi, G., Wang, J., Cobry, K., Peterson, M., Gilron, J., and Greenberg, A. R., 2012, "Ultrasonic Sensor Control of Flow Reversal in RO Desalination—Part 1: Mitigation of Calcium Sulfate Scaling," Journal of Membrane Science, **419–420**, pp. 20–32.

[34] Mizrahi, G., Wong, K., Lu, X., Kujundzic, E., Greenberg, A. R., and Gilron, J., 2012, "Ultrasonic Sensor Control of Flow Reversal in RO Desalination. Part 2: Mitigation of Calcium Carbonate Scaling," Journal of Membrane Science, **419–420**, pp. 9–19.

[35] Gu, H., Bartman, A. R., Uchymiak, M., Christofides, P. D., and Cohen, Y., 2013, "Self-Adaptive Feed Flow Reversal Operation of Reverse Osmosis Desalination," Desalination, **308**, pp. 63–72.

[36] McCool, B. C., Rahardianto, A., and Cohen, Y., 2012, "Antiscalant Removal in Accelerated Desupersaturation of RO Concentrate via Chemically-Enhanced Seeded Precipitation (CESP)," Water Research, **46**(13), pp. 4261–4271.

[37] Fane, T., 2015, "Inorganic Scaling," *Encyclopedia of Membranes*, E. Drioli, and L. Giorno, eds., Springer Berlin Heidelberg, Berlin, Heidelberg, pp. 1–2.

[38] Tay, K. G., and Song, L., 2005, "A More Effective Method for Fouling Characterization in a Full-Scale Reverse Osmosis Process," Desalination, **177**(1), pp. 95–107.

[39] Uchymiak, M., Rahardianto, A., Lyster, E., Glater, J., and Cohen, Y., 2007, "A Novel RO Ex Situ Scale Observation Detector (EXSOD) for Mineral Scale Characterization and Early Detection," Journal of Membrane Science, **291**(1–2), pp. 86–95.

[40] Benecke, J., Haas, M., Baur, F., and Ernst, M., 2018, "Investigating the Development and Reproducibility of Heterogeneous Gypsum Scaling on Reverse Osmosis Membranes Using Real-Time Membrane Surface Imaging," Desalination, **428**, pp. 161–171.

[41] Sarker, N. R., and Bilton, A. M., 2021, "Real-Time Computational Imaging of Reverse Osmosis Membrane Scaling under Intermittent Operation," Journal of Membrane Science, **636**, p. 119556.

[42] Mairal, A. P., Greenberg, A. R., Krantz, W. B., and Bond, L. J., 1999, "Real-Time Measurement of Inorganic Fouling of RO Desalination Membranes Using Ultrasonic Time-Domain Re¯ectometry," Journal of Membrane Science, p. 12.

[43] Mairal, A. P., Greenberg, A. R., and Krantz, W. B., 2000, "Investigation of Membrane Fouling and Cleaning Using Ultrasonic Time-Domain Reflectometry," Desalination, **130**(1), pp. 45–60.

[44] Sanderson, R., Li, J., Koen, L. J., and Lorenzen, L., 2002, "Ultrasonic Time-Domain Reflectometry as a Non-Destructive Instrumental Visualization Technique to Monitor Inorganic Fouling and Cleaning on Reverse Osmosis Membranes," Journal of Membrane Science, **207**(1), pp. 105–117.

[45] Cobry, K. D., Yuan, Z., Gilron, J., Bright, V. M., Krantz, W. B., and Greenberg, A. R., 2011, "Comprehensive Experimental Studies of Early-Stage Membrane Scaling during Nanofiltration," Desalination, **283**, pp. 40–51.

[46] Kavanagh, J. M., Hussain, S., Chilcott, T. C., and Coster, H. G. L., 2009, "Fouling of Reverse Osmosis Membranes Using Electrical Impedance Spectroscopy: Measurements and Simulations," Desalination, **236**(1), pp. 187–193.

[47] Antony, A., Chilcott, T., Coster, H., and Leslie, G., 2013, "In Situ Structural and Functional Characterization of Reverse Osmosis Membranes Using Electrical Impedance Spectroscopy," Journal of Membrane Science, **425–426**, pp. 89–97.

[48] Sim, L. N., Gu, J., Coster, H. G. L., and Fane, A. G., 2016, "Quantitative Determination of the Electrical Properties of RO Membranes during Fouling and Cleaning Processes Using Electrical Impedance Spectroscopy," Desalination, **379**, pp. 126–136.

[49] Coster, H. G. L., Kim, K. J., Dahlan, K., Smith, J. R., and Fell, C. J. D., 1992, "Characterisation of Ultrafiltration Membranes by Impedance Spectroscopy. I. Determination of the Separate Electrical Parameters and Porosity of the Skin and Sublayers," Journal of Membrane Science, **66**(1), pp. 19–26.

[50] Park, J.-S., Chilcott, T. C., Coster, H. G. L., and Moon, S.-H., 2005, "Characterization of BSA-Fouling of Ion-Exchange Membrane Systems Using a Subtraction Technique for Lumped Data," Journal of Membrane Science, **246**(2), pp. 137–144.

[51] Kögler, M., Zhang, B., Cui, L., Shi, Y., Yliperttula, M., Laaksonen, T., Viitala, T., and Zhang, K., 2016, "Real-Time Raman Based Approach for Identification of Biofouling," Sensors and Actuators B: Chemical, **230**, pp. 411–421.

[52] Virtanen, T., Reinikainen, S.-P., Kögler, M., Mänttäri, M., Viitala, T., and Kallioinen, M., 2017, "Real-Time Fouling Monitoring with Raman Spectroscopy," Journal of Membrane Science, **525**, pp. 312–319.

[53] Supekar, O. D., Brown, J. J., Greenberg, A. R., Gopinath, J. T., and Bright, V. M., 2018, "Real-Time Detection of Reverse-Osmosis Membrane Scaling via Raman Spectroscopy," Ind. Eng. Chem. Res., pp. 16021–16026.

[54] Virtanen, T., Parkkila, P., Koivuniemi, A., Lahti, J., Viitala, T., Kallioinen, M., Mänttäri, M., and Bunker, A., 2018, "Characterization of Membrane–Foulant Interactions with Novel Combination of Raman Spectroscopy, Surface Plasmon Resonance and Molecular Dynamics Simulation," Separation and Purification Technology, **205**, pp. 263–272.

[55] Supekar, O. D., Park, D. J., Greenberg, A. R., Gopinath, J. T., and Bright, V. M., 2020, "Real-Time Detection of Early-Stage Calcium Sulfate and Calcium Carbonate Scaling Using Raman Spectroscopy," Journal of Membrane Science, **596**, p. 117603.

[56] Park, D. J., Supekar, O. D., Greenberg, A. R., Gopinath, J. T., and Bright, V. M., 2021, "Real-Time Monitoring of Calcium Sulfate Scale Removal from RO Desalination Membranes Using Raman Spectroscopy," Desalination, **497**, p. 114736.

[57] Li, J.-X., Sanderson, R. D., and Chai, G. Y., 2006, "A Focused Ultrasonic Sensor for in Situ Detection of Protein Fouling on Tubular Ultrafiltration Membranes," Sensors and Actuators B: Chemical, **114**(1), pp. 182–191.

[58] Liu, J., Li, J., Chen, X., and Zhang, Y., 2006, "Monitoring of Polymeric Membrane Fouling in Hollow Fiber Module Using Ultrasonic Nondestructive Testing," Transactions of Nonferrous Metals Society of China, **16**, pp. s845–s848.

[59] Munn, R. W., 2010, "Contribution of Molecular Displacements to Linear and Nonlinear Electric Susceptibilities of Molecular Crystals," The Journal of Chemical Physics, **132**(10), p. 104511.

[60] Lafuente, B., Downs, R. T., Yang, H., and Stone, N., 2015, "1. The Power of Databases: The RRUFF Project," *Highlights in Mineralogical Crystallography*, T. Armbruster, and R.M. Danisi, eds., De Gruyter (O), pp. 1–30.

[61] Szymanski, H. A., ed., 1967, *Raman Spectroscopy: Theory and Practice*, Springer US, Boston, MA.

[62] Ferraro, J. R., Nakamoto, K., and Brown, C. W., 2003, "Chapter 1 - Basic Theory," *Introductory Raman Spectroscopy (Second Edition)*, J.R. Ferraro, K. Nakamoto, and C.W. Brown, eds., Academic Press, San Diego, pp. 1–94.

[63] 2007, "Theory of Infrared Absorption and Raman Spectroscopy," *Vibrational Spectroscopy in Life Science*, John Wiley & Sons, Ltd, pp. 11–61.

[64] McCreery, R. L., "Raman Microscopy and Imaging - Raman Spectroscopy for Chemical Analysis - Wiley Online Library" [Online]. Available: https://onlinelibrary-wiley-com.colorado.idm.oclc.org/doi/10.1002/0471721646.ch11. [Accessed: 03-Nov-2021].

[65] Mitra, S. S., 1962, "Vibration Spectra of Solids," *Solid State Physics*, Elsevier, pp. 1–80.

[66] Buzgar, N., Buzatu, A., and Sanislav, I., 2009, "The Raman Study of Certain Sulfates," Analele Stiintifice ale Universitatii "Al. I. Cuza" din Iasi. Seria Geologie, **LV**, pp. 5–23.

[67] Qiu, J., Li, X., and Qi, X., 2019, "Raman Spectroscopic Investigation of Sulfates Using Mosaic Grating Spatial Heterodyne Raman Spectrometer," IEEE Photonics Journal, **11**(5), pp. 1–12.

[68] Brüesch, P., 1982, *Phonons: Theory and Experiments I*, Springer Berlin Heidelberg, Berlin, Heidelberg.

[69] Ramabadran, U., and Roughani, B., 2018, "Intensity Analysis of Polarized Raman Spectra for off Axis Single Crystal Silicon," Materials Science and Engineering: B, **230**, pp. 31–42.

[70] Norrby, L. J., 1990, "Factor Groups, Point Groups, Space Groups: A Review of Some Central Concepts with Application to Vibrational Spectroscopy on Crystalline Solids," Journal of Crystallographic and Spectroscopic Research, **20**(6), pp. 595–604.

[71] Rousseau, D. L., Bauman, R. P., and Porto, S. P. S., 1981, "Normal Mode Determination in Crystals," Journal of Raman Spectroscopy, **10**(1), pp. 253–290.

[72] Bayarjargal, L., Fruhner, C.-J., Schrodt, N., and Winkler, B., 2018, "CaCO3 Phase Diagram Studied with Raman Spectroscopy at Pressures up to 50 GPa and High Temperatures and DFT Modeling," Physics of the Earth and Planetary Interiors, **281**, pp. 31–45.

[73] Frantz, J. D., 1998, "Raman Spectra of Potassium Carbonate and Bicarbonate Aqueous Fluids at Elevated Temperatures and Pressures: Comparison with Theoretical Simulations," Chemical Geology, **152**(3–4), pp. 211–225.

[74] Ferraro, J. R., Nakamoto, K., and Brown, C. W., 2003, "Acknowledgments," *Introductory Raman Spectroscopy (Second Edition)*, J.R. Ferraro, K. Nakamoto, and C.W. Brown, eds., Academic Press, San Diego, p. xi.

[75] Li, Z., Wang, J., and Li, D., 2016, "Applications of Raman Spectroscopy in Detection of Water Quality," Applied Spectroscopy Reviews, **51**(4), pp. 333–357.

[76] Iosin, M., Toderas, F., Baldeck, P. L., and Astilean, S., 2009, "Study of Protein–Gold Nanoparticle Conjugates by Fluorescence and Surface-Enhanced Raman Scattering," Journal of Molecular Structure, **924–926**, pp. 196–200.

[77] Stammeier, J. A., Purgstaller, B., Hippler, D., Mavromatis, V., and Dietzel, M., 2018, "In-Situ Raman Spectroscopy of Amorphous Calcium Phosphate to Crystalline Hydroxyapatite Transformation," MethodsX, **5**, pp. 1241–1250.

[78] Xu, Z., He, Z., Song, Y., Fu, X., Rommel, M., Luo, X., Hartmaier, A., Zhang, J., and Fang, F., 2018, "Topic Review: Application of Raman Spectroscopy Characterization in Micro/Nano-Machining," Micromachines, **9**(7), p. 361.

[79] Madaeni, S. S., and Samieirad, S., 2010, "Chemical Cleaning of Reverse Osmosis Membrane Fouled by Wastewater," Desalination, **257**(1–3), pp. 80–86.

[80] Yu, T., Meng, L., Zhao, Q.-B., Shi, Y., Hu, H.-Y., and Lu, Y., 2017, "Effects of Chemical Cleaning on RO Membrane Inorganic, Organic and Microbial Foulant Removal in a Full-Scale Plant for Municipal Wastewater Reclamation," Water Research, **113**, pp. 1–10.

[81] Kim, H. J., Fouda, A. E., and Jonasson, K., 2000, "In Situ Study on Kinetic Behavior during Asymmetric Membrane Formation via Phase Inversion Process Using Raman Spectroscopy," Journal of Applied Polymer Science, **75**(1), pp. 135–141.

[82] Prieto-Taboada, N., Gómez-Laserna, O., Martínez-Arkarazo, I., Olazabal, M. Á., and Madariaga, J. M., 2014, "Raman Spectra of the Different Phases in the CaSO4–H2O System," Anal. Chem., **86**(20), pp. 10131–10137.

[83] Hasson, D., and Semiat, R., 2006, "Scale Control in Saline and Wastewater Desalination," Israel Journal of Chemistry, **46**(1), pp. 97–104.

[84] Creber, S. A., Vrouwenvelder, J. S., van Loosdrecht, M. C. M., and Johns, M. L., 2010, "Chemical Cleaning of Biofouling in Reverse Osmosis Membranes Evaluated Using Magnetic Resonance Imaging," Journal of Membrane Science, **362**(1–2), pp. 202–210.

[85] Uchymiak, M., Rahardianto, A., Lyster, E., Glater, J., and Cohen, Y., 2007, "A Novel RO Ex Situ Scale Observation Detector (EXSOD) for Mineral Scale Characterization and Early Detection," Journal of Membrane Science, **291**(1–2), pp. 86–95.

[86] Cen, J., Vukas, M., Barton, G., Kavanagh, J., and Coster, H. G. L., 2015, "Real Time Fouling Monitoring with Electrical Impedance Spectroscopy," Journal of Membrane Science, **484**, pp. 133–139.

[87] Amin Saad, M., 2004, "Early Discovery of RO Membrane Fouling and Real-Time Monitoring of Plant Performance for Optimizing Cost of Water," Desalination, **165**, pp. 183–191.

[88] Uchymiak, M., Lyster, E., Glater, J., and Cohen, Y., 2008, "Kinetics of Gypsum Crystal Growth on a Reverse Osmosis Membrane," Journal of Membrane Science, **314**(1), pp. 163–172.

[89] Parkhurst, D. L., 1995, *User's Guide to PHREEQC, a Computer Program for Speciation, Reaction-Path, Advective-Transport, and Inverse Geochemical Calculations*, 95–4227, U.S. Geological Survey, Reston, VA.

[90] Guo, S., Popp, J., and Bocklitz, T., 2021, "Chemometric Analysis in Raman Spectroscopy from Experimental Design to Machine Learning–Based Modeling," Nat Protoc, **16**(12), pp. 5426–5459.

[91] Mazet, V., Carteret, C., Brie, D., Idier, J., and Humbert, B., 2005, "Background Removal from Spectra by Designing and Minimising a Non-Quadratic Cost Function."

[92] Sablani, S., Goosen, M., Al-Belushi, R., and Wilf, M., 2001, "Concentration Polarization in Ultrafiltration and Reverse Osmosis: A Critical Review," Desalination, **141**(3), pp. 269–289.

[93] Zydney, A. L., 1997, "Stagnant Film Model for Concentration Polarization in Membrane Systems," Journal of Membrane Science, **130**(1–2), pp. 275–281.

[94] Brian, P. L. T., 1965, "Concentration Polar Zation in Reverse Osmosis Desalination with Variable Flux and Incomplete Salt Rejection," Ind. Eng. Chem. Fund., **4**(4), pp. 439–445.

[95] Sheikholeslami, R., and Ng, M., 2001, "Calcium Sulfate Precipitation in the Presence of Nondominant Calcium Carbonate: Thermodynamics and Kinetics," Industrial & Engineering Chemistry Research, **40**(16), pp. 3570–3578.

[96] Tzotzi, Ch., Pahiadaki, T., Yiantsios, S. G., Karabelas, A. J., and Andritsos, N., 2007, "A Study of CaCO3 Scale Formation and Inhibition in RO and NF Membrane Processes," Journal of Membrane Science, **296**(1), pp. 171–184.

[97] De La Pierre, M., Carteret, C., Maschio, L., André, E., Orlando, R., and Dovesi, R., 2014, "The Raman Spectrum of $CaCO_3$ Polymorphs Calcite and Aragonite: A Combined Experimental and Computational Study," The Journal of Chemical Physics, **140**(16), p. 164509.

[98] Buzgar, N., Ionu, A., and Apopei, Ț., "THE RAMAN STUDY OF CERTAIN CARBONATES," p. 16.

[99] Borromeo, L., Zimmermann, U., Andò, S., Coletti, G., Bersani, D., Basso, D., Gentile, P., Schulz, B., and Garzanti, E., 2017, "Raman Spectroscopy as a Tool for Magnesium Estimation in Mg-Calcite," Journal of Raman Spectroscopy, **48**(7), pp. 983–992.

[100] Schindelin, J., Arganda-Carreras, I., Frise, E., Kaynig, V., Longair, M., Pietzsch, T., Preibisch, S., Rueden, C., Saalfeld, S., Schmid, B., Tinevez, J.-Y., White, D. J., Hartenstein, V., Eliceiri, K., Tomancak, P., and Cardona, A., 2012, "Fiji: An Open-Source Platform for Biological-Image Analysis," Nat Methods, **9**(7), pp. 676–682.

[101] Lyster, E., and Cohen, Y., 2007, "Numerical Study of Concentration Polarization in a Rectangular Reverse Osmosis Membrane Channel: Permeate Flux Variation and Hydrodynamic End Effects," JOURNAL OF MEMBRANE SCIENCE, **303**(1–2), pp. 140–153.

[102] Osada, Y., and Nakagawa, T., 2014, *Membrane Science and Technology*, CRC Press, Boca Raton.

[103] Zhu, C., Tong, N., Song, L., and Zhang, G., 2015, "Investigation of Raman Spectra of Polyethylene Terephthalate," *International Symposium on Photonics and Optoelectronics 2015*, SPIE, pp. 72–76.

[104] Matousek, P., Clark, I. P., Draper, E. R. C., Morris, M. D., Goodship, A. E., Everall, N., Towrie, M., Finney, W. F., and Parker, A. W., 2005, "Subsurface Probing in Diffusely Scattering Media Using Spatially Offset Raman Spectroscopy," Appl. Spectrosc., AS, **59**(4), pp. 393–400.

[105] Rahardianto, A., McCool, B. C., and Cohen, Y., 2008, "Reverse Osmosis Desalting of Inland Brackish Water of High Gypsum Scaling Propensity: Kinetics and Mitigation of Membrane Mineral Scaling," Environ. Sci. Technol., **42**(12), pp. 4292–4297.

[106] Supekar, O. D., Park, D. J., Greenberg, A. R., Gopinath, J. T., and Bright, V. M., 2019, "Real-Time Detection of Early-Stage Calcium Sulfate and Calcium Carbonate Scaling Using Raman Spectroscopy," Journal of Membrane Science, p. 117603.

[107] Tai, C. Y., and Chen, F.-B., 1998, "Polymorphism of CaCO3, Precipitated in a Constant-Composition Environment," AIChE Journal, **44**(8), pp. 1790–1798.

[108] Brusilovsky, M., Borden, J., and Hasson, D., 1992, "Flux Decline Due to Gypsum Precipitation on RO Membranes," Desalination, **86**(2), pp. 187–222.

[109] Carteret, C., Dandeu, A., Moussaoui, S., Muhr, H., Humbert, B., and Plasari, E., 2009, "Polymorphism Studied by Lattice Phonon Raman Spectroscopy and Statistical Mixture Analysis Method. Application to Calcium Carbonate Polymorphs during Batch Crystallization," Crystal Growth & Design, **9**(2), pp. 807–812.

[110] Feoktistova, N., Rose, J., Prokopović, V. Z., Vikulina, A. S., Skirtach, A., and Volodkin, D., 2016, "Controlling the Vaterite $CaCO_3$ Crystal Pores. Design of Tailor-Made Polymer Based Microcapsules by Hard Templating," Langmuir, **32**(17), pp. 4229–4238.

[111] Niedermayr, A., Köhler, S. J., and Dietzel, M., 2013, "Impacts of Aqueous Carbonate Accumulation Rate, Magnesium and Polyaspartic Acid on Calcium Carbonate Formation (6–40°C)," Chemical Geology, **340**, pp. 105–120.

[112] Waly, T., Kennedy, M. D., Witkamp, G.-J., Amy, G., and Schippers, J. C., 2012, "The Role of Inorganic Ions in the Calcium Carbonate Scaling of Seawater Reverse Osmosis Systems," Desalination, **284**, pp. 279–287.

[113] Sudmalis, M., and Sheikholeslami, R., 2000, "Coprecipitation of CaCO3 and CaSO4," The Canadian Journal of Chemical Engineering, **78**(1), pp. 21–31.

[114] Liu, J., Li, Z., Wang, Y., Liu, X., Tu, G., and Li, W., 2021, "Analyzing Scaling Behavior of Calcium Sulfate in Membrane Distillation via Optical Coherence Tomography," Water Research, **191**, p. 116809.

[115] Beckmann, W., 2013, *Crystallization: Basic Concepts and Industrial Applications*, John Wiley & Sons, Incorporated, Weinheim, GERMANY.

[116] Stawski, T. M., van Driessche, A. E. S., Ossorio, M., Diego Rodriguez-Blanco, J., Besselink, R., and Benning, L. G., 2016, "Formation of Calcium Sulfate through the Aggregation of Sub-3 Nanometre Primary Species," Nat Commun, **7**(1), p. 11177.

[117] Mitrouli, S., Karabelas, A. J., Karanasiou, A., and Kostoglou, M., 2013, "Incipient Calcium Carbonate Scaling of Desalination Membranes in Narrow Channels with Spacers—Experimental Insights," Journal of Membrane Science, **425–426**, pp. 48–57.

[118] Dydo, P., Turek, M., Ciba, J., Wandachowicz, K., and Misztal, J., 2004, "The Nucleation Kinetic Aspects of Gypsum Nanofiltration Membrane Scaling," Desalination, **164**(1), pp. 41–52.

[119] Wiechers, H. N. S., Sturrock, P., and Marais, G. v. R., 1975, "Calcium Carbonate Crystallization Kinetics," Water Research, **9**(9), pp. 835–845.

[120] Thompson, J., Lin, N., Lyster, E., Arbel, R., Knoell, T., Gilron, J., and Cohen, Y., 2012, "RO Membrane Mineral Scaling in the Presence of a Biofilm," Journal of Membrane Science, **415–416**, pp. 181–191.

[121] Christoffersen, M. R., Christoffersen, J., Weijnen, M. P. C., and Van Rosmalen, G. M., 1982, "Crystal Growth of Calcium Sulphate Dihydrate at Low Supersaturation," Journal of Crystal Growth, **58**(3), pp. 585–595.

[122] Yoreo, J. J. D., "3 Principles of Crystal Nucleation and Growth," p. 37.

[123] Bristow, N. W., Vogt, S. J., Bucs, S. S., Vrouwenvelder, J. S., Johns, M. L., and Fridjonsson, E. O., 2021, "Novel Magnetic Resonance Measurements of Fouling in Operating Spiral Wound Reverse Osmosis Membrane Modules," Water Research, **196**, p. 117006.

[124] Kavanagh, J. M., Hussain, S., Chilcott, T. C., and Coster, H. G. L., 2009, "Fouling of Reverse Osmosis Membranes Using Electrical Impedance Spectroscopy: Measurements and Simulations," Desalination, **236**(1), pp. 187–193.

[125] Cen, J., Vukas, M., Barton, G., Kavanagh, J., and Coster, H. G. L., 2015, "Real Time Fouling Monitoring with Electrical Impedance Spectroscopy," Journal of Membrane Science, **484**, pp. 133–139.

[126] García-Triñanes, P., Chairopoulou, M. A., and Campos, L. C., 2021, "Investigating Reverse Osmosis Membrane Fouling and Scaling by Membrane Autopsy of a Bench Scale Device," Environmental Technology, pp. 1–14.

[127] Adel, M., Nada, T., Amin, S., Anwar, T., and Mohamed, A. A., 2022, "Characterization of Fouling for a Full-Scale Seawater Reverse Osmosis Plant on the Mediterranean Sea: Membrane Autopsy and Chemical Cleaning Efficiency," Groundwater for Sustainable Development, **16**, p. 100704.

[128] Zarga, Y., Ben Boubaker, H., Ghaffour, N., and Elfil, H., 2013, "Study of Calcium Carbonate and Sulfate Co-Precipitation," Chemical Engineering Science, **96**, pp. 33–41.

[129] Chong, T. H., and Sheikholeslami, R., 2001, "Thermodynamics and Kinetics for Mixed Calcium Carbonate and Calcium Sulfate Precipitation," Chemical Engineering Science, **56**(18), pp. 5391–5400.

[130] Karabelas, A. J., Kostoglou, M., and Mitrouli, S. T., 2011, "Incipient Crystallization of Sparingly Soluble Salts on Membrane Surfaces: The Case of Dead-End Filtration with No Agitation," Desalination, **273**(1), pp. 105–117.

[131] Sheikholeslami, R., 2004, "Assessment of the Scaling Potential for Sparingly Soluble Salts in RO and NF Units," Desalination, **167**, pp. 247–256.

[132] Song, K. S., Lim, J., Yun, S., Kim, D., and Kim, Y., 2019, "Composite Fouling Characteristics of CaCO3 and CaSO4 in Plate Heat Exchangers at Various Operating and Geometric Conditions," International Journal of Heat and Mass Transfer, **136**, pp. 555–562.

[133] Virtanen, T., Parkkila, P., Koivuniemi, A., Lahti, J., Viitala, T., Kallioinen, M., Mänttäri, M., and Bunker, A., 2018, "Characterization of Membrane–Foulant Interactions with Novel Combination of Raman Spectroscopy, Surface Plasmon Resonance and Molecular Dynamics Simulation," Separation and Purification Technology, **205**, pp. 263–272.

[134] Sarma, L. P., Prasad, P. S. R., and Ravikumar, N., 1998, "Raman Spectroscopic Study of Phase Transitions in Natural Gypsum," Journal of Raman Spectroscopy, **29**(9), pp. 851–856.

[135] Krishnamurthy, N., and Soots, V., 1971, "Raman Spectrum of Gypsum," Can. J. Phys., **49**(7), pp. 885–896.

[136] Liu, Y., 2009, "Raman, MIR, and NIR Spectroscopy Study of Calcium Sulfates: Gypsum, Bassanite, and Anhydrite."

[137] Jung, O., Saravia, F., Wagner, M., Heißler, S., and Horn, H., 2019, "Quantifying Concentration Polarization – Raman Microspectroscopy for In-Situ Measurement in a Flat Sheet Cross-Flow Nanofiltration Membrane Unit," Sci Rep, **9**(1), p. 15885.

[138] De La Pierre, M., Carteret, C., Maschio, L., André, E., Orlando, R., and Dovesi, R., 2014, "The Raman Spectrum of CaCO3 Polymorphs Calcite and Aragonite: A Combined Experimental and Computational Study," J. Chem. Phys., **140**(16), p. 164509.

[139] Harris, J., Mey, I., Hajir, M., Mondeshki, M., and Wolf, S. E., 2015, "Pseudomorphic Transformation of Amorphous Calcium Carbonate Films Follows Spherulitic Growth Mechanisms and Can Give Rise to Crystal Lattice Tilting," CrystEngComm, **17**(36), pp. 6831–6837.

[140] Thompson, J., 2017, "Real-Time Direct Detection of Silica Scaling on RO Membranes," Journal of Membrane Science, p. 13.

[141] Singh, R., 2015, "Water and Membrane Treatment," *Membrane Technology and Engineering for Water Purification*, Elsevier, pp. 81–178.

[142] Chu, Q., Jin, Z., Yu, X., Li, C., Zhang, W., Ji, W., Lin, B., Shum, P. P., Zhang, X., and Wang, G., 2019, "Volumetric Enhancement of Raman Scattering for Fast Detection Based on a Silver-Lined Hollow-Core Fiber," Opt. Express, **27**(7), p. 10370.

[143] Boulos, R. A., Zhang, F., Tjandra, E. S., Martin, A. D., Spagnoli, D., and Raston, C. L., 2015, "Spinning up the Polymorphs of Calcium Carbonate," Sci Rep, **4**(1), p. 3616.

[144] Tai, C. Y., and Chen, F.-B., 1998, "Polymorphism of CaCO3, Precipitated in a Constant-Composition Environment," AIChE Journal, **44**(8), pp. 1790–1798.

[145] Tang, H., Yu, J., and Zhao, X., 2009, "Controlled Synthesis of Crystalline Calcium Carbonate Aggregates with Unusual Morphologies Involving the Phase Transformation from Amorphous Calcium Carbonate," Materials Research Bulletin, **44**(4), pp. 831–835.

[146] Morse, J. W., Arvidson, R. S., and Lüttge, A., 2007, "Calcium Carbonate Formation and Dissolution," Chem. Rev., **107**(2), pp. 342–381.

[147] Ashfaq, M. Y., Al-Ghouti, M. A., Da'na, D. A., Qiblawey, H., and Zouari, N., 2020, "Effect of Concentration of Calcium and Sulfate Ions on Gypsum Scaling of Reverse Osmosis Membrane, Mechanistic Study," Journal of Materials Research and Technology, **9**(6), pp. 13459–13473.

[148] Benecke, J., Haas, M., Baur, F., and Ernst, M., 2018, "Investigating the Development and Reproducibility of Heterogeneous Gypsum Scaling on Reverse Osmosis Membranes Using Real-Time Membrane Surface Imaging," Desalination, **428**, pp. 161–171.

[149] Benecke, J., Rozova, J., and Ernst, M., 2018, "Anti-Scale Effects of Select Organic Macromolecules on Gypsum Bulk and Surface Crystallization during Reverse Osmosis Desalination," Separation and Purification Technology, **198**, pp. 68–78.

[150] Edinger, S. E., 1973, "An Investigation of the Factors Which Affect the Size and Growth Rates of the Habit Faces of Gypsum," Journal of Crystal Growth, **18**(3), pp. 217–224.

[151] Pastero, L., Giustetto, R., and Aquilano, D., 2017, "Calcite Passivation by Gypsum: The Role of the Cooperative Effect," CrystEngComm, **19**(26), pp. 3649–3659.

[152] Ruiz-Agudo, E., Álvarez-Lloret, P., Ibañez-Velasco, A., and Ortega-Huertas, M., 2016, "Crystallographic Control in the Replacement of Calcite by Calcium Sulfates," Crystal Growth & Design, **16**(9), pp. 4950–4959.

[153] Gill, J. S., and Varsanik, R. G., 1986, "Computer Modeling of the Specific Matching between Scale Inhibitors and Crystal Structure of Scale Forming Minerals," Journal of Crystal Growth, **76**(1), pp. 57–62.

[154] Sulpis, O., Agrawal, P., Wolthers, M., Munhoven, G., Walker, M., and Middelburg, J. J., 2022, "Aragonite Dissolution Protects Calcite at the Seafloor," Nat Commun, **13**(1), p. 1104.

[155] Plummer, L. N., and Busenberg, E., "The Solubilities of Calcite, Aragonite and Vaterite in COrHzO Solutions between 0 and 9O"C, and an Evaluation of the Aqueous Model for the System CaC03-CO*-Hz0," p. 30.

[156] Ge, Y., Sun, M., and Pu, Y., 2019, "Geographic Information System-Based Edge Effect Correction for Ripley's K-Function under Irregular Boundaries," Geographical Research, **57**(4), pp. 436–447.

[157] Huang, X., Zhou, Q., Zeng, L., and Li, X., 2017, "Monitoring Spatial Uniformity of Particle Distributions in Manufacturing Processes Using the K Function," IEEE Transactions on Automation Science and Engineering, **14**(2), pp. 1031–1041.

[158] Ruan, Y., Yin, P., Li, F., Li, D., Lin, Q., and Li, K., 2019, "The Accuracy of Determining Cluster Size by Analyzing Ripley's K Function in Single Molecule Localization Microscopy," Applied Sciences, **9**(16), p. 3271.

[159] Kiskowski, M. A., Hancock, J. F., and Kenworthy, A. K., 2009, "On the Use of Ripley's K-Function and Its Derivatives to Analyze Domain Size," Biophys J, **97**(4), pp. 1095–1103.

[160] Baddeley, A., and Turner, R., 2005, "**Spatstat**: An *R* Package for Analyzing Spatial Point Patterns," J. Stat. Soft., **12**(6).

[161] Hess, S. T., Kumar, M., Verma, A., Farrington, J., Kenworthy, A., and Zimmerberg, J., 2005, "Quantitative Electron Microscopy and Fluorescence Spectroscopy of the Membrane Distribution of Influenza Hemagglutinin," Journal of Cell Biology, **169**(6), pp. 965–976.

[162] Kato, D., 1974, "Improvement of Raman Spectroscopy by Quenching the Fluorescence," Journal of Applied Physics, **45**(5), pp. 2281–2282.

[163] Zięba-Palus, J., and Michalska, A., 2014, "Photobleaching as a Useful Technique in Reducing of Fluorescence in Raman Spectra of Blue Automobile Paint Samples," Vibrational Spectroscopy, **74**, pp. 6–12.

[164] Schaefer, J. J., Fox, C. B., and Harris, J. M., 2012, "Confocal Raman Microscopy for Monitoring the Membrane Polymerization and Thermochromism of Individual, Optically Trapped Diacetylenic Phospholipid Vesicles," Journal of Raman Spectroscopy, **43**(3), pp. 351–359.

[165] Gonzalez-Gil, G., Behzad, A. R., Farinha, A. S. F., Zhao, C., Bucs, S. S., Nada, T., Das, R., Altmann, T., Buijs, P. J., and Vrouwenvelder, J. S., 2021, "Clinical Autopsy of a Reverse Osmosis Membrane Module," Frontiers in Chemical Engineering, **3**.

# Appendix A

Table A-0-1. Raman bands of relevant materials in this work.

| Ref. | Spectral Information | | |
|---|---|---|---|
| | Foulant | Wavenumbers ($cm^{-1}$) | Assignment/Notes |
| [82] | $CaSO_4 \cdot 2H_2O$ | 414, 493 | Gypsum is the most stable polymorph. Any reported deviations in Raman bands are likely due to differences in instrument resolution or impurities present in the measured crystal. |
| [82] | $CaSO_4 \cdot 2H_2O$ | 619, 670 | $\nu_4$ mode |
| [82] | $CaSO_4 \cdot 2H_2O$ | 1008 | $\nu_1$ mode |
| [82] | $CaSO_4 \cdot 2H_2O$ | 1135 | $\nu_3$ mode |
| [137] | $SO_4^{2-}$ (Sulphate) | 981 | Sulfate has 9 modes of internal vibration that are Raman active. Linear symmetrical stretching vibrational mode ($\nu_1$) is the strongest. |
| [139] | $CaCO_3$ (Calcite) | 1082 | $\nu_1$ mode |
| [138] | $CaCO_3$ (Calcite) | 1086.2 | $\nu_1$ mode |
| [109] | $CaCO_3$ (Calcite) | 1086 | Internal vibration mode, symmetric stretching |
| [139] | $CaCO_3$ (Calcite) | 716 | In-plane bending ($\nu_4$) |
| [109] | $CO_3^{2-}$ (Carbonate) | 680-750 | Internal vibration mode ($\nu_4$), out-of-plane bending |
| [109] | $CO_3^{2-}$ (Carbonate) | 850-900 | Internal vibration mode ($\nu_2$), in-plane bending |
| [138] | $CaCO_3$ (Aragonite) | 1085.3 | $A_g$ (at 300K [26.85°C]) |

| | | | |
|---|---|---|---|
| [109] | $CaCO_3$ (Aragonite) | 1085 | Internal vibration mode, symmetric stretching. Relative intensity is very strong |
| [109] | $CaCO_3$ (Vaterite) | 1075, 1090 | Internal vibration mode, symmetric stretching. Relative intensity is strong. Vaterite is the most unstable polymorph out of the three |
| [109] | $CO_3^{2-}$ (Carbonate) | 1075-1090 | Internal vibration mode ($\nu_1$), symmetric stretching |
| [109] | $CO_3^{2-}$ (Carbonate) | 1430-1600 | Internal vibration mode ($\nu_3$), antisymmetric stretching |
| [73] | $HCO_3^{2-}$ | 1015, 1360 | |
| [81] | Polysulfone | 739.3 | Antisymmetric C-S-C stretching |
| [81] | Polysulfone | 788.1 | Out-of-plane benzene ring C-H deformation |
| [81] | Polysulfone | 1073.3 | Symmetric $SO_2$ stretching |
| [81] | Polysulfone | 1108.3 | Antisymmetric $SO_2$ stretching |
| [81] | Polysulfone | 1149.5 | C-O-C stretching mode |

# Appendix B

These are the procedural guidelines for operation of the RO system.

**WHEN HANDLING THE FLOW CELL, ALWAYS KEEP THE PROTECTED LID ON TO AVOID BREAKING THE OPTICAL WINDOW**

**DAY BEFORE EXPERIMENT:**

1. Wash all four reservoirs
2. Create new data file folder with today's date
    i. Create the following files:
        1. metadata excel sheet for Raman acquisition settings
        2. folder called 'raw-Raman-data'
        3. folder called 'proc-Raman-data'
2. Open Master Experiment Log and add entry for experiment
1. Install flow cell in RO system (you can use half the number of bolts since we are not pressurizing, but just flushing at low pressures).
    i. Make sure the optical window cover is on
2. Install permeate sensor
3. Place "SALT" tank with fresh DI water and "DI" tank with fresh DI water on cart
4. Place intake lines in each respective tank
5. Place return lines in "SALT" tank
6. Open intake valve for " SALT" tank, close "DI" tank intake valve
7. Fully open bypass valve
8. Close backpressure regulator
9. Open feed inlet valve
10. Put on goggles and turn on pumps
11. Flush system for 30 minutes with "SALT" tank
    i. Check flow is coming out of outlet
    ii. Check flow rate
    iii. Check for leaks
        1. Flow cell
        2. Water tanks
        3. Permeate sensor
12. Soak membrane in 1:1 DI and IPA
13. Wipe down heat exchanger with DI, then IPA
14. Prep feed solution
15. After pressurizing the lines to ~50 psi, stop flushing
    i. Turn off pumps
    ii. Fully open bypass valve
    iii. Close backpressure regulator
    iv. Close feed inlet valve
    v. Remove flow cell from stage

16. Remove the flow cell from the RO system. Open it up. Put pins on the flow cell to avoid having to do it later when you are installing the membrane and risk getting grease on the membrane.
17. Clean flow cell, O-rings, and optical window with DI, then IPA
18. Put the pins in the bottom component of flow cell to prevent getting grease on your fingers
19. While membrane is soaking:
    i. Set up Raman microscope
    ii. Turn on shutter
    iii. Turn on laser source
    iv. Turn on spectrometer and CCD
    v. Open LightField
    vi. Change laser line
    vii. Focus on silicon standard
    viii. Take spectrum to verify optimal Raman microscope performance
    ix. Record SNR in Raman metadata excel sheet
20. Reinstall chiller and empty salt feed reservoir
21. Turn on chiller, set to ~16 °C, and set valve so that it begins to chill DI #2
22. When the membrane's done soaking
    i. center it on the bottom component of the flow cell
    ii. Mark the center using the stencil
    iii. Make sure the membrane is lying as flat as possible
23. Close the flow cell and tighten the bolts in a star pattern
24. Connect inlet and outlet to flow cell
25. Tighten inlet and outlet to flow cell
26. Place feed inlet, feed outlet, and permeate line in fresh DI feed tank (DI #2)
27. Open bypass valve and close backpressure regulator
28. Open inlet feed valve
29. Turn on pumps
30. Lift flow cell to get rid of any bubbles
31. Open all the necessary software
    i. Open Arduino: Script can be found at G:\My Drive\Graduate work\Research\(08) GOALI\(09) RO-data-acquisition\ → Upload program and open ArduSpreadsheet
    ii. Open MATLAB data acquisition program and run program
        1. Unplug and plug thermocouple USB → open and close analog input data (this is the hack to get MATLAB to recognize TC in the DAQ's)

```
Collecting data for membrane compaction? (y/n, case sensitive)
y
Where would you like to save the data?
Enter filepath

Where would you like to save Raman data?
G:\My Drive\Graduate work\Research\(07) Data\yyyy (##) Month dd
Enter target temperature (degC):
23.5
Enter initial chiller setpoint temperature (degC)
14
```

32. Turn on both pumps
33. Adjust pressure, crossflow velocity, and temperature until they stabilize (~15 minutes)

**START COMPACTION**: Record the time once the pressure, velocity, and temperature stabilize

34. Make sure TeamViewer is open and running

35. Make sure water sensors are all connected to app
36. Tap on the permeate line to get rid of any bubbles OR raise the flow cell to get rid of bubbles
37. Save data first! Image capture may cause MATLAB to crash

*Check on pressure, crossflow velocity, temperature, and permeate flux to make sure they are within expected levels for duration of membrane compaction*

**END COMPACTION:**

1. Save compaction backup files using backup_data.m script
2. Stop data collection in MATLAB by typing the following in the command window

```
listOfTimers = timersfindall

stop(listOfTimers)
```

3. Rename 'data.mat' to 'data_compaction.mat' and store in `G:\MY DATA FILEPATH`
4. Run data collection program again, this time marking 'n' for "Collecting membrane compaction data?"
5. Change backup data save file to `backup_scaling.mat`
6. Change permeate flux .csv sheet to `'scaling-permeate-data.csv'`
7. Move `data_compaction.mat, backup_data_compaction.mat, and scaling-permeate-data.csv` to today's data folder
8. Turn on laser source, spectrograph, and CCD
9. Update laser use log
10. Pour salt solution into salt tank to begin bringing it to temperature
11. Making sure the objective is safely out of the way, bolt down the flow cell to the stage
12. Turn on shutter, open shutter (green light on)
13. Lower objective into flow cell guide and focus the laser onto the membrane inside the flow cell, find the z-height that minimizes the fluorescent background
    i. 10 s acquisition
    ii. Save the LF experiment settings
    iii. Check 600 lines/mm grating
    iv. When focusing the laser, find the z-height that minimizes the fluorescent background
    v. Also check the focus at all the interrogated points.
    vi. 10 s acquisition
    vii. Check the laser line
14. Settings to change: the export data file folder
15. Make sure you are exporting in the units '$cm^{-1}$' not wavenumber
16. Change export file location to `G:\My Drive\Graduate work\Research\(07) Data\(date)\raw-Raman-data`
17. Change acquisition time back to 10 s
18. Save experiment settings
19. 'Remove from experiment' both detector and ccd
20. 'Exit' from LightField instead of clicking the **X** button (**do not save** when it prompts you again, it has reverted my settings back to default settings before)

**BEFORE SWITCHING THE FEED TO A SALT FEED:**

1. Is the shutter on external control mode? (Turn off device. Turn it on. Hold control button for 3 seconds. If the LED light is green and blinks three times, it is in the correct setting).
2. Cool salt feed to 23 degrees Celsius or lower
3. **Record about 30 minutes of data collection with DI water**
4. Replace DI #1 with salt feed by moving intake line

a. As best as you can, simultaneously complete the following:
b. Switch feed outlet, feed inlet, permeate outlet lines from DI feed to salt feed reservoir
    i. I think switch the feed gradually to minimize bubbles in the line
    ii. Then switch the permeate line, because the return line will contain leftover DI water in the system
c. Readjust temperature, crossflow velocity, pressure
d. Tap the permeate line to get rid of any bubbles, make sure permeate line is submerged in feed reservoir to get the best, steadiest readings

**SHUTDOWN PROCEDURE:**

1. Collect feed sample for turbidity measurements or test pH
2. Turn off pumps
3. Stop all MATLAB timers
4. Before removing flow cell, turn valve to prevent excessive leaking
5. Close backpressure regulator and open bypass valve
6. Lower stage
7. Remove detector and CCD from LightField
8. Exit LightField
9. Laser off – update laser use log
10. Detector off
11. Spectrometer off
12. Shutter off
13. Unscrew flow cell from stage
14. Loosen inlet and outlet feed and permeate ports
15. Remove flow cell
16. Put protective optical window cover back on the flow cell. Remove membrane
17. Mark which end is downstream on membrane
18. Short circuit flow cell inlet and outline with straight connector. Open feed valve, and bypass valve, close backpressure valve.
19. Switch feed to DI reservoir used for last run's flush
20. Flush RO system
21. Turn chiller direction back to DI side. Remove chiller and clean with IPA
22. Drain salt tank
23. Switch DI compaction tank with compaction DI reservoir for additional flush.
24. **Remove permeate sensor and clean and dry**
25. Restart computer
26. Unplug conductivity controllers. Make sure you unplug the conductivity controller, NOT THE COMPUTER TOWER

**If Raman microscscope needs to be recalibrated**

- Check optical power of laser
- Check fiber alignment using photodetector and oscilloscope
- Take out dichroic
- Put dichroic back in

# Appendix C

The code provided in this appendix was self-written unless otherwise noted.

### C.1 Baseline removal

This code removes the background signal of the spectra.

```
function [z,a,it,ord,s,fct] = backcor(n,y,ord,s,fct)

% BACKCOR   Background estimation by minimizing a non-quadratic cost
function.
%
%   [EST,COEFS,IT] = BACKCOR(N,Y,ORDER,THRESHOLD,FUNCTION) computes and
estimation EST %   of the background (aka. baseline) in a spectroscopic
signal Y with wavelength N.
%   The background is estimated by a polynomial with order ORDER using a
cost-function
%   FUNCTION with parameter THRESHOLD. FUNCTION can have the four following
values:
%       'sh'  - symmetric Huber function : f(x) = { x^2  if abs(x) <
THRESHOLD,
%                                                 { 2*THRESHOLD*abs(x)-
THRESHOLD^2
%                                               otherwise.
%       'ah'  - asymmetric Huber function :f(x) = { x^2  if x < THRESHOLD,
%                                                 { 2*THRESHOLD*x-THRESHOLD^2
%                                                     otherwise.
%       'stq' - symmetric truncated quadratic :  f(x) = { x^2  if abs(x) <
THRESHOLD,
%                                                       { THRESHOLD^2
otherwise.
%       'atq' - asymmetric truncated quadratic :  f(x) = { x^2  if x <
THRESHOLD,
%                                                        { THRESHOLD^2
otherwise.
%   COEFS returns the ORDER+1 vector of the estimated polynomial coefficients
%   (computed with n sorted and bounded in [-1,1] and y bounded in [0,1]).
%   IT returns the number of iterations.
%
%   [EST,COEFS,IT] = BACKCOR(N,Y) does the same, but run a graphical user
interface
%   to help setting ORDER, THRESHOLD and FCT.
%
% For more information, see:
% - V. Mazet, C. Carteret, D. Brie, J. Idier, B. Humbert. Chemom. Intell.
Lab. Syst.
%   76 (2), 2005.
% - V. Mazet, D. Brie, J. Idier. Proceedings of EUSIPCO, pp. 305-308, 2004.
% - V. Mazet. PhD Thesis, University Henri Poincaré Nancy 1, 2005.
```

```
%
% 22-June-2004, Revised 19-June-2006, Revised 30-April-2010,
% Revised 12-November-2012 (thanks E.H.M. Ferreira!)
% Comments and questions to: vincent.mazet@unistra.fr.


% Check arguments
if nargin < 2, error('backcor:NotEnoughInputArguments','Not enough input
arguments'); end;
% delete this line if you do not need GUI
if nargin < 5, [z,a,it,ord,s,fct] = backcorgui(n,y); return; end;
if ~isequal(fct,'sh') && ~isequal(fct,'ah') && ~isequal(fct,'stq') &&
~isequal(fct,'atq'),
    error('backcor:UnknownFunction','Unknown function.');
end;

% Rescaling
N = length(n);
[n,i] = sort(n);
y = y(i);
maxy = max(y);
dely = (maxy-min(y))/2;
n = 2 * (n(:)-n(N)) / (n(N)-n(1)) + 1;
y = (y(:)-maxy)/dely + 1;

% Vandermonde matrix
p = 0:ord;
T = repmat(n,1,ord+1) .^ repmat(p,N,1);
Tinv = pinv(T'*T) * T';

% Initialisation (least-squares estimation)
a = Tinv*y;
z = T*a;

% Other variables
alpha = 0.99 * 1/2;     % Scale parameter alpha
it = 0;                 % Iteration number
zp = ones(N,1);         % Previous estimation

% LEGEND
while sum((z-zp).^2)/sum(zp.^2) > 1e-9,

    it = it + 1;        % Iteration number
    zp = z;             % Previous estimation
    res = y - z;        % Residual

    % Estimate d
    if isequal(fct,'sh'),
        d = (res*(2*alpha-1)) .* (abs(res)<s) + (-alpha*2*s-res) .* (res<=-s)
+ (alpha*2*s-res) .* (res>=s);
    elseif isequal(fct,'ah'),
        d = (res*(2*alpha-1)) .* (res<s) + (alpha*2*s-res) .* (res>=s);
    elseif isequal(fct,'stq'),
        d = (res*(2*alpha-1)) .* (abs(res)<s) - res .* (abs(res)>=s);
    elseif isequal(fct,'atq'),
```

```
        d = (res*(2*alpha-1)) .* (res<s) - res .* (res>=s);
    end;

    % Estimate z
    a = Tinv * (y+d);    % Polynomial coefficients a
    z = T*a;             % Polynomial

end;

% Rescaling
[~,j] = sort(i);
z = (z(j)-1)*dely + maxy;

    a(1) = a(1)-1;
    a = a*dely;% + maxy;

end

% delete lines below if you do not need GUI

function [z,a,it,ord,s,fct] = backcorgui(n,y)

% BACKCORGUI   Graphical User Interface for background estimation.

% Initialization
z = [];
a = [];
it = [];
ord = [];
s = [];
fct = [];

order = 4;
threshold = 0.01;
costfunction = 'atq';

% Main window
hwin = figure('Visible','off','Position',[0 0 750
400],'NumberTitle','off','Name','Background Correction',...

'MenuBar','none','Toolbar','figure','Resize','on','ResizeFcn',{@WinResizeFcn}
);
bgclr = get(hwin,'Color');

% Axes
haxes = axes('Units','pixels');

% Buttons OK & Cancel
hok =
uicontrol('Style','pushbutton','String','OK','Position',[600,40,80,25],'Callb
ack',{@OKFcn},'BackgroundColor',bgclr);
hcancel =
uicontrol('Style','pushbutton','String','Cancel','Position',[510,40,80,25],'C
allback',{@CancelFcn},'BackgroundColor',bgclr);
```

```
% Cost functions menu
hfctlbl = uicontrol('Style','text','String','Cost
function:','HorizontalAlignment','left','BackgroundColor',bgclr);
hfct =
uicontrol('Style','popupmenu','Value',4,'BackgroundColor','white','Callback',
{@CostFunctionFcn},...
    'String',{'Symmetric Huber function','Asymmetric Huber
function','Symmetric truncated quadratic','Asymmetric truncated quadratic'});

% Threshold text
hthresholdlbl =
uicontrol('Style','text','String','Threshold:','HorizontalAlignment','left','
BackgroundColor',bgclr);
hthreshold =
uicontrol('Style','edit','String',num2str(threshold),'BackgroundColor','white
','Callback',{@ThresholdFcn});

% Order slider
horderlbl = uicontrol('Style','text','String','Polynomial
order:','HorizontalAlignment','left','BackgroundColor',bgclr);
horder = uicontrol('Style','slider','SliderStep',[0.5
0.5],'Min',0,'Max',10,'Value',order,'SliderStep',[0.1
0.1],'Callback',{@OrderFcn});
horderval =
uicontrol('Style','text','String',num2str(order),'BackgroundColor',bgclr);

% Move the GUI to the center of the screen
movegui(hwin,'center');

% Plot a first estimation
[ztmp,atmp,ittmp,order,threshold,costfunction] =
compute(n,y,order,threshold,costfunction);

% Make the GUI visible
set(hwin,'Visible','on');

% Callback functions

    function CancelFcn(source,eventdata)
        % Just close the window
        uiresume(gcbf);
        close(hwin);
    end

    function OKFcn(source,eventdata)
        % Return the current estimation and close the window
        z = ztmp;
        a = atmp;
        it = ittmp;
        ord = order;
        s = threshold;
        fct = costfunction;
        uiresume(gcbf);
        close(hwin);
```

```
    end

    function CostFunctionFcn(source,eventdata)
        % Change cost function
        cf = get(hfct,'Value');
        if cf == 1,
            costfunction = 'sh';
        elseif cf == 2,
            costfunction = 'ah';
        elseif cf == 3,
            costfunction = 'stq';
        elseif cf == 4,
            costfunction = 'atq';
        end
        [ztmp,atmp,ittmp,ord,s,fct] =
compute(n,y,order,threshold,costfunction);
    end

    function OrderFcn(source,eventdata)
        % Change order
        order = get(horder,'Value');
        set(horderval,'String',num2str(order));
        [ztmp,atmp,ittmp,ord,s,fct] =
compute(n,y,order,threshold,costfunction);
    end

    function ThresholdFcn(source,eventdata)
        % Change threshold
        threshold = get(hthreshold,'String');
        threshold = str2double(threshold);
        [ztmp,atmp,ittmp,ord,s,fct] =
compute(n,y,order,threshold,costfunction);
    end

    function [ztmp,atmp,ittmp,order,threshold,costfunction] =
compute(n,y,order,threshold,costfunction)
        % Compute and plot an estimation (need to sort the data)
        [ztmp,atmp,ittmp,order,threshold,costfunction] =
backcor(n,y,order,threshold,costfunction);
        [~,i] = sort(n);
        plot(n(i),y(i),'b-',n(i),ztmp(i),'r-');
    end

    function WinResizeFcn(source,eventdata)
        % Resize the window
        pos = get(hwin,'Position');
        w = pos(3);
        h = pos(4);
        if w>400 && h>100,
            set(haxes,'Position',[40,40,w-320,h-70]);
        end;
        set(hok,'Position',[w-90,30,80,25]);
        set(hcancel,'Position',[w-180,30,80,25]);
        set(hfctlbl,'Position',[w-240,h-30,220,20]);
        set(hfct,'Position',[w-240,h-50,220,25]);
        set(hthresholdlbl,'Position',[w-240,h-80,220,20]);
```

```
        set(hthreshold,'Position',[w-240,h-100,220,20]);
        set(horderlbl,'Position',[w-240,h-130,220,20]);
        set(horder,'Position',[w-210,h-150,190,20]);
        set(horderval,'Position',[w-240,h-150,20,20]);
    end
uiwait(gcf);
end
```

### C.2 Cosmic ray removal

This code uses the native MATLAB function 'findpeaks' to identify cosmic rays and replaces the cosmic ray using linear interpolation.

```
function [intensity_spikeremoved] = removespikes(intensity)
    % Spike detction: Find cosmic spike using 'findpeaks'
        [~, locs] = findpeaks(intensity, 'MaxPeakWidth', 4,
'MinPeakProminence', 1000);
    if ~isempty(locs)
    % Spike removal: establish spike removal region
        smooth_section = zeros(1340,1);

        left = locs(1)-5;
        right = locs(1)+5;
        if left < 0
            left = 1;
        end
        if right > 1339
            right = 1339;
        end
    % Define the cosmic spike: it occurs where the change in intensity
    % exceeds a threshold value
        dIntensitydIndex = diff(intensity);
        threshold = 250;
        % Find the change in intensities that exceed threshold values,
        % i.e., are not smooth (indicated by a 1 in 'smooth_section')
            if left == 0
                left = 1;
            end
            for index = left:right
                smooth_section(index) = abs(dIntensitydIndex(index)) >
threshold;
            end

    % Find the indices of the 'smooth_section' marked false
    % 'diffarray' is used to find a cluster of false values in
'smooth_section'
    % 'array' stores the indices of the cluster of false values, if it
doesn't
    % belong to the cluster, it will be discarded
    % efining the entire spike (start to end)
    % of index values for dI that exceeded threshold
        array = find(smooth_section==1);
        diffarray = diff(array);
        for i = 1:numel(array)-1
            if diffarray(i) > 2
```

```
                if numel(array) >= (i+1)
                    array(i+1) = [];
                else
                end
            end
        end
  % Calculate new values to patch the spike via linear interpolation
        if ~isempty(array)
            slope = (intensity(array(end)+1)-intensity(array(1))) ...
            /(array(end)+1-array(1));
            x_new = 0:numel(array(1):array(end));
            y_new = (slope*x_new)+intensity(array(1));

        % Create new intensity array with spike intensities patched with new
        % values
            intensity_spikeremoved = intensity;
            intensity_spikeremoved([array(1):array(end), array(end)+1]) =
y_new;
        else
            intensity_spikeremoved = intensity;
        end
    else
        intensity_spikeremoved = intensity;
    end

    % Check if there are more spikes
    if numel(locs) > 1
        % Spike removal: establish spike removal region
        smooth_section = zeros(1340,1);

        left = locs(2)-5;
        right = locs(2)+5;
        if left < 0
            left = 1;
        end
        if right > 1340
            right = 1339;
        end
    % Define the cosmic spike: it occurs where the change in intensity
    % exceeds a threshold value
        dIntensitydIndex = diff(intensity);
        threshold = 250;
        % Find the change in intensities that exceed threshold values,
        % i.e., are not smooth (indicated by a 1 in 'smooth_section')
            for index = left:right
                smooth_section(index) = abs(dIntensitydIndex(index)) >
threshold;
            end

    % Find the indices of the 'smooth_section' marked false
    % 'diffarray' is used to find a cluster of false values in
'smooth_section'
    % 'array' stores the indices of the cluster of false values, if it
    % doesn't belong to the cluster, it will be discarded
    % (defining the entire spike (start to end) of index values for dI)
        array = find(smooth_section==1);
```

```
        diffarray = diff(array);
        for i = 1:numel(array)-1
            if diffarray(i) > 2
                if numel(array) >= (i+1)
                    array(i+1) = [];
                end
            end
        end

  % Calculate new values to patch the spike via linear interpolation
        if ~isempty(array)
            if (array(end)+1) <= numel(intensity)
            slope = (intensity(array(end)+1)-intensity(array(1))) ...
            /(array(end)+1-array(1));
                x_new = 0:numel(array(1):array(end));
                y_new = (slope*x_new)+intensity(array(1));

                % Create new intensity array with spike intensities patched
with new
                % values
                intensity_spikeremoved([array(1):array(end), array(end)+1]) =
y_new;
            end
        end
    end
end

% close; plot(array(1):array(end)+1, y_new); hold; plot(intensity);
% hold; plot(intensity);


function [ramanshift_br, intensity_br] = removebaseline(ramanshift,
intensity, ord, s, offset)

% Declare variables
    ord = 15;
    s = 0;
    fcn = 'atq';
    intensity_br = zeros(1, numel(ramanshift));
    ramanshift_br = zeros(1, numel(ramanshift));
    normintensity = zeros(1, numel(ramanshift));
    z_array = zeros(1331,  numel(ramanshift));
    a_array = zeros(ord+1,  numel(ramanshift));

    [z_array,a_array,~,ord,s,~] =
backcor(ramanshift(offset:end),intensity(offset:end),ord,s,fcn);
    intensity_br = intensity(offset:end) - z_array;
    ramanshift_br = ramanshift(offset:end);

end
```

### C.3 Conveniently toggle between matrix indices and wavenumbers

```
% Inputs
      % peak_of_interest - Raman band
```

```
      % ramanbands       - vector of wavenumbers used in the conversion
% Output
      % ramanindex            - matrix index []
function [ramanindex] = peak2index(peak_of_interest, ramanbands)
    x = round(ramanbands(:, 1));
    ramanindex = find(x==peak_of_interest);
end

% Inputs
      % index_of_interest - matrix index
      % ramanbands        - vector of wavenumbers used in the conversion
% Output
      % ramanindex             - ramanpeak [cm-1]
function [ramanpeak] = index2peak(index_of_interest, ramanbands)
    ramanpeak = ramanbands(index_of_interest);
end
```

### C.4 Script for data acquisition during scaling experiment

```
    %This code was written to collect data during an RO experiment using
    %an NI daq (USB-6001) and various 0-5 V sensors (temp, pressure, flow
    %rate)

    %(Single Ended Analog Input)Channel 0 - Feed flow rate sensor
    %(Single Ended Analog Input)Channel 1 - Upstream Pressure sensor 1
    %(Single Ended Analog Input)Channel 5 - Downstream Pressure sensor 2
    %(Differential Analog Input)Channel 2 - Permeate conductivity sensor
    %(Differential Analog Input)Channel 3 - Feed conductivity sensor
%%%%%%%%%%%%%%%%%%%%%%%%%%%% Clear workspace%%%%%%%%%%%%%%%%%%%%%%%%%%%%
clc;
clear;
%% Delete all timers from memory
    listOfTimers = timerfindall;
    if ~isempty(listOfTimers)
        stop(listOfTimers(:));
        delete(listOfTimers(:));
    end
%% To stop the experiment and SAVE DATA
    % RUN backup_data SCRIPT FIRST
    listOfTimers = timerfindall
    stop(listOfTimers)
%% Establish connection between MATLAB and NI DAQ (USB-6001)
%%%%%%%%%%%%%%%%%%%%%%%% Connect MATLAB with NI USB-6001 %%%%%%%%%%%%%%%%%%
    d_usb6001  = daq("ni");                                    % Matlab
recognizes NI DAQ device
        ch0 = addinput(d_usb6001, "Dev2", 0, "Voltage");       % Add voltage
analog input channels
        ch1 = addinput(d_usb6001, "Dev2", 1, "Voltage");       % Add voltage
analog input channels
        ch5 = addinput(d_usb6001, "Dev2", 5, "Voltage");       % Add voltage
analog input channels
            ch1.TerminalConfig = "SingleEnded";
            ch5.TerminalConfig = "SingleEnded";
        ch2 = addinput(d_usb6001, "Dev2", 2, "Voltage");       % Add voltage
analog input channels
```

```
        ch3 = addinput(d_usb6001, "Dev2", 3, "Voltage");      % Add voltage
analog input channels
            ch0.TerminalConfig = "SingleEnded";
            ch2.TerminalConfig = "Differential";
            ch3.TerminalConfig = "Differential";
        addoutput(d_usb6001,"Dev2","Port2/Line0","Digital");  % Add voltage
digital output channels
    d_usb6001.Channels
%% %%%%%%%%%%%%%%%%%%%%  Connect MATLAB with NI TC-01 %%%%%%%%%%%%%%%%%%%%%%
    d_tc01  = daq("ni");                                      % Matlab
recognizes NI DAQ device
        ch_tc01 = addinput(d_tc01,"Dev1", 0, "Thermocouple");
    d_tc01.Channels(1).ThermocoupleType = 'T';
    d_tc01.Channels(1).Units            = 'Celsius';
    d_tc01.Channels
%% Establish connection between MATLAB and Thermotek chiller via serial
communication
%%%%%%% Connect MATLAB with Thermotek chiller's COM port  %%%%%%%%%%%%%%%%%
ports = serialportlist                                     % show list of serial
ports
chillerSerialPort = serialport('COM6', 9600);              % device =
serial('COM3') <-- this doesn't throw an error
                                                           % however, 'serialport'
is recommended
configureTerminator(chillerSerialPort,"CR");               % configure terminator
chillerSerialPort.Terminator;                              % confirm change

%%%%%%%%%%%%%%%%%    Check if connection was set up properly  %%%%%%%%%%%%%
writeline(chillerSerialPort, ".0101WatchDog01");
msg = extract(readline(chillerSerialPort),6);
if double(msg) ~= 0
    disp('Response: ')
    disp(msg)
    error('Error. Double check that the USB cable is connected and the
chiller is on.');
end
%% Find zero stage position
%%%%%%%%%%%%%% ENSURE FLOW CELL IS FULLY LOWERED %%%%%%%%%%%%%%
    disp('Find membrane dot:');
    zaber_initialize('COM4', 61, 7);
%% Setup Raman sampling parameters
%%%%%%%%%%%%%% ENSURE FLOW CELL IS FULLY LOWERED %%%%%%%%%%%%%%
spot_distance = 0.5; % mm
total_distance = 5; % mm
total_spots = round(total_distance/spot_distance);

global location experiment
location = input('Downstream (1) or upstream (0)? ');
experiment = input(strcat('Collecting data for membrane compaction? ...
                          '(y/n, case sensitive) ', 's'));
if experiment == 'y'
   instance1 = [];
end

if location == 1
    downstream = 1;
```

```
    init_position = 92;
    loc_str = 'downstream';
else
    downstream = 0;
    init_position = 32+total_distance;
    loc_str = 'upstream';
end

% Initialize stage position
%     disp(strcat('Initializing stage position to', " ", loc_str));
%     zaber_initialize('COM4', init_position, 6);
%% Establish LightField environment (Princeton Instruments)
% for Raman acquistion
Setup_LightField_Environment;
instance1 = lfm(true);
% experiment_name = input('Name of LightField experiment: ','s');
instance1.load_experiment('20220317-ro-run');
%% Data collection
MakeTimer(d_usb6001, d_tc01, ...
    instance1, experiment, downstream, ...
    init_position, spot_distance, total_spots);
%% Functions I need
function MakeTimer(d_usb6001, d_tc01, ...
    instance1, experiment, downstream, ...
    init_position, spot_distance, total_spots)
%%%%%%%%%%%%%%%%%%%%%%%%%%%%  Declare Variables   %%%%%%%%%%%%%%%%%%%%%%%%%%
    % User input - store file path of data
        backup_data_filepath = input('Where would you like to save the backup
data? ','s');
        raw_raman_filepath = input('Where would you like to export Raman .csv
files? ', 's');
        program_filepath = 'G:\My Drive\Graduate work\Research\(08)
GOALI\(09) RO-data-acquisition';
        total_distance = round(total_spots*spot_distance); % mm
        if true(downstream)
            matfilename = strcat('data_downstream.mat');
        else
            matfilename = strcat('data_upstream.mat');
        end
        save(matfilename, 'raw_raman_filepath', ...
            'backup_data_filepath', ...
            'program_filepath');

    % NI
        frequency = 5; %measurements per second

    % Declare counters to keep track of NI DAQ scans, number of times
    % Arduino serial output is stored, and Raman acquistions
        index_ni = 1; % NI
        numacq = 1; % LightField


%%%%%%%%%%%%%%%%%%%%%%%%%%%%%%%  Create Timers %%%%%%%%%%%%%%%%%%%%%%%%%%%%%%%
    % Create NI timer
        tNI = timer;
        tNI.ExecutionMode  = 'fixedSpacing';
```

```
        tNI.StartFcn       = @niStartFcn;
        tNI.TimerFcn       = @niTimerFcn;
        tNI.StopFcn        = @niStopFcn;
        tNI.Period         = 60;
        tNI.BusyMode       = 'drop';
%         tNI.TasksToExecute = 3;

    % Create LightField timer
        tLF = timer;
        tLF.ExecutionMode  = 'fixedSpacing';
        tLF.StartFcn       = @LightFieldStartFcn;
        tLF.TimerFcn       = @LightFieldTimerFcn;
        tLF.StopFcn        = @LightFieldStopFcn;
        tLF.Period         = 10;
        tLF.BusyMode       = 'queue';
%         tLF.TasksToExecute = 3;

%%%%%%%%%%%%%%%%%%%%%%%%%%%%%% Start Timers %%%%%%%%%%%%%%%%%%%%%%%%%%%%%%%%
if experiment == 'y'
    start(tNI);
else
    start(tLF)
    start(tNI);
end

%%%%%%%%%%%%%%%%%%%% Establish Timer Callback Functions %%%%%%%%%%%%%%%%%%%
    % NI
    function niStartFcn(~,~)
        disp('[NI  DAQ] Starting data acquisition...')
    end
    function niTimerFcn(src, ~)
        % Store data in 'UserData' property of timer object, passed as
        % 'src'. acquired data will be stored in the struct called 'data'
            data = get(src, 'UserData'); % create a struct 'data' that
            % stores data in 'UserData' property of timer object

        % Acquire data
            currentTime = datetime('now');
            % Average data
                Dev1_ai0 = zeros(1, 5);
                Dev2_ai0 = zeros(1, 5);
                Dev2_ai1 = zeros(1, 5);
                Dev2_ai5 = zeros(1, 5);
                Dev2_ai2 = zeros(1, 5);
                Dev2_ai3 = zeros(1, 5);

                for i=1:10
                    scannedData = read(d_usb6001);
                    scannedTemp = read(d_tc01);
                    Dev1_ai0(1, i) = scannedTemp.Dev1_ai0;
                    Dev2_ai0(1, i) = scannedData.Dev2_ai0;
                    Dev2_ai1(1, i) = scannedData.Dev2_ai1;
                    Dev2_ai5(1, i) = scannedData.Dev2_ai5;
                    Dev2_ai2(1, i) = scannedData.Dev2_ai2;
                    Dev2_ai3(1, i) = scannedData.Dev2_ai3;
                    pause(1/frequency)
```

```
                end

                mean_Dev1_ai0 = mean(Dev1_ai0);
                mean_Dev2_ai0 = mean(Dev2_ai0);
                mean_Dev2_ai1 = mean(Dev2_ai1);
                mean_Dev2_ai5 = mean(Dev2_ai5);
                mean_Dev2_ai2 = mean(Dev2_ai2);
                mean_Dev2_ai3 = mean(Dev2_ai3);

        % Store averaged data in variable called data
            data.time(index_ni) = currentTime;
            data.elapsed_time(index_ni) = data.time(index_ni) - data.time(1);
             % Populates nth row of 'temp' column in the 'data' table with
scanned data from channel 'ai0'
             data.temp(index_ni) = mean_Dev1_ai0;
            % Populates nth row of 'flowrate_f' column in the 'data' table
with scanned data from channel 'ai3'
            data.flowrate_f_raw(index_ni) = mean_Dev2_ai0;
                data.flowrate_f_scaled(index_ni) =
VtoLPH(data.flowrate_f_raw(index_ni));
            % Populates nth row of 'pres_upstream' column in the 'data' table
with scanned data from channel 'ai1'
            data.pres_upstream_raw(index_ni) = mean_Dev2_ai1;
                data.pres_upstream_scaled(index_ni) =
VtoPSI(data.pres_upstream_raw(index_ni));
            % Populates nth row of 'pres_downstream' column in the 'data'
table with scanned data from channel 'ai2'
            data.pres_downstream_raw(index_ni) = mean_Dev2_ai5;
                data.pres_downstream_scaled(index_ni) =
VtoPSI(data.pres_downstream_raw(index_ni));
             % Populates nth row of 'pres_downstream' column in the 'data'
table with scanned data from channel 'ai2'
             data.cond_permeate_raw(index_ni) = mean_Dev2_ai2;
                data.cond_permeate_scaled(index_ni) =
VtoCOND(data.cond_permeate_raw(index_ni), 0.1, 180);
            % Populates nth row of 'pres_downstream' column in the 'data'
table with scanned data from channel 'ai2'
            data.cond_feed_raw(index_ni) = mean_Dev2_ai3;
                data.cond_feed_scaled(index_ni) =
VtoCOND(data.cond_feed_raw(index_ni), 1.0, 179);

        % Print scanned data to command window
            fprintf(['[NI  DAQ] Scan #%d \n',...
             '          Elapsed time: %s \n'...
             '          Temperature: %2.2f degC\n'...
             '          Upstream Pressure: %2.2f psi\n'...
             '          Downstream Pressure: %2.2f psi\n'...
             '          Feed flow rate: %2.2f LPH\n',...
             '          Permeate conductivity: %2.2f /muS/cm\n',...
             '          Feed conductivity: %2.2f /muS/cm\n'],...
             index_ni, char(data.elapsed_time(index_ni)),
data.temp(index_ni), ...
             data.pres_upstream_scaled(index_ni), ...
             data.pres_downstream_scaled(index_ni), ...
             data.flowrate_f_scaled(index_ni), ...
             data.cond_permeate_scaled(index_ni), ...
```

```
            data.cond_feed_scaled(index_ni));

        % Update variables
            % update index_ni which tracks which scan you're on
            index_ni = index_ni + 1;
            % store struct 'data' within 'UserData' property of this timer
object
            set(src, 'UserData', data);

    end
    function niStopFcn(src, ~)
        data_ni = get(src, 'UserData');
        delete(tNI)
        save(matfilename, 'data_ni', '-append');
    end

    % LightField
    function LightFieldStartFcn(~, ~)
        disp('Starting Raman acquisition...')
    end
    function LightFieldTimerFcn(src, ~)
        data = get(src, 'UserData');

        % Open shutter to acquire Raman data
            fprintf('Opening shutter in \n');
                for k = 3:-1:1
                    disp(k)
                    pause(1)
                end
            write(d_usb6001, 1);
            pause(1);

        % Acquire Raman data
            instance1.acquire;

        % Close shutter
            pause(1);
            write(d_usb6001, 0);

        % Store acquired Raman data
            extracteddata = extractdata_func(raw_raman_filepath, numacq);
            data.time(numacq) = datetime('now');
            data.elapsedtime(numacq) = data.time(numacq) - data.time(1);
            data.ramanshift(:, numacq) = extracteddata(:,1);
            data.intensity(:, numacq) = extracteddata(:,2);

        % Write to command window
            currentTime = datetime('now');
            fprintf(['[Raman] Scan  #%d completed at %s \n', ...
                    'Elapsed time: %s \n'], ...
                    numacq, char(currentTime), ...
                    char(currentTime - data.time(1)) ...
                    );

        % Move the stage if preset amount of time has pass (keep track
```

```
        % using index_ni)
            spot_dwell = 1; % number of indices to stay at a spot

            % Add total_distance to UserData
                data.total_distance = total_distance;
                data.total_spots = total_spots;
                data.spot_distance = spot_distance;
                spot_number = rem(numacq, total_spots);
                if rem(numacq, spot_dwell*total_spots) > 0
                    if numacq == 1
                       disp('Moved to Spot 1');
                        position = zaber_move_absolute('COM4', init_position,
                        1);
                       data.spot_number(2, numacq) = position;
                    elseif spot_number ~= 0
                       data.spot_number(1, numacq) = spot_number;
                       [position] = zaber_move('COM4', -1*spot_distance, .5);
                       data.spot_number(2, numacq) = position;
                       disp('Moved to next spot');
                    else
                       disp('Stayed at current spot');
                    end
                else
                   disp('Moved back to Spot 1');
                   data.spot_number(1, numacq) = spot_number;
                   position = zaber_move_absolute('COM4', init_position, 1);
                   data.spot_number(2, numacq) = position;
                end

                data.numtasks(1, numacq) = tLF.TasksExecuted;

        % Update counter for number of Raman acquisitions
            numacq = numacq + 1;
            set(src, 'UserData', data);

        % Write to command window that Raman acq is complete
            fprintf('LightField timer complete');
                for k = 3:-1:1
                    disp(k)
                    pause(0.5)
                end
    end
    function LightFieldStopFcn(src, ~)
        data_LF = get(src, 'UserData');
        delete(tLF)
        save(matfilename, 'data_LF', '-append');
    end
end
%% Functions used in Timer Callback Functions
function [psi] = VtoPSI(voltage)
if (voltage > 0.5) && (voltage < 1.5)
    psi = 0   + (voltage-0.5)*(75-0)/(1.5-0.5);
elseif (voltage >=1.5) && (voltage < 2.5)
    psi = 75  + (voltage-1.5)*(150-75)/(2.5-1.5);
else
    psi = 150 + (voltage-2.5)*(225-150)/(3.5-2.5);
```

```
end
end

function [lph] = VtoLPH(voltage)
lph = 2/5*(voltage)*60;
end

function [D] = VtoCOND(V, k, R)
% k - cell constant
% R - resistance that converst the current into voltage (NI DAQ only
% accepts voltages)
% V=IR, so to convert voltage to current, I = V/R
% D - conductivity in uS/cm
switch k
    case 0.1 %CF02 20 to 180
        U4 = 20;
        U20 = 180;
        if V < (R*0.004)
            D = 0;
            disp('Permeate Under Range (20)');
        elseif V > (R*0.02)
            disp('Permeate Over Range (200)');
            D = 180;
        else
            D = ((1/16)*((V/R*1000)-4)*(U20-U4)) + U4;
        end
    case 1 %CF02 200 to 1800
        U4 = 200;
        U20 = 1800;
        if V < (R*0.004)
            D = 0;
            disp('Feed Under Range (200)');
        elseif V > (R*0.02)
            disp('Feed Over Range (2000)');
            D = 1800;
        else
            D = ((1/16)*((V/R*1000)-4)*(U20-U4)) + U4;
        end
end
end

function extracteddata = extractdata_func(data_filepath, numacq)
% current_filepath - the filepath of where the function is originally called
     current_filepath = cd(strcat(data_filepath, '\raw-Raman-data'));

% The function, dir(), is used to create a struct with all the .csv files
% found one folder under data_filepath, denoted by "\*\*.csv"
    dir_array = dir(strcat(data_filepath, '\*\*.csv'));

% readmatrix() turns .csv files into variables. Store these variables
% in the struct 'data'
    % Current folder is \My-system, but to use the function,
readmatrix(file.csv),
    % I need to change the folder to where 'file.csv' is located.
    cd(dir_array(end).folder);
```

```
    % Add a "data" cell to the "files" struct
    extracteddata = readmatrix(dir_array(end).name);

% Change directory back to current_filepath where this function was
originally
% called from
    cd(current_filepath);
end

function [position] = zaber_initialize(COM, init_position, maxspeed)
    import zaber.motion.Library;
    import zaber.motion.ascii.Connection;
    import zaber.motion.Units;

    Library.enableDeviceDbStore();

    % Open a serial port
    connection = Connection.openSerialPort(COM);
    try
        deviceList = connection.detectDevices();
        fprintf('Executing zaber_initialize... Found %d devices.\n',
deviceList.length);

        % The rest of your program goes here
            % Home device
            device = deviceList(1);
                % Access axis handle
                axis = device.getAxis(1);
                % Access settings of axis
                axisSettings = axis.getSettings();
                    % Set the settings of the axis
                    axisSettings.set('maxspeed', maxspeed,
Units.VELOCITY_MILLIMETRES_PER_SECOND)

            axis.home();
            axis.moveAbsolute(init_position, Units.LENGTH_MILLIMETRES);
            position = axis.getPosition(Units.LENGTH_MILLIMETRES)

         connection.close();

    catch exception
        connection.close();
        rethrow(exception);
    end
end

function [position] = zaber_move(COM, distance, maxspeed)
    import zaber.motion.Library;
    import zaber.motion.ascii.Connection;
    import zaber.motion.Units;

    Library.enableDeviceDbStore();
```

```
    % Open a serial port
    connection = Connection.openSerialPort(COM);
    try
        deviceList = connection.detectDevices();
        fprintf('Executing zaber_move... (found %d device(s).)\n',
deviceList.length);


        % The rest of your program goes here
            % Get device
                device = deviceList(1);
                % Access axis handle
                axis = device.getAxis(1);
                % Access settings of axis
                axisSettings = axis.getSettings();
                    % Set the settings of the axis
                    axisSettings.set('maxspeed', maxspeed, ...
                        Units.VELOCITY_MILLIMETRES_PER_SECOND)

            % Move to the 10mm position
                axis.moveRelative(distance, Units.LENGTH_MILLIMETRES);
                position = axis.getPosition(Units.LENGTH_MILLIMETRES)

         connection.close();
    catch exception
        connection.close();
        rethrow(exception);
    end
end

function [position] = zaber_move_absolute(COM, init_position, maxspeed)
    import zaber.motion.Library;
    import zaber.motion.ascii.Connection;
    import zaber.motion.Units;

    Library.enableDeviceDbStore();

    % Open a serial port
    connection = Connection.openSerialPort(COM);
    try
        deviceList = connection.detectDevices();
        fprintf('Executing zaber_initialize... Found %d devices.\n',
deviceList.length);

        % The rest of your program goes here
            % Home device
            device = deviceList(1);
                % Access axis handle
                axis = device.getAxis(1);
                % Access settings of axis
                axisSettings = axis.getSettings();
                    % Set the settings of the axis
                    axisSettings.set('maxspeed', maxspeed, ...
                        Units.VELOCITY_MILLIMETRES_PER_SECOND)
```

```
            axis.moveAbsolute(init_position, Units.LENGTH_MILLIMETRES);
            position = axis.getPosition(Units.LENGTH_MILLIMETRES)

         connection.close();

    catch exception
        connection.close();
        rethrow(exception);
    end
end
```

### C.5 Script for data processing data from a scaling experiment

```
% Summary: cosmic ray/baseline removal, normalization, sync data from NI
% and LF
%%%%%%%%%%%%%%%%%%%%%%%%%%%%%% Workspace setup %%%%%%%%%%%%%%%%%%%%%%%%%%%%%%
    % Housekeeping
    close all;
    clc;
    clear;
    % Change directory to the directory of this particular script
    directory = strcat('C:Enter filepath');
    cd(directory);

    %% Automated: enter desired 'date' and experiment 'id' of data
    % Replace dates and experiment id's with your own
    id_list = {'RRM6A', 'RRM7A', 'RRM8A', 'RRM9A', ...
               'RRM10A', 'RRM11A', 'RRM12A', 'RRM13A', ...
               'RRM14A', 'RRM15A', 'RRM16A', 'RRM17A'};
    [indx,~] = listdlg('ListString',id_list, 'PromptString',...
    'Select experiment ID');
    id = id_list{indx};

    date_list = {'2022 (04) April 19', ...
                 '2022 (04) April 25', ...
                 '2022 (04) April 26', ...
                 '2022 (05) May 05', ...
                 '2022 (05) May 10', ...
                 '2022 (05) May 12', ...
                 '2022 (05) May 16', ...
                 '2022 (05) May 17', ...
                 '2022 (05) May 18', ...
                 '2022 (05) May 31', ...
                 '2022 (06) June 01', ...
                 '2022 (06) June 02'};
    [indx,~] = listdlg('ListString', date_list, 'PromptString',...
    'Select experiment date');
    date = date_list{indx};

    location = input('Location (string ds or us): ');
    %% newFolder: change directory to where the copy of raw data is stored
    newFolder = strcat('C:Enter filepath');
    oldFolder = cd(newFolder);
    %% UPDATE: Load copy of raw data file
    % Click on .mat file of interest
```

```
    disp('Click on .mat file of interest');
    arduino_csv_scaling = strcat('C:\my permeate filepath, date,
'\data.csv');
    arduino_data_scaling = readtable(arduino_csv_scaling);
    arduino_csv_compaction = strcat('C:\my permeate filepath, date,
'\data.csv');
    arduino_data_compaction = readtable(arduino_csv_compaction);
    %% Return to directory of this script
    cd(oldFolder);
%% %%%%%%%%%%%%%%%%%%%%%%%% Build struct for preprocessed data
%%%%%%%%%%%%%%%%%%%%%%
   % Build new .mat file with preprocessed data
        data_preproc = struct();
    %%  Load Raman data
        data_preproc.ramantimestamp = data_LF.time';
        data_preproc.ramanelapsedtime = data_LF.elapsedtime';
        data_preproc.ramanshift_raw = data_LF.ramanshift;
        data_preproc.intensity_raw = data_LF.intensity;
    %% Raman data preprocessing: detect and remove spikes
        for acqnum = 1:numel(data_preproc.ramantimestamp)
            intensity = data_preproc.intensity_raw(:, acqnum);
            [intensity_spikeremoved] = removespikes(intensity);
            data_preproc.intensity_spikeremoved(:, acqnum) =
intensity_spikeremoved;
        end
        %% Populate removed_spectra, numspots
            oldFolder = cd(newFolder);
            removed_spectra = [];
            matfilename = strcat('removed_spectra_', id);
            save(matfilename, 'removed_spectra');
            cd(oldFolder);

        %% Raman data preprocessing: Remove baseline
        ord = 15;
        s = 0;
        offset = 300;
            for acqnum = 1:numel(data_preproc.ramantimestamp)
                ramanshift = data_preproc.ramanshift_raw(:, acqnum);
                intensity = data_preproc.intensity_spikeremoved(:, acqnum);
                [data_preproc.ramanshift_br(:,acqnum),
       data_preproc.intensity_br(:,acqnum)] = ...
                removebaseline(ramanshift, intensity, ord, s, offset);
            end
        %% Raman data preprocessing: Remove irregular Raman spectra
        % Remove spectra with spikes after baseline removal
            % Create variables for 'clean' copies of raman data
            data_preproc.ramantimestamp_brclean =
data_preproc.ramantimestamp;
            data_preproc.ramanelapsedtime_brclean =
data_preproc.ramanelapsedtime;
            data_preproc.ramanshift_brclean = data_preproc.ramanshift_br;
            data_preproc.intensity_brclean = data_preproc.intensity_br;
            numwavenumber = numel(data_preproc.ramanshift_brclean(:,1));
            numacq = numel(data_preproc.ramantimestamp_brclean);

            % Remove spectra specified in 'removed_spectra' array
```

```
            blank_spectra = zeros(numwavenumber, numel(removed_spectra));
            data_preproc.intensity_brclean(:, removed_spectra) =
blank_spectra;

        %% This is only applicable for the automated scanning experiments
        % Sort all indices of spots into an array.
        % For each col, the first row is the absolute position (mm),
        % the remaining rows are the indices
        cd(newFolder)
        start_mm = input('Start absolute position: ');
        end_mm = input('End absolute position: ');

        % Load data into variables
        total_spots = data_LF.total_spots;
        total_spots_adj = total_spots+1;
        spot_distance = data_LF.spot_distance;
        total_distance = data_LF.total_distance;

        i_spots = zeros(round(numacq/total_spots)+1, total_spots);
        spot_position_list = round(fliplr(end_mm:spot_distance:start_mm), 2);
        i_spots(1, :) = spot_position_list;

        for i = 1:numel(spot_position_list)
            num_matches = numel(find(round(data_LF.spot_number(2, :), 2) ...
                                == spot_position_list(rem(i,
total_spots_adj))));
            match_list =        find(round(data_LF.spot_number(2, :), 2) ...
                                == spot_position_list(rem(i,
total_spots_adj)));
            for j = 2:num_matches+1
                i_spots(j, i) = match_list(j-1);
            end
        end

        matfilename = strcat('numspot_', id);
        save(matfilename, 'total_distance', 'total_spots', ...
                          'spot_distance', 'i_spots');
        cd(oldFolder);

    %% UPDATE: Raman data preprocessing
            ramanshift = data_preproc.ramanshift_brclean(:, 2);

            %%%%%%% Define membrane of interest %%%%%%%
            peak_rel = '1149';
            %%%%%%%% Define scalant of interest %%%%%%%
            peak_scalant = {'1008', '1085', '1086', '1090'};
            %%%%%%%%%%%%%%%%%%%%%%%%%%%%%%%%%%%%%%%%%%%

            i_peak_1008 = peak2index(str2double(peak_scalant{1}),
ramanshift);
            i_peak_1085 = peak2index(str2double(peak_scalant{2}),
ramanshift);
            i_peak_1086 = peak2index(str2double(peak_scalant{3}),
ramanshift);
```

```
            i_peak_1090 = peak2index(str2double(peak_scalant{4}),
ramanshift);
            i_peak_rel = peak2index(str2double(peak_rel), ramanshift);
            i_integrate_over_peakrel = i_peak_rel-2:i_peak_rel+2;

            if numel(i_peak_1008) > 1
                i_peak_1008 = i_peak_1008(1);
            end
            if numel(i_peak_1085) > 1
                i_peak_1085 = i_peak_1085(1);
            end
            if numel(i_peak_1086) > 1
                i_peak_1086 = i_peak_1086(1);
            end
            if numel(i_peak_1090) > 1
                i_peak_1090 = i_peak_1090(1);
            end
            if numel(i_peak_rel) > 1
                i_peak_rel = i_peak_rel(1);
                i_integrate_over_peakrel = i_peak_rel-2:i_peak_rel+2;
            end
            peak_1008 = strcat(peak_scalant{1}, 'cm-1');
            peak_1085 = strcat(peak_scalant{2}, 'cm-1');
            peak_1086 = strcat(peak_scalant{3}, 'cm-1');
            peak_1090 = strcat(peak_scalant{4}, 'cm-1');
            peak_rel = strcat(peak_rel, 'cm-1');

        % Raman data preprocessing: Normalization method 1 (membrane peak)
        % and peak find method 1: Normalization by membrane peak
            % Divide by signal intensity of 'peaknorm' aka 'normalizedto'
            data_preproc.normintensity = data_preproc.intensity_brclean./...
            max(data_preproc.intensity_brclean(i_peak_rel,:));

        % Raman data preprocessing: Normalization method 2 (area)
            % peaknorm aka normalizedto
            for i=1:numacq
                  data_preproc.normintensityarea(:, i) =
                  data_preproc.intensity_brclean(:, i)./...
                    trapz(data_preproc.ramanshift_brclean(:, i),...
                    data_preproc.intensity_brclean(:, i));
            end
        % Raman data preprocessing: Normalization method 3 (vector norm)
            % peaknorm aka normalizedto
            for i=1:numacq
                data_preproc.normintensityvec(:,
data_preproc.intensity_brclean(:,
i)./norm(data_preproc.intensity_brclean(:, i));
            end
        % Raman data preprocessing: Normalization method 4 (minmax)
            % peaknorm aka normalizedto
            for i=1:numacq
                minintensity = min(data_preproc.intensity_brclean(:, i));
                maxintensity = max(data_preproc.intensity_brclean(:, i));
                data_preproc.normintensityminmax(:, i) =
(data_preproc.intensity_brclean(:, i)-minintensity)./(maxintensity-
minintensity);
```

```
            end
        % Raman data preprocessing: Normalization method 5 (snv)
            % peaknorm aka normalizedto
            for i=1:numacq
                meanintensity = mean(data_preproc.intensity_brclean(:, i));
                sd = std(data_preproc.intensity_brclean(:, i)-meanintensity);
                data_preproc.normintensitysnv(:, i) =
(data_preproc.intensity_brclean(:, i)-meanintensity)./sd;
            end
    %% Load scaling permeate data
        permeateoffset = 1;
        data_preproc.scalingpermeatetimestamp =
arduino_data_scaling.Var1(permeateoffset:end);
        data_preproc.scalingpermeateelapsedtime =
duration(arduino_data_scaling.Var1(permeateoffset:end)-
arduino_data_scaling.Var1(1));
        data_preproc.scalingpermeate =
arduino_data_scaling.Var6((permeateoffset:end));
        data_preproc.scalingnormpermeate =
data_preproc.scalingpermeate/mean(data_preproc.scalingpermeate(5:10))*100;

    %% Load scaling permeate data
        data_preproc.comppermeatetimestamp =
arduino_data_compaction.Var1(permeateoffset:end);
        data_preproc.comppermeateelapsedtime =
duration(arduino_data_compaction.Var1(permeateoffset:end)-
arduino_data_compaction.Var1(1));
        data_preproc.comppermeate =
arduino_data_compaction.Var6((permeateoffset:end));
        data_preproc.compnormpermeate =
data_preproc.comppermeate/mean(data_preproc.comppermeate(5:10))*100;

%% Load NI data
        data_preproc.nitimestamp = data_ni.time';
        data_preproc.nielapsedtime = data_ni.elapsed_time';
        data_preproc.nitemp = data_ni.temp';
        data_preproc.niflowrate_f_raw = data_ni.flowrate_f_raw';
        data_preproc.niflowrate_f_scaled = data_ni.flowrate_f_scaled';
        data_preproc.nipres_upstream_raw = data_ni.pres_upstream_raw';
        data_preproc.nipres_upstream_scaled = data_ni.pres_upstream_scaled';
        data_preproc.nipres_downstream_raw = data_ni.pres_downstream_raw';
        data_preproc.nipres_downstream_scaled =
data_ni.pres_downstream_scaled';
        data_preproc.nicond_permeate_raw = data_ni.cond_permeate_raw';
        data_preproc.nicond_permeate_scaled = data_ni.cond_permeate_scaled';
        data_preproc.nicond_feed_raw = data_ni.cond_feed_raw';
        data_preproc.nicond_feed_scaled = data_ni.cond_feed_scaled';

%% %%%%%%%%%%%%%% Synchronize timestamps of preprocessed data
%%%%%%%%%%%%%%%%
    % Build new .mat file for synchronized preprocessed data
    data_preproc_synced = struct();
    %% Synchronize Raman, NI DAQ, and permeate data to Raman timestamps
    fns = fieldnames(data_preproc);

    % Create master timetable with timestamps from the Raman data
```

```
            TT_master =
      array2timetable(data_preproc.ramanelapsedtime_brclean, 'RowTimes',
      data_preproc.ramantimestamp_brclean);
        TT_master = renamevars(TT_master, 1, fns{2});

    % Create timetable with timestamps from the LF data
            TT_LF = array2timetable(data_preproc.ramanelapsedtime_brclean,
      'RowTimes', data_preproc.ramantimestamp_brclean);
        TT_LF = renamevars(TT_LF, 1, fns{2});

        % Create timetable with timestamps from the arduino data for permeate
flux
            TT_perm =
      array2timetable(data_preproc.scalingpermeateelapsedtime, 'RowTimes',
      data_preproc.scalingpermeatetimestamp);
        TT_perm = renamevars(TT_perm, 1, fns{17});

        for i=18:20
            TT_perm = addvars(TT_perm, data_preproc.(fns{i}));
            TT_perm = renamevars(TT_perm, rem(i,18)+2, fns{i});
        end

        % Create timetable with timestamps from the NI DAQ data
        TT_ni = array2timetable(data_preproc.nielapsedtime, 'RowTimes',
      data_preproc.nitimestamp);
        TT_ni = renamevars(TT_ni, 1, fns{26});

        for i=27:37
            TT_ni = addvars(TT_ni, data_preproc.(fns{i}));
            TT_ni = renamevars(TT_ni, rem(i,27)+2, fns{i});
        end



    % Synchronize TT_ni and TT_perm to TT_master
        TT_master.Time = dateshift(TT_master.Time,'start','minute');
        TT_LF.Time = dateshift(TT_LF.Time,'start','second');
        TT_ni.Time = dateshift(TT_ni.Time,'start','minute');
        TT_perm.Time = dateshift(TT_perm.Time,'start','minute');
        TT_master = synchronize(TT_LF, TT_ni, TT_perm, 'first', 'previous');


        TT_master(isnan(TT_master.ramanelapsedtime),:) = [];
        data_preproc_synced = data_preproc;
        data_preproc_synced.nitimestamp = TT_master.Time;
        data_preproc_synced.nielapsedtime = TT_master.nielapsedtime;
        data_preproc_synced.nitemp = TT_master.nitemp;
        data_preproc_synced.niflowrate_f_raw = TT_master.niflowrate_f_raw;
        data_preproc_synced.niflowrate_f_scaled =
TT_master.niflowrate_f_scaled;
        data_preproc_synced.nipres_downstream_raw =
TT_master.nipres_downstream_raw;
        data_preproc_synced.nipres_downstream_scaled =
      TT_master.nipres_downstream_scaled;
```

```
        data_preproc_synced.nipres_upstream_raw =
TT_master.nipres_upstream_raw;
        data_preproc_synced.nipres_upstream_scaled =
TT_master.nipres_upstream_scaled;
        data_preproc_synced.nicond_permeate_raw =
TT_master.nicond_permeate_raw;
        data_preproc_synced.nicond_permeate_scaled =
TT_master.nicond_permeate_scaled;
        data_preproc_synced.nicond_feed_raw = TT_master.nicond_feed_raw;
        data_preproc_synced.nicond_feed_scaled =
TT_master.nicond_feed_scaled;

        data_preproc_synced.scalingpermeatetimestamp = TT_master.Time;
        data_preproc_synced.scalingpermeateelapsedtime =
      TT_master.scalingpermeateelapsedtime;
        data_preproc_synced.scalingpermeate = TT_master.scalingpermeate;
        data_preproc_synced.scalingnormpermeate =
TT_master.scalingnormpermeate;
    %% Correct the copy of raw data file
    [datadir, ramanshift, intensity, timestamp] ...
        = extractdata_func(strcat('G:\My Drive\Graduate work\', ...
                            'Research\(07) Data\', ...
                            date, ...
                            '\raw-Raman-data'));

    % Make sure TT_LF is loaded from .mat file
    TT_rawLF = array2timetable(timestamp', 'RowTimes', timestamp');

    TT_master2 = synchronize(TT_LF, TT_rawLF);
    % First two entries are edge cases handled separately
        if ~isnan(TT_master2.ramanelapsedtime(1))
            TT_master2.TasksExecuted(1) = 1;
            count = 1;
        else
            TT_master2.TasksExecuted(1) = 0;
            count = 0;
        end

        if ~isnan(TT_master2.ramanelapsedtime(2))
            TT_master2.TasksExecuted(2) = 1;
            count = count+1;
        else
            TT_master2.TasksExecuted(2) = 0;
            count = count;
        end

    % Rest of the entires are counted in a for loop
        for i = 3:height(TT_master2)
            if ~isnan(TT_master2.ramanelapsedtime(i))
                if TT_master2.TasksExecuted(i-2) == 0
                    count = count+2;
                else
                    count = count+1;
                end
                TT_master2.TasksExecuted(i) = count;
            end
```

```
        end

    % Synchronize the .csv timestamps to the data_LF timestamps
        TT_master2.Time = dateshift(TT_master2.Time, 'start','second');
        TT_master3 = synchronize(TT_master, TT_master2, 'first', 'previous');

    %% Correct data_LF struct
        numDownstream = input(strcat('Enter number of downstream spectra:', "
"));
        for i = 1:height(TT_master3)
                  data_LF.ramanshift(:, i) = ramanshift(:,
      TT_master3.TasksExecuted(i)+numDownstream);
           data_LF.intensity(:, i) = intensity(:,
      TT_master3.TasksExecuted(i)+numDownstream);
        end

    % Last but not least, update data_preproc_synced struct with numTasks
        data_preproc_synced.tLF_TasksExecuted = TT_master3.TasksExecuted;

%% UPDATE: Save preprocessed data for use in processing
    % Change directory to where 'RR##_preproc.mat' is stored
    newFolder = strcat('C:\Save data filepath', date, '\filepath2');
    cd(newFolder);

    matfilename = strcat(id, '_', location, ...
                             '_len', num2str(total_distance), ...
                             '_res', num2str(spot_distance*100), ...
                             '_preproc');
    workspacename = strcat(matfilename, '_workspace');
    save(workspacename);


    cd(oldFolder);

%% Functions
% Data extraction with baseline removal
function [datadir, ramanshift, intensity, timestamp] =
extractdata_func(data_filepath)
% current_filepath - the filepath of where the function is originally called
     current_filepath = cd(data_filepath);

% The function, dir(), is used to create a struct with all the .csv files
% found one folder under data_filepath, denoted by "\*\*.csv"
    datadir = dir(strcat(data_filepath, '\*.csv'));

% readmatrix() turns .csv files into variables. Store these variables
% in the struct 'data'
    numelt = numel(datadir);
    ramanshift = zeros(1340, numelt);
    intensity = zeros(1340, numelt);
    timestamp = NaT(1, numelt);
    for i=1:numelt
        % Current folder is \My-system, but to use the function,
readmatrix(file.csv),
        % I need to change the folder to where 'file.csv' is located.
```

```
        preproc_filepath = cd(datadir(i).folder);

        % Extract data from .csv files using readmatrix
        ramandata = readmatrix(datadir(i).name);

            % Assign extracted data to output variables
                ramanshift(:, i) = ramandata(:,1);
                intensity(:, i) = ramandata(:,2);
                timestamp(1, i) = datetime(datadir(i).date);

        % Change the directory from where file.csv lives back to
preproc_filepath so
        % I can do the same for the next file.csv
        cd(preproc_filepath);
    end

% Change directory back to current_filepath where this function was
originally
% called from
    cd(current_filepath);
end
```